

The background of the image is a world map where the landmasses are colored with a gradient. The colors range from deep blue on the left side (representing cooler temperatures) through cyan, green, yellow, and orange to bright red on the right side (representing warmer temperatures). The map is centered on the Atlantic Ocean, with North and South America on the left and Europe and Africa on the right.

Carbon Cycle Feedbacks and Climate Tipping Behavior

Amber Boot

Carbon Cycle Feedbacks and Climate Tipping Behavior

Amber Boot

February 2024

Copyright © 2024 by Amber Boot

Institute for Marine and Atmospheric research Utrecht (IMAU)
Faculty of Science, Department of Physics, Utrecht University.
Princetonplein 5, 3584 CC Utrecht, The Netherlands.

ISBN: 978-90-393-7645-4

Printed by ProefschriftMaken | | www.proefschriftmaken.nl

Carbon Cycle Feedbacks and Climate Tipping Behavior

Koolstofcyclus Feedbacks en Kantelgedrag in het Klimaat

(met een samenvatting in het Nederlands)

Proefschrift

ter verkrijging van de graad van doctor aan de Universiteit Utrecht op
gezag van de rector magnificus, prof. dr. H.R.B.M. Kummeling, in-
gevolge het besluit van het college voor promoties in het openbaar te
verdedigen op woensdag 3 april 2024 des middags te 4.15 uur

door

Amber Adore Boot

geboren op 13 september 1994

te Ede

Promotor: Prof. dr. ir. H.A. Dijkstra
Copromotor: Dr. A.S. von der Heydt

Beoordelingscommissie: Prof. V. Brovkin
Prof. dr. S.C. Dekker
Prof. dr. S.S. Drijfhout
Prof. dr. C.A. Katsman
Prof. dr. L.J. Lourens

This thesis was accomplished with financial support from the Dutch Ministry of Education, Culture and Science as a part of the Netherlands Earth System Science Centre (NESSC) and organised by the Netherlands Organization for Scientific Research (NWO).

“The search for love continues even in the face of great odds.”

bell hooks

Contents

	Page
Front Matter	
Figures and Tables	v
List of Figures	vii
List of Tables	viii
Frequently used Acronyms	ix
Summary	xi
Samenvatting	xiii
Main Matter	
1 Introduction	1
1.1 The Earth System	3
1.1.1 Tipping points	
1.1.2 Climate change	
1.2 Atlantic Meridional Overturning Circulation	6
1.2.1 Definitions and driving mechanisms	
1.2.2 Multiple equilibria	
1.2.3 Role in the climate system	
1.3 Carbon cycle	10
1.3.1 Global carbon cycle	
1.3.2 Marine carbon cycle	
1.3.3 Carbon cycle modeling	
1.4 Research Questions and Outline.	15
1.4.1 Specific Scientific Questions	
1.4.2 Outline of the Thesis	
2 Methods	21
2.1 The Simple Carbon Project Model v1.0.	23
2.2 The Cimatoribus ocean circulation box model.	25

2.3	Continuation and bifurcation software	27
2.4	The Community Earth System Model v2.	27
2.4.1	The Parallel Ocean Program	
2.4.2	The Marine Biogeochemistry Library	
2.4.3	Other components	
2.4.4	Relevant biases in the CESM2 and MARBL	
2.4.5	Simulations	
3	Effect of the Atlantic Meridional Overturning Circulation on Atmospheric pCO₂ Variations	37
3.1	Introduction.	39
3.2	Methods	41
3.2.1	SCP-M	
3.2.2	Representation of carbon cycle processes and feedbacks	
3.2.3	Parameter continuation methodology	
3.3	Results.	45
3.3.1	Sensitivity of atmospheric pCO ₂ to the AMOC	
3.3.2	Coupling AMOC - carbon cycle	
3.3.3	Internal oscillation	
3.4	Summary and discussion.	54
4	Potential effect of the marine carbon cycle on the multiple equilibria window of the Atlantic Meridional Overturning Circulation	59
4.1	Introduction.	61
4.2	Methods	62
4.2.1	Coupled model	
4.2.2	Solution method	
4.3	Results.	65
4.3.1	CMIP6 freshwater fluxes	
4.3.2	The AMOC multiple equilibria window	
4.3.3	Sensitivity to total carbon content	
4.4	Summary and discussion.	70
5	Effect of plankton composition shifts in the North Atlantic on atmospheric pCO₂	75
5.1	Introduction.	77
5.2	Method	79
5.3	Results.	80
5.4	Summary and discussion.	86
6	Response of atmospheric pCO₂ to a strong AMOC weakening under low and high emission scenarios	89
6.1	Introduction.	91
6.2	Method	92

6.3 Results	93
6.3.1 Climate response	
6.3.2 Marine carbon cycle response	
6.3.3 Terrestrial carbon cycle response	
6.3.4 Total response	
6.4 Summary and discussion	104
7 Summary, Conclusion and Outlook	107
7.1 Summary	109
7.2 Conclusion	114
7.3 Outlook	115
Back Matter	
Appendices:	117
A SCP-M parameter values	117
A.1 Parameter values	117
B Parameter values and model equations for the coupled carbon cycle - ocean circulation box model	123
B.1 Additional couplings, feedbacks and simulations	123
B.2 Model parameters	126
B.3 Model equations	128
C List of CMIP6 models used in Chapter 4	131
D Additional results NCAR SSP5-8.5 simulation	133
E Additional results IMAU CESM2 simulations	139
Bibliography	151
Acknowledgements	166
List of Publications	169
Curriculum Vitae	171

Figures and Tables

List of Figures

1 Introduction

1.1	The Earth System	4
1.2	Cenozoic temperature record	6
1.3	GHG concentrations and GMST record	7
1.4	AMOC bifurcation diagram	9
1.5	Global carbon cycle	11
1.6	Marine carbon pumps	13
1.7	Seawater carbonate chemistry	14
1.8	Coupled system of interest	17

2 Methods

2.1	Simple Carbon Project Model v1.0	24
2.2	Cimatoribus box model	26
2.3	Pseudo-arc length method in AUTO	28
2.4	Structure CESM2	29
2.5	Bathymetry and topography in CESM2	30
2.6	Structure MARBL	31
2.7	Historical CO ₂ concentrations	34
2.8	SSP emissions	35
2.9	Hosing region	35

3 Effect of the Atlantic Meridional Overturning Circulation on Atmospheric pCO₂ Variations

3.1	Reference bifurcation diagram	46
3.2	Sensitivity to AMOC strength	47
3.3	Sensitivity to carbon cycle parameters	49
3.4	Internal oscillation	51
3.5	Mechanism of the internal oscillation	52
3.6	CO ₂ , alkalinity and its sinks and sources	53

4 Potential effect of the marine carbon cycle on the multiple equilibria window of the Atlantic Meridional Overturning Circulation

4.1 Coupled box model	63
4.2 CMIP6 analysis	66
4.3 Bifurcation diagram	68
4.4 System sensitivity to E_s	69
4.5 Sensitivity to changes in total carbon	70
4.6 Mechanisms	72

5 Effect of plankton composition shifts in the North Atlantic on atmospheric $p\text{CO}_2$

5.1 Ocean-atmosphere CO_2 exchange	81
5.2 Net Primary Production and Export Production	82
5.3 Net Primary Production per Plankton Functional Type	83
5.4 Limitation and growth rate per Plankton Functional Type	84
5.5 Biological fluxes and feedback strength	85
5.6 Feedback mechanism	86

6 Response of atmospheric $p\text{CO}_2$ to a strong AMOC weakening under low and high emission scenarios

6.1 Climate response	94
6.2 Surface Air Temperature response	95
6.3 Ocean-atmosphere CO_2 exchange integrated over 2016-2100	96
6.4 Transient response of ocean-atmosphere CO_2 exchange	96
6.5 Carbon cycle response	97
6.6 Zonally averaged DIC concentrations	99
6.7 Zonally averaged PO_4^{3-} concentrations	99
6.8 Net Biosphere Production integrated over 2016-2100	101
6.9 Transient Net Biosphere Production response	101
6.10 Mechanism	104

B Parameter values and model equations for the coupled carbon cycle - ocean circulation box model

B.1 Bifurcation diagram additional cases	125
--	-----

D Additional results NCAR SSP5-8.5 simulation

D.1 CO_2 emissions and concentration	133
D.2 Reservoir distribution of CO_2 emissions	134
D.3 Ocean-atmosphere CO_2 exchange integrated	134
D.4 Sea Surface Temperature	134
D.5 Mixed Layer Depth	135
D.6 AMOC strength	135
D.7 Stratification	135
D.8 e-ratio	136

D.9	Advection of small phytoplankton biomass	136
D.10	Advection of diatom biomass	137
D.11	Phytoplankton biomass	137

E Additional results IMAU CESM2 simulations

E.1	Precipitation	140
E.2	Zonal wind stress	140
E.3	Arctic ice fraction	141
E.4	Antarctic ice fraction	141
E.5	Net Primary Production	142
E.6	Sea Surface Temperature	142
E.7	Sea Surface Salinity	143
E.8	Stratification	143
E.9	Upwelling velocities	144
E.10	PO_4^{3-} concentration	144
E.11	DIC concentration	145
E.12	Alkalinity concentration	145
E.13	DIC upwelling flux	146
E.14	PO_4^{3-} upwelling flux	146
E.15	Surface pH	147
E.16	Biomass loss due to fire	147
E.17	Gross Primary Production	148
E.18	Active layer thickness	148
E.19	Soil respiration	149
E.20	AMOC structure	149

List of Tables

2 Methods

2.1	Parameter values SCP-M for two configurations	25
-----	---	----

3 Effect of the Atlantic Meridional Overturning Circulation on Atmospheric pCO₂ Variations

3.1	Overview of cases	45
-----	-----------------------------	----

4 Potential effect of the marine carbon cycle on the multiple equilibria window of the Atlantic Meridional Overturning Circulation

4.1	Overview of cases	67
-----	-----------------------------	----

A SCP-M parameter values

A.1	Model parameters used in Chapter 3	118
A.2	Dimensions of boxes	119
A.3	Other parameters used in Chapter 3	120
A.4	Equilibrium constants	121

B Parameter values and model equations for the coupled carbon cycle - ocean circulation box model

B.1	Additional cases	124
B.2	Ocean circulation box model parameters	126
B.3	Ocean circulation box model parameters changed or added	127
B.4	Carbon cycle box model parameters that are changed	127

C List of CMIP6 models used in Chapter 4

C.1	CMIP6 model list	132
-----	----------------------------	-----

List of Frequently used Acronyms

Alk	Alkalinity
AUTO	AUTO-07p
AMOC	Atlantic Meridional Overturning Circulation
CaCO₃	Calcium carbonate
CO₃²⁻	Carbonate ion
AMOC	Atlantic Meridional Overturning Circulation
CESM2	Community Earth System Model v2
CICE5	Community Ice Code v5.1.2
CAM6	Community Atmosphere Model v6
CLM5	Community Land Model v5
CMIP	Coupled Model Inter-comparison Project
CMIPx	Coupled Model Inter-comparison Project phase x (5, 6 or 7)
DIC	Dissolved Inorganic Carbon
EP	Export Production at 100 m depth
ESM	Earth System Model
GMST	Global Mean Surface Temperature
GPP	Gross Primary Production
GOC	Global Overturning Circulation
HB	Hopf bifurcation
IPCC	Intergovernmental Panel on Climate Change
ITCZ	Intertropical Convergence Zone
LGM	Last Glacial Maximum
MARBL	Marine Biogeochemistry Library
MEW	Multiple Equilibria Window
MLD	Mixed Layer Depth
NBP	Net Biosphere Production
NPP	Net Primary Production

NPZD	Nutrient - Phytoplankton - Zooplankton - Detritus
pCO₂	Partial pressure of CO ₂
PFT	Plankton Functional Type
pH	$-\log_{10}$ of the hydrogen ion concentration
PI	Pre-industrial
PO₄³⁻	Phosphate
POM	Particulate Organic Matter
POP	Parallel Ocean Program
RCP	Representative Concentration Pathway
SCP-M	Simple Carbon Project Model v1.0
SAT	Sea Air Temperature
SSP	Shared Socioeconomic Pathway
SST	Sea Surface Temperature
Sv	Sverdrup (1 Sv \equiv 10 ⁶ m s ⁻¹)

English Summary

The Earth System is a non-linear system with many different non-linear components that act on different timescales. In some of these components there are tipping elements that can show tipping behavior. Tipping points can be defined as relatively fast and large changes in a component of the Earth System compared to changes in its forcing. Tipping can result in large disturbances in the system and pose a large risk to the Earth System as we know it due to the large consequences involved.

An important component in the Earth System is the carbon cycle, often divided in a marine and terrestrial cycle. The carbon cycle regulates atmospheric CO₂ concentrations and is therefore important in regulating Earth's temperature and climate. In this thesis, we mainly focus on the marine part of the carbon cycle and its interaction with atmospheric pCO₂. The marine carbon cycle is a non-linear system where biological, chemical and physical processes are important on timescales ranging from a day to a million years. These processes are coupled to the physical climate system. They depend on, for example, ocean circulation, water temperature and salinity, which in turn are influenced by atmospheric forcings such as wind and precipitation.

In the ocean, an important circulation system is the Atlantic Meridional Overturning Circulation (AMOC). The AMOC is a potential tipping element in the Earth System with possibly multiple equilibria: an on- and an off-state. In the on-state, there is a strong AMOC transporting warm waters from the South Atlantic Ocean to the North Atlantic Ocean. This net heat transport northwards is important for modulating global, and especially, European climate. The AMOC can tip from an on- to an off-state. In an off-state, the AMOC is weak or non-existent, meaning the northward transport stops with a large response in the climate system as a result.

In this thesis, we study these two components of the Earth System, the (marine) carbon cycle and the AMOC. We want to answer the following three questions regarding these components:

1. Are there tipping points in the (marine) carbon cycle?
2. How do the marine carbon cycle and the AMOC interact in the climate system on long (i.e. 10³ - 10⁶ years) timescales?
3. How do the marine carbon cycle and the AMOC interact in the climate system under future climate change?

We study the first two questions with simple box models and parameter continuation techniques, whereas the third question is studied using simulations of the Community Earth System Model v2 (CESM2), a state-of-the-art Earth System Model.

We have studied the first question by extensively scanning the parameter space in a simple carbon cycle box model. To represent non-linear interactions necessary for tipping behavior, we have included multiple non-linear feedbacks in the model. We did not find tipping points in the marine carbon cycle. However, we did find an internal oscillation with a period of 5,000 to 6,000 years which might be relevant for studying atmospheric $p\text{CO}_2$ variations in past climates.

By varying the AMOC strength in the same box model we were able to study its effect on atmospheric $p\text{CO}_2$. We found that the AMOC strength had little effect on atmospheric $p\text{CO}_2$ on long timescales. We varied several parameters over a large range to test how sensitive atmospheric $p\text{CO}_2$ is to changes in these parameters when the AMOC strength is a function of atmospheric $p\text{CO}_2$, and again a low sensitivity was found. When we used a similar model with an AMOC that is able to tip from an on- to an off state and vice versa, we found that when the AMOC tips, atmospheric $p\text{CO}_2$ changes by 25 to 40 ppm. Furthermore, we found that the marine carbon cycle can influence the window that the AMOC has multiple equilibria when a coupling between atmospheric $p\text{CO}_2$ and atmospheric freshwater transport is introduced.

When studying future climate change, different processes are relevant compared to the main processes relevant on long timescales. Because we study the system on much shorter timescales, i.e. multi-decadal to centennial, we can use a much more complex model. We found that under climate change, the marine ecosystem can provide a relatively strong positive feedback to atmospheric $p\text{CO}_2$ through a phytoplankton composition shift. We found that large phytoplankton (diatoms) are replaced with smaller phytoplankton in the North Atlantic under climate change, resulting in a lower efficiency of the biological carbon pump in transporting carbon to the deep ocean. As a consequence, the uptake capacity of the ocean decreases, and more carbon remains in the atmosphere to raise atmospheric $p\text{CO}_2$. We also found a positive feedback between atmospheric $p\text{CO}_2$ and the AMOC. We found that as the AMOC weakens, atmospheric $p\text{CO}_2$ increases creating a positive feedback loop. However, the found feedback was very small because of compensating effects within the carbon cycle and between different regions. Even though the global response was small, locally large changes occurred in climate and carbon cycle variables.

To conclude, in this thesis we have looked at the interactions between the marine carbon cycle and the AMOC in the climate system. Compensating effects in the carbon cycle and between regions make atmospheric $p\text{CO}_2$ quite insensitive to changes in the AMOC. As a consequence, no large global response of atmospheric $p\text{CO}_2$ is expected when the AMOC tips based on this research. However, locally the changes can be severe for both the climate and the local carbon cycle potentially threatening society and both marine and terrestrial ecosystems.

Samenvatting in het Nederlands

Het Systeem Aarde is een non-lineair systeem met verschillende non-lineaire componenten die actief zijn op verschillende tijdschalen. In sommige van deze componenten zijn er elementen aanwezig die kantelgedrag kunnen vertonen. 'Kantelen' kan gedefinieerd worden als relatief snelle en grote veranderingen in een systeem ten opzichte van de forcering van het systeem. Kantelpunten kunnen resulteren in grote verstoringen in het systeem en vormen een groot risico voor het Systeem Aarde vanwege de grote gevolgen.

Een belangrijke component in het Systeem Aarde is de koolstofcyclus. De koolstofcyclus reguleert atmosferische CO₂ concentraties en is daarom belangrijk in het reguleren van de temperatuur en het klimaat op Aarde. In dit proefschrift ligt de aandacht voornamelijk op hoe de oceanische cyclus en atmosferische CO₂ concentraties op elkaar inwerken. De oceanische koolstofcyclus is een non-lineair systeem met biologische, chemische en fysische processen die werken op dagelijkse tijdschalen tot tijdschalen op een miljoen jaar. Deze processen zijn gekoppeld aan het fysieke klimaatsysteem en hangen, bijvoorbeeld, af van de oceaan circulatie, de temperatuur en het zoutgehalte van het water, die op hun beurt weer beïnvloed worden door atmosferische forceringen als wind en precipitatie.

In de oceaan is de Atlantic Meridional Overturning Circulation (AMOC), zoals deze in het Engels genoemd wordt, een belangrijke stroming. De AMOC is een mogelijk kantel element in het Systeem Aarde met mogelijk meerdere evenwichten: een aan-staat en een uit-staat. In de aan-staat transporteert de AMOC warm water van de Zuid Atlantische Oceaan naar de Noord Atlantische Oceaan. Dit netto warmte transport in noordelijke richting is belangrijk voor het reguleren van het globale, en voornamelijk, het Europese klimaat. De AMOC kan kantelen van een aan-staat naar een uit-staat waardoor het noordwaartse transport stopt met een grote reactie in het klimaat systeem als gevolg.

In dit proefschrift bestuderen we deze twee componenten in het Systeem Aarde: de oceanische koolstofcyclus en de AMOC. We pogen de volgende drie vragen over deze componenten te beantwoorden:

1. Zijn er kantelpunten in de oceanische koolstofcyclus?
2. Hoe beïnvloeden de oceanische koolstofcyclus en de AMOC elkaar in het kli-

maat systeem op lange (10^3 - 10^6 jaar) tijdschalen?

3. Hoe beïnvloeden de oceanische koolstofcyclus en de AMOC elkaar onder toekomstige klimaat verandering?

We bestuderen de eerste twee vragen met simpele ‘box’ modellen en parameter continueringstechnieken. De derde vraag is bestudeerd door gebruik te maken van simulaties van het klimaatmodel het Community Earth System Model v2 (CESM2).

Door in een simpel model met meerdere non-lineaire feedbacks de parameter ruimte uitgebreid te scannen hebben we gekeken naar de eerste vraag. We hebben geen kantelpunten in de oceanische koolstofcyclus kunnen vinden. Wel hebben we een interne oscillatie gevonden met een periode van 5.000 tot 6.000 jaar die mogelijk relevant is om het klimaat van het verleden te begrijpen.

Door de sterkte van de AMOC te variëren in hetzelfde model, kunnen we kijken naar het effect van de AMOC op atmosferische $p\text{CO}_2$. De resultaten laten zien dat de AMOC weinig invloed heeft of de CO_2 concentratie op lange tijdschalen, ook als variabelen in de koolstofcyclus sterk gevarieerd worden. Als de AMOC kantelt zien we wel een effect op CO_2 concentraties. Deze daalt met 25-40 ppm als de AMOC van een aan- naar een uit-staat gaat. Het gebied waar de AMOC meerdere evenwichten heeft, kan worden beïnvloed door de koolstofcyclus door een koppeling tussen CO_2 en zoetwater transport in de atmosfeer.

Voor het bestuderen van toekomstige klimaatverandering zijn andere processen relevant vergeleken met de relevante processen op lange tijdschalen. Omdat we het systeem onderzoeken op kortere tijdschalen, namelijk tientallen tot honderd jaar, kunnen we een veel complexer model gebruiken. Hier vinden we dat onder klimaatverandering, mariene ecosystemen een relatief sterke positieve feedback kunnen geven op atmosferische CO_2 concentraties door een wijziging van dominant phytoplankton soort. We laten zien dat grote phytoplankton (diatomeeën) vervangen worden door kleine phytoplankton in de Noord Atlantische Oceaan waardoor de biologische koolstof pomp minder efficiënt werkt om koolstof naar de diepe oceaan te transporteren. Dit heeft als gevolg dat de oceaan minder koolstof op kan nemen en dat de atmosferische CO_2 concentratie groeit. We hebben ook een positieve feedback gevonden tussen CO_2 en de AMOC. Als de AMOC zwakker wordt, zien we een toename in CO_2 concentraties. Echter, deze feedback is heel erg klein omdat er veel compenserende effecten zijn in de koolstofcyclus zelf, maar ook tussen verschillende regio's. De globale respons is klein, maar lokaal kunnen er grote veranderingen voorkomen in belangrijke klimaat en koolstofcyclus variabelen.

In dit proefschrift hebben we gekeken naar de interacties tussen de oceanische koolstofcyclus en de AMOC in het klimaatsysteem. Verschillende compenserende effecten zorgen ervoor dat de atmosferische CO_2 concentratie vrij ongevoelig lijkt te zijn voor veranderingen in de AMOC. Dit heeft als gevolg dat, gebaseerd op dit onderzoek, er geen groot effect wordt verwacht op de CO_2 concentratie als de AMOC kantelt. Echter, lokaal kunnen de effecten desastreus zijn voor de samenleving en ecosystemen door groten veranderingen in het klimaat en de koolstofcyclus.

Introduction

The Earth's climate is warming due to rising greenhouse gas concentrations in the atmosphere caused by anthropogenic emissions. How much the climate will warm depends on future emissions, and how sensitive the Earth System is to the rise in greenhouse gas concentrations. It is the responsibility of the scientific community to provide the public and policymakers with reliable assessments to inform decision making. This is challenging because of several reasons. One of these reasons is that the Earth System is a non-linear system in which not all processes are fully understood yet. An important example of non-linearities in the Earth System are so-called tipping points. Tipping points are relatively large and fast changes in a component of the Earth System compared to its forcing changes. Naturally, passing such a tipping point poses a large risk since the effects can be very disruptive. As the climate changes due to anthropogenic activities, the probability that a tipping point is passed in the foreseeable future increases.

In this thesis, we focus on interactions in the Earth System between the carbon cycle, a system important for regulating the temperature on Earth, and the Atlantic Meridional Overturning Circulation (AMOC), a tipping element. The carbon cycle is a non-linear system where physical, biological and chemical processes are at play on a wide range of timescales. Throughout the Cenozoic (i.e. the past 66 Ma), the carbon cycle and Earth's climate have been tightly coupled. The AMOC is important for the Earth's heat budget and climate since it transports heat from the Southern Hemisphere to the Northern Hemisphere. However, the AMOC can tip into an off-state in which this heat transport is disrupted causing dramatic changes in several climate variables. The AMOC and carbon cycle can interact through many processes, but the exact mechanisms and timescales involved are complex. These interactions

are studied in this thesis on different timescales.

In this introduction an overview of the Earth System, tipping elements in the Earth System, and changes in the climate over the Cenozoic is provided. Next, we describe both the AMOC and the marine carbon cycle, the two elements in the Earth System which are at the center of this thesis. The introduction is finalized with the research questions covered in this thesis.

1.1 The Earth System

The Earth System is a non-linear system consisting of several components: the atmosphere, the cryosphere, the land, the lithosphere and the ocean (Fig. 1.1). The different components are coupled and share several feedbacks that act on different timescales (von der Heydt et al., 2021).

The atmosphere is an important component of the Earth System. Physical and chemical processes regulate the weather and climate on timescales starting at a few seconds (e.g. turbulence) to sub-annual variability (e.g. the North Atlantic Oscillation). Another reason why the atmosphere is important, is that it enables feedbacks between the other components in the Earth System, e.g. carbon emitted from the ocean can be taken up by the terrestrial biosphere through the atmosphere and vice versa.

The cryosphere covers all frozen water on Earth, e.g. sea ice, ice shelves, ice sheets and glaciers. Most elements in the cryosphere are active on multi-millennial timescales since it takes a long time to grow and melt large ice sheets and glaciers. Ice affects the climate through the albedo effect (i.e. the light surface of snow and ice reflects a lot of radiation) and is important for regulating global mean sea level. The land is a complex component where there is a whole array of different processes at play. There are, for example, the terrestrial biogeochemical cycles that are affected by different vegetation types, soil processes, agriculture and other anthropogenic influences. Since there are so many different processes, the timescales involved vary from seasonal to multi-millennial.

The lithosphere is the slowest system involving processes such as the lithification of ocean sediments, weathering and volcanism. This component regulates the Earth's climate on timescales of 10^5 - 10^6 years. Feedbacks involving the lithosphere are hypothesized to be the reason that the Earth's climate has remained fairly bounded over the Cenozoic (Caves et al., 2016).

The final component is the ocean. The ocean is active on timescales ranging from seasonal to multi-millennial and is the most important component on centennial to multi-millennial timescales. In the ocean there are the wind and density driven ocean circulation as well as ecosystems that have several functions such as the transport of carbon to the deep ocean and providing a food source to humans.

In this thesis we will mainly focus on the ocean. We also focus on the carbon cycle, which is active in the atmosphere, on the land and in the lithosphere acting on timescales ranging from sub-annual to millions of years. We will therefore make use of models that capture processes of these components as well.

1.1.1 Tipping points

Climate subsystems can show so-called tipping behavior by crossing a tipping point. These subsystems are also called tipping elements and are present in several components of the Earth System. In the sixth assessment report of the IPCC (IPCC, 2021) a tipping point is defined as 'a critical threshold beyond which a system reorganizes,

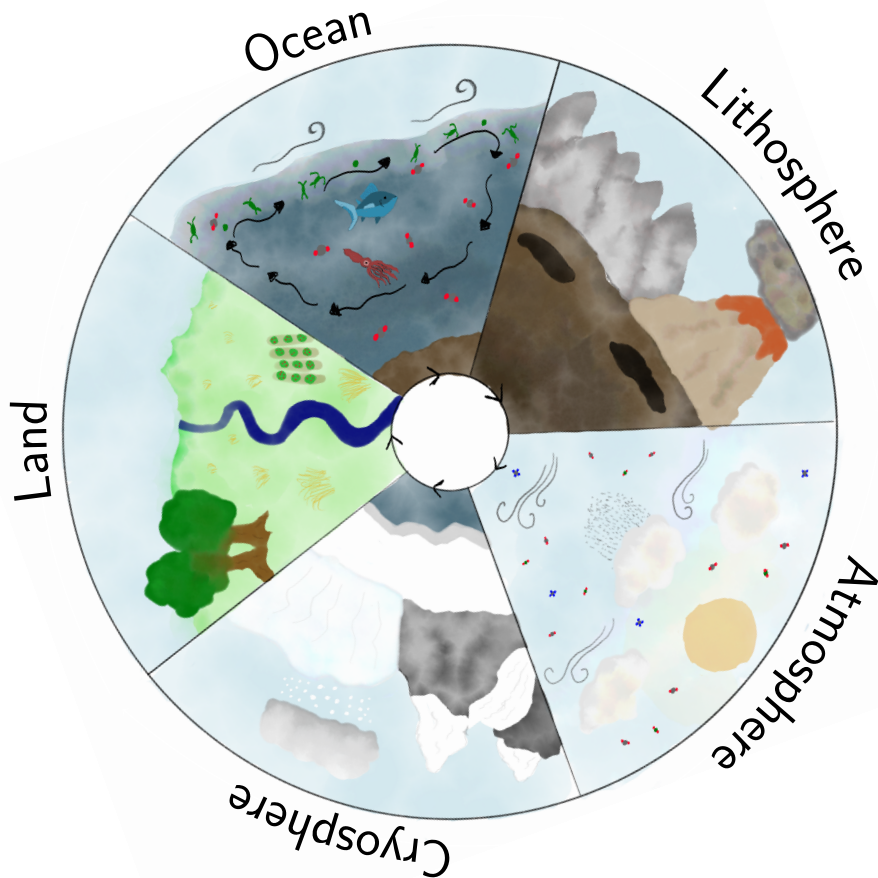


Figure 1.1: Illustration of the Earth System and its coupled components. The main focus in this thesis is on the ocean, but the carbon cycle is also present in the other four components.

often abruptly and/or irreversibly'. In literature, more comprehensive definitions of tipping points are also used (e.g. Lenton et al., 2008). From a dynamical systems point of view, tipping points can be viewed as crossing a bifurcation point such as a saddle node bifurcation (Kaszás et al., 2019). Crossing these bifurcations are often associated with subsystems with multiple (stable) equilibria. The paleo record shows several large abrupt changes over the Cenozoic that are often associated with tipping points. Under anthropogenic climate change the risk of crossing tipping points, which can have long (multi-millennial) effects on the Earth System, increases (e.g. Armstrong-McKay et al., 2022; Lenton et al., 2008).

Important tipping elements are the Greenland, West-Antarctic and East-Antarctic ice sheets, arctic sea-ice cover, and permafrost melt. In the ocean the major tipping element is the Atlantic Meridional Overturning Circulation (AMOC), but also low latitude coral reefs have been identified as tipping elements. Over the land the major tipping elements are diebacks of the Amazonian rainforest and boreal forests.

Armstrong-McKay et al. (2022) have identified the warming thresholds for these tipping elements, some of which (e.g. the Greenland Ice Sheet) are around the current warming levels. Timescales involved with these tipping elements range from multi-decadal (e.g. coral reefs) to multimillennial (e.g. the ice sheets).

The tipping elements are also coupled to each other, meaning that when one component in the Earth System tips, it can influence the tipping probability of other elements. When passing one tipping point increases the likelihood that a different tipping point is passed as well, so-called tipping cascades can occur (Dekker et al., 2018). There is still a large uncertainty around tipping cascades, but obviously these cascades can have a large disruptive effect on human society and ecosystems. It is therefore of vital importance to prevent tipping points and tipping cascades from occurring.

1.1.2 Climate change

Climate change has occurred constantly throughout the Earth's history on various timescales (Fig. 1.2). In the Cenozoic the Earth went from a hothouse with CO₂ concentrations up to 1500 ppm and without permanent polar ice sheets in the Paleocene to an icehouse in the Pleistocene and Holocene with CO₂ concentrations as low as 180 ppm, including permanent polar ice sheets (Rae et al., 2021). These changes have occurred over millions of years. However, on top of this trend, shorter climatic changes have occurred such as the hyperthermal events in the Paleocene and Eocene, the Eocene-Oligocene transition, and the glacial-interglacial cycles in the Pleistocene. The paleo record shows many of these climatic changes that can be associated with strong positive feedbacks in the Earth System (e.g. the hyperthermals in the Paleocene and Eocene; Arnscheidt & Rothman, 2021), or are paced by orbital forcing (e.g. the glacial-interglacial cycles; Hays et al., 1976). The proxy records clearly show that the Earth System is a highly non-linear system on a whole range of timescales where the temperature and carbon cycle are tightly coupled (Westerhold et al., 2020). The changes we are currently experiencing in the Anthropocene, however, are unprecedentedly fast and large.

The climate change in the Anthropocene (Fig. 1.3) is caused by emissions of greenhouse gasses such as carbon dioxide (CO₂), methane (CH₄) and nitrous oxide (N₂O) by human activity. Since the start of the industrial revolution, CO₂ concentrations in the atmosphere have increased more than 50%, CH₄ concentrations have more than doubled, and N₂O concentrations have increased by 25% (Fig. 1.3). The increase in these concentrations have caused a radiative imbalance for the Earth leading to net warming. Compared to the pre-industrial (PI), Global Mean Surface Temperature (GMST) now has warmed by approximately 1.2°C, leading to various other changes in the climate system. Examples of these changes are melting of sea-ice, glaciers and ice sheets; changes in ocean circulation; changes in weather patterns and weather extremes; sea level rise by thermal expansion of the seawater and land ice; bleaching of coral reefs due to higher temperatures and lower pH; and many more (IPCC, 2021). All these effects are a major threat for many ecosystems on our planet and a major challenge for human societies (IPCC, 2022).

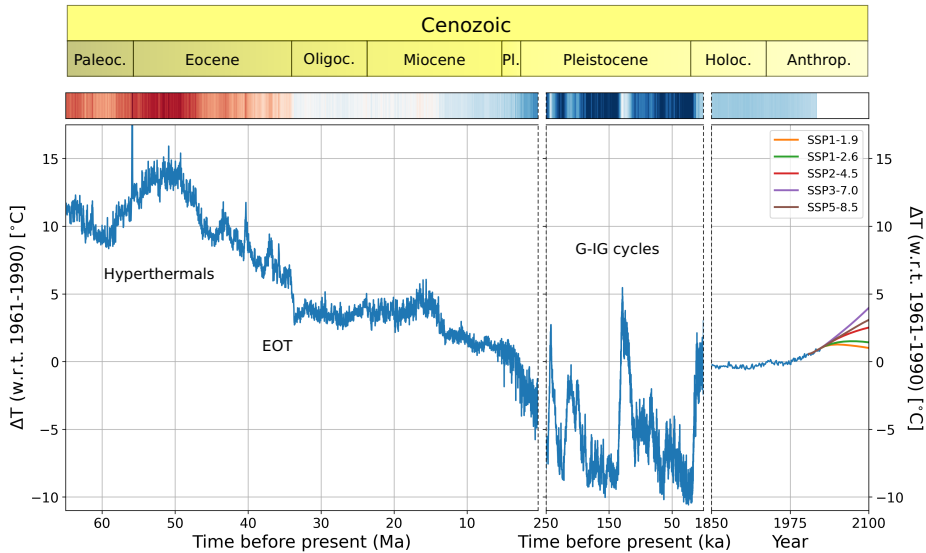


Figure 1.2: Temperature anomalies with respect to the mean temperature between 1961 and 1990 in °C over the past 65 million years including projections up to 2100 based on 5 different SSP scenarios. The different epochs are denoted in the yellow bar. The climate stripes also represent the temperature record where white colors represent a temperature anomaly of 4°C. Note the different scaling and units on the time-axis. Abbreviated epochs are the Oligocene (Oligoc.), the Pliocene (Pl.), the Holocene (Holoc.) and the Anthropocene (Anthrop.). Source of data: the CENOGRID database (65 Ma - 0.25 Ma; Westerhold et al., 2020), EPICA Dome C (250 ka - 1850; Jouzel et al., 2007), HadCRUT5 (1850-2014; Morice et al., 2021), and Riahi et al. (2017)(2015-2100).

1.2 Atlantic Meridional Overturning Circulation

1.2.1 Definitions and driving mechanisms

The Atlantic Meridional Overturning Circulation (AMOC) is defined as the zonally integrated meridional volume transport in the Atlantic Ocean (Buckley & Marshall, 2016). It is an important part of the deep ocean circulation and a pathway connecting the surface ocean with the deep ocean. It consists of two cells: (1) an upper cell with clockwise circulation flowing northward at the surface and southward at depth; and (2) a bottom cell with anti-clockwise circulation flowing northward in the deep ocean. The upper cell involves deep water formation in the North Atlantic and is therefore sometimes also called the North Atlantic Deep Water (NADW) cell, and the bottom cell involves deep water formation in the Southern Ocean and is therefore also known as the Antarctic Bottom Water (AABW) cell (Kuhlbrodt et al., 2007).

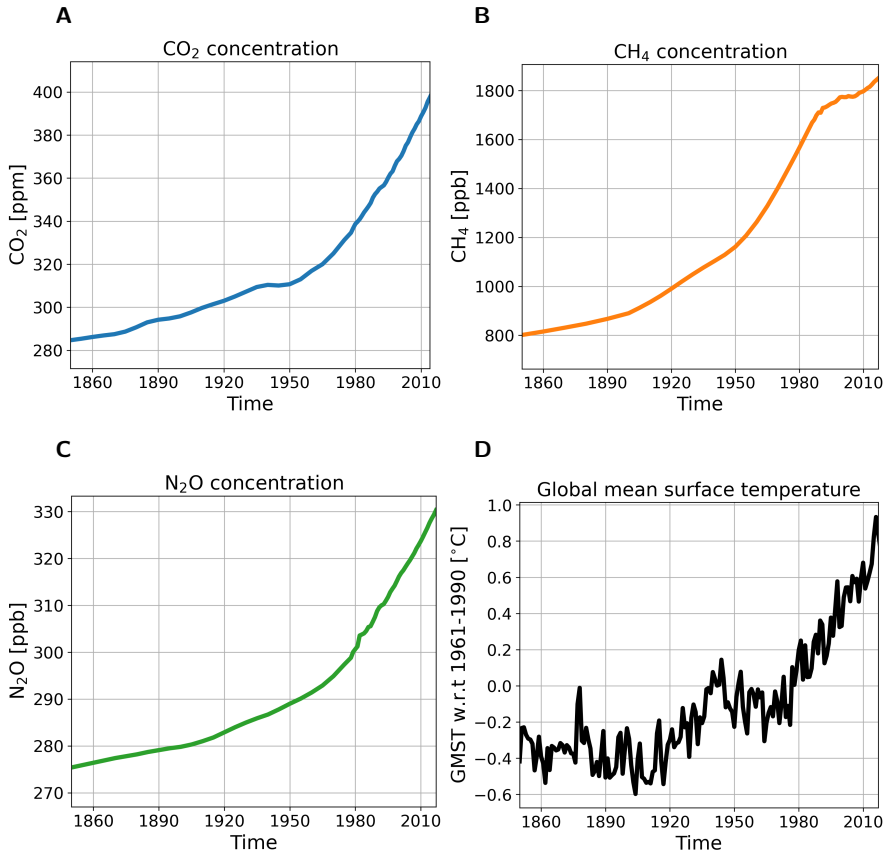


Figure 1.3: Records of atmospheric greenhouse gas concentrations and global mean surface temperature over the historical record (1850-2014). (a) CO₂ concentration in ppm. (b) CH₄ concentration in ppb. (c) N₂O concentration in ppb. (d) GMST w.r.t. 1961-1990 in °C. Data retrieved from the EEA (2019).

The AMOC can be defined mathematically as a stream function by:

$$\psi(y, z, t) = \int_z^\eta \int_{X_W}^{X_E} v(x, y, z, t) dx dz \quad (1.1)$$

where v is the meridional velocity that is integrated upward over depth from a level z to the ocean surface (η), and integrated from west (X_W) to east (X_E) in the basin. This particular definition is in depth coordinates; it is, however, also possible to use temperature and density coordinates. In this thesis, the AMOC stream function is used with help of depth coordinates. The AMOC strength per latitude can be determined from this stream function as the maximum in the water column.

A common misconception is that the AMOC is solely a thermohaline circulation. However, the AMOC consists of both a thermohaline component and a wind driven component (Kuhlbrodt et al., 2007). The thermohaline forcing is related to a merid-

ional density gradient between low and high latitudes forcing a circulation. At the surface, there is advection of water masses poleward to the high latitudes where the surface layer becomes denser due to atmospheric cooling and brine rejection resulting in deep water formation. At depth, the deep water masses flow towards the low latitudes, closing the circulation.

The wind-driven component is related to strong circumpolar westerly winds in the Southern Ocean that induce strong upwelling and northward Ekman transport at the surface of the ocean. The strength of the winds regulate the amount of upwelling. The northward Ekman transport flows into the Atlantic, and eventually the water masses flow towards the deep water formation region in the North Atlantic.

1.2.2 Multiple equilibria

As stated in Section 1.1.1, the AMOC is a tipping element and may have multiple equilibria. This was already shown by Stommel (1961) using a simple two box model which had three circulation types: (1) deep water formation at the poles, (2) deep water formation in the subtropics, and (3) no deep water formation, where the latter is an unstable configuration. After Stommel (1961), the existence of multiple equilibria was shown in a hierarchy of models. From box models with more than two boxes (e.g. Cimatoribus et al., 2014; Rooth, 1982), to ocean-only circulation models (e.g. Bryan, 1986; Dijkstra & Weijer, 2005), coupled atmosphere-ocean global circulation models (AOGCMs; e.g. Manabe & Stouffer, 1988), to global climate models (e.g. Orihuela-Pinto et al., 2022; van Westen & Dijkstra, 2023b). From a dynamical systems point of view, tipping of the AMOC is viewed as the passing of a saddle node bifurcation with two stable states: (1) an AMOC 'on' state with a NADW cell, and (2) an AMOC 'off' state where there is no NADW cell (Lynch-Stieglitz, 2017; Weijer et al., 2019)). This can be visualized in a bifurcation diagram (Fig. 1.4), with a surface freshwater flux on the x-axis.

There are three regimes in the diagram: (1) a monostable AMOC 'on' regime, (2) a monostable AMOC 'off' regime, and (3) a bistable regime. The bistable regime is located between the saddle nodes and is called the bistability or multiple equilibria window (MEW) (Barker & Knorr, 2021). Paleo proxies have provided evidence that the AMOC has been switching from 'on' to 'off' mode frequently in the Pleistocene, i.e. during the Dansgaard-Oeschger cycles (Broecker et al., 1985).

An often used estimator to determine whether the AMOC is in a monostable or bistable regime is the F_{ovS} estimator, defined as the AMOC carried freshwater flux into the Atlantic basin at 34°S (Rahmstorf, 1996; Weijer et al., 2019). If the AMOC is importing salt (i.e. $F_{ovS} > 0$) the AMOC is in a monostable regime, whereas if the AMOC is importing freshwater (i.e. exporting salt, $F_{ovS} < 0$), the AMOC is thought to be in a bistable regime. Observations suggest that in our current climate the AMOC is in a bistable regime, but due to a lack of observations it is impossible to say whether we are close to a tipping point. A recent study by Ditlevsen & Ditlevsen (2023) suggests that the AMOC will tip in 2057, however, they make use of an uncertain proxy for AMOC strength and these results have therefore a large uncertainty. Most of the current state-of-the-art models suggest that the AMOC is in a monostable regime which indicates that these models have a bias towards a too stable AMOC (van Westen & Dijkstra, 2023a).

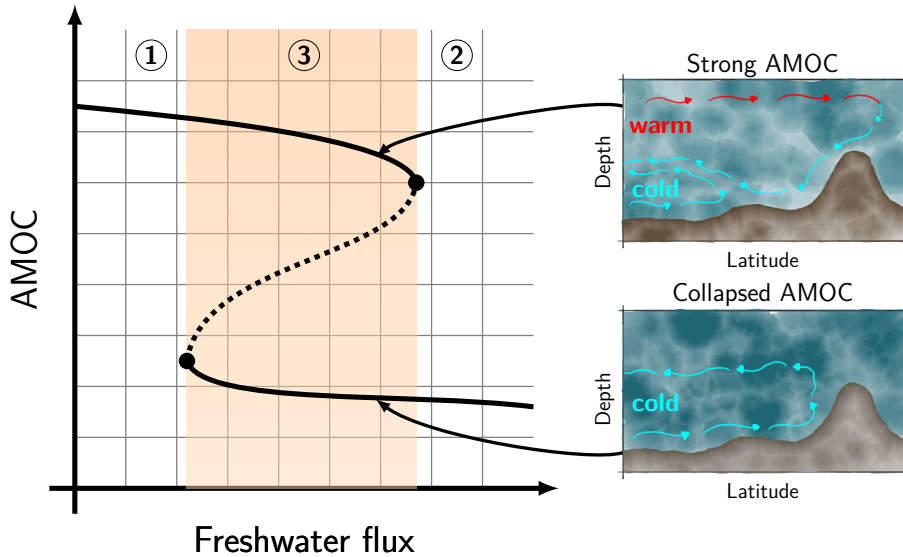


Figure 1.4: Conceptual bifurcation diagram of the AMOC strength versus a control parameter, in this case a surface freshwater flux. Solid lines represent stable steady states, and the dashed line is an unstable state. The markers represent two saddle node bifurcations. The upper branch corresponds to a strong AMOC circulation (conceptual circulation displayed at the top right), and the lower branch to a collapsed AMOC state (conceptual circulation at the bottom right). Regimes 1 and 3 are monostable, and regime 2, denoted by the orange shading is bistable. The orange shading is also termed the multiple equilibria window.

1.2.3 Role in the climate system

The surface branch of the AMOC transports heat from the Southern Hemisphere to the Northern Hemisphere. This creates an asymmetry in how heat is distributed around the equator with relatively warmer temperatures north of the equator (Buckley & Marshall, 2016). It is thought that due to this asymmetry, the mean location of the ITCZ is north of the equator (Kang et al., 2009, 2008). This northward heat transport towards Europe is also one of the reasons that Europe is generally 10°C warmer than regions on similar latitudes in the western United States and Canada (Palter, 2015). The downward branch is important for longer timescales since it is a pathway of both heat and carbon to the deep ocean with a residence time of more than 1000 years. Variability in the AMOC is associated with modes of variability in the North Atlantic such as the Atlantic multi-decadal Variability (AMV). Through the mechanisms above, the AMOC has a large impact on the climate of Europe, and to a lesser extent on the entire globe.

When the AMOC tips, the northward heat transport is disrupted leading to cooling in the Northern Hemisphere and warming in the Southern Hemisphere (Rahmstorf, 2002). This process is also termed the bipolar seesaw and thought to be present in

the Pleistocene during the Dansgaard-Oeschger cycles (Stocker & Johnsen, 2003). Cooling in the Northern Hemisphere can be as large as 10°C locally which can increase the sea-ice cover in the Arctic Ocean (Rahmstorf, 2002). The disrupted heat transport, and changing temperatures also result into changes in the atmosphere. The ITCZ shifts southward, trade winds strengthen, and the Walker circulation weakens (e.g. Orihuela-Pinto et al., 2022). Furthermore, due to changes in ocean circulation and temperatures, the sea level is affected with the largest amplitudes in the North Atlantic (Saenko et al., 2017). The changes in these climatic variables also influence other components in the Earth System such as the terrestrial and marine biosphere (e.g. Zickfeld et al., 2008).

1.3 Carbon cycle

1.3.1 Global carbon cycle

As stated in Section 1.1, the global carbon cycle is active from timescales smaller than one year to timescales over a million years. In the Earth System there are several reservoirs that contain carbon: the atmosphere, the ocean, ocean sediments, terrestrial biota, terrestrial soils, and sedimentary rocks in which also fossil fuels are present (Fig. 1.5). These reservoirs can exchange carbon with each other on different timescales. Generally, the carbon cycle is a very stable system and is thought to have been more or less in equilibrium on 10^5 year timescales throughout the Cenozoic (Caves et al., 2016). Also on shorter timescales the carbon cycle can be relatively stable proven by the near constant atmospheric CO_2 concentrations throughout the Holocene.

For the carbon cycle, the lithosphere is the most important component on very long timescales. On these timescales, there is a balance between weathering of silicate rocks and the burial of carbon in the ocean sediments. Why these two processes balance each other is not clear a priori, but can be explained. Weathered material is transported to the ocean by rivers, and when the weathering rate increases, more carbon is transported into the ocean, raising the total carbon content in the ocean. As a consequence, the carbonate (CO_3^{2-}) content of the ocean increases which results in less calcium carbonate (CaCO_3) dissolution in the deep ocean, meaning more CaCO_3 reaches the sediments to be buried there. This all results in a feedback mechanism where increased weathering rates lead to increased carbon burial in the ocean sediments and eventually more carbon storage in sedimentary rocks (Sarmiento & Gruber, 2006).

The terrestrial biosphere acts on a whole range of timescales. There are fast processes that act on timescales as short as days (e.g. primary production), to multi-millennial timescales (e.g. burial of CaCO_3 in soils). The ocean generally also acts on these timescales, though the most important processes, i.e. the transport of carbon to the deep ocean, work on centennial to multi-millennial timescales. The atmosphere connects the terrestrial and marine biosphere and acts on the shortest timescales.

This balance in the carbon cycle is disturbed due to anthropogenic activity (red numbers in Fig. 1.5). Fossil fuels, carbon rich material stored in sedimentary rocks,

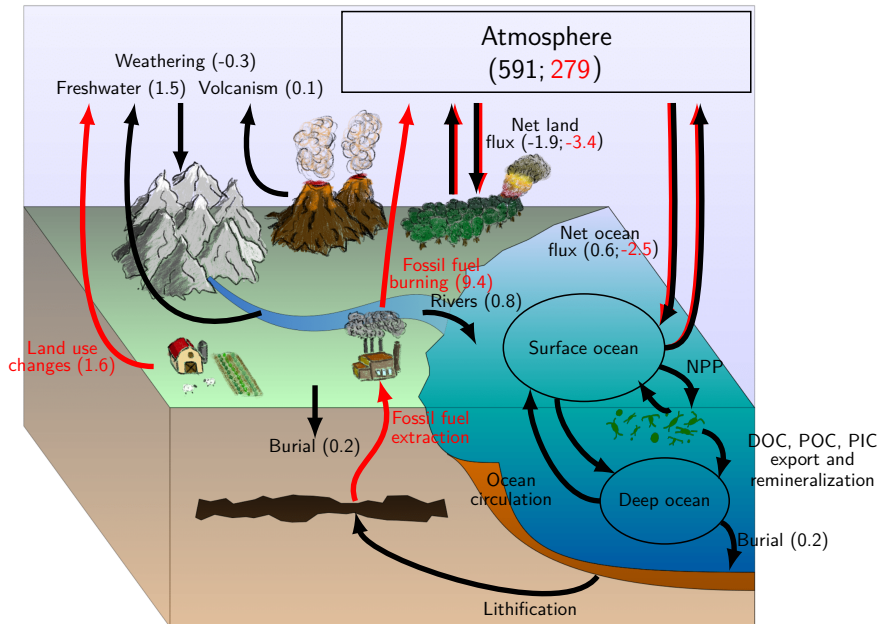


Figure 1.5: Conceptual overview of the global carbon cycle with different reservoirs. Black arrows and numbers represent the natural, undisturbed carbon cycle and red arrows and numbers the additional anthropogenic contribution. The numbers behind the fluxes are in PgC/yr. The numbers in the atmosphere box are the storage in PgC. Only the fluxes between different reservoirs are displayed. Numbers are based on the Global Carbon Budget (Friedlingstein et al., 2020).

are burned releasing the carbon that is part of the long term carbon cycle into the atmosphere. As a response to the carbon emissions, both the oceans (26%) and land (31%) have taken up part of these emissions, meaning approximately 43% remained in the atmosphere (Friedlingstein et al., 2022). The ocean and the land therefore play a large role in mitigating anthropogenic climate change, and are important components of the carbon cycle determining how the Earth System will respond to greenhouse gas emissions.

1.3.2 Marine carbon cycle

The ocean acts as a reservoir of carbon by taking up CO_2 out of the atmosphere. As stated before, the ocean has taken up approximately 26% of anthropogenic CO_2 emissions (Friedlingstein et al., 2022; Sabine et al., 2004). The CO_2 that is taken up can be stored in the deep ocean and therefore exerts an important control on atmospheric CO_2 concentrations on millennial timescales. Not only inorganic car-

bon plays an important role in the marine carbon cycle, but organic carbon as well. Phytoplankton are able to fixate inorganic carbon in the surface ocean through photosynthesis. These phytoplankton are at the base of the marine food web and play therefore an important role in marine ecosystems and can influence fish biomass and fishery yields through bottom up processes. Besides the importance for our ecosystem, oxygen is formed during photosynthesis of the phytoplankton. It is estimated that approximately 50% of the oxygen in the atmosphere is sourced by marine photosynthesis (Grégoire et al., 2023). The marine carbon cycle is therefore an important component of the Earth System for human society by keeping the atmospheric CO_2 concentrations within habitable bounds, by providing food sources, and by oxygenating the atmosphere.

A traditional view of the marine carbon cycle uses the paradigm of the three marine carbon pumps (Volk & Hoffert, 1985) that are responsible for the vertical gradient of dissolved inorganic carbon (DIC) in the ocean: (1) the physical carbon pump, (2) the soft tissue pump, and (3) the carbonate pump (Fig. 1.6).

The physical carbon pump, sometimes called the solubility pump, considers the transport of both DIC and dissolved organic carbon (DOC). The transport is determined by ocean physics, i.e. advection and diffusion, and is therefore mainly determined by the large scale ocean circulation. Another part of the physical carbon pump is the exchange of CO_2 between the atmosphere and ocean which is proportional to the difference in partial pressure of CO_2 ($p\text{CO}_2$) between the two. When the $p\text{CO}_2$ of the ocean is larger, there is transfer of CO_2 from the ocean into the atmosphere (outgassing). CO_2 enters the ocean when atmospheric $p\text{CO}_2$ is larger than the oceanic $p\text{CO}_2$ (uptake). An important process here is the dissolution of CO_2 into the ocean through the following reaction:



Once dissolved, it quickly reacts into the three different components of DIC:

$$\text{DIC} = [\text{H}_2\text{CO}_3] + [\text{HCO}_3^-] + [\text{CO}_3^{2-}] \quad (1.3)$$

where the three components are: (1) carbonic acid (H_2CO_3), (2) the bicarbonate ion (HCO_3^-) and (3) the carbonate ion (CO_3^{2-}). The relative ratios of the components is dependent on the pH of the seawater (Fig. 1.7). Following reaction (1.2), the rate of dissolution is dependent on the concentration of CO_3^{2-} , and the solubility of CO_2 which is dependent on temperature and salinity (Fig. 1.7b). CO_3^{2-} is only a small part of DIC and decreases under ocean acidification (i.e. decreasing pH). It is therefore expected that the uptake capacity of the ocean will decrease in the future. The pH system of the ocean is dependent on temperature, salinity, DIC and alkalinity. Alkalinity can be defined as the excess of proton acceptors over donors (Middelburg et al., 2020) and can also be interpreted as a buffer function of the ocean.

The other two carbon pumps are both biological pumps. The soft tissue pump considers the fixation of DIC by photosynthesis into organic carbon. Part of this organic carbon will be in a dissolved state and be advected with the ocean circulation and is therefore part of the physical pump. However, the organic carbon can also be in a

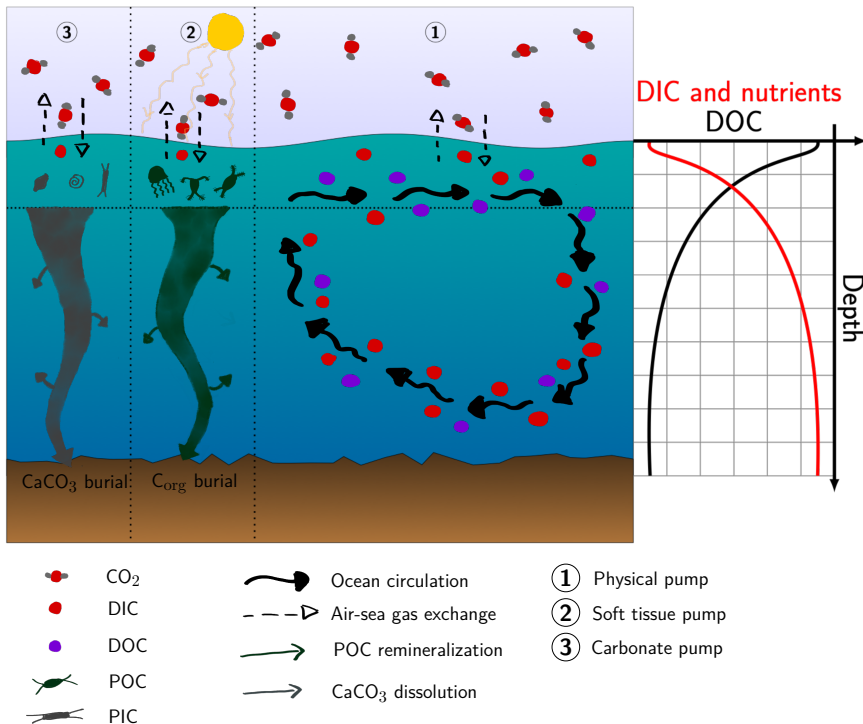


Figure 1.6: Schematic of the three marine carbon pumps with from left to right the carbonate (3), soft tissue (2) and physical (1) pump. On the right is the effect of these pumps on the gradient over depth for DOC (in black), DIC and nutrients (in red). Different elements in the figure are explained in the legend.

particulate state, i.e. particulate organic carbon (POC). Through various processes this POC can sink. While sinking, the POC usually remineralizes through oxidation with oxygen, and nutrients and DIC are released to the deeper ocean. POC that reaches the sediments can be buried there and eventually lithify into sedimentary rocks.

The third and last pump is the carbonate pump. There are marine organisms, e.g. coccolithophores and foraminifera, that construct calcium carbonate (CaCO_3) shells, and by doing so take up one carbonate ion. By fixating a mole of carbonate, DIC is reduced by one mole and alkalinity by two moles. The CaCO_3 shells are a form of particulate inorganic carbon (PIC) that can sink from the surface ocean to the deep ocean. As the shells sink, they can dissolve in the seawater which effectively transports DIC and alkalinity from the surface ocean to the deep ocean. Whether

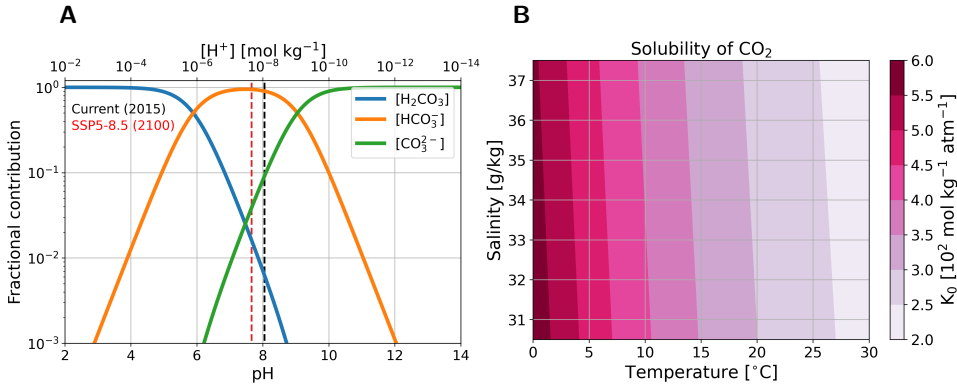


Figure 1.7: (a) Fractional contribution to the DIC concentration of the three different constituents: H_2CO_3 (blue), HCO_3^- (orange), and CO_3^{2-} (green) versus pH (lower x-axis) and equivalent to that the H^+ concentration in mol kg $^{-1}$ (upper x-axis). The black dotted line represents the global mean surface pH in 2015, and the red dashed line the projected global mean surface pH in 2100 following SSP5-8.5. (b) Solubility of CO_2 (K_0) as a function of temperature (x-axis in °C) and salinity (y-axis in g/kg) in 10^2 mol kg $^{-1}$ atm $^{-1}$.

the shells dissolve, is dependent on the dissolution state of $CaCO_3$, defined by:

$$\Omega = \frac{[Ca^{2+}][CO_3^{2-}]}{K_{sp}} \quad (1.4)$$

where Ω represents the saturation state, $[Ca^{2+}]$ the calcium ion concentration, $[CO_3^{2-}]$ the carbonate ion concentration, and K_{sp} the equilibrium constant of the formation and dissolution of $CaCO_3$.

Just as with the POC, the $CaCO_3$ shells can be buried in the sediments if they are not dissolved in the water column.

The saturation state of $CaCO_3$ plays an important role on timescales longer than those typically associated with the ocean circulation, i.e. 10^4 - 10^5 years. On these timescales there is a balance between the influx of DIC and alkalinity in the ocean through rivers, and the outflux through burial in the sediments.

1.3.3 Carbon cycle modeling

The different timescales involved in the carbon cycle make the modeling of the carbon cycle challenging. Similar to climate models, there are a whole range of models of different complexity. There are, for example, box models suitable for modeling the carbon cycle on million year timescales, e.g. the Long-term Ocean-atmosphere-Sediment Carbon cycle Reservoir Model (LOSCAR; Zeebe, 2012) and the Simple Carbon Project Model (SCP-M O'Neill et al., 2019). These models generally contain all relevant processes for the carbon cycle, albeit many in a parameterized way. For example, ocean circulation is often assumed to be constant and biological production is also constant or estimated using Michaelis-Menten kinetics.

Several Earth system Models of Intermediate Complexity (EMICs), e.g. UVic-ESCM (Mengis et al., 2020) and LOVECLIM (Goosse et al., 2010), have been fitted with a

simple carbon cycle model. These models typically run on a low, horizontal resolution of e.g. 3° or 5° and the ecosystem model is generally quite simple. Due to the low resolution and simple carbon cycle component these models are typically used to study the carbon cycle on multi-millennial timescales.

The most complex models are the Earth System Models (ESMs). These are the type of models typically used in the Coupled Model Intercomparison Projects (CMIP). In CMIP6 (Eyring et al., 2016) the number of models with a carbon cycle module has increased compared to CMIP5 (Taylor et al., 2012). The ESMs with a carbon cycle module are typically run on a 1° resolution and are able to resolve the carbon cycle dynamics better than the EMICs, but this comes at a high computational cost. In global configurations, there are almost no models that run on an eddy permitting, or even eddy resolving resolution. One of the reasons this is not possible is because the ecosystem models are more advanced and require high computational resources. The ecosystem modules are generally based on a Nutrient-Phytoplankton-Zooplankton-Detritus (NPZD) model. Over the years the NPZD models have become more complex resolving more nutrients, phytoplankton and zooplankton groups. Future challenges for the carbon cycle module in ESMs are, for example, running the models on a higher resolution and increasing the complexity of the NPZD models allowing for example for trait based modeling (e.g. Le Gland et al., 2021; Negrete-García et al., 2022).

1.4 Research Questions and Outline

The marine carbon cycle described in the previous section is a non-linear system. Such systems can contain bifurcation points and can therefore show tipping behavior as discussed in Section 1.1.1. An example of a tipping element in the Earth System is the AMOC, which, as described in Section 1.2.2 may have multiple (stable) equilibria. In this thesis, there are two main issues of interest: (1) tipping behavior in the (marine) carbon cycle, and (2) interactions between the (marine) carbon cycle and tipping elements in the climate system. The tipping element central in this thesis is the AMOC.

The carbon cycle is comprised of an extremely complex entangled set of processes which act in the different components of the climate system (e.g., land, ocean) on many different timescales (Section 1.3). Given this strongly nonlinear system, it would be strange if it would not show strong internal variability, i.e. variability which would exist even if the carbon-cycle system would be driven by tipping behavior or a time independent external forcing. Proxy records also show large transitions in past carbon cycle records which can be driven by carbon cycle dynamics (Setty et al., 2023). Tipping behavior in the terrestrial carbon cycle are, for example, permafrost melt and dieback of the Amazonian rainforest (Armstrong-McKay et al., 2022). However, tipping behavior in the marine carbon cycle is much less studied, and no study has shown that sharp transitions in marine carbon cycle quantities are easily linked to a transition between different steady states. Using conceptual modeling, studies have shown that the marine carbon cycle can sustain internal oscillations on multi-millennial timescales (Rothman, 2015, 2019).

The effect of an AMOC collapse on several climatic variables has been well re-

searched in both proxy data and in a hierarchy of models (see Section 1.2.3). In addition to the climate system, also the carbon cycle is affected by an AMOC collapse. In the ocean, the change in ocean circulation affects the advection of important tracers such as Dissolved Inorganic Carbon (DIC) and nutrients (Zickfeld et al., 2008). An AMOC collapse can also change upwelling rates and surface stratification, processes that are important for driving Net Primary Production (NPP) and carbon sequestration in the deep ocean. Terrestrial primary productivity is affected by the changing temperature and precipitation patterns. Several studies have looked into a potential feedback between AMOC dynamics and atmospheric $p\text{CO}_2$, which is controlled by the exchange of the atmosphere with the ocean and land carbon stocks. These studies (e.g. Köhler et al., 2005; Marchal et al., 1998; Schmittner & Galbraith, 2008), mostly focused on Pleistocene and pre-industrial conditions, show a wide range of possible responses. There is no clear consensus on the responses of the terrestrial and ocean carbon stock to an AMOC weakening, or to the net effect on atmospheric $p\text{CO}_2$, which can be attributed to different climatic boundary conditions, timescales assessed, and model detail used in these studies (Gottschalk et al., 2019).

As the AMOC can influence atmospheric $p\text{CO}_2$, there is a potential feedback mechanism since atmospheric $p\text{CO}_2$ influences the hydrological cycle (Barker & Knorr, 2021; Weijer et al., 2019), which through changes in buoyancy fluxes, affects the AMOC. Previous studies suggest that there may be a relation between atmospheric $p\text{CO}_2$ and the MEW of the AMOC (Barker et al., 2015, 2010). However, a clear mechanistic view has not been given yet in literature.

In this thesis we will investigate the knowledge gaps described above centered around three main elements: the atmosphere (e.g. temperature and precipitation), the AMOC, and the (marine) carbon cycle (Fig. 1.8). We consider the system in two different configurations: in steady state on long (i.e. 10^3 - 10^6 years) timescales (Fig. 1.8a) and for future climate change on multi-decadal to centennial timescales (Fig. 1.8b). As described in Sections 1.1 and 1.3, the separation of these timescales is important since the dominant processes are dependent on these timescales.

Studying the coupled system on long timescales will help us to get a better understanding on how it operates. This can be used to help interpret proxy records from past climates, and help improve models used for climate change projections. We also study the system under future climate change projections. Climate change can be a major threat for the livability of planet Earth, and it is therefore vital to be able to give reliable projections of future climates. Non-linear processes in the Earth System can make these projections uncertain. Moreover, passing of tipping points poses a great risk due to the large consequences of such events. It is therefore important to get a better understanding of the interactions in the Earth System between the different components. In this thesis we specifically look at the interactions between the atmosphere, the (marine) carbon cycle and the AMOC.

1.4.1 Specific Scientific Questions

We address the different feedbacks and couplings between the three elements in Fig. 1.8. The processes behind the coupling between the atmosphere and AMOC (coupling 1), and AMOC and carbon cycle (coupling 3) are similar in both configurations,

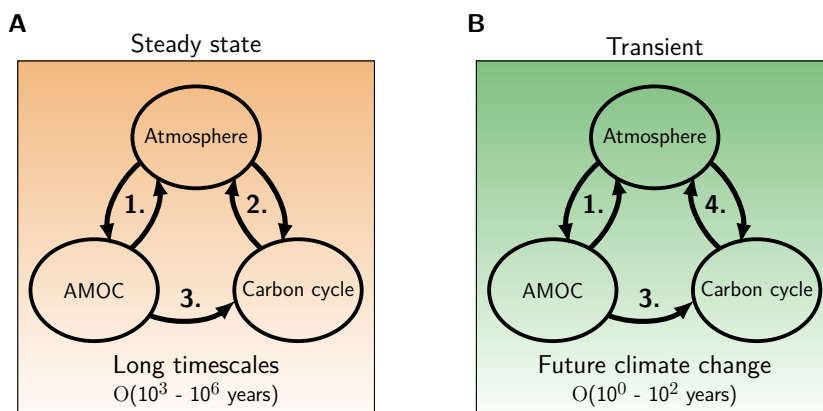


Figure 1.8: Schematic of the studied coupled components in the Earth System in this thesis in steady state (a) and in transient simulations (b). The different numbers represent couplings between the elements. Couplings 1 and 3 are present in both (a) and (b) but might differ in relative importance. The coupling between the atmosphere and the carbon cycle differs in (a) and (b).

but the relative importance of these processes might differ. Coupling 1 represents the effect of atmospheric forcing (e.g. wind fields) on the driving mechanisms of the AMOC (Section 1.2.1), and the effect of the AMOC on the heat distribution on Earth and how the atmosphere responds to this (Section 1.2.3). Coupling 3 represents the effects of advection by the AMOC of important tracers (i.e. DIC, alkalinity and nutrients) for the carbon cycle. The main differences between the two configurations are the most important processes underlying the coupling between the atmosphere and carbon cycle (couplings 2 and 4). In Fig. 1.8a the most important processes in coupling 2 are the weathering feedback and CaCO_3 dynamics in the ocean that regulate atmospheric pCO_2 values on these long timescales. In Fig. 1.8b, coupling 4 represents the effect of atmospheric forcing on the terrestrial and marine carbon cycles by, for example, changing the amount of precipitation affecting terrestrial productivity or changing the solubility of CO_2 in water. Coupling 4 also represents how the processes in the carbon cycle on multi-decadal and centennial timescales regulate atmospheric pCO_2 . In each chapter a specific question related to the couplings in Fig. 1.8 is answered:

1. What is the effect of the Atlantic Meridional Overturning Circulation on atmospheric pCO_2 on long timescales?

For this question we are interested in how changes in the AMOC strength influences the steady state atmospheric CO_2 concentrations. We are specifically interested in how the marine carbon cycle responds to changes in advection on long timescales (i.e. coupling 3 in Fig. 1.8a). Studying this question can help to explain proxy records and show whether coupling 3 is important for carbon

cycle transitions seen in these proxy records, as well as provide information on how the carbon cycle might respond to changes in the AMOC in the future on long timescales. We will discuss this question in Chapter 3.

2. How does the marine carbon cycle influence the multiple equilibria window of the Atlantic Meridional Overturning Circulation?

This question considers how the representation of coupling 2 in Fig. 1.8a influences the multiple equilibria window of the AMOC. Specifically we will address how the coupling between the carbon cycle and the hydrological cycle affects the thermohaline forcing of the AMOC, and how this affects the stability of the AMOC on long timescales. Just as the previous question, this study can help to explain proxy records. Furthermore, it can inform how the stability of the AMOC might change under different background carbon content of the ocean-atmosphere system which is relevant as the total carbon content is currently increasing by anthropogenic activities. This research question is discussed in Chapter 4.

3. How do climate change induced adjustments in the marine biosphere feed back to atmospheric $p\text{CO}_2$?

Currently, the climate is changing rapidly due to anthropogenic greenhouse gas emissions (Section 1.1.2), causing warming (Fig. 1.3d). Depending on emissions this warming might continue well past 2100, i.e. past centennial timescales. For this question we specifically study how coupling 4 in Fig. 1.8b responds to future climate change up to 2100. We study the response of the (marine) carbon cycle to the changes in atmospheric forcing, and how these changes feed back on atmospheric $p\text{CO}_2$ values providing information about possible positive or negative feedbacks in the Earth System. This question is discussed in Chapter 5.

4. What is the carbon cycle response to a strong AMOC weakening under low and high emission scenarios?

As the climate changes in the future, the AMOC might collapse. For this question we specifically study how the combined effect of anthropogenic climate change and a strong AMOC weakening affects the carbon cycle through couplings 1, 3 and 4 in Fig. 1.8b. Just as for the previous question this will provide information about a possible positive or negative feedback in the Earth System and potentially also cascading effects of an AMOC weakening. This question is discussed in Chapter 6.

1.4.2 Outline of the Thesis

The used models, numerical methods, and Earth System Model simulations are described in Chapter 2. In Chapters 3 and 4 the relation between the AMOC and the

carbon cycle are explored in box models for long timescales. In Chapter 3 we specifically look at the effect of the AMOC on atmospheric $p\text{CO}_2$, and in Chapter 4 we look at the effect of the marine carbon cycle on the multiple equilibria window of the AMOC. In Chapters 5 and 6 we have used Earth System Models to look into the interactions between the AMOC and the marine carbon cycle under climate change. Chapter 5 looks at the effect of a phytoplankton composition shift in the North Atlantic on atmospheric $p\text{CO}_2$. Chapter 6 looks at the carbon cycle response to a strong AMOC weakening under climate change. The main matter of this thesis is concluded in Chapter 7 with a conclusion and an outlook for possible future research. Several appendices have been included in this thesis. Appendices A and B contain parameter values and model equations, Appendix C has a list of CMIP6 models used in Chapter 4, and appendices D and E contain additional results of the used ESM simulations.

Methods

In this thesis we have made use of several numerical models of varying complexity. We have used two different box models: a carbon cycle box model called the Simple Carbon Project Model (SCP-M) and a box model simulating AMOC dynamics. Both these box models have been implemented in the continuation software AUTO-07p (AUTO). Besides these box models, we have also used several simulations of the Community Earth System Model v2 (CESM2). In this chapter, the models, AUTO and the CESM2 simulations are discussed.

2.1 The Simple Carbon Project Model v1.0

In this thesis we have used the Simple Carbon Project Model v1.0 (O'Neill et al., 2019) (Fig. 2.1). The SCP-M is a carbon cycle box model focused on the marine carbon cycle. Because of its simple structure, it is well suited to test high level concepts in both modern and past configurations. In the ocean several tracers are resolved, but in this thesis we will only use three: DIC, alkalinity (Alk), and phosphate (PO_4^{3-}), to reduce the problem size. Included in the SCP-M is also a simple representation of the terrestrial biosphere, and several sources of CO_2 to the atmosphere. The ocean part of the model resolves the ocean overturning circulation, air-sea gas exchange, biological production, calcium carbonate (CaCO_3) production and dissolution, and river and sediment fluxes.

The model consists of 10 boxes: 1 atmospheric box and 7 oceanic boxes, and 2 terrestrial biosphere boxes (Fig. 2.1). This means that the sediment carbon stock is not explicitly solved for in the model. In the model, the ocean boxes are differentiated on latitude and depth. Consequently, there is no longitudinal variation, and no differentiation between ocean basins. The used boxes are: (1) a low-latitude surface box, (2) a northern high latitude surface box, (3) an intermediate ocean box, (4) a deep ocean box, (5) a southern high latitude surface box, (6) an abyssal ocean box, and (7) a sub-polar surface box. This division in the ocean is based on regions in the ocean where the water masses have similar characteristics. The two boxes in the terrestrial biosphere represent a short-term box with fast respiration, and a long-term box with slow respiration.

The different boxes are connected via ocean circulation and mixing, which is based upon a conceptual view of the ocean circulation (Talley, 2013). The largest circulation is the Global Overturning Circulation (GOC; ψ_1). This circulation connects boxes 4-7 and represents the formation of Antarctic Bottom Water. Next to the GOC, the other major circulation is the AMOC (ψ_2) which connects boxes 2-4 and 7. Lastly, there is bidirectional (vertical) mixing between boxes 4 and 6 (γ_1) and boxes 1 and 3 (γ_2).

To be able to solve for several fluxes, such as the air-sea gas exchange, the pH in the ocean needs to be determined. Unfortunately, pH is not a conservative tracer, which means that we need a carbonate chemistry module to solve for pH. In the SCP-M, a direct solver is used where the pH value of the previous time step is used as an estimate for the new step (Follows et al., 2006). Using this carbonate chemistry, the model is able to determine the carbonate ion (CO_3^{2-}) concentration and oceanic pCO_2 . This latter quantity is used to model the exchange of CO_2 between the atmosphere and ocean. For each surface box, the flux is proportional to the pCO_2 difference between atmosphere and ocean, and a constant piston velocity (k_w).

Biological export production (EP) is constant in the SCP-M. Per surface box, a constant value is used to denote the EP at 100 m depth. The organic flux is remineralized in the subsurface boxes following the power law of Martin et al. (1987). The biological export production is also important for the carbonate pump. Via a constant rain ratio, the biological production is linked to the production of calcifiers.

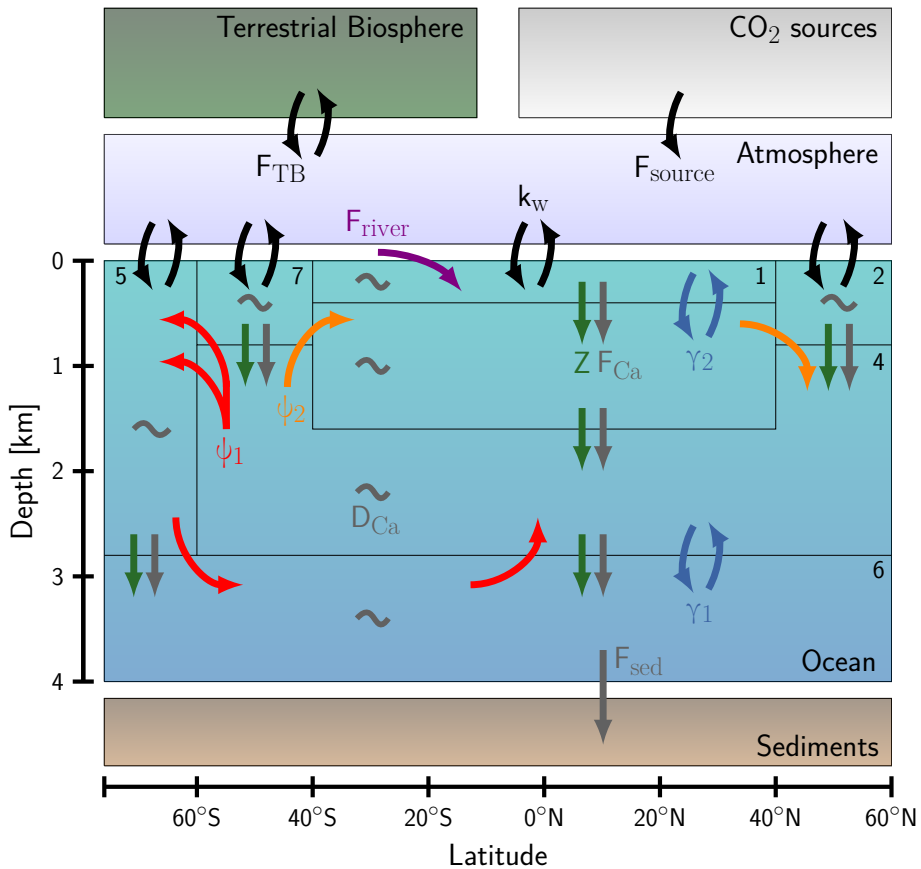


Figure 2.1: The box structure and fluxes for the SCP-M based on O'Neill et al. (2019). ψ_1 (red) is the GOC, ψ_2 (orange) is the AMOC, and γ_1 and γ_2 (blue) represent bidirectional mixing. Biological fluxes are represented by the green arrows (Z), calcifier fluxes by the gray arrows (F_{Ca}), and general dissolution of calcium carbonate by the gray wiggles in the boxes (D_{Ca}). Black arrows represent fluxes of CO_2 where k_w represents the gas exchange between the ocean and the atmosphere. Lastly, there is an influx in box 1 via the rivers (purple; F_{river}) and an outflux to the sediments (gray; F_{sed}).

Besides organic growth via photosynthesis, calcifiers also take up DIC and Alk to form calcium carbonate shells ($CaCO_3$). Upon death, these calcifiers sink to deeper boxes where their shells are dissolved. The dissolution of the shells is dependent on a constant dissolution and a saturation dependent solution. If the total dissolution of $CaCO_3$ in the ocean is smaller (larger) than the production in the surface ocean, there is an outflux (influx) of DIC and Alk to (from) the sediments. The river flux for PO_4^{3-} is constant in the SCP-M and balanced by a constant outflux into the sediments. Influx of DIC and Alk via the rivers is variable and related to constant silicate and variable silicate and carbonate weathering. Here the variable component is lin-

early proportional to atmospheric $p\text{CO}_2$. The difference between the influx of DIC and Alk and the outflux into the sediments determines the change in total carbon and Alk in the system.

A big advantage of the SCP-M is that it has two configurations: a PI configuration, and an LGM configuration. The parameter values in both configurations have been determined via extensive tuning of the model to observations and proxies in O'Neill et al. (2019). The configurations are differentiated on surface ocean temperature and salinity, ocean circulation, sea-ice cover in box 5, and total volume of the ocean. The parameter values of the two different SCP-M configurations can be found in Table 2.1.

Table 2.1: The parameter values that are different between the two configurations (PI and LGM). In columns 1 and 2 the parameter symbol and description are given. In column 3 the PI value is given and in column 4 the LGM value.

Parameter		PI-value	LGM-value
T_1	Temperature box 1	23.44 °C	17.34°C
T_2	Temperature box 2	9.1 °C	3.1 °C
T_7	Temperature box 7	5.83 °C	0.33 °C
S_1	Salinity box 1	35.25 psu	36.25 psu
S_2	Salinity box 2	34.27 psu	35.27 psu
S_5	Salinity box 5	34.34 psu	35.34 psu
S_7	Salinity box 7	34.17 psu	35.17 psu
γ_1	Mixing deep - abyssal ocean	29 Sv	31 Sv
ψ_1	General Overturning Circulation	29 Sv	18 Sv
ψ_2	AMOC	19 Sv	15 Sv
V_n	Volume box n	$1 \times V_n$	$0.97 \times V_n$
A_n	Surface area box n	$1 \times S_n$	$0.97 \times S_n$
k_{w_5}	Piston velocity box 5	3 m/day	1 m/day
$p\text{CO}_{2,base}$	Base atmospheric $p\text{CO}_2$	244 ppm	145 ppm

2.2 The Cimatoribus ocean circulation box model

AMOC dynamics can be captured in simple models such as box models. In this thesis we have used such a model (Fig. 2.2), i.e. a model developed by Cimatoribus et al. (2014), and extended by Castellana et al. (2019). This box model simulates the depth of the pycnocline and the distribution of salt in the Atlantic Ocean and the Southern Ocean, and is able to capture important AMOC dynamics. It consists of 5 boxes, and 6 prognostic variables. The northern box n represents the regions of deep water formation in the North Atlantic and box s represents the entire Southern Ocean (i.e. all longitudes). There are two thermocline boxes t and ts where box ts represents the region between 30°S and 40°S which is characterized by strong sloping isopycnals where the pycnocline becomes shallower moving poleward. Un-

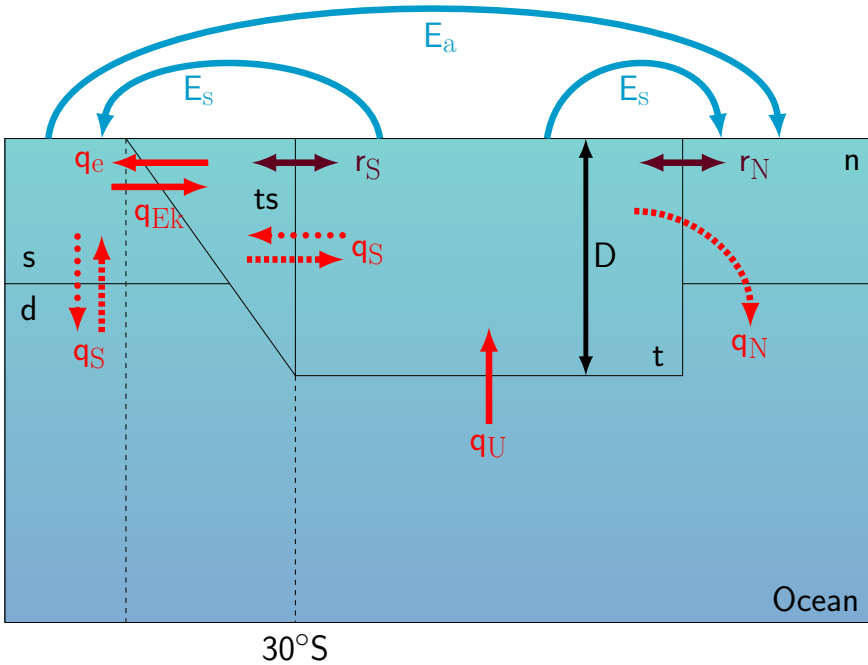


Figure 2.2: Box structure and processes simulated in the ocean circulation box model. Red arrows represent volume transports where dashed arrows are only present during an on-state, and dotted arrows only present during an off-state. The purple arrows represent gyre exchange (r_N and r_S), and blue arrows freshwater fluxes (E_s for the symmetrical forcing, and E_a for the asymmetrical forcing). Based on Castellana et al. (2019).

derneath the four surface boxes, there is one box (d) representing the deep ocean. The distribution of salinity in the model is dependent on the ocean circulation and surface freshwater fluxes. There are multiple volume fluxes in the model. In the Southern Ocean, there is wind-induced Ekman transport into the Atlantic (q_{Ek}), and there is an eddy induced transport from the Atlantic into the Southern Ocean (q_e) which is dependent on the pycnocline depth D . The difference between the two, defined as q_s , represents upwelling in the Southern Ocean and net volume transport into the Atlantic thermocline. The thermocline also is sourced with water from box d through diffusive upwelling (q_U). The strength of the downward branch of the AMOC is represented in the North Atlantic by q_N . This downwelling is dependent on the meridional density gradient between box ts and box n i.e.,

$$q_N = \eta \frac{\rho_n - \rho_{ts}}{\rho_0} D^2 \quad (2.1)$$

where η is a hydraulic constant, D the pycnocline depths, ρ_0 a reference density, and ρ_n and ρ_{ts} the densities of boxes n and ts , which are determined using a linear equation of state. Wind driven gyre transport is modeled by r_N in the Northern Hemisphere, and r_S in the Southern Hemisphere. Salinity is also affected by two surface

freshwater fluxes, modeled as virtual salt fluxes. First, there is a symmetrical forcing E_s , i.e. the freshwater flux is the same for both hemispheres; and secondly, there is an asymmetrical forcing E_a which results in interhemispheric differences. This last parameter can be viewed as a hosing parameter for the AMOC strength since it regulates the salinity of box n . By increasing this parameter, the AMOC strength would decrease because the meridional density gradient (Eq. 2.1) decreases. The pycnocline depth is an important state variable in this model since several volume fluxes are dependent on it. This depth is dependent on four different volume fluxes going in and out of the two thermocline boxes t and ts (q_e, q_{Ek}, q_U, q_N).

The model provides a simple framework to study AMOC dynamics and has already been used to show both slow (Cimatoribus et al., 2014) and fast, noise-induced (Castellana et al., 2019; Jacques-Dumas et al., 2023) tipping of the AMOC by freshwater forcing. However, several assumptions are made in this model. The most important assumptions are that we neglect diapycnal mixing, and that temperature anomalies do not affect the AMOC strength (i.e. temperature is not a prognostic variable), since temperature anomalies have a faster decay timescales compared to salinity anomalies.

2.3 Continuation and bifurcation software

In this thesis we have used continuation and bifurcation techniques to follow branches of steady state solutions. To do this we have used the software AUTO-07p (AUTO; Doedel et al., 2007, 2021). Box models as presented in Section 2.1 and 2.2 are a system of ordinary differential equations of the form

$$\frac{d\mathbf{u}}{dt} = \mathbf{f}(\mathbf{u}(t), \mathbf{p}), \quad (2.2)$$

where \mathbf{u} is the state vector (containing all the dependent quantities in all boxes), \mathbf{f} contains the right-hand-side of the equations and \mathbf{p} is the parameter vector.

Usually, such models are integrated in time from a certain initial condition and the equilibrium behavior is determined for different values of the parameters. However, this is not very efficient to scan the parameter space and, moreover, it is difficult to detect tipping behavior. A much more efficient approach is to determine the equilibrium solutions directly versus parameters, avoiding time-integration, using continuation methods. Furthermore, using this software we are able to detect, for example, limit points and Hopf bifurcations. AUTO uses a pseudo-arc length continuation combined with a Newton-Raphson method (Fig. 2.3).

2.4 The Community Earth System Model v2

The Community Earth System Model v2 (CESM2) (Danabasoglu et al., 2020) is a state-of-the-art Earth System Model developed for the use in the Coupled Model Intercomparison Project 6 (CMIP6) (Eyring et al., 2016). The CESM2 is a coupled model and includes modules for atmospheric dynamics and chemistry, land processes, sea- and land ice processes, ocean dynamics and biogeochemistry, rivers and

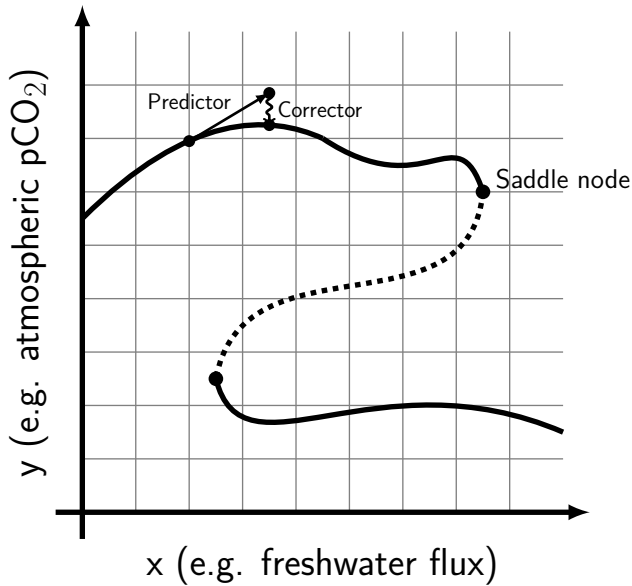


Figure 2.3: Illustration of pseudo-arc length method used in AUTO.

waves (simplified structure in Fig. 2.4). In this thesis we use simulations with static land ice, and vegetation type. The equilibrium climate sensitivity of CESM2 is 5.3°C (Danabasoglu et al., 2020) making it one of the most sensitive CMIP6 models. The transient climate sensitivity is similar to that of the CESM1 and is 2.0°C . The ocean circulation and biogeochemistry module are discussed in more detail in Sections 2.4.1 and 2.4.2. The atmospheric, land and sea-ice modules and the coupling are shortly described in Section 2.4.3.

2.4.1 The Parallel Ocean Program

In the CESM2, ocean dynamics are represented by the Parallel Ocean Program 2 (POP2) (Danabasoglu et al., 2020, 2012; Smith et al., 2010). The version of POP2 used in this thesis solves the primitive equations on a nominal horizontal grid of 1° with 60 non-equidistant vertical layers on level coordinates. The used horizontal grid has a displaced pole into Greenland and spherical coordinates in the Southern Hemisphere. The zonal resolution is constant with a grid size of 1.125° , resulting in 320 grid points. Meridionally, the grid size is variable with the highest resolution of 0.27° near the equator. Moving southward the grid size increases to 0.53° at 32°S remaining constant further south. The displaced pole in the Northern Hemisphere creates a zonal asymmetry in grid size in the northern hemispheric high latitudes. The highest resolution is found in the Atlantic basin (0.38°), and the lowest resolution in the Pacific basin (0.64°). In total there are 384 grid points in meridional direction, meaning that the ocean grid has dimensions $384 \times 320 \times 60$ for the latitu-

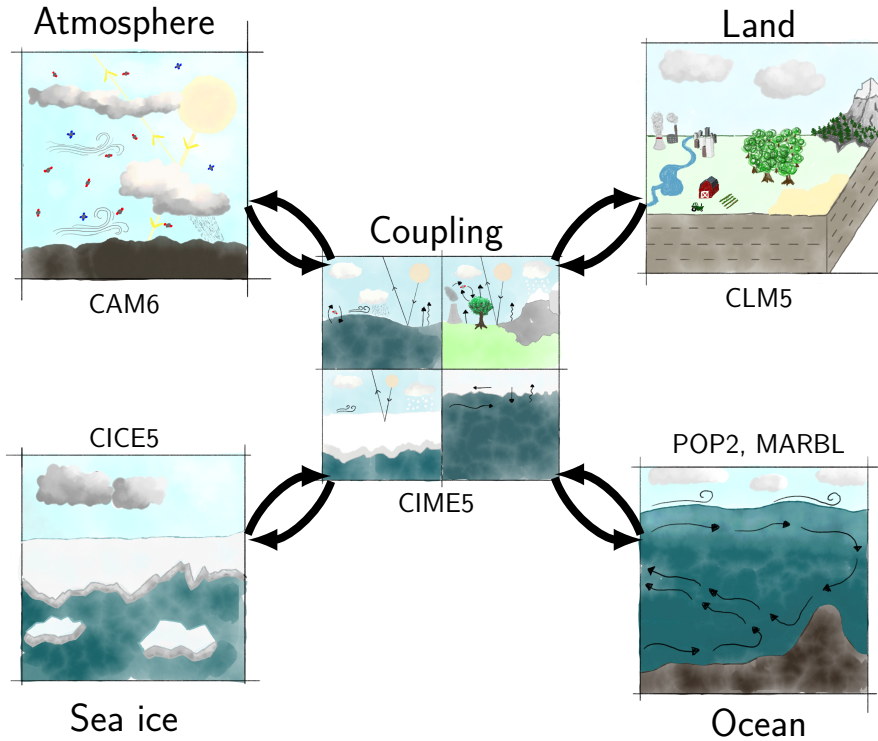


Figure 2.4: Simplified structure of the Community Earth System Model v2 with a land model (CLM5), an atmosphere model (CAM6), a sea-ice model (CICE5) (all Section 2.4.3), and an ocean dynamical model (POP2; Section 2.4.1), and an ocean biogeochemical model (MARBL; Section 2.4.2).

dinal, longitudinal and depth coordinates. The vertical resolution is the highest near the surface and decreases with depth. The layer thickness in the top 150 m is 10 m after which it increases to 250 m at approximately 3500 m remaining constant after. The minimum ocean depth is 30 m and the maximum depth is 5500 m (Fig. 2.5). POP2 is a volume conserving ocean model, meaning that the volume of the ocean can not change and that freshwater fluxes are treated as virtual salt fluxes. Since we use the model on a nominal 1° resolution, eddies are not resolved in our model simulations. To account for sub-grid scale mixing processes, the model employs the Gent and McWilliams scheme (Gent & McWilliams, 1990). Also overflow processes in for example the Denmark Strait, Faeroe Bank Channel and in the Southern Ocean are parameterized.

2.4.2 The Marine Biogeochemistry Library

Ocean biogeochemistry in the CESM2 is represented by the Marine Biogeochemistry Library (MARBL) (Long et al., 2021), which is an updated version of the Biological

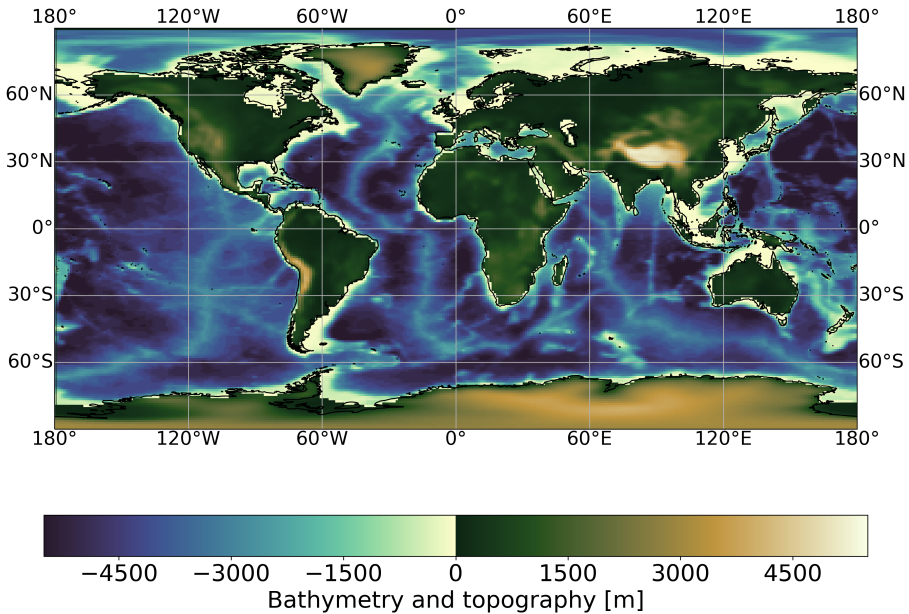


Figure 2.5: Bathymetry and topography in CESM2.

Elemental Cycling (BEC) model (Moore et al., 2013a; Moore et al., 2004, 2013b; Moore et al., 2001). MARBL is based on a so-called NPZD-model (Nutrient - Phytoplankton - Zooplankton - Detritus), and resolves 4 nutrient groups (N, P, Fe, and Si), 3 explicit phytoplankton groups (diatoms, diazotrophs and small phytoplankton), 1 implicit phytoplankton group (calcifiers) and 1 zooplankton group (Fig. 2.6). In total, MARBL simulates 32 additional tracers in the ocean, which increases the computational time of the model. This is the main reason why there are almost no eddy resolving ocean biogeochemical models, and why the ocean biogeochemistry has not always been resolved in Earth System Models. Important tracers are for example Dissolved Inorganic Carbon (DIC), alkalinity (Alk), nutrients (e.g. PO_4^{3-} , NO_3^-) and elemental (C, N, P, Fe, Si) plankton biomass. All tracers are governed by an equation of the form

$$\frac{\partial C}{\partial t} + \nabla \cdot (\mathbf{u}C) - \nabla \cdot (K\nabla C) = J_C(\mathbf{x}) \quad (2.3)$$

Where the left-hand side represents the change of the concentration of tracer C over time (term 1) and the advection (term 2) and diffusion (term 3) of the tracer. The right-hand side represents the sink and source terms of the tracer C. These terms can be either treated as boundary conditions (e.g. river inflow), or determined by MARBL itself (e.g. net primary production).

All biological productivity in MARBL is simulated in the top 150 m of the ocean. Phytoplankton biomass can increase due to NPP and decrease due to mortality, aggregation and grazing by zooplankton. Growth of phytoplankton is co-limited by

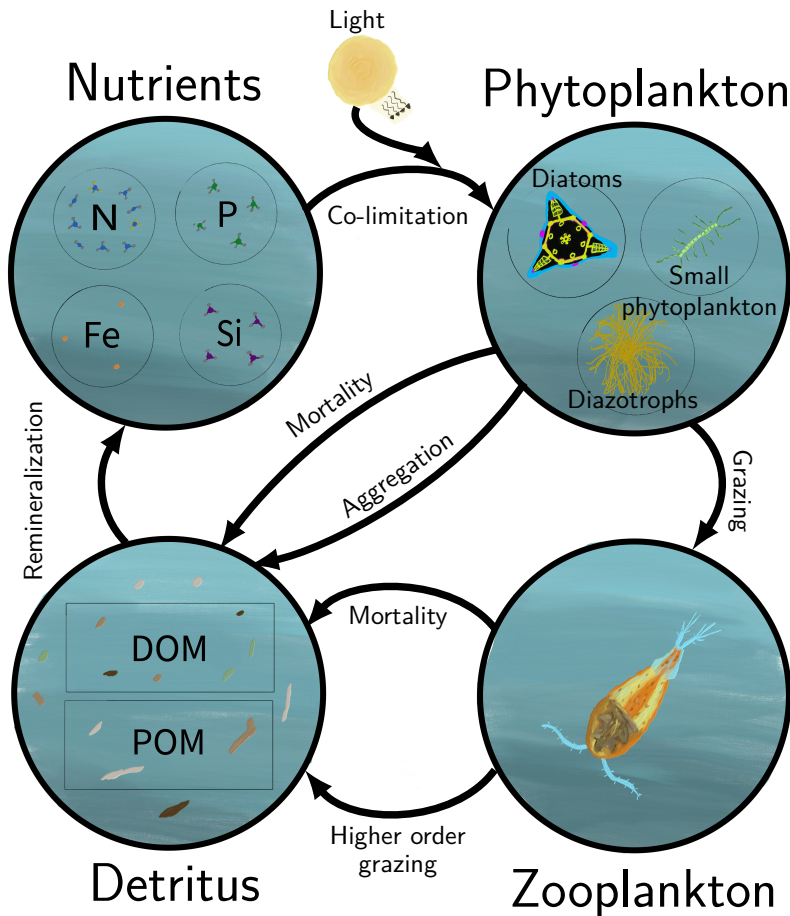


Figure 2.6: Illustration of the structure of MARBL which is based on an NPZD model with four nutrients (N: nitrogen, P: phosphorus, Si: silicate, and Fe: iron), three phytoplankton groups, one zooplankton group, and a detritus group consisting of dissolved organic matter (DOM) and particulate organic matter (POM).

light and nutrients. Nutrient limitation follows Michaelis-Menten kinetics and there is only a single limiting nutrient (i.e. there is no nutrient co-limitation). Zooplankton gain biomass by differential grazing on the phytoplankton species, and lose mass due to mortality and parameterized higher-trophic level grazing. By using the differential grazing an attempt is made to simulate an adaptive class representing different types of zooplankton, e.g. micro- and mesozooplankton. The sinking of particulate organic matter (POM) is not explicitly resolved in the model but simulated implicitly. Every time step, production in the surface ocean is immediately redistributed over the subsurface ocean where the POM is remineralized following Armstrong et

al. (2001). The depth to which POM is remineralized is dependent on the remineralization length scale and the efficiency is dependent on ballast material such as mineral dust, biogenic calcium carbonate (CaCO_3), and Si, which act to increase the efficiency. MARBL also simulates dissolved oxygen in the ocean, which enables it to simulate, for example, oxygen minimum zones. However, due to biases in the POP2 model, the North Pacific became too depleted in oxygen in the testing phase of CESM2 and MARBL. This was discovered late in the development process, and an ad hoc measure was used to prevent this large scale deoxygenation of the Pacific Ocean by artificially changing stoichiometric ratios. As a consequence it is advised not to use the oxygen fields simulated by CESM2. To determine the carbonate chemistry in the ocean, MARBL uses the Ocean Carbon Model Intercomparison Project (OCMIP) formulation (Doney et al., 2009).

The elements simulated in MARBL need to be conserved. For the nitrogen cycle, the formulation in the ocean guarantees that the input of nitrogen through e.g. rivers is balanced by losses in the ocean. For other elements, i.e. C, Fe and Si, there needs to be burial in sediments to compensate for the sources of these elements to the ocean. The burial coefficients have been tuned such that the burial fluxes equal the input on 10 year timescales. CaCO_3 burial is also simulated in the model. If the saturation state of CaCO_3 (Ω) is larger than a critical value (Ω_{crit}) burial occurs and otherwise (i.e. $\Omega < \Omega_{crit}$) all CaCO_3 is dissolved.

2.4.3 Other components

The Community Atmosphere Model 6 (CAM6)

The atmosphere model in the CESM2 in the Community Atmosphere Model 6 (CAM6). In the CAM6 several processes are resolved, for example radiative transfer, a representation of boundary layer turbulence, and aerosols. The CAM6 is run on a nominal 1° horizontal grid (0.9° in latitude and 1.25° in longitude). The vertical dimension is in pressure coordinates. In total 32 vertical levels with a model top at 2.26 hPa are resolved. It is good to note that CESM2 is also used combined with a different atmosphere model (the Whole Atmosphere Community Climate Model version 6; WACCM6), but this configuration is not used in this thesis.

The Community Ice Code 5.1.2 (CICE5)

The Community Ice Code version 5.1.2 (CICE5) (Hunke et al., 2015) is used to represent sea-ice in the model. It is run on the same horizontal grid as the ocean component POP2 (see Section 2.4.1) at a nominal horizontal resolution of 1° and with eight vertical layers. Coupled to the ocean model, a salinity dependent freezing temperature is used.

The Community Land Model 5 (CLM5)

Land processes are represented by the Community Land Model version 5 (CLM5) (Lawrence et al., 2019). This module represents several surface processes such as biogeochemistry, ecology, human influences, biogeophysics and the hydrological cycle. As we use the default CESM2 version, there is no dynamic vegetation. It simulates both the terrestrial carbon and nitrogen cycle. The Model for Scale Adaptive River Transport (MOSART) (Li et al., 2013) uses the surface and subsurface runoff

from CLM5 to determine river discharges.

Coupling (CIME5)

The coupling between the components is controlled by the Common Infrastructure for Modeling the Earth (CIME). Information between the atmosphere, land, wave, and sea-ice components are communicated every 30 min. The coupler determines the fluxes between the atmosphere and ocean. Every hour the ocean module receives this information, and the atmosphere every 30 minutes.

2.4.4 Relevant biases in the CESM2 and MARBL

As with all models, the CESM2 and MARBL have biases. These biases are thoroughly described in Danabasoglu et al. (2020) (CESM2) and Long et al. (2021) (MARBL). We will describe the relevant biases for this thesis in detail in this section.

In CESM2, mixed layer depth is defined as the where in the water column the potential density is 0.125 kg m^{-3} larger compared to its surface value (Long et al., 2021). Deep water formation regions can be identified by deep (i.e. in the order of kilometers) mixed layer depths. In the North Atlantic ocean, observations indicate that deep water is formed in the Greenland – Iceland – Norwegian (GIN) Seas, the Irminger Sea, and the Labrador Sea. In CESM2, mixed layer depth in the summer is too deep in the GIN and Labrador Seas. However, the largest and most important biases are found in the winter. The mixed layer is too shallow in the GIN Seas, and too deep in the Labrador Sea. However, among CMIP6 models, CESM2 is one of the most accurate models (Heuzé, 2021). The mean AMOC strength in the CESM2 is not necessarily biased. Comparing observations from the RAPID array at 26.5°N between 2004 and 2015 and to a 3 member ensemble mean of the CESM2 emission driven historical simulations shows a very comparable strength, i.e. $17 \pm 4.5 \text{ Sv}$ for the observations (Smeed et al., 2015), and $19 \pm 2.0 \text{ Sv}$ for the ensemble mean. The biases in mixed layer depth also result in a North Atlantic that is more ventilated than observations suggest. The Atlantic thermocline, and especially the deep Pacific Ocean are less ventilated compared to observations. In the deep Pacific the circulation is very sluggish which is probably related to interactions between the atmosphere and ocean physics.

This sluggish circulation has several important biogeochemical effects. First of all, the reduced ventilation results in lower oxygen concentrations in the deep Pacific Ocean. Oxygen is necessary to remineralize organic matter, and when the oxygen concentrations are too low, organic matter is remineralized using nitrogen compounds directly affecting the nitrogen cycle in the ocean. Since this bias was noted only late in the development process in CESM2, an ad hoc fix was used to prevent large oxygen minimum zones in the deep Pacific (see Section 2.4.2).

Another effect of the sluggish circulation is potential nutrient trapping in the deep Pacific, depleting the rest of the ocean of nutrients. This may have caused the too low surface concentrations of PO_4^{3-} and NO_3^- in the Southern Ocean. Other biases with respect to surface nutrient concentrations are depleted concentrations in the North Pacific, and increased concentrations in the oligotrophic subtropical gyres. Integrated over the entire ocean, total NPP falls within the range of satellite derived estimates. For chlorophyll the biases are mostly regional. In the northern hemi-

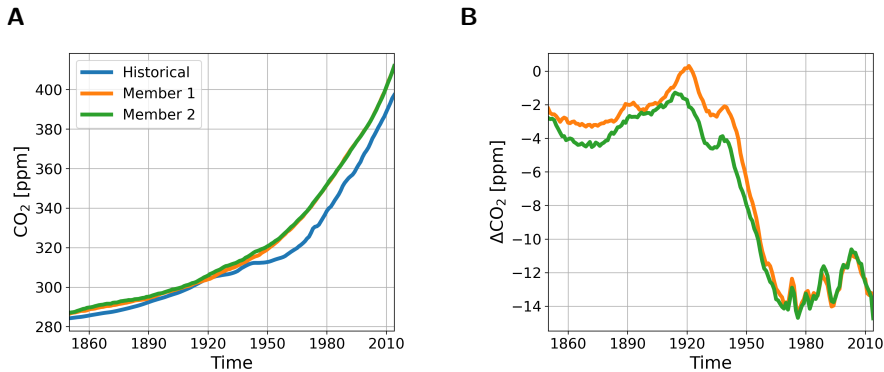


Figure 2.7: (a) Historical CO₂ concentrations in ppm as prescribed for historical concentration driven simulations (blue), and as prognostically determined by CESM2 in emission driven simulations (2 members, orange and green). (b) Difference between the prescribed CO₂ concentration (blue in a) and calculated concentrations in CESM2. All data is based on yearly averaged data.

sphere growing season, there are large positive biases in chlorophyll in the North Pacific and North Atlantic. In the southern hemisphere growing season, south of Australia and in the Atlantic Southern Ocean there are large positive biases.

With respect to CO₂ concentrations, CESM2 misses the slowdown in CO₂ increase between the 1940s and 1960s (Fig. 2.7). This causes a disagreement of eventually 14 ppm in 2014. Except for missing this slowdown between the 1940s and 1960s, very comparable trends are observed, but the land uptake of CO₂ is slightly overestimated and the ocean uptake of CO₂ is slightly underestimated. However, when corrected for riverine influences, it falls within observed estimates.

2.4.5 Simulations

In this thesis we have made use of 5 different simulations. In Chapter 5 we use simulations performed by NCAR for the CMIP6. The specific simulation we use is the emission driven SSP5-8.5 ('esm-ssp585') simulation (Danabasoglu, 2019a) downloaded from the Earth System Grid Federation (ESGF). This simulation runs from 2015 to 2100 and uses high emissions (Fig. 2.8). In this thesis we will refer to these simulations as the NCAR SSP5-8.5 simulation.

In Chapter 6 we use four simulations using the CESM2 performed on the Dutch supercomputer Snellius. We use results from emission driven simulations with two different emission scenarios, the low emission scenario SSP1-2.6 (126) and the high emission scenario SSP5-8.5 (585). For each scenario we have performed a control (CTL) and a hosing (HOS) simulation. The CTL simulations are only forced with the greenhouse gas emissions, while the HOS simulations are forced with greenhouse gas emissions and an additional, artificial freshwater forcing in the North Atlantic. The hosing is located in the North Atlantic Ocean in the region 50°N - 70°N (Fig. 2.9), and is kept constant at a rate of 0.5 Sv over the entire simulation period. We

will refer to the simulations by their simulation type (CTL or HOS) and the respective emission scenario (126 or 585), e.g. CTL-126 and HOS-585. All simulations are run from 2015 to 2100 and are initialized by values of the NCAR CMIP6 emission driven historical simulation (Danabasoglu, 2019c). In this thesis we will refer to these simulations as the IMAU CESM2 simulations.

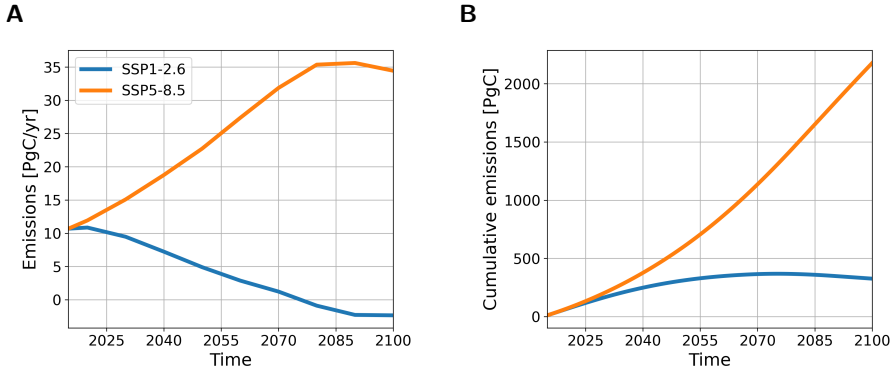


Figure 2.8: (a) Emissions for SSP1-2.6 (blue) and SSP5-8.5 (orange) in PgC/yr. (b) Cumulative emissions for SSP1-2.6 (blue) and SSP5-8.5 (orange) in PgC.

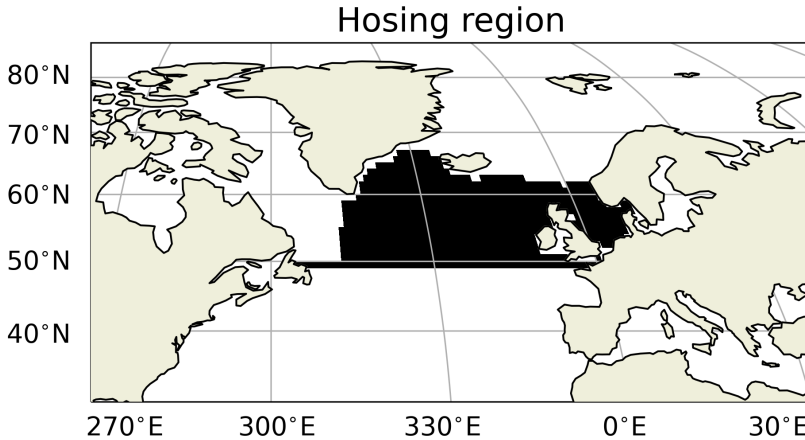


Figure 2.9: Region in black corresponds to the region where the freshwater forcing is applied. The freshwater forcing integrated over this region is 0.5 Sv throughout the entire simulation period.

Effect of the Atlantic Meridional Overturning Circulation on Atmospheric pCO₂ Variations

Proxy records show large variability of atmospheric pCO₂ on different timescales. Most often such variations are attributed to a forced response of the carbon cycle to changes in external conditions. Here, we address the problem of internally generated variations in pCO₂ due to pure carbon-cycle dynamics. We focus on the effect of the strength of Atlantic Meridional Overturning Circulation (AMOC) on such internal variability. Using the Simple Carbon Project Model v1.0 (SCP-M), which we have extended to represent a suite of non-linear carbon-cycle feedbacks, we efficiently explore the multi-dimensional parameter space to address the AMOC - pCO₂ relationship. We find that climatic boundary conditions, and the representation of biological production in the model are most important for this relationship. When climate sensitivity in our model is increased, we find intrinsic oscillations due to Hopf bifurcations with multi-millennial periods. The mechanism behind these oscillations is clarified and related to the coupling of atmospheric pCO₂ and the alkalinity cycle, via the river influx and the sediment outflux. This mechanism is thought to be relevant for explaining atmospheric pCO₂ variability during glacial cycles.

This chapter is based on:

Boot, A., A.S. von der Heydt, and H.A. Dijkstra (2022), Effect of the Atlantic Meridional Overturning Circulation on Atmospheric pCO₂ variations, *Earth System Dynamics*, vol. 13, no. 3, pp. 1041-1058

3.1 Introduction

Atmospheric $p\text{CO}_2$ values show large variations on many different timescales. Over the Cenozoic, $p\text{CO}_2$ values have gradually decreased from values of up to 2,500 ppmv in the Eocene to 300 ppmv at the end of the Pliocene. When considering the Pleistocene glacial-interglacial cycles, one of the remarkable results is the strong correlation between $p\text{CO}_2$ and temperature, with dominant variations of about 100 ppmv in 100,000 years, as reconstructed from ice cores (Petit et al., 1999). Over the industrial period, $p\text{CO}_2$ values have increased by 130 ppmv due to human activities (Friedlingstein et al., 2020). This forced trend is superposed on natural variability associated with the seasonal cycle and longer timescale climate variability (Gruber et al., 2019). The effect of the natural variability is much lower than the forced trend on such relatively short timescales. For example, the El Niño-Southern Oscillation (ENSO), a dominant mode of interannual climate variability, induces atmospheric $p\text{CO}_2$ variations of only 1-2 ppmv (Jiang & Yung, 2019). Most studies seek to explain such variations in $p\text{CO}_2$ as a forced response of the carbon cycle to changes in external conditions. For example, glacial cycles are thought to be caused by orbital variations in insolation, possibly amplified by physical processes in the climate system (Muller & MacDonald, 2000). Such variations in temperature (and other quantities, e.g., precipitation) then affect the carbon cycle, leading to changes in $p\text{CO}_2$. On the other hand, changes in $p\text{CO}_2$ will affect global mean temperature and hence may amplify any temperature anomaly. Hence it is questionable whether the $p\text{CO}_2$ response to orbital insolation changes can be considered as a solely forced response, with no internal dynamics of the carbon cycle being involved (Rothman, 2015).

The carbon cycle is comprised of an extremely complex entangled set of processes which act in the different components of the climate system (e.g., land, ocean) on many different timescales. The marine carbon cycle, with its three main carbon pumps is a major player in this cycle, at present-day resulting in the uptake of about 25% of the human released emissions (Sabine et al., 2004). The carbon pumps involve physical processes, biological processes and processes in ocean sediments. Many carbon cycle feedbacks exist, either between only physical quantities or between biological and physical quantities. An example of such a feedback is the solubility feedback: for higher atmospheric $p\text{CO}_2$, solubility of CO_2 decreases due to higher ocean temperatures, resulting in relatively less CO_2 uptake by the ocean and thus relatively higher atmospheric $p\text{CO}_2$. Given this strongly non-linear system, it would be strange if it would not show strong internal variability, i.e. variability which would exist even if the carbon-cycle system would be driven by a time-independent external forcing. There are indeed examples (Rothman, 2019), where oscillatory behavior in the carbon cycle has been attributed to internal carbon-cycle dynamics.

The physical context of all carbon pumps is the three-dimensional ocean circulation, which can be roughly decomposed in a wind-driven and an overturning component, the latter strongly related to the deep-ocean circulation. The Atlantic Meridional

Overturing Circulation (AMOC) is a major component of the global overturning circulation because of its associated meridional transport of heat, salt and nutrients. The relation between the AMOC and atmospheric $p\text{CO}_2$ is complicated. A direct effect of a changing AMOC is a change in the distribution of tracers such as temperature, dissolved inorganic carbon (DIC), alkalinity (Alk) and nutrients. For example, after an AMOC weakening the distributions of these tracers affect biological export production via reduced nutrient upwelling (Marchal et al., 1998; Mariotti et al., 2012; Menviel et al., 2008; Nielsen et al., 2019), and gas exchange via changing solubility of CO_2 in the ocean (Menviel et al., 2014). Besides these direct effects, the AMOC also influences mixing in the Southern Ocean. Changes in this mixing due to a weaker AMOC can result in a higher outgoing flux of carbon to the atmosphere (e.g. Huiskamp & Meissner, 2012; Menviel et al., 2014; Schmittner et al., 2007). Furthermore, changes in the AMOC also influence the general sensitivity of the marine carbon cycle to, for example, changes in the wind field (Munday et al., 2014). These processes form a complex puzzle where the sign of atmospheric $p\text{CO}_2$ change following an AMOC strength change is difficult to determine. Currently, different models produce different results with respect to the sign of the atmospheric $p\text{CO}_2$ change, which can be attributed to the assessed timescale, model used, and what climatic boundary conditions are used (Gottschalk et al., 2019).

On the other hand, $p\text{CO}_2$ also influences the AMOC (Toggweiler & Russell, 2008) and present-day climate models forced with anthropogenic emissions, simulate a weaker AMOC for larger atmospheric $p\text{CO}_2$ (Gregory et al., 2005; Weijer et al., 2020). By contrast, proxy data suggest that in the Last Glacial Maximum both atmospheric $p\text{CO}_2$ and the strength of the AMOC were lower (Duplessy et al., 1988). This shows that there is also a sensitivity to climatic boundary conditions in the relation (Zhu et al., 2015) between the AMOC and atmospheric $p\text{CO}_2$. The AMOC can also display tipping behavior (Weijer et al., 2019) under an increase of $p\text{CO}_2$, which can have large effects on climate. Examples of these effects are disrupted heat transport (Ganachaud & Wunsch, 2000), changing precipitation patterns (Vellinga & Wood, 2002) and a different distribution of important tracers in the ocean. Such tipping can hence have strong consequences on the carbon cycle, and hence on atmospheric $p\text{CO}_2$.

In this paper, we perform a systematic study of internal carbon-cycle variability and the relation AMOC- $p\text{CO}_2$ connection, using the Simple Carbon Project Model v1.0 (SCP-M). This model (O'Neill et al., 2019) simulates the most important carbon cycle processes in a simple global ocean box structure. The simple box setup enables us to efficiently scan the parameter space of the carbon-cycle model using parameter continuation methods. With this approach we aim answering the following three questions: (i) How does atmospheric $p\text{CO}_2$ respond to changes in the strength of a constant (in time) AMOC? (ii) Does the $p\text{CO}_2$ -AMOC feedback lead to new variability phenomena? And (iii), are there tipping points and internal oscillations in the carbon cycle?

When answering these questions, we pay special attention to different (non-linear) carbon cycle feedbacks. We will also use two different model configurations to take account of different climatic boundary conditions, the pre-industrial (PI) configuration and the Last Glacial Maximum (LGM) configuration. The SCP-M, its configura-

tions, the different additional feedbacks implemented, and the parameter continuation approach are described in Sections 2.1 and 3.2. In Section 3.3 we present the results of the different cases considered, and we conclude the paper with a summary and discussion in Section 3.4.

3.2 Methods

3.2.1 SCP-M

The SCP-M is a carbon cycle box model focused on the marine carbon cycle and a description is given in Chapter 2. In this study we will only use the three most important tracers: DIC, Alk, and phosphate (PO_4^{3-}), to reduce the problem size. In the original model there is also a terrestrial biosphere component, and several sources of CO_2 to the atmosphere. We will not use these, since our focus is on the marine carbon cycle. For this study we have implemented several (non-linear) feedbacks in the original SCP-M. A description of these feedbacks, the solution method, and the changes made to the model to make it suitable for this solution model are given in Sections 3.2.2 and 3.2.3.

3.2.2 Representation of carbon cycle processes and feedbacks

The carbon cycle has many (non-linear) feedbacks which are not represented in the original SCP-M version to keep the model as simple as possible. The absence of these feedbacks can lead to non-physical behavior (e.g. negative concentrations) when parameter values, such as the AMOC strength, are changed. We have implemented several additional feedbacks which can be divided into two categories: those that mostly concern physical processes and those associated with biological processes. The feedbacks are included through parameters λ 's; when such a parameter is zero, the feedback is not active in the SCP-M and the original version applies. For all feedbacks, except the feedback on the rain ratio (Eq. 3.9 below), the sign of the feedback (positive or negative) is unclear beforehand as multiple (carbon cycle) processes are involved.

Physical processes

An important feedback is the coupling of temperature to atmospheric pCO_2 . There are several ways temperature effects the carbon cycle. For example, decreasing temperatures increase the solubility of CO_2 , which results in more uptake of CO_2 by the ocean. For this feedback, we make a distinction between box 5 and boxes 1, 2 and 7. Box 5, the southern high latitude surface box, is more isolated than the other boxes due to the Antarctic Circumpolar Circulation (ACC). Therefore, we have included the option in the model to use a different sensitivity in Box 5. The temperature in the boxes is calculated as follows

$$T_i = T_{i,base} + \Delta T_i, \quad i = 1, 2, 5, 7 \quad (3.1)$$

$$\Delta T_i = \lambda_T \times 0.54 \times 5.35 \times \ln \frac{CO_2}{CO_{2,base}}, \quad i = 1, 2, 7 \quad (3.2)$$

$$\Delta T_5 = \lambda_{T5} \times 0.54 \times 5.35 \times \ln \frac{CO_2}{CO_{2,base}} \quad (3.3)$$

Here $T_{i,base}$ is the base temperature in the SCP-M. The change in temperature is dependent on atmospheric pCO_2 and a base value of atmospheric pCO_2 . This base value is the steady state solution in the SCP-M without feedbacks (Table 2.1). Climate sensitivity can be changed via the λ parameters. For a λ of 1, sea surface temperatures increase 2 K per CO_2 doubling. As a reference, a 2 K warming for surface air temperatures is at the lower end of the range found in CMIP6 models (Zelinka et al., 2020).

Besides an effect on solubility, temperature can also affect the piston velocity. In the often used Wanninkhof (1992) formulation, the piston velocity is dependent on temperature via the Schmidt number (Eq. 3.4 and 3.5). In our model, we use this dependency on the Schmidt number, which causes the piston velocity to increase for warmer temperatures. Hence

$$k_{w,i} = (1 - \lambda_P) \times k_{w,i,base} + \lambda_P \times k_{w,i,base} \times \left(\frac{Sc_i}{660}\right)^{-0.5}, \quad i = 1, 2, 5, 7 \quad (3.4)$$

Where

$$Sc_i = 2116.8 - 136.25T_i + 4.7353T_i^2 - 0.092307T_i^3 + 0.0007555T_i^4, \quad i = 1, 2, 5, 7 \quad (3.5)$$

In these equations, k_w is the used piston velocity, $k_{w,base}$ is the piston velocity in the SCP-M (3 m/day), and T is the temperature of the box in $^{\circ}C$. The λ parameter needs to be either 0 (constant piston velocity, as in SCP-M) or 1 (variable piston velocity). Notice that if the temperature feedback is used ($\lambda_T > 0$), the Schmidt number depends on atmospheric pCO_2 .

Biological processes

A large limitation in the original SCP-M is the constant biological production. Nutrient availability introduces a large constraint on biological production, but this process is completely absent in the original SCP-M. This process is introduced in the model here by adopting the expression used in the Long-term Ocean-atmosphere-Sediment Carbon cycle Reservoir model (LOSCAR) (Zeebe, 2012). In LOSCAR, production is dependent on the upwelling of nutrients, which in our model translates to the expressions

$$Z_1 = (1 - \lambda_{BI}) \times Z_{1,base} + \lambda_{BI} \times (\gamma_2 \times [PO_4^{3-}]_3 + R_{PO4}) \times \epsilon_1 \quad (3.6a)$$

$$Z_2 = (1 - \lambda_{BI}) \times Z_{2,base} + \lambda_{BI} \times \psi_2 \times [PO_4^{3-}]_3 \times \epsilon_2 \quad (3.6b)$$

$$Z_5 = (1 - \lambda_{BI}) \times Z_{5,base} + \lambda_{BI} \times \alpha \times [PO_4^{3-}]_7 \times \epsilon_5 \quad (3.6c)$$

$$Z_7 = (1 - \lambda_{BI}) \times Z_{7,base} + \lambda_{BI} \times (\alpha \times \psi_1 + \psi_2) \times [PO_4^{3-}]_4 \times \epsilon_7 \quad (3.6d)$$

In these equations Z represents the production in the surface box, and Z_{base} the value used in the original SCP-M. Furthermore, α is the fraction of ψ_1 that moves from Box 4 to Box 7, and ϵ is the biological efficiency in the box. As with the piston velocity, λ_{BI} is either 0 (SCP-M) or 1. Notice that the current branch represented by ψ_1 which flows from Box 4 to Box 5, does not influence the production in Box 5.

We do not use this branch, since it is assumed to flow into Box 5 below the euphotic zone.

In the equations (3.6) also the biological efficiency (ϵ) is introduced. There are studies (e.g. Cael et al., 2017) where they relate biological efficiency to temperature. We have adopted a simple linear relation to represent the influence of temperature on biological efficiency, i.e.,

$$\epsilon_i = \lambda_\epsilon \times (-0.1\Delta T_i) + \epsilon_{i,base}, \quad i = 1, 2, 5, 7 \quad (3.7)$$

In this equation, λ_ϵ controls how strong the relation is between the efficiency and temperature change (ΔT). In addition, ϵ_{base} is the base value of the biological efficiency. These values have been fitted so that Z is equal to Z_{base} under the original parameter values in the SCP-M.

In the SCP-M, PO_4^{3-} is the only nutrient. In the real ocean, additional nutrients play a role in biological production, one of them being nitrate (NO_3^-). During photosynthesis, organisms take up nitrate, and thereby increase Alk. This biological influence on Alk is not incorporated in the SCP-M, but present in many other models (e.g. Kwon & Primeau, 2008). We have included this influence as follows:

$$A_{Bio,i} = \lambda_{BA} \times \left(-\frac{16}{106}\right) \times C_{Bio,i}, \quad i = 1, 2, 3, 4, 5, 6, 7 \quad (3.8)$$

In this equation A_{Bio} is the biological flux affecting Alk. This flux is related to the DIC biological flux (C_{Bio}) and the N:C Redfield ratio ($\frac{16}{106}$). For this relation, the λ_{BA} parameter can be 0 (not included, original SCP-M), or 1 (included).

Finally, we have also included a feedback for the rain ratio, which is the fraction of calcifiers in the total biological production. In the original SCP-M this is a constant value for all boxes. Calcifiers can be limited in growth when CO_3^{2-} concentrations are too low. Ridgwell et al. (2007) model this limitation via the saturation state of CaCO_3 as

$$F_{Ca,i} = (1 - \lambda_F) \times F_{Ca,base} + \lambda_F \times 0.022 \left(\frac{[\text{Ca}^{2+}]_i [\text{CO}_3^{2-}]_i}{K_{sp_i}} - 1 \right)^{0.81}, \quad i = 1, 2, 5, 7 \quad (3.9)$$

Here, F_{Ca} is the used rain ratio, and $F_{Ca,base}$ is the value used in the original SCP-M (0.07). The saturation state is determined via the concentrations of calcium ($[\text{Ca}^{2+}]$), the carbonate ion concentration $[\text{CO}_3^{2-}]$, and an equilibrium constant K_{sp} . In this feedback, λ_F is either 0 (SCP-M) or 1. The rain ratio feedback is a negative feedback. When carbonate concentrations increase in the surface layer, the rain ratio increases and therefore more calcium carbonate is removed from the surface layer effectively lowering the carbonate concentration.

3.2.3 Parameter continuation methodology

The SCP-M, including our representations of the additional feedbacks, leads to a system of ordinary differential equations of the form

$$\frac{d\mathbf{u}}{dt} = \mathbf{f}(\mathbf{u}(t), \mathbf{p}), \quad (3.10)$$

where \mathbf{u} is the state vector (containing all the dependent quantities in all boxes), \mathbf{f} contains the right-hand-side of the equations and \mathbf{p} is the parameter vector. Here, we use the continuation and bifurcation software AUTO (see Chapter 2) to scan the parameter space and detect bifurcations efficiently (Doedel et al., 2007, 2021). The SCP-M is very suitable to be implemented into AUTO and to easily compute branches of equilibrium solutions, such as steady states of Eq. (3.10), versus parameters.

The equations of the SCP-M turn out to have a singular Jacobian matrix (because both carbon, alkalinity and phosphate quantities are determined up to an additive constant), which requires adding integral conservation equations. We have added such integral conservation equations for carbon (DIC and atmospheric pCO_2), Alk and PO_4^{3-} to the model equations to replace the equations for Box 4. The conservation law for PO_4^{3-} is straightforward and already present in the model equations. The constant influx of PO_4^{3-} via the rivers is equal to the constant outflux via the sediments.

In the original SCP-M model, carbon and Alk are conserved in the ocean, atmosphere, continents, and sediments. However, the continental and sediment stocks are not explicitly represented in the version of the SCP-M we use. However, we can describe the change of total carbon and total Alk in the combined atmosphere and ocean stocks over time as

$$\frac{dT C}{dt} = C_{river} \times V_1 + \sum_{n=1}^7 (C_{carb,n} \times V_n) + \sum_{n=1}^7 (C_{bio,n} \times V_n) \quad (3.11a)$$

$$\frac{dT Alk}{dt} = A_{river} \times V_1 + \sum_{n=1}^7 (A_{carb,n} \times V_n) \quad (3.11b)$$

In these equations TC and $TAlk$ are the total carbon and alkalinity in the system. As with PO_4^{3-} , total carbon and Alk change due to influx via the rivers (C_{river} and A_{river}) and outflux via the sediments. The carbon outflux via the sediments is determined by the sum of carbonate (C_{carb}) and biological (C_{bio}) fluxes in the system. For Alk, the biological influence is absent. Model simulations with the original SCP-M have shown that the influence of the biological fluxes is negligible, i.e. all biologically produced organic matter is respired in the ocean itself. Therefore, this term can be set to zero in Eq. (3.11a). This makes Eq. (3.11b) proportional to Eq. (3.11a) and hence we include only the latter and use it to determine the change in total Alk in the model.

We also changed the carbonate chemistry in the model. The original SCP-M uses the algorithm of Follows et al. (2006), which solves the carbonate chemistry by using hydrogen ion concentrations from a previous time step. Therefore, the algorithm is inherently transient and, since we directly solve for steady-state solutions, not suitable. We therefore adopted a simple ‘textbook’ carbonate chemistry based on carbonate alkalinity (Munhoven, 2013; Williams & Follows, 2011). This method approximates oceanic pCO_2 by assuming that Alk is equal to carbonate alkalinity ($A_C = [\text{HCO}_3^-] + 2 [\text{CO}_3^{2-}]$). A disadvantage of this method is that pH values are generally a bit higher (0.15-0.2) than using more complicated algorithms (Munhoven, 2013). These higher pH values are one of the reasons our atmospheric pCO_2 values

are lower than in the original SCP-M (approximately 60 ppm for case P-0 described in Section 3.3).

Eventually, by including Eq. (3.11a) and the overall conservation equations, the version of SCP-M used is a dynamical system with a state vector of dimension $d = 20$. There is one equation for atmospheric $p\text{CO}_2$, six for DIC, Alk and PO_4^{3-} in the ocean, and one equation for the total carbon content. Except for the new carbonate chemistry, the necessary changes made to the SCP-M do not change the outcome of the model compared to the original model. When the original model is fitted with the same carbonate chemistry based on carbonate alkalinity, the AUTO implementation and the original code produce the same results.

3.3 Results

In Section 3.3.1 we present the general sensitivity of atmospheric $p\text{CO}_2$ to variations in the AMOC strength. We extend these results in Section 3.3.2 by adding a coupling between the AMOC strength and atmospheric $p\text{CO}_2$. Internal variability found in the model will be presented in Section 3.3.3. An overview of all cases considered is given in Table 3.1. Our control experiment uses the original model, which is tuned to accurately represent the pre-industrial and last glacial maximum carbon cycle. From this ‘realistic’ model we investigate the sensitivity of the carbon cycle to specific carbon cycle feedbacks which can be found in more detailed models. By gradually increasing the amount of feedbacks in the model, we can assess the effects of the (combined) feedbacks.

Table 3.1: Overview of the cases considered and their notation. The left column displays the used feedback. The other columns show the notation and what feedback are included in the specific case. The ‘x’ in the notation is replaced with either P for the PI configuration, or L for the LGM configuration. Shaded columns indicate that this combination of feedbacks is also used for cases with a coupling between the AMOC and atmospheric $p\text{CO}_2$ (Section 3.3.2). For these cases, ‘C’ is added to either ‘P’ or ‘L’ to denote the coupling. The last column represents the feedback combinations used in Section 3.3.3. Case x-CTL is the original SCP-M.

Notation	λ_{BI}	λ_T	λ_P	λ_{BA}	λ_F	λ_ϵ	λ_{T5}
x-CTL	0	0	0	0	0	0	0
x-BIO	1	0	0	0	0	0	0
x-TEMP	0	1	0	0	0	0	0
x-PV	0	0	1	0	0	0	0
x-BALK	0	0	0	1	0	0	0
x-RAIN	0	0	0	0	1	0	0
x-BIO-TEMP	1	1	0	0	0	0	0
x-BIO-PV	1	0	1	0	0	0	0
x-BIO-BALK	1	0	0	1	0	0	0
x-BIO-RAIN	1	0	0	0	1	0	0
x-BIO-TEMP-PV	1	1	1	0	0	0	0
x-BIO-TEMP(A)-EFF	1	1	0	0	0	1	1
x-ALL	1	1	1	1	1	1	1
x-HB	1	2.085	1	0	0	1.5	1

3.3.1 Sensitivity of atmospheric pCO₂ to the AMOC

In this section the AMOC strength is used as a control parameter and steady states are calculated versus this parameter. For each configuration (PI and LGM) we use three reference cases (x-CTL, the original SCP-M configuration, x-BIO, with a different parameterization for biological production, and, x-ALL, with all feedbacks included, in Table 3.1, where x is either P for the PI or L for the LGM configuration). The steady-state value of atmospheric pCO₂ versus AMOC is shown for the reference cases in Fig. 3.1, where all branches represent stable fixed points. For the cases where the biological feedback is not included, the solutions for smaller values of AMOC (< ~12 Sv) display negative PO₄³⁻ concentrations in Box 2 and hence are not allowed. Such boundaries can be automatically monitored in AUTO and the continuation is stopped once a boundary is exceeded.

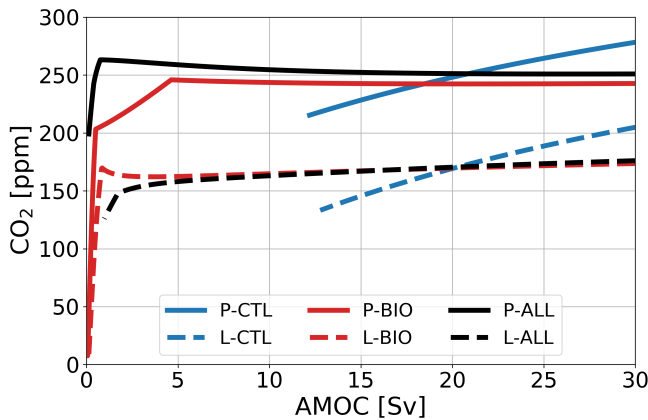


Figure 3.1: Atmospheric pCO₂ in ppm under varying AMOC strength in Sv for three reference cases (blue: no feedback, red: with biological feedback, black: all feedbacks) in two configurations (solid: PI, dashed: LGM). All branches represent stable fixed points.

For the PI-configuration, Fig. 3.1 shows that, whereas pCO₂ increases for larger AMOC strengths in case P-CTL, it remains fairly constant in P-BIO and P-ALL. Atmospheric pCO₂ in case P-BIO peaks around 5 Sv, then decreases until approximately 20 Sv after which it increases slightly again. This different behavior occurs because, in case P-BIO, the AMOC has competing influences on DIC concentrations of the surface ocean. A first effect of an increasing AMOC is to increase the ventilation of the deep ocean, which also increases DIC concentrations in the surface layer. This promotes outgassing to the atmosphere. However, by increasing the AMOC strength, biological production in Boxes 2 and 7 is also increased. As a result, DIC and PO₄³⁻ are transported from the surface layer to the deep ocean. The first effect is dominant after 20 Sv, and the second effect in the range of 5 to 20 Sv. The absence of the second effect in P-CTL explains the difference in sensitivity between P-CTL and P-BIO. P-ALL behaves fairly similar as P-BIO, except in the regime with a weak AMOC strength (< ~4 Sv). This behavior is caused by the saturation dependent rain ratio. When we look at the other cases (Fig. 3.2a), we see that they either behave qual-

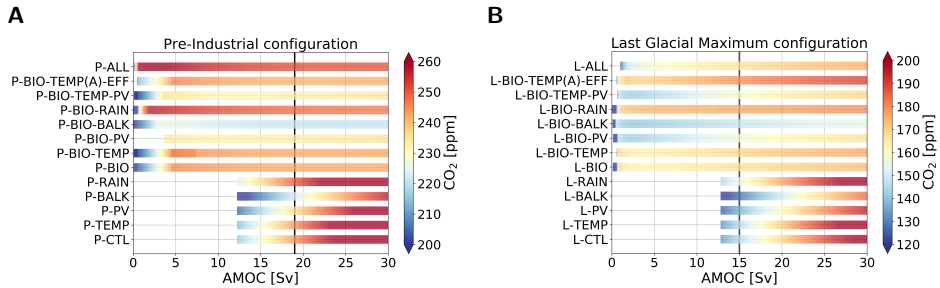


Figure 3.2: Atmospheric pCO₂ in ppm (color shading) under varying AMOC strength in Sv for the cases considered in Table 3.1. (a) Pre-industrial configuration. (b) Last Glacial Maximum configuration. Note that the range of the color shading differs between the two configurations and that some CO₂ concentrations fall outside the displayed range. The AMOC range of the bars differ, because for some cases the steady solution becomes nonphysical (e.g. negative concentrations or large subzero temperature). The vertical black lines represent the AMOC strength in the original SPC-M.

itatively like P-CTL (the cases without ‘BIO’), or P-BIO (cases with ‘BIO’). Looking in more detail, we can see that when we include the rain ratio feedback (cases P-RAIN, P-BIO-RAIN) atmospheric pCO₂ is higher, and when we include the biological influence on alkalinity, atmospheric pCO₂ is lower (cases P-BALK, P-BIO-BALK). The results in Fig. 3.2a show that the biological feedback ($\lambda_{BI} = 1$) is the most dominant feedback in the PI configuration, i.e., including this feedback leads to a completely different sensitivity of the carbon cycle to changes in the AMOC strength.

For the LGM configuration (Fig. 3.2), two important differences with respect to the PI-configuration appear: (1) atmospheric pCO₂ is approximately 80 ppm lower, and (2) cases L-BIO and L-ALL have a different sensitivity than cases P-BIO and P-ALL for lower AMOC values. Where in P-BIO atmospheric pCO₂ decreases for an increasing AMOC between 5 and 20 Sv, L-BIO shows a monotonous increase of atmospheric pCO₂ from 3 Sv onward. We see this different relation, because in the LGM-configuration, deep-ocean ventilation, which can be seen as the sum of the GOC and AMOC, is lower due to a weaker GOC. Consequently, deep-ocean ventilation is more sensitive to changes in the AMOC. This eventually causes the different response of cases L-BIO and L-ALL with respect to case P-BIO and P-ALL. Cases L-TEMP to L-BIO-TEMP(A)-EFF (Fig. 3.2b) relate to the L-CTL and L-BIO as in the PI-configuration. Fig. 3.2b shows that in the LGM configuration, as is the case in the PI configuration, the biological feedback is most dominant. The other feedbacks only influence the offset of CO₂ concentrations, but do not result in large changes to the relation between the AMOC and atmospheric pCO₂.

3.3.2 Coupling AMOC - carbon cycle

The AMOC strength depends also on atmospheric pCO₂ and below we will discuss the steady state model solutions when a coupling between the AMOC and atmospheric pCO₂ is applied. This coupling is based on how the AMOC responds to

increasing atmospheric $p\text{CO}_2$ in CMIP6 models (e.g. Bakker et al., 2016) and given by

$$\psi_2 = \psi_{2,base} \times \left(1 - \lambda_A \times 0.1 \times 0.54 \times 5.35 \times \ln \frac{CO_2}{CO_{2,base}}\right) \quad (3.12)$$

In this equation $\psi_{2,base}$ is a base value of the AMOC taken from the uncoupled case (where the AMOC is prescribed), ψ_2 is the actual AMOC strength in m^3/s in the coupled case and λ_A determines the strength of the coupling. We use three different values of λ_A in this section: (1) 0 (no coupling), 1 (20 % decrease for a CO_2 doubling), and 4 (80% decrease for a CO_2 doubling). As the AMOC strength ψ_2 is now part of the state vector, we need other quantities as control parameters. We will use three different parameters here: (1) the rain ratio (F_{Ca}), (2) the biological production (Z), and (3) the piston velocity (k_w). We have chosen these three parameters since they (approximately) represent the three carbon pumps: the carbonate pump, the soft tissue pump, and the solubility pump, respectively. We follow the steady-state solution in these parameters, where possible, between 0.1 to 10 times the reference value (indicated by the multiplier in Fig. 3.3). This large, though not necessarily realistic, range is used to test the sensitivity of the carbon cycle to the parameters, and to see whether bifurcations can arise in the carbon cycle. When we look at the effect of increasing λ_A , i.e. the coupling, we see that the general sensitivity of the solution to changes in model parameters decreases. This effect is best seen in case LC-CTL, but also present in the other cases, though less pronounced.

In Fig. 3.3a, b we plot the results when we use the rain ratio as a control parameter in the continuation. There are no large differences between the different cases and configurations. Generally, we see two regimes. For low rain ratios, the solution is quite sensitive to changes in the rain ratio. Where the coloring in Fig. 3.3a, b is yellow (around 230 ppm for the PI and around 140 ppm for the LGM configuration), we see a shift: the solution becomes less sensitive to changes in the rain ratio. To explain the regimes of sensitivity, we note that the CaCO_3 production is linearly related to the rain ratio. The production minus the dissolution of CaCO_3 in the water column determines the outflux of Alk and DIC via the sediments. The different regimes can be explained by the amount of CaCO_3 dissolution in the deep and abyssal ocean. For low rain ratios, the saturation state in the ocean is larger than 1, which means there is no saturation driven dissolution and only constant dissolution. This makes the outflux of Alk and DIC linearly proportional to the production: if the rain ratio is low, the outflux is also low. Because we are looking at a steady state solution, this decrease in burial has to be compensated for by a weaker influx, i.e. a lower river influx. This is only possible when atmospheric $p\text{CO}_2$ is lower. For larger rain ratios, we have both saturation dependent and constant dissolution in the subsurface boxes, i.e. more dissolution in the water column. Due to the variable dissolution, the outflux of Alk and DIC is no longer fully determined by CaCO_3 production. This results in a lower sensitivity of the outflux to changes in the rain ratio. Therefore, atmospheric $p\text{CO}_2$ is also less sensitive to the rain ratio.

For biological production as a control parameter (Fig. 3.3c, d) again all cases show comparable behavior. We can see that the parameter range for higher biological production is short. This is because PO_4^{3-} concentrations become negative at this point, even when we include the biological feedback. All cases have a maximum

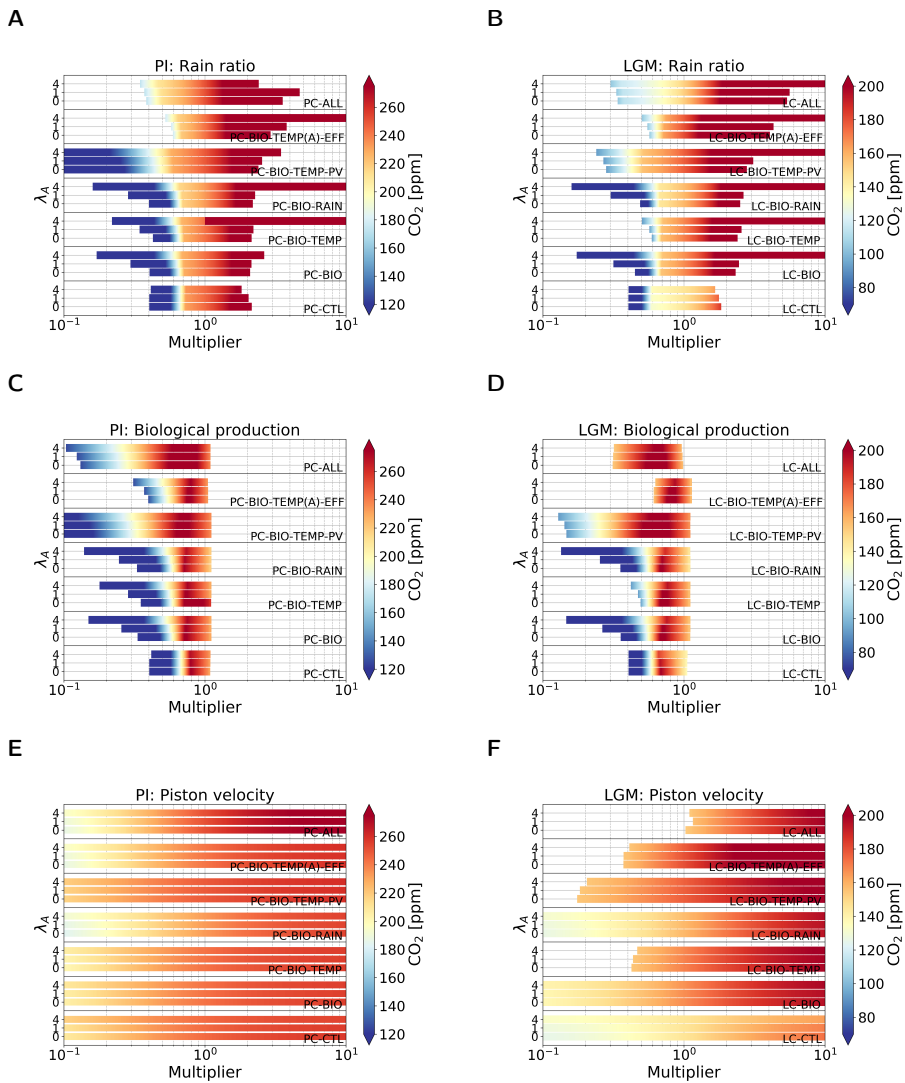


Figure 3.3: Atmospheric pCO₂ in ppm (color shading) under varying parameter values. The left column represents cases of the PI configuration, and the right column of the LGM configuration. The top row shows cases where the strength of the rain ratio is varied between 0.1 and 10 times the original value. The other rows show the same but for cases where biological production (middle row) and the piston velocity (bottom row) are varied. In total 7 feedback combinations are used, denoted by the text within the graph. For each case, three different coupling strengths have been used: (1) $\lambda_A=0$, (2) $\lambda_A=1$, and (3) $\lambda_A=4$.

in atmospheric $p\text{CO}_2$ around 0.7-0.8 times the original value. When the multiplier is lower than this value, we see a positive relation (higher biological production, higher atmospheric $p\text{CO}_2$). For values larger than the maximum, we see an opposite relation, i.e. lower atmospheric $p\text{CO}_2$ for higher biological production. This second regime is generally what we would expect when biological production is increased, i.e. when biological production removes more carbon from the surface layer, more carbon can be taken out of the atmosphere by the surface ocean which reduces atmospheric $p\text{CO}_2$. The first regime is not what we would expect at first, but this can be explained by the same mechanism as for the rain ratio: reduced biological production leads to low production of CaCO_3 leading to low burial rates of CaCO_3 . Lower burial rates lead to lower river influx because the sources and sinks of alkalinity to the ocean balance, which can only be achieved by decreasing atmospheric $p\text{CO}_2$. Again, increasing the AMOC coupling only reduces the sensitivity of the solutions. In Fig. 3.3e-f, we plot the results when we use the piston velocity parameter (k_w) as a control parameter. By the gradually changing colors, we can see a logarithmic relation with higher sensitivities for lower piston velocities. The different feedbacks, configurations, and coupling strengths have the same effect as for the other two control parameters discussed above.

3.3.3 Internal oscillation

The feedback strengths we have used so far have been quite modest. The continuation methodology enables us to efficiently look at cases with different feedback strengths and to see whether different combinations can induce bifurcations in the carbon cycle and by extensively scanning the parameter space we found such bifurcations. Especially in the LGM-configuration, when climate sensitivity (λ_T) and the biological efficiency feedback (λ_ϵ) are increased, bifurcations arise on the branches of steady solutions. With case L-HB (for parameter values, see Table 3.1), we present an example where we find a supercritical Hopf Bifurcation (HB) around 13 Sv (Fig. 3.4a) in the uncoupled case ($\lambda_A = 0$, so the AMOC strength is a control parameter again). The HB produces a stable limit cycle extending to larger AMOC strengths with a period between 5,000 and 6,000 years where all state variables oscillate. In this section we look at the internal oscillation at 15 Sv (Fig. 3.4b). The oscillation has a period of 5,814 years, and atmospheric $p\text{CO}_2$ has a range of 72 ppm.

The HB described in this section exists for a large range of parameter values and is thus robust. One important constraint on the existence of the bifurcation is the coupling strength between atmospheric $p\text{CO}_2$ and biological production. This coupling comes down to the effect of atmospheric $p\text{CO}_2$ on the biological efficiency (ϵ), which can be increased by increasing the temperature feedback (λ_T) and/or the efficiency feedback (λ_ϵ). We do not find this bifurcation in the PI-configuration, because when the biology feedback ($\lambda_{BI} = 1$) is included, atmospheric $p\text{CO}_2$ is insensitive to changes in the AMOC strength (case P-BIO, Fig. 3.1). Because of this low sensitivity, surface ocean temperature and biological efficiency are also insensitive to changes in the AMOC strength in the PI-configuration. Therefore, the coupling between the two is less effective in this configuration and we do not find a HB.

To explain the mechanism behind the oscillation, we have to look at the time-dependent solution of the model. What is important for this oscillation is the cou-

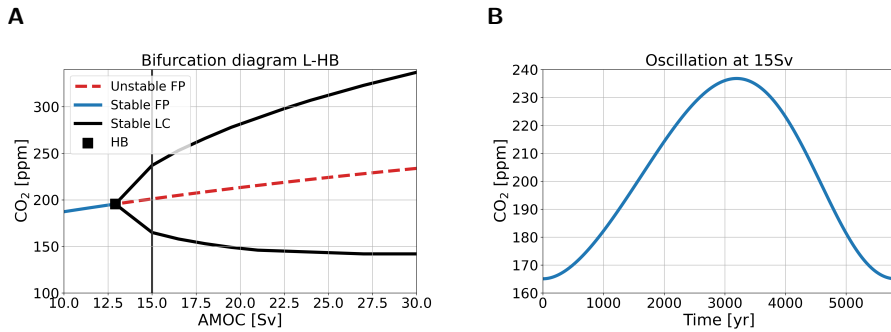


Figure 3.4: (a) Bifurcation diagram for case L-HB in atmospheric $p\text{CO}_2$ - AMOC space. Blue, solid lines denote stable steady states (or fixed points, FPs); red, dashed lines indicate unstable steady states; black, solid lines indicate a stable limit cycle (LC), and the black square denotes the location of a (supercritical) Hopf Bifurcation (HB). (b) The oscillation of atmospheric $p\text{CO}_2$ in ppm versus time in years for the limit cycle at 15 Sv. The period is 5,814 yr.

pling between atmospheric $p\text{CO}_2$ and the alkalinity cycle. Alkalinity influences the gas exchange between the ocean and the atmosphere via the carbonate chemistry and is, in turn, influenced by atmospheric $p\text{CO}_2$ because the source and sink of alkalinity are coupled to $p\text{CO}_2$. The source, the river influx, is linearly proportional to atmospheric $p\text{CO}_2$.

The sink, i.e. outfluxing via the sediments, is related to CaCO_3 burial, which is the difference between CaCO_3 production in the surface ocean and CaCO_3 dissolution in the ocean and sediments. In the oscillation, the saturation state of CaCO_3 in the ocean is everywhere larger than 1. This happens when the river influx is larger than the biogenic flux in the surface ocean (Zeebe & Westbroek, 2003), which is plausible for the past oceans. Therefore, total dissolution in the ocean is constant and does not vary. This means that CaCO_3 burial becomes a function of CaCO_3 formation and thus biological production. Since this production is dependent on the biological efficiency, which is directly proportionate to atmospheric $p\text{CO}_2$, the sink is also influenced by atmospheric $p\text{CO}_2$. However, the effect of atmospheric $p\text{CO}_2$ on the source and sink is opposite. When atmospheric $p\text{CO}_2$ is high, the river influx is high, while the sediment outflux is low. This is key to the general mechanism sketched in Fig. 3.5.

The results show that atmospheric $p\text{CO}_2$ is affected by the amount of ingassing into Box 1. Therefore, we start the explanation of the oscillation in Fig. 3.5 at this point. At the beginning of the oscillation (time $t = 0$ in Fig. 3.5), ingassing in Box 1 starts to decrease. As a result, atmospheric $p\text{CO}_2$ starts to increase approximately 200 years later. There is a delay, since atmospheric $p\text{CO}_2$ is not solely determined by the gas exchange with Box 1. The increase in atmospheric $p\text{CO}_2$ has multiple effects. First of all, temperatures start to increase, which lowers biological efficiency. This in turn reduces CaCO_3 production, and thus the sink of alkalinity is also reduced. Another effect of increasing atmospheric $p\text{CO}_2$, is an increasing river flux, i.e. an increasing source of alkalinity into the ocean. After a quarter period (time $t = T/4$ in Fig. 3.5), the source becomes larger than the sink, and total alkalinity in the ocean starts to increase. Meanwhile, atmospheric $p\text{CO}_2$ is still increasing. As a result, the river

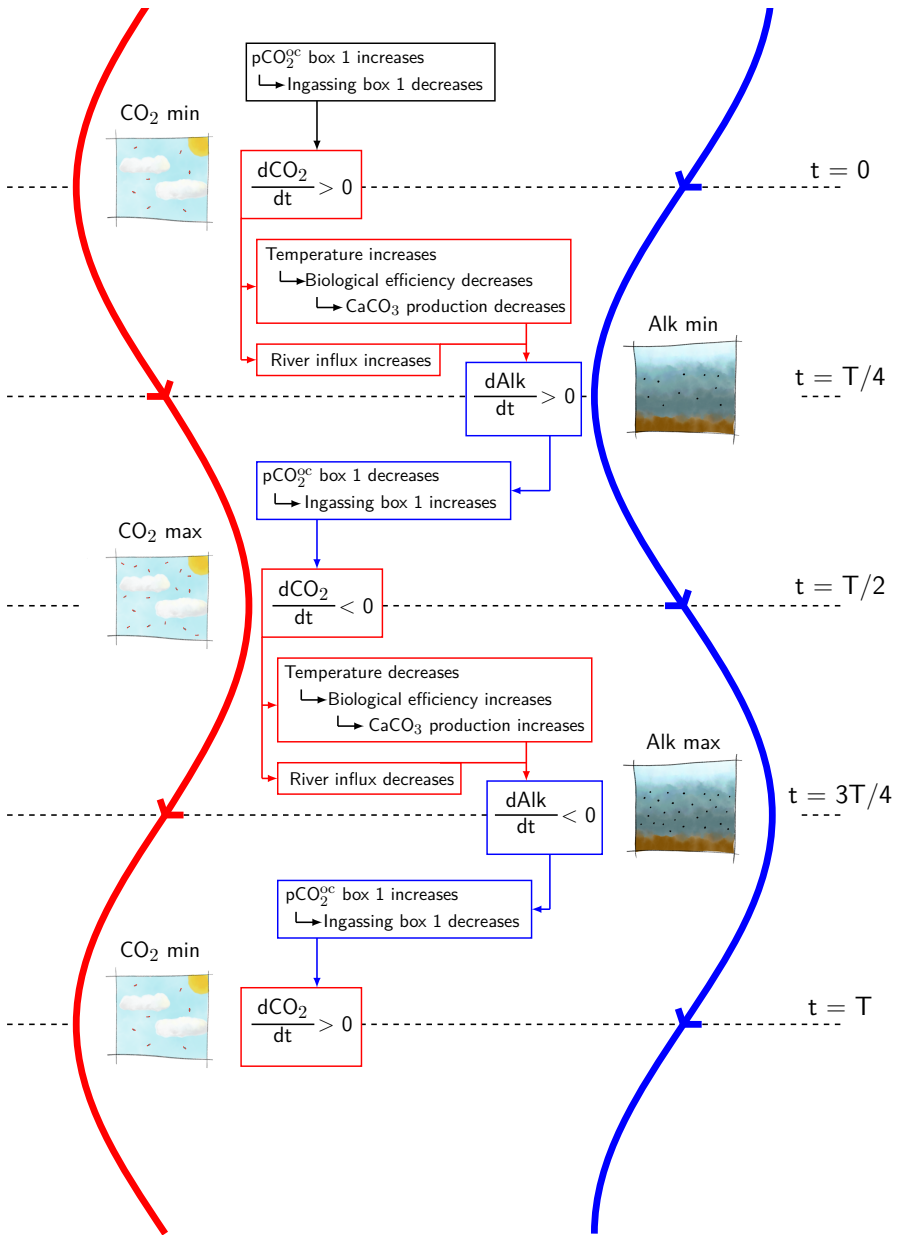


Figure 3.5: Schematic representation of the mechanism of the internal oscillation. Red colors represent processes related to CO_2 , while blue colors are related to Alk. The period starts at the top with a minimum in atmospheric CO_2 and follows the processes in the boxes following the arrows.

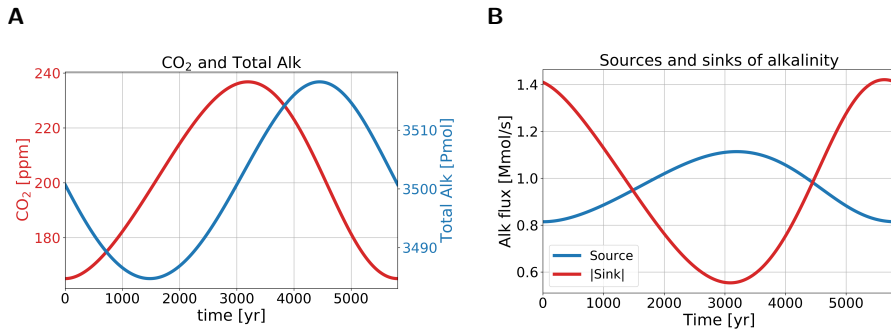


Figure 3.6: (a) Atmospheric pCO₂ (red, left y-axis) in ppm, and total alkalinity (blue, right y-axis) in the ocean in Pmol for one oscillation. Total alkalinity lags pCO₂ by approximately a quarter period. (b) The source (blue) and the absolute value of the sink (red) of alkalinity in the ocean. The source represents river influx, and the sink represents the sediment outflux. When the lines cross, i.e. around 1,500 yr and 4,400 years, total alkalinity in (a) has a minimum and a maximum respectively.

influx also keeps increasing, while the sediment outflux keeps decreasing. After half a period (time $t = T/2$ in Fig. 3.5), oceanic pCO₂ in Box 1 starts to decrease because alkalinity concentrations in Box 1 have increased. The lower oceanic pCO₂ causes ingassing into Box 1 to increase, which in turn decreases atmospheric pCO₂. The other half of the period is as explained above, but then the opposite.

The processes described above are important for driving the oscillation. However, these are not the only processes represented in the model. The concentrations of DIC, Alk and PO₄³⁻ in the ocean boxes are subtle balances of multiple larger fluxes where the sum of these fluxes can be more than 100 times smaller than the individual fluxes. It is therefore difficult to assess the effects of all the individual fluxes, since they also depend on each other. We do see that the DIC concentrations in the surface ocean boxes lag atmospheric pCO₂ by multiple centuries. It thereby increases oceanic pCO₂ after atmospheric pCO₂ has reached its maximum, which dampens the amplitude of the oscillation. The solubility constant (K_0) and dissociation constants (K_1 and K_2), which are also important for the air-sea gas exchange, oscillate due to the dependency on temperature and also dampen the amplitude of the oscillation. It is good to note that all these processes are responsible for the exact shape and amplitude of the oscillation. However, the coupling between atmospheric pCO₂ and the alkalinity cycle appears to be the driving mechanism.

In Fig. 3.6a, we can see that total alkalinity in the ocean lags atmospheric pCO₂ by approximately a quarter period. In Fig. 3.6b we can also see the anti-correlation between the source and sink of alkalinity to the ocean. Comparing the sink and source, we can clearly see a strong (anti-) correlation between atmospheric pCO₂ and the (sink) source of alkalinity. The anti-correlation between the source and sink is the driving mechanism behind the oscillatory behavior. It is good to point out that the amplitude of the sink of alkalinity is larger than that of the source. The timescale of the oscillation ($\sim 6,000$ years) is related to the adjustment time of CO₃²⁻ to an imbalance between the influx and outflux of alkalinity and DIC in the ocean. This process, termed the calcium carbonate homeostat (Sarmiento & Gruber, 2006), has

a timescale between 5 and 10 kyr (Archer et al., 1997). The period of the internal oscillation corresponds well to this range. The river influx, which plays a role in the oscillation, is usually viewed as a slow process because of the long timescales of silicate weathering (10 kyr or more). In the oscillation, however, the river flux is varying on shorter timescales. This is because in the model, carbonate weathering is more important than silicate weathering and acts on shorter timescales (1 kyr to 10 kyr timescales). Furthermore, the system does not reach equilibrium and continuously oscillates whereby the river flux responds directly to the oscillations in atmospheric $p\text{CO}_2$. It is also good to note that, even though it seems box 1 is a main driver in the oscillation, it is in fact a global process due to the role of CaCO_3 burial; the amplitude of CaCO_3 burial is more than two times larger than the amplitude of the river flux.

3.4 Summary and discussion

In this study we investigated steady states of an extended version of the Simple Carbon Project Model v1.0 (SCP-M), where additional feedbacks have been included. Focus was on the relation between the AMOC and atmospheric $p\text{CO}_2$ for these steady states, with a special attention to the effect of feedbacks and climatic boundary conditions on this relation. Although the model we use is a simple box model, the original SCP-M was shown to be quite capable of simulating present-day observations and proxy data (LGM) (O'Neill et al., 2019).

In Section 3.3.1 we looked into how the carbon cycle, and specifically atmospheric $p\text{CO}_2$ responds to changes in the AMOC. These cases include different combinations of additional feedbacks. Our results (Section 3.3.1) suggest that the most important feedback, is the biological feedback, represented by Eq. (3.6). In both the PI and the LGM configurations, this feedback leads to a different sensitivity of atmospheric $p\text{CO}_2$ to the AMOC (Fig. 3.1). Other feedbacks did not introduce large effects on the sensitivity (Fig. 3.2). This shows that biology can exert a large effect on atmospheric $p\text{CO}_2$, which support studies with more detailed models where biological production plays a role in the response of atmospheric $p\text{CO}_2$ to changes in the AMOC (e.g. Nielsen et al., 2019). The results also show the importance of the climatic boundary conditions, as was already stated in Gottschalk et al. (2019). Generally, cases with the biological feedback (x-BIO, and other cases including 'BIO') respond differently in the LGM configuration than in the PI configuration. This is related to the difference in deep ocean ventilation between the two configurations. When a coupling between the AMOC and atmospheric $p\text{CO}_2$ is included (Section 3.3.2), the $p\text{CO}_2$ of the steady solutions becomes less sensitive to changes in model parameters (k_w , Z , F_{Ca}). This shows that the coupling works as a negative feedback in the carbon-cycle dynamics. What is interesting to see, is that the carbon cycle feedbacks do not have a large effect on the AMOC- $p\text{CO}_2$ relation. This implies that ocean circulation is very effective in damping changes in gas exchange (k_w), biological (Z) and CaCO_3 (F_{Ca}) production.

When considering bifurcations of the steady solutions, an important result is what we did not find: saddle-node bifurcations. Hence, although quite non-linear carbon cycle processes have been captured in this model, no multiple equilibrium regimes

and associated hysteresis occur. As a consequence, any sharp transition in carbon cycle quantities cannot be easily linked to a transition between different steady states. However, we did find internal oscillations in the model, in particular with a period of 5,000 to 6,000 years related to the CaCO_3 homeostat (Fig. 3.5). Important for this oscillation is the process representation that CaCO_3 production reduces for increasing temperatures, which is supported by studies that suggest a decreased production under high atmospheric CO_2 concentrations (Barker & Elderfield, 2002). However, this assumption is under debate as there are studies that find an increased calcifier production for higher temperatures (Cole et al., 2018) in specific situations. Whether this internal oscillation also exists in a system where the AMOC strength and atmospheric pCO_2 are coupled (as in Section 3.3.2), is not known. The internal oscillations were found using the AMOC strength as control parameter, which is not possible with a relation as in Section 3.3.2.

Linking this oscillation to proxy data is difficult, especially since the variation in atmospheric pCO_2 is relatively high (72 ppm) for reasonable AMOC values. If we look for example at the record of the last glacial period, pCO_2 variations are of the order of 20 ppm (Bauska et al., 2021). The variation found in our model is closer to that during the Pleistocene glacial cycles, but on a much shorter timescale. The timescale is actually closer to that of the Heinrich events. It is therefore hard to find an oscillation like this in the past record, but this does not mean the mechanism is not relevant. If we look at more fundamental work, our mechanism shares similarities to the internal oscillation found in a conceptual model where only Alk and DIC are resolved (Rothman, 2019). The mechanism in Rothman (2019) is based on the imbalance between the influx and outflux of DIC in the surface ocean, and is thus comparable to our mechanism. The phase differences in our model between quantities in the carbonate system (i.e. DIC, Alk, pH, CO_3^{2-} , HCO_3^- , and H_2CO_3) in the top 250m compare well to those in Rothman (2019) (not shown). However, the responsible processes are different. In Rothman (2019) there is an important role for respiration of organic matter. In our model, this flux is implicitly modeled and we can reconstruct a similar flux from the export production. This reconstructed flux has comparable phase differences with the carbonate content as in Rothman (2019), but the relative strength of the flux does not match the burial flux in our model. This means that the SCP-M captures a different internal oscillation. In Rothman (2019) there is an important role for the ballast feedback because it couples the sources and sinks of DIC using the carbonate-ion concentration. In our oscillation, it is not the ballast feedback that drives the oscillation, but the CaCO_3 homeostat, coupling the sources and sinks of alkalinity through atmospheric pCO_2 .

The results in this study are achieved with a very simple framework with multiple assumptions and limitations. The main assumption we make is that the SCP-M is a well performing model for the Last Glacial Maximum and Pre-industrial periods. Comparison of the model results with observations in O'Neill et al. (2019) support this assumption. Assumptions in the river flux parameterization that possibly affect the oscillation are the parameter values and the fact there is no delay between the river influx and atmospheric pCO_2 . The parameter values are important for the amplitude of the oscillation and decreasing the parameters would result in a decrease in amplitude of the oscillation. However, the assumed parameters are fitted to repre-

sent estimated river influx in present-day conditions. The river flux parameterization assumes that changes in atmospheric $p\text{CO}_2$ result in changes in the river flux into the ocean mainly due to carbonate weathering. These changes are not relevant on short (annual to centennial) timescales, but will affect model results on (multi) millennial timescales. In our results, this parameterization is relevant since the approximate quarter period delay between atmospheric $p\text{CO}_2$ and total alkalinity (and alkalinity in box 1) is important in the oscillation mechanism. The river influx plays a role in this by changing the alkalinity in box 1. It would be interesting to introduce a time delay between atmospheric $p\text{CO}_2$, continental weathering and the river flux. The inclusion of such a time delay would make the carbon system more complicated, and moreover, additional oscillatory behavior is expected. However, this extension is outside the scope of this paper and will not affect our results regarding the existence of oscillatory behaviour in the carbon cycle.

We also made assumptions for the features we added to the model. The first assumption is that refitting of the parameters is not necessary. For most changes we made, we do expect this assumption to be valid since for most features the elemental cycles remained the same and constant parameter values were replaced by equations which keep the parameter values close to their original values. The addition of the biological alkalinity flux might make refitting of parameters necessary since a completely new process is added to the alkalinity cycle. Refitting of the parameters would be a large exercise and would also make comparison between the different cases difficult. However, cases with this feedback do not show divergent results compared to other cases. Maybe the most impactful change we made is the simplification of the carbonate chemistry. This change typically reduces pH by 0.15-0.2 (Munhoven, 2013), and changes equilibrium $p\text{CO}_2$ values by 20% (Munhoven, 2013) explaining the approximate 60 ppm lower atmospheric $p\text{CO}_2$ in our model. The assumption that biological efficiency is linearly related to change in temperature might not be valid while this assumption is important for the driving mechanism of the internal oscillation. However, what seems to be important for the oscillation is that the coupling between atmospheric $p\text{CO}_2$ and the biological efficiency is strong enough and not necessarily the exact formulation of the feedback. Limitations of the model include the incapability to discern between ocean boxes and strict, slightly arbitrary box boundaries. Due to these limitations, this model is not suitable to look at regional processes. However, the original SCP-M simulates representative global values, making it suitable for the application in this study.

In this study we have scanned large ranges of parameter values, with some values outside realistic ranges. The parameters we have varied are AMOC strength, the rain ratio, biological production, the piston velocity and climate sensitivity. By using such a wide range for certain parameters, we can be quite certain that there are no saddle-node bifurcations and therefore no multiple equilibria in realistic parameter ranges. We believe that most results are within a realistic range for the AMOC strength since present-day model simulations show maximum AMOC strengths of around 25 Sv (Weijer et al., 2019), while model simulations simulating an AMOC collapse show very weak AMOC strengths. In Section 3.3.2, we studied a large range of rain ratio, biological production and piston velocity values. The main purpose of this large range was to see whether bifurcations would occur, which did not. The climate

sensitivity variations we used are all within CMIP6 ranges (1.8K-5.6K; Zelinka et al., 2020). Cases without the temperature feedback, however, do yield unrealistic results since ocean temperatures remain above freezing temperature even for near zero atmospheric $p\text{CO}_2$ values.

In conclusion, we have found that the relation between atmospheric $p\text{CO}_2$ and the AMOC strength relies mostly on biological processes and climatic boundary conditions. Therefore, we suggest that by comparing results of different models, special attention should be given to the way biological production is represented. Our study also shows that atmospheric $p\text{CO}_2$ appears to be rather insensitive to changes in the AMOC strength, which suggests that projected weakening of the AMOC in the future does not lead to a large response in atmospheric $p\text{CO}_2$. In this study we also searched for saddle-node bifurcations, but we did not find any, suggesting that tipping points in the carbon cycle are unlikely to occur. Our most interesting result is the discovery of an internal oscillation in the carbon cycle and we hope that the mechanism behind this oscillation will stimulate further model work and be useful for explaining past atmospheric $p\text{CO}_2$ variability.

Potential effect of the marine carbon cycle on the multiple equilibria window of the Atlantic Meridional Overturning Circulation

The Atlantic Meridional Overturning Circulation (AMOC) is considered to be a tipping element in the Earth System due to possible multiple (stable) equilibria. Here, we investigate the multiple equilibria window of the AMOC within a coupled ocean circulation-carbon cycle box model. We show that adding couplings between the ocean circulation and the carbon cycle model affects the multiple equilibria window of the AMOC. Increasing the total carbon content of the system widens the multiple equilibria window of the AMOC, since higher atmospheric $p\text{CO}_2$ values are accompanied by stronger freshwater forcing over the Atlantic Ocean. The important mechanisms behind the increase of the multiple equilibria window are the balance between the riverine source and the sediment sink of carbon and the sensitivity of the AMOC to freshwater forcing over the Atlantic Ocean. Our results suggest that changes in the marine carbon cycle can influence AMOC stability in future climates.

This chapter is based on:

Boot, A.A., A.S. von der Heydt, and H.A. Dijkstra (2023), Potential effect of the marine carbon cycle on the multiple equilibria window of the Atlantic Meridional Overturning Circulation, *Earth Syst. Dynam. Discuss.*

4.1 Introduction

The Atlantic Meridional Overturning Circulation (AMOC) plays a large role in modulating global climate (Palter, 2015; Vellinga & Wood, 2008) because it transports heat from the Southern to the Northern Hemisphere and is one of the prominent tipping elements in the Earth System (Armstrong-McKay et al., 2022; Lenton et al., 2008). Model studies suggest that the AMOC can have multiple stable equilibria: the on-state, representing the current AMOC state with a strong northward flow at the surface and a southward return flow at intermediate depths; and the off-state, representing a weak or even reversed AMOC state (Weijer et al., 2019). From a dynamical systems point of view, a bi-stable AMOC regime appears through the occurrence of two saddle node bifurcations (Dijkstra, 2007) and the region in parameter space where both on- and off-states co-exist is the multiple equilibria window (MEW), also referred to as the bi-stability window (Barker & Knorr, 2021).

Climate variability in the past, such as Heinrich events, has been linked to tipping of the AMOC (Lynch-Stieglitz, 2017; Rahmstorf, 2002). Under anthropogenic forcing, the global warming threshold for AMOC tipping has been estimated to be around 4 °C (Armstrong-McKay et al., 2022). Using model data from the Coupled Model Intercomparison Project 6 (CMIP6, Eyring et al., 2016), a consistent weakening of the AMOC under future climate change is projected (Weijer et al., 2020), with a 34-45% decrease in AMOC strength in 2100, but no clear tipping was found. However, these models may have a too stable AMOC (Weijer et al., 2019) affecting the probability of AMOC tipping before 2100. Under AMOC tipping, a strong cooling in the Northern Hemisphere (Drijfhout, 2015; Rahmstorf, 2002), changes in the water cycle (Jackson et al., 2015; Vellinga & Wood, 2002), and potential interactions with other tipping elements in the Earth System (Dekker et al., 2018; Sinet et al., 2023; Wunderling et al., 2021) are expected.

The AMOC can also interact with the marine carbon cycle and therefore influence atmospheric $p\text{CO}_2$. By affecting the transport of important tracers, such as dissolved inorganic carbon (DIC), total alkalinity, and nutrients, the AMOC affects the solubility and biological carbon pumps. Evidence for a coupling between the AMOC and marine carbon cycle is provided in proxy data (Bauska et al., 2021). Model studies show a wide range of potential carbon cycle responses to a collapse of the AMOC. While most models show an increase in atmospheric $p\text{CO}_2$ (e.g., Marchal et al., 1998; Matsumoto & Yokoyama, 2013; Schmittner & Galbraith, 2008), the magnitude and precise mechanisms are dependent on the model used and climatic boundary conditions (Gottschalk et al., 2019).

As the AMOC can influence atmospheric $p\text{CO}_2$, there is a potential feedback mechanism since atmospheric $p\text{CO}_2$ influences the hydrological cycle (Barker & Knorr, 2021; Weijer et al., 2019), which through changes in buoyancy fluxes, affects the AMOC. Previous studies suggest that there may be a relation between atmospheric $p\text{CO}_2$ and the MEW of the AMOC (Barker et al., 2015, 2010). However, a clear mechanistic view has not been given yet. Here, we study the mechanisms on how the marine carbon cycle can affect the MEW of the AMOC using a coupled ocean

circulation-carbon cycle box model.

4.2 Methods

We have coupled a box model suitable for simulating AMOC dynamics (Section 2.2) to a carbon cycle box model (Section 2.1). To be able to accurately represent atmospheric CO_2 concentrations, the coupled model extends the AMOC box model by including boxes that represent the Indo-Pacific Ocean. Steady states of the coupled model, where several non-linear couplings are implemented (Section 4.2.1), are determined using continuation software (Sections 2.3, 3.2.3, and 4.2.2). Parameter values and model equations are described in Appendix B.

4.2.1 Coupled model

The Cimatoribus ocean circulation box model (Section 2.2) and carbon cycle equations based on the SCP-M (Section 2.1) are coupled forming the model used in this study (Fig. 4.1). For this, several parameter assumptions had to be made, since the carbon cycle model requires more parameters than the AMOC model. First of all, the depth of boxes n and s is not given in Cimatoribus et al. (2014) but are necessary for the carbon cycle model. We assume these to be 300 m, and the total depth of the ocean is assumed to be 4000 m. Secondly, a first version of the model showed a too strong sensitivity of atmospheric CO_2 concentrations to AMOC tipping causing very low CO_2 concentrations on the AMOC off-branch. We therefore have included two additional boxes in the AMOC model representing the Indo-Pacific basin: box ps for the surface ocean and box pd for the deep ocean. In these boxes the same carbon cycle processes are present as in the Atlantic and Southern Ocean boxes of the model. Between these two boxes there is a bidirectional mixing term ($\gamma_1 = 30 \text{ Sv}$), and the boxes are connected with the Southern Ocean through a Global Overturning Circulation (GOC; $\psi_1 = 18 \text{ Sv}$), and gyre-driven exchange ($r_P = 90 \text{ Sv}$). γ_1 and ψ_1 are taken from the SCP-M (O'Neill et al., 2019), and r_P is based on the model of Wood et al. (2019). Both box t and ps receive DIC, Alk and PO_4^{3-} input through a river flux. The total river flux is modeled similarly as in the SCP-M and is partitioned over the two boxes based on the volume fraction of the Atlantic Ocean and the Indo-Pacific Ocean, meaning 20% of the river flux flows into box t , while the remainder flows into box ps .

The first coupling between the physical and the carbon cycle model is through the ocean circulation. The AMOC determined in the circulation model is used for the advective transport of the three tracers in the carbon cycle model. We have implemented additional couplings between the model and specific feedbacks within the carbon cycle model. Several of these feedbacks have been introduced into the SCP-M before (Chapter 3), and the feedbacks used in this study are repeated for convenience.

Firstly, we create a dependency of the biological export production in the surface boxes to the amount of PO_4^{3-} advected into the specific surface box and therefore introducing a dependency on the ocean circulation

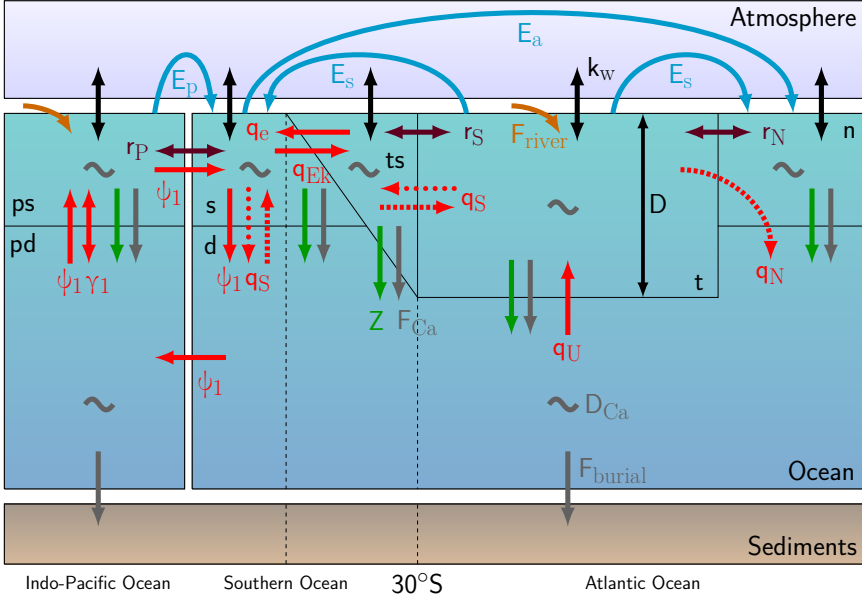


Figure 4.1: Box structure and processes simulated in the coupled circulation – carbon cycle model. Red arrows represent volume transports where dashed arrows are only present during an on-state, and dotted arrows only present during an off-state. The purple arrows represent gyre exchange (r_N , r_S , and r_P), and blue arrows freshwater fluxes (E_s , E_a , and E_p). Carbon cycle processes that are represented are riverine input (orange), air-sea gas exchange (black; k_w), biological export production (green; Z), CaCO_3 rain (grey; F_{Ca}), CaCO_3 dissolution (grey; D_{Ca}), and sediment burial (grey; F_{burial}). Based on Castellana et al. (2019) and Boot et al. (2022).

$$Z_i = (1 - \lambda_{BI}) \times Z_{i,base} + \lambda_{BI} \times (q_{j \rightarrow i} \times [PO_4^{3-}]_j + P_{river}) \times \epsilon_i. \quad (4.1)$$

Here Z_i represents the export production in surface box i , λ_{BI} a parameter to switch between the default value of Z in box i ($Z_{i,base}$; $\lambda_{BI} = 0$) and the variable export production ($\lambda_{BI} = 1$). In addition, $q_{j \rightarrow i}$ represents the volume transport from box j into box i . P_{river} the riverine influx of PO_4^{3-} , which is only present in boxes t and ps , and ϵ_i represents a biological efficiency term in box i . i represents all surface boxes, i.e. n , t , ts , s and ps . j can be any box and depends on the direction of the ocean circulation.

We also introduce a coupling between the symmetric freshwater forcing E_s and atmospheric $p\text{CO}_2$. This coupling is based on a fit to an ensemble of CMIP6 Earth System Models and is described in Section 4.3.1.

We allow the sea surface temperatures (SSTs) to vary with atmospheric $p\text{CO}_2$ following a logarithmic function and a climate sensitivity parameter, according to

$$T_i = T_{i,base} + \Delta T_i, \quad (4.2)$$

$$\Delta T_i = \lambda_T \times 0.54 \times 5.35 \ln\left(\frac{CO_2}{CO_{2,0}}\right). \quad (4.3)$$

Here i represents the different surface ocean boxes. By varying the parameter λ_T we are able to change the climate sensitivity of the model. In this study we use a value of $\lambda_T = 0$ (default), $\lambda_T = 1$ (CS_{LO}) and a value of $\lambda_T = 2$ (CS_{HI}), representing SST warming of 0 K, 2 K and 4 K per CO_2 doubling. For the default value, sea surface temperature remains constant independent of atmospheric pCO_2 values. For surface air temperature in CMIP6 models, the response to a CO_2 doubling is between 1.8 and 5.6 K (Zelinka et al., 2020). When this coupling is used, the changes in SSTs will also change the density in the ocean circulation model. However, since we use a linear equation of state and the change of SST is homogeneous over all surface boxes, it does not influence the ocean circulation.

Lastly, we have introduced a coupling on the rain ratio (Eq. (4.4)) making it dependent on the saturation state of $CaCO_3$ following

$$F_{Ca,i} = (1 - \lambda_F) \times F_{Ca,base} + \lambda_F \times 0.022 \left(\frac{[Ca_i^{2+}][CO_3^{2-}]}{K_{sp,i}} \right)^{0.81}, \quad (4.4)$$

where i represents the different surface ocean boxes. Similar to the biological coupling coefficient λ_{BI} , λ_F is either 0 or 1, and including this feedback will introduce different rain ratios per box.

We have used other couplings in the model that are described in Appendix B. They are not included in the main text since they do not show large effects on the results. In the main text only the couplings described above are used. We refer to the couplings as BIO for the biological coupling, E_s for the E_s -coupling described in Section 4.3, FCA for the rain ratio coupling, CS_{LO} for a low climate sensitivity and CS_{HI} for a high climate sensitivity.

4.2.2 Solution method

The coupled model is a system of 30 ODEs (four tracers per box, the pycnocline depth and atmospheric pCO_2) of the form

$$\frac{d\mathbf{u}}{dt} = f(\mathbf{u}(t), \mathbf{p}). \quad (4.5)$$

Here \mathbf{u} is the state vector (containing all the dependent quantities in all boxes), f contains the right-hand-side of the equations and \mathbf{p} is the parameter vector. To solve this system of equations we use the continuation software AUTO as described in Section 2.3. To be able to solve the system of equations with AUTO, the same adaptations to the carbon cycle model are made as described in Section 3.2.3. However, in this study we increase the value of the rain ratio to 0.15 compared to 0.07 in the original SCP-M (Section 2.1 and Chapter 3) to increase the background atmospheric pCO_2 values closer to pre-industrial concentrations.

In this study, the absolute and relative accuracy are set to a base value of 10^{-6} , but sometimes a higher accuracy is used. The accuracy for the detection of special points (e.g. saddle-nodes and Hopf bifurcations) is set to 10^{-7} .

4.3 Results

4.3.1 CMIP6 freshwater fluxes

The freshwater fluxes E_s and E_p used in the model are constrained using results from a CMIP6 ensemble. For this we use 28 different CMIP6 models forced with a 1% increase per year in atmospheric CO_2 concentrations ('1pctco2'). We integrate the variables 'wfo' (water flux) and 'vsf' (virtual salt flux) over the regions representing the Atlantic thermocline (Atlantic basin between 30°S and 50°N) and the Indo-Pacific basin (the rest of the ocean north of 30°S and south of 66°N) in the coupled box model. Based on these 28 models we determine a multimodel mean and we are able to constrain both E_p and E_s . A list of the used models and members is presented in Appendix C.

Fig. 4.2a shows that most models, and the multimodel mean, show no, or at most a very weak relation between E_p and atmospheric pCO_2 , whereas there seems to be a relation between E_s and atmospheric pCO_2 . For E_p , we will use the mean value over the entire simulation (0.99 Sv). For E_s , we will use as a default value 0.39 Sv since this is the value of E_s at $\text{pCO}_{2,0}$ (320 ppm). Furthermore, we introduce an additional coupling in the model where we implement E_s as a function of atmospheric pCO_2 based on a logarithmic fit to represent the relation between E_s and atmospheric pCO_2 present in the CMIP6 ensemble. This relation is modeled as:

$$E_s = (1 - \lambda_E) \times E_{s,base} + \lambda_E \times (-0.142 + 0.097 \times \ln(\text{CO}_2)) \quad (4.6)$$

Here λ_E is a parameter controlling whether the coupling is used ($\lambda_E = 1$) or the default value of $E_{s,base}$ (0.39 Sv) is used ($\lambda_E = 0$). Compared to earlier versions of the model we will use a different default value for E_s . In previous studies values of 0.25 Sv (Cimatoribus et al., 2014) and 0.17 Sv (Castellana et al., 2019) have been used. Here we choose the default value based on the value of E_s at an atmospheric pCO_2 value of 320 ppm ($\text{pCO}_{2,0}$) in the CMIP6 fit. The value of 0.39 Sv is of the same order as seen in the HOAPS4.0 dataset based on satellite observations (Andersson et al., 2017). This dataset shows a net freshwater flux of 1 Sv averaged over the period 1987-2015 into the region representing the thermocline box, which results in an E_s value of 0.5 Sv.

We have made two important choices for using these CMIP6 constrained freshwater fluxes. First of all, we set the freshwater transport through the atmosphere from the Atlantic to the Indo-Pacific basin to 0. There are studies showing there is moisture transport between the two basins through the atmosphere (e.g., Dey & Döös, 2020), but it is challenging to constrain this flux from Earth System Models. However, in our model set up, the exact value of this flux is not relevant for our results. The total freshwater flux integrated over the Indo-Pacific basin diagnosed from the CMIP6

ensemble is independent of the moisture transport between the Atlantic and Indo-Pacific basin. By rescaling the freshwater flux from the Indo-Pacific basin (box *ps*) to the Southern Ocean (box *s*) we can set the freshwater flux from the Atlantic to the Indo-Pacific to 0 without changing the AMOC dynamics. Tests where this flux was not set to 0, but net evaporation out of boxes *t* and *ps* were kept constant show this (not shown). The only effect of this freshwater transport is a shift of the diagram along the E_a -axis and a small effect on atmospheric $p\text{CO}_2$ of a couple of ppm due to salinity changes.

The second choice we have made is that the net evaporation from the Atlantic thermocline is symmetrically divided over the northern and southern high latitudes. For this model, the exact direction of the freshwater flux out of box *t* is irrelevant. What is relevant is the total freshwater flux at each surface box. Through this we can see that the asymmetric freshwater flux, E_a , creates an asymmetry in freshwater forcing over the Atlantic basin. Through this, E_a creates the asymmetry that is potentially more realistic. Since we use E_a as our control parameter in the continuations, we do not need to constrain this parameter.

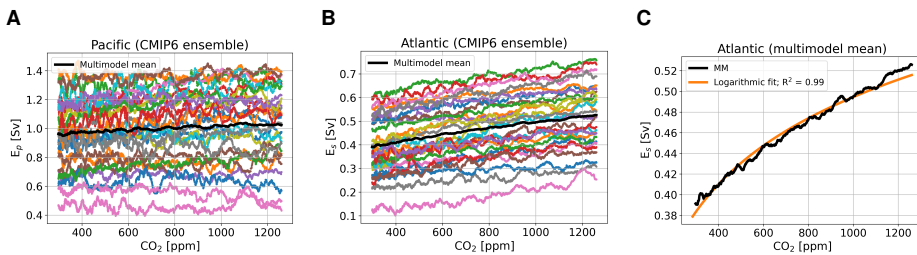


Figure 4.2: (a) Net evaporation from the Indo-Pacific basin representing the freshwater flux E_p in Sv for the CMIP6 ensemble with the multimodel mean in black. (b) As in (a) but for the freshwater flux E_s . (c) The multimodel mean for E_s in black with a logarithmic fit in orange.

4.3.2 The AMOC multiple equilibria window

In Fig. 4.3 the bifurcation diagrams for the AMOC strength (Fig. 4.3a, c) and atmospheric $p\text{CO}_2$ (Fig. 4.3b, d) versus E_a are shown for 6 different model configurations. The model configurations are differentiated on feedbacks and couplings included (see Table 4.1). The bifurcation diagrams show that to be able to simulate both the on- and off-branch, it is vital that the BIO coupling is used. When this coupling is not used, PO_4^{3-} concentrations will become negative in the surface ocean under a collapsed AMOC regime. This behavior is illustrated in Fig. 4.3a, b by the cases REF and BIO. In case REF the off-branch (with negative PO_4^{3-}) is not shown, while for case BIO the full bifurcation diagram with two saddle-node bifurcations is plotted. In Fig. 4.3b, d we can also see the effect of AMOC tipping on atmospheric $p\text{CO}_2$. On both the on- and the off-branch, atmospheric $p\text{CO}_2$ values are relatively constant and the difference between the branches is approximately 25 to 40 ppm depending on the exact case, values that are of the same order as values reported in more complex models (Gottschalk et al., 2019).

Table 4.1: Overview of the used cases. The left column represents the name of the case. The other columns represent whether a coupling denoted in the top row is used in the case mentioned in the first column by indicating the λ parameter associated to the coupling. For λ_T the value represents the strength of the coupling.

Case name	λ_{BI}	λ_E	λ_F	λ_T
REF	0	0	0	0
BIO	1	0	0	0
E_s + BIO	1	1	0	0
E_s + BIO + FCA	1	1	1	0
E_s + BIO + FCA + CS_{LO}	1	1	1	1
E_s + BIO + FCA + CS_{HI}	1	1	1	2

To explain the lower pCO_2 values on the off-branch we consider the constraint in the model on total carbon content in the ocean-atmosphere system. In steady state, the riverine input and sediment outflux of DIC must balance to keep the total carbon content constant (over time). In our model, the sediment outflux is a function of the saturation state of $CaCO_3$ and $CaCO_3$ flux which is a function of the rain ratio (constant in non-FCA cases) and the export production. However, in the AMOC off state, the saturation state of $CaCO_3$ in the ocean is in every box larger than 1, meaning that there is no saturation driven dissolution of $CaCO_3$ and the sediment outflux is purely a function of the export production and a constant background dissolution rate. In an AMOC off-state, nutrient advection is relatively low causing a reduction in export production, and therefore a smaller sediment outflux. In steady state, the riverine influx must balance this small outflux, which is only possible by decreasing atmospheric pCO_2 values.

From the 6 cases considered here (Table 4.1) we can see the effect of the individual couplings. As described earlier, the biological coupling is necessary to determine the off-branch but does not influence the bifurcation diagrams otherwise. The rain ratio coupling (FCA) decreases atmospheric CO_2 concentrations by 35 ppm and slightly increases the difference in CO_2 concentration between the on- and off-branch (green lines Fig. 4.3b). The climate sensitivity coupling increases this effect, with a larger effect for the higher climate sensitivity (purple and red lines Fig. 4.3d). In the cases using the rain ratio, the potential of the E_s -coupling becomes visible. In these cases, atmospheric pCO_2 values deviate more from $pCO_{2,0}$ and therefore have a larger effect on E_s . When E_s differs from the default value (0.39 Sv), both saddle nodes move to different E_a values.

To explain the movement of the saddle nodes, we consider the sensitivity of the model to E_s (Fig. 4.4). In Fig. 4.4 the location of the saddle nodes on both the on- and the off-branch are shown versus the value of E_s . This figure shows that as E_s increases, the MEW also increases. The default value used for cases REF and BIO for E_s is 0.39 Sv. The CMIP6 CO_2 -dependent fit (Eq. (4.6)) results in a slightly smaller value. Due to decreased E_s , the thermocline becomes fresher, and in combination with the salt-advection feedback, this leads to a smaller meridional density gradient and therefore a weaker AMOC. Furthermore, decreased E_s decreases the net evaporation over the Atlantic, given by $(E_s - E_a)$ and this means that a smaller E_a is necessary to tip the AMOC. On the off-branch, a smaller E_s results in salinification of

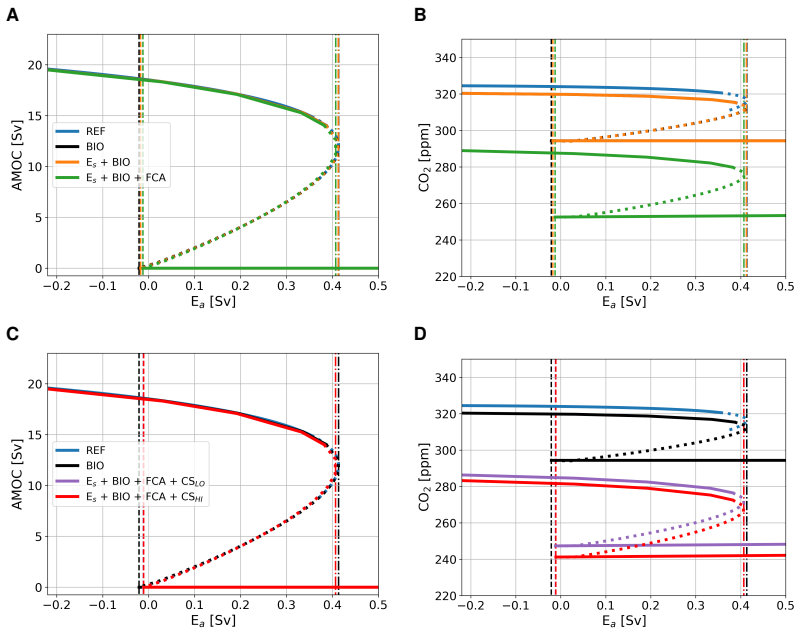


Figure 4.3: Bifurcation diagram showing the sensitivity of the AMOC and atmospheric $p\text{CO}_2$ to E_a . Solid lines represent stable steady state solutions, dotted lines represent unstable solutions, dash-dotted lines represent the location of the saddle node on the on-branch, and dashed lines the location of the saddle node on the off-branch. The blue lines represent a case without additional coupling (REF), the black lines with only the biological coupling (BIO), the orange lines with the CMIP6 based E_s and biological coupling ($E_s + \text{BIO}$), and the green lines represent a case where also the rain ratio feedback is applied ($E_s + \text{BIO} + \text{FCA}$). The purple and red lines also include the climate sensitivity feedback, where purple lines represent a low sensitivity ($E_s + \text{BIO} + \text{FCA} + \text{CS}_{LO}$) and red lines a high sensitivity, ($E_s + \text{BIO} + \text{FCA} + \text{CS}_{HI}$). Results are for the AMOC strength in Sv (a, c) and atmospheric $p\text{CO}_2$ in ppm (b, d). Especially for the AMOC strength results are very similar and overlap in the plots. In (b) the black curve (BIO) is under the orange curve ($E_s + \text{BIO}$).

box t_s and a less negative freshwater flux (E_a) is needed to decrease the meridional density gradient and reinvigorate the AMOC. For cases with the FCA feedback, it reduces the MEW by moving the off-branch saddle node to larger values of E_a , and the saddle node on the on-branch to smaller values, which can be explained by the fact that CO_2 is smaller than $\text{CO}_{2,0}$ and therefore E_s is smaller than $E_{s,base}$ in Eq. (4.6).

In the bifurcation diagrams in Fig. 4.3 we find that the solution on the on-branch becomes unstable before passing the saddle node. This change in stability can be explained by the presence of a subcritical Hopf bifurcation in the circulation model. The internal oscillation corresponding to this Hopf bifurcation is unstable and has a multi-decadal periodicity. In this study we are only interested in the MEW of the AMOC, and we therefore do not consider the Hopf bifurcation further.

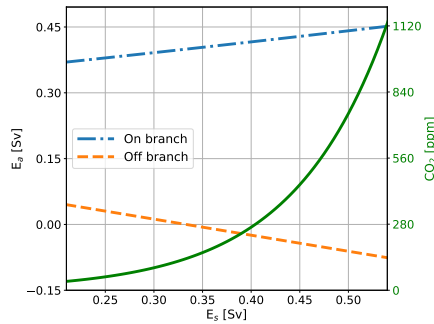


Figure 4.4: E_a -value corresponding to the saddle node on the on-branch (dash-dotted blue line, left y-axis) and the off-branch (dashed orange line, left y-axis) for different values of E_s in Sv. The distance between the orange and blue line represents the MEW. The green line (right y-axis) represent the CO_2 values corresponding to the E_s -values following the used fit (Eq. (4.6)).

4.3.3 Sensitivity to total carbon content

Over the Cenozoic, both the AMOC (Lynch-Stieglitz, 2017) and total carbon content in the ocean-atmosphere system have varied (Caves et al., 2016; Zeebe et al., 2009). In Caves et al. (2016) it is suggested that total carbon content has varied between 24,000 PgC and 96,000 PgC. In the previous section, the model was studied with approximately 40,000 PgC in the global system. In this section, we analyze how the sensitivity of the AMOC MEW changes under different total carbon contents in the model. To test the sensitivity, we remove approximately 4,000 (-10%) PgC, and add approximately 4,000 (+10%), 10,000 (+25%) and 20,000 (+50%) PgC. We do this for the cases considered in Section 4.3.2 excluding case REF (Fig. 4.5).

In case BIO there is no change in the MEW, which is to be expected since there is no back coupling from the carbon cycle model to the AMOC model, and the AMOC solution is therefore independent of the carbon cycle. We see only the effect of total carbon content on atmospheric pCO_2 values. When carbon is removed, the CO_2 concentrations at the saddle nodes both decrease. However, when carbon is added, only the saddle node on the on-branch has higher CO_2 concentrations, independent of whether 4,000, 10,000 or 20,000 PgC is added. We see a similar pattern for the $E_s + \text{BIO}$ case, but here the MEW increases for larger total carbon content due to the different CO_2 concentrations at the saddle nodes. The cases including the rain ratio feedback show a different pattern. Here, the CO_2 concentrations at both saddle nodes are dependent on the amount of carbon added to the ocean-atmosphere system, i.e. the higher the content, the higher the CO_2 concentrations at the saddle nodes (Fig. 4.5b). This influences the value of E_s at the saddle nodes (Fig. 4.5c), which increases the MEW for increasing carbon content (Fig. 4.5a). The MEW shift increases when the climate sensitivity coupling is used (CS_{Lo} and CS_{Hi}), with a larger response for the higher sensitivity (CS_{Hi}). Another effect visible in the cases using the FCA feedback is the difference in CO_2 concentration between the on- and the off-branch increases as total carbon content increases. This effect is larger when climate sensitivity is increased.

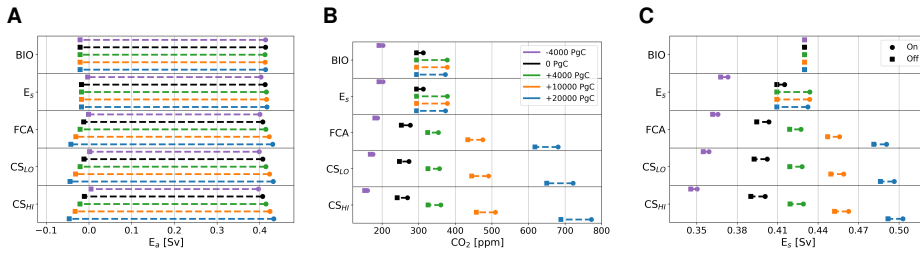


Figure 4.5: Panel a shows the location of the saddle nodes versus E_s in Sv, panel b shows the corresponding CO_2 concentration in ppm, and c shows the corresponding value of E_s in Sv. The top row of the figure represents case BIO, the second row case E_s + BIO, and the middle row case E_s + BIO + FCA, the fourth row case E_s + BIO + FCA + CS_{LO} , and the bottom row E_s + BIO + FCA + CS_{HI} . Square markers represent the location of the saddle node on the off-branch and round markers the location of the saddle node on the on-branch for cases where 4000 PgC is removed (purple), the default carbon content (black), 4000 PgC is added (green), 10,000 PgC is added (orange) and where 20,000 PgC is added (blue).

We can explain the behavior of the MEW in the E_s + BIO case by looking at the atmospheric pCO_2 values, and therefore also E_s , at the saddle nodes, which are similar for the three high total carbon cases. However, when the rain ratio feedback is used, we see that the MEW keeps increasing for larger carbon contents since also the atmospheric pCO_2 increases. We can explain the difference between E_s + BIO and the cases where the rain ratio feedback is used by the constraint on total carbon in the ocean-atmosphere system. In E_s + BIO, biological export production in the Atlantic is mainly a function of the AMOC strength, whereas in the E_s + BIO + FCA case it is also dependent on the $CaCO_3$ saturation state which is coupled to atmospheric pCO_2 through the pH of the surface ocean. This leads to a larger outflux of DIC and Alk to the sediments, which, in steady state, needs to be balanced by a higher influx of DIC and Alk through the river flux, which can only be achieved by increasing atmospheric pCO_2 .

A second result for the cases with the rain ratio feedback is that the CO_2 concentration difference between the on- and off-branch increases for higher total carbon content. As we increase total carbon content in the system, the rain ratio increases on both the on- and the off-branch because the saturation state of $CaCO_3$ increases. Due to non-linearities in the carbonate chemistry, the more carbon is present in the system, the larger the difference in rain ratio between the two branches. This explains why the difference between the on- and off-branch increases as total carbon content increases in the system.

4.4 Summary and discussion

In this paper we investigated the multiple equilibria window (MEW) of the AMOC in a coupled ocean circulation-carbon cycle box model. When freshwater forcing is coupled to atmospheric pCO_2 using a CMIP6 multimodel fit (Eq. (4.6)), the MEW changes slightly due to a dependency on atmospheric pCO_2 . We also assessed the

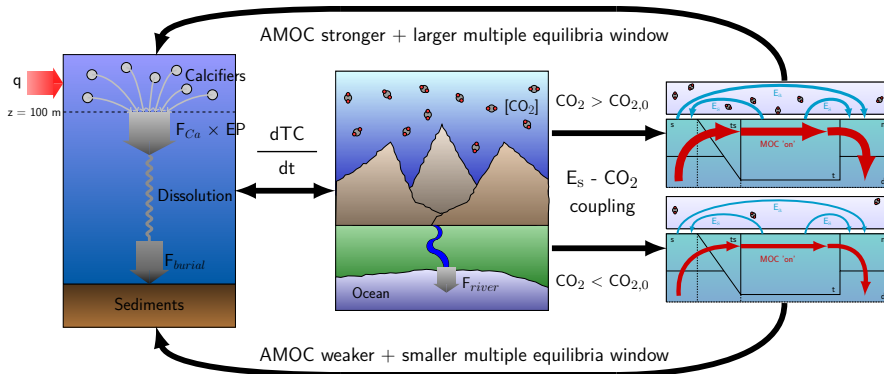
sensitivity to total carbon content in the system and found that the MEW is larger with more carbon in the system due to a shift of both the on- and off-branch saddle nodes. These results show the potential of the marine carbon cycle to influence the MEW of the AMOC.

We acknowledge that it is difficult to assess the validity of the CMIP6 E_s - $p\text{CO}_2$ fit since that fit is based on a transient simulation with a strong forcing. However, longer (i.e. more than 3000 year) simulations by Galbraith & Lavergne (2019) show a similar, slightly stronger relation than the one used in this study. The clear and plausible mechanisms presented in this study, however, are more important than the precise quantitative estimates and are summarized in Fig. 4.6. Two processes explain the results on the MEW: (1) the balance between the river flux and sediment flux that constrains atmospheric $p\text{CO}_2$ (first two panels in Fig. 4.6a, b); and (2) the sensitivity of the AMOC to E_s (last panel in Fig. 4.6a, b). In the model, atmospheric $p\text{CO}_2$ is dependent on the ocean circulation through the effect of export production on the burial of DIC and Alk in the sediments. In steady state, this burial needs to balance the riverine influx which is dependent on atmospheric $p\text{CO}_2$. When the E_s -coupling is used, E_s is dependent on atmospheric $p\text{CO}_2$, and the ocean circulation is dependent on E_s , creating a feedback loop (Fig. 4.6). If the CO_2 concentration in the atmosphere is larger than $\text{CO}_{2,0}$, the MEW increases, while it decreases if it is smaller than $\text{CO}_{2,0}$. This results in that when atmospheric $p\text{CO}_2$ is high, so is E_s which results in a stronger AMOC on the on-branch. As a consequence, export production is increased and there will be a larger outflux of carbon and alkalinity through the sediments, which is balanced by a high influx of carbon through the rivers, consistent with high atmospheric $p\text{CO}_2$ values. Of the feedbacks that we have implemented, only the rain ratio feedback (FCA) affects this mechanism because it directly influences the sediment outflux and makes the carbon cycle less sensitive to the ocean circulation.

The results here can be relevant when studying climate transitions in past and future climates as mechanisms how AMOC stability can depend on background climate and atmospheric $p\text{CO}_2$ values are identified. Previous work focused on the Pleistocene suggest an influence of atmospheric $p\text{CO}_2$ on the stability structure of the AMOC through temperature (Sun et al., 2022) and moisture transport (Zhang et al., 2017). In our model, there is no direct effect of temperature changes on the AMOC strength, but the E_s -coupling used here is similar to the moisture transport described in Zhang et al. (2017). The only difference is that this moisture transport is directly to the Pacific basin in their study, whereas in our model we rescale freshwater fluxes to set this direct flux to 0.

We have used a model that provides a simple framework for studying AMOC dynamics that allows us to efficiently test the concept of AMOC stability in a wide range of parameter values. However, a limitation is that in the model temperature is not a state variable, based on the assumption that the timescales of salinity variations is longer than that of temperature and thus dominant in steady state. This means that the AMOC strength in our model is not influenced by changes in temperature, which is a caveat of this study. Under high carbon content in the ocean-atmosphere system, this might not be valid. However, we also have explored relatively small changes in the total carbon content and the mechanisms presented here are also valid for this

A



B

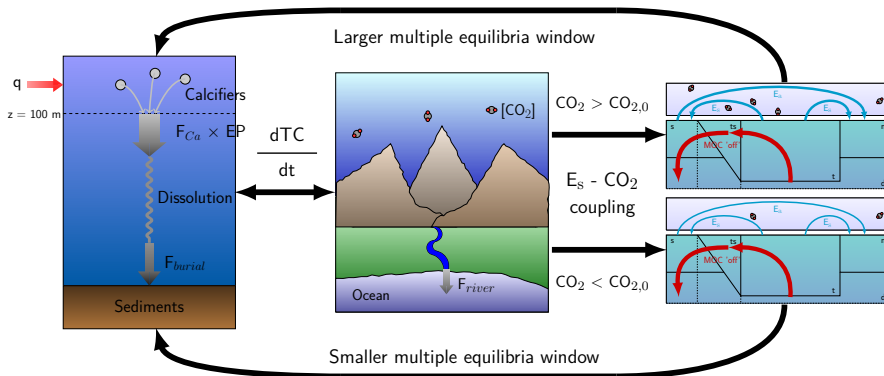


Figure 4.6: Illustrations of the main mechanisms affecting atmospheric $p\text{CO}_2$ and AMOC stability. Panel a shows the mechanisms for the on-branch. A strong AMOC increases export production through increased nutrient advection (left panel), which is accompanied by a high atmospheric $p\text{CO}_2$ due to the necessary balance between the river influx and sediment burial (middle panel). If the CO_2 concentration is larger (smaller) than $\text{CO}_{2,0}$ then the AMOC will strengthen (weaken) and the MEW increases (decreases) (right panels). Panel b shows the mechanisms for the off-branch. The absence of an AMOC decreases export production through decreased nutrient advection (left panel), accompanied by a low atmospheric $p\text{CO}_2$ (middle panel). When $p\text{CO}_2$ is larger (smaller) than $p\text{CO}_{2,0}$ the MEW increases (decreases) (right panel).

smaller range, suggesting that the main mechanism presented in this study is at least valid for small changes in the total carbon content. We do not expect that the MEW shift described in this study is fully compensated for when temperature is a state variable. Though not a limitation in the model, it is good to note that the

range of timescales in the carbon cycle model is larger than in the circulation model, which does not affect our results but does affect the time dependent response of the system.

Our work also holds implications for assessing AMOC stability in future climates. Currently, the global warming threshold for an AMOC collapse is estimated to be 4°C (Armstrong-McKay et al., 2022). In the future, the carbon content of the ocean-atmosphere system will increase, potentially increasing the MEW which can change the likelihood of a bifurcation induced AMOC collapse. In this study we focused on slow, bifurcation induced tipping of the AMOC, while the AMOC is also able to tip due to faster processes (e.g. density changes related to temperature variations) resulting in noise-induced tipping (Castellana et al., 2019; Jacques-Dumas et al., 2023). The mechanisms presented here might influence these noise-induced transitions as well. We hope this work inspires further research on the dependency of the AMOC MEW on the carbon cycle in more detailed models, to further investigate the relevance of the mechanism found in this study, and provide a better quantification for the influence of the marine carbon cycle on the MEW of the AMOC.

Effect of plankton composition shifts in the North Atlantic on atmospheric pCO₂

Marine carbon cycle processes are important for taking up atmospheric CO₂ thereby reducing climate change. Net primary and export production are important pathways of carbon from the surface to the deep ocean where it is stored for millennia. Climate change can interact with marine ecosystems via changes in the ocean stratification and ocean circulation. In this study we use results from the Community Earth System Model version 2 (CESM2) to assess the effect of a changing climate on biological production and phytoplankton composition in the high latitude North Atlantic Ocean. We find a shift in phytoplankton type dominance from diatoms to small phytoplankton which reduces net primary and export productivity. Using a conceptual carbon-cycle model forced with CESM2 results, we give a rough estimate of a positive phytoplankton composition-atmospheric CO₂ feedback of approximately 60 GtCO₂/°C warming in the North Atlantic which lowers the 1.5 °C and 2.0 °C warming safe carbon budgets.

This chapter is based on:

Boot, A., A.S. von der Heydt, and H.A. Dijkstra (2023), Effect of plankton composition shifts in the North Atlantic on atmospheric pCO₂, *Geophysical Research Letters*, vol. 50, no. 2, e2022GL100230

5.1 Introduction

To avoid crossing tipping points in the Earth system, it is important to keep warming of our planet to a maximum of 1.5 to 2°C (Lenton et al., 2019). Policymakers need to know how much carbon we can still emit before we exceed this warming. However, estimates of this safe carbon budget are difficult and subject to large uncertainties because the Earth system has many processes and feedbacks that are not completely understood yet (Matthews et al., 2021).

The marine carbon pumps are currently responsible for taking up 25-40 percent of anthropogenic carbon (DeVries et al., 2017; Sabine et al., 2004). It is estimated that the biological carbon pump exports approximately 11 GtC yr⁻¹ to the deep ocean (Sanders et al., 2014) and that without this export, atmospheric pCO₂ values would be 200-400 ppm higher (Henson et al., 2022; Ito & Follows, 2005). This export production (EP) is dependent on the net primary productivity (NPP). It also depends on food web dynamics and plankton composition, since different phyto- and zooplankton species have different remineralization depths (Li et al., 2009; Marinov et al., 2013; Morán et al., 2010).

Both EP and NPP are strongly dependent on temperature, ocean circulation, stratification and nutrient input (Doney et al., 2011) which can all affect phytoplankton composition. This is important because changes in phytoplankton composition can transfer through the food web affecting fish and mammals (Beaugrand, 2009; Richardson & Schoeman, 2004) which can affect fishery yields. Furthermore, phytoplankton composition also affects EP which indirectly influences the air-sea gas exchange of CO₂ that could result in a positive feedback loop under climate change (Cabré et al., 2015). In such a feedback higher CO₂ levels change phytoplankton composition, reducing EP and thus the uptake of CO₂ by the ocean. Finally, a changing phytoplankton composition is one of the hypotheses suggested to explain (part of) the atmospheric pCO₂ (80-100 ppm) variations in the Pleistocene glacial-interglacial cycles (Archer & Maier-Reimer, 1994; Kohfeld et al., 2005), showing the potential of this feedback to affect the climate.

Though climate change is likely to affect plankton stocks, the extent is still uncertain (Osman et al., 2019). Expected effects of global warming are changes in NPP (Behrenfeld et al., 2006), reduced nutrient concentrations in the surface ocean due to stronger stratification (Bopp et al., 2005; Bopp et al., 2001; Fu et al., 2016), and phytoplankton composition changes, the latter also due to changing co-limitation of light and nutrients (Marinov et al., 2013; Moore et al., 2013a). Furthermore, on longer timescales, severe nutrient trapping in the Southern Ocean is possible, which reduces biological productivity over most of the ocean (Moore et al., 2018). However, uncertainties remain in most (model) studies. This is because the complex timing of blooms are difficult to simulate in highly seasonal regions such as the high latitudes (Martinez et al., 2011), and also because ecosystem models that have more extensive plankton dynamics show larger community composition shifts with climate change (Dutkiewicz et al., 2013; Fu et al., 2016). Comparing CMIP6 models with CMIP5 models, we see an increase in intermodel spread in both NPP and EP

(Henson et al., 2022; Kwiatkowski et al., 2020; Tagliabue et al., 2021), highlighting the complexity of the system.

One of the regions that is projected to be affected by climate change is the North Atlantic, a region where biological processes are known to be important for gas exchange of CO₂ (Bennington et al., 2009). Model simulations under high emission scenarios project that the future North Atlantic will have relatively low warming rates, relatively high acidification rates and a (medium to large) decrease of subsurface oxygen (Bopp et al., 2013). In addition, the stratification and ocean circulation are projected to change, such as a decrease in the strength of the Atlantic Meridional Overturning Circulation (AMOC), which could possibly result in a collapse of phytoplankton and zooplankton stocks in the North Atlantic (Schmittner, 2005). These projected changes would lead to large decreases of NPP and EP (Bopp et al., 2013; Steinacher et al., 2010).

There are multiple regions in the ocean where plankton composition has been observed to shift under the influence of interannual variability and climate change. Especially the Northeast Atlantic and the North Sea are well sampled and studied regions where phytoplankton composition shifts have been observed (e.g., Allen et al., 2020; Hinder et al., 2012) and where changes in phytoplankton biomass are related to sea surface temperature changes (Edwards et al., 2022; Richardson & Schoeman, 2004). An example of such a response is the increase in abundance of coccolithophores (Rivero-Calle et al., 2015; Rousseaux & Gregg, 2015). These kind of phytoplankton composition shifts are not only occurring in the North Atlantic Ocean, but also in for example the Canadian Arctic Ocean (Blais et al., 2017) and the Northern and Equatorial Indian Ocean (Gregg et al., 2017). Also shifts in zooplankton species have been reported in for example the North California Current (Francis et al., 2012) and the North Atlantic (Beaugrand et al., 2002). These studies show that both phyto- and zooplankton respond to changes in climate, and this can affect the future ocean carbon sink (Hilligsøe et al., 2011).

The main novel aspect of this study is to provide an estimate of the phytoplankton composition-atmospheric pCO₂ feedback (Cabr e et al., 2015) using a climate model simulation for a high emission scenario (SSP5-8.5). We aim to answer the following questions: How do NPP and EP respond to higher pCO₂ levels? Does this lead to a positive or a negative feedback on atmospheric CO₂? And lastly, what does this imply for the safe carbon budget? To investigate these issues we have used two models, the Community Earth System Model v2 (CESM2) and the Simple Carbon Project Model v1.0 (SCP-M). The CESM2 is a state-of-the-art Earth System Model, simulating processes related to the atmosphere, land, ocean and sea ice at a relatively high spatial resolution and is therefore useful to study complex processes in much detail (Section 2.4). The SCP-M is a simple carbon cycle box model consisting of 1 atmospheric box, 2 terrestrial biosphere boxes and 7 oceanic boxes (Section 2.1). Results from a box model like the SCP-M are, in comparison to the CESM2, easier to understand and suitable to test (higher-order) hypotheses.

5.2 Method

In this chapter we analyse the output from the NCAR CESM2 SSP5-8.5 simulation as described in Section 2.4.5 (Danabasoglu, 2019a). Since it is an emission driven case, atmospheric $p\text{CO}_2$ is affected by feedbacks from the land and ocean reservoirs of carbon. The simulation period is from 2015-2100 and analysis results are based on monthly and yearly mean data.

Important for this study is how the plankton groups are resolved and defined in MARBL (Section 2.4.2). The three phytoplankton functional types (PFTs) are defined in Moore et al. (2001) where the small phytoplankton group represents nano and pico phytoplankton. Larger phytoplankton groups are modeled as diatoms in MARBL and are therefore limited by silicate and consequently also influence the Si-cycle. The last group, the diazotrophs, are nitrogen fixers. Coccolithophores (calcifiers) are only implicitly resolved in MARBL as part of the small phytoplankton group using a variable rain ratio. Per PFT, parameters for the growth rate, mortality and aggregation rates vary (Long et al., 2021). Only one zooplankton functional group is represented in MARBL. This group is modeled as an adaptive class, meaning that various types of zooplankton are simulated using a differential routing of grazing of the zooplankton depending on the prey (the three phytoplankton groups) (Long et al., 2021).

Ideally, we would use a suite of CESM simulations to study the feedback processes between the marine carbon cycle and atmospheric CO_2 . The main component connecting the two is the air-sea gas exchange of CO_2 which is dependent on multiple tracers (i.e. temperature, salinity, DIC and total alkalinity). These tracers all have several different sink and source terms in the ocean, making it very difficult to assess the importance of the processes simulated by CESM2. Setting up a simulation strategy to be able to study feedback processes as, for example, the effects of the EP on outgassing, is not only difficult, but also computationally expensive. Therefore, to be able to study these feedback processes in more detail, we use the Simple Carbon Project Model v1.0 (SCP-M; O'Neill et al., 2019) as described in Chapter 2 including adaptations from Chapter 3. Processes in the model that affect dissolved inorganic carbon (DIC) and alkalinity (Alk) are the ocean circulation, biological production, calcium carbonate production and dissolution, river fluxes, sediment fluxes and the air-sea gas exchange of CO_2 (DIC only).

Since we are interested in the high latitude North Atlantic Ocean, we need to look at the dynamics in Box 2 of the SCP-M. Carbon and alkalinity in Box 2 are affected by the Atlantic Meridional Overturning Circulation (AMOC, ψ_2 , orange arrow in Fig. 2.1), biological production (green arrow in Fig. 2.1), calcium carbonate production and dissolution (light gray arrow and wiggle in Fig. 2.1), and air-sea gas exchange (carbon only; dark gray arrow in Fig. 2.1). From these processes the AMOC, the biological and calcium carbonate production are constant in the model. Calcium carbonate dissolution is saturation dependent and therefore dependent on the pH of the ocean water. This pH is determined using a direct solver which uses the pH from the previous time step as a first estimate (Follows et al., 2006). To increase accuracy we run the solver twice each time step (note that in the original model the solver is run once). With the pH, oceanic $p\text{CO}_2$ can also be determined

which is important for the air-sea gas exchange of CO_2 , which is also dependent on the CO_2 concentration in the atmosphere. Temperature is affected by anthropogenic forcing, but this is prescribed and not dependent on atmospheric pCO_2 ; the salinity is constant.

For the purpose of studying the feedback processes we have made slight adaptations to the SCP-M. First of all, we have included biological fluxes that affect alkalinity following

$$A_{bio} = -\frac{16}{106}C_{bio} \quad (5.1)$$

Where A_{bio} is the biological alkalinity flux, C_{bio} the biological carbon flux, and the fraction $\frac{16}{106}$ represents the uptake of nitrate following constant stoichiometric ratios. Just as the biological DIC flux, it is constant. Secondly, we have updated the anthropogenic forcing to represent SSP5-8.5 instead of RCP8.5 (Green et al., 2021; O'Neill et al., 2020).

5.3 Results

The prescribed emissions (in Pg CO_2 per year) top in the year 2085 and decrease afterwards (Fig. D.1a). By the year 2100, 88 GtC has been emitted into the atmosphere (Meinshausen et al., 2020). Under the influence of the emissions and the exchange with the land and the ocean, the atmospheric CO_2 concentration in the CESM2 simulation increases from 400 ppm in 2015 to 1069 ppm in 2100 (Fig. D.1b). Part of this carbon (Fig. D.2a) is taken up by the terrestrial biosphere (6%), and part by the ocean (6%). Over time, relatively less carbon is taken up by these two reservoirs, which means more remains in the atmosphere (Fig. D.2b).

The changes in the global air-sea gas CO_2 exchange are shown in Fig. 5.1, where a positive sign indicates CO_2 transfer into the ocean. Whereas almost the entire ocean takes up more (or gasses out less) carbon at the end of the century compared to present-day, the North Atlantic actually takes up less. This becomes even more clear when we compare globally integrated gas exchange with the gas exchange integrated over the North Atlantic. Air-sea gas exchange increases globally until the end of the century but in the North Atlantic, it starts to decrease around the year 2040 (Fig. D.3), suggesting substantial carbon cycle changes in the North Atlantic.

The response in the North Atlantic stands out for several reasons. First of all, the warming rate of Sea Surface Temperature (SST) is relatively low in the North Atlantic, and SSTs even decrease locally (Fig. D.4). There are also large changes in the annual maximum mixed layer depth in the deep water formation regions around Greenland (Fig. D.5). These are related to ocean circulation changes in particular a decrease in AMOC strength at 26.5°N from 17 Sv to 10 Sv over the simulation period (Fig. D.6). We also see a stronger upper ocean stratification (Fig. D.7), where stratification is measured here by the density difference between 200 m depth and the surface.

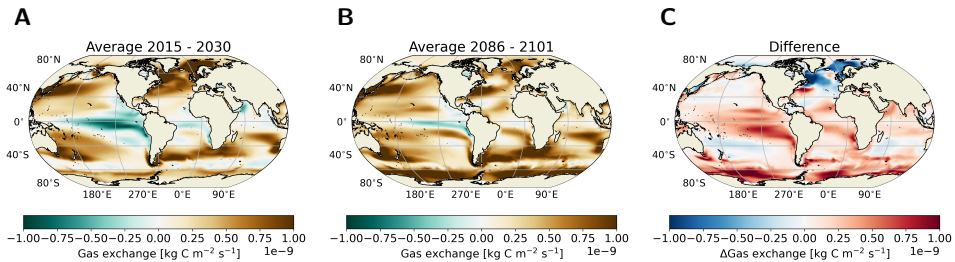


Figure 5.1: Changes in gas exchange in $\text{kg C m}^{-2} \text{s}^{-1}$ in the CESM2 SSP5-8.5 emission driven simulation. Note the different scaling per row; within a row, each subplot is scaled in a similar way. Left column: averages over period 2015-2030; middle column: averaged over period 2086-2101; right column: differences between the two (middle - left).

There is a large decrease in both NPP and EP (at 100 m depth) in the North Atlantic region and especially in the deep water formation areas around Greenland (Fig. 5.2). The decrease in EP cannot completely be explained by a decrease in NPP, since EP decreases more than NPP (Fig. D.8). This suggests that the plankton functional types (PFTs) in MARBL respond differently in this region to climate change. Diazotrophs do not play a role here due to temperature limitation and hence we focus on changes in diatoms and small phytoplankton. We can determine the effect of these two PFTs by using the equation (used in CESM2) $NPP_i = \mu_{ref} T_f L_i V_i P_i$. Here i refers to the two PFTs (small phytoplankton and diatoms), μ_{ref} is the maximum C-specific growth rate (which is the same for both PFTs) and T_f is a temperature dependent function. Furthermore, L_i is a light limitation function, V_i a nutrient limitation function, and P_i is the biomass of PFT i . Both diatoms and small phytoplankton are limited by nitrogen (N), phosphorus (P), and iron (Fe); diatoms are also limited by silica (Si).

In the beginning of the 21st century we see that diatoms are dominant in the high latitude North Atlantic (Fig. 5.3), whereas small phytoplankton are not very abundant. However, at the end of the century we see a change in PFT dominance as diatoms have almost completely disappeared, while the small phytoplankton NPP and biomass (Fig. D.11) have increased. The large decrease in diatom NPP decreases total NPP in this region. This shift in plankton type dominance also explains why the EP decreases faster than the NPP (Fig. D.8) since diatoms are more efficient in exporting carbon than small phytoplankton. Since diatoms become less abundant, the carbon transport from the surface to the deep ocean also becomes less efficient. To investigate why the plankton composition changes in the North Atlantic, and why diatom NPP decreases, we look into what determines the production of the different PFTs. Both PFTs are generally nitrogen limited in this region, though nitrogen limitation is stronger for diatoms. Light limitation decreases by a small amount for the diatoms in the beginning of the 21st century before becoming more or less stable. Light limitation for small phytoplankton decreases throughout the entire century. The difference in light limitation explains mostly the co-limitation: diatom co-limitation of light and nutrients increases, whereas for small phytoplankton it decreases (Fig. 5.4). We can also see this in the growth rate (NPP divided by biomass)

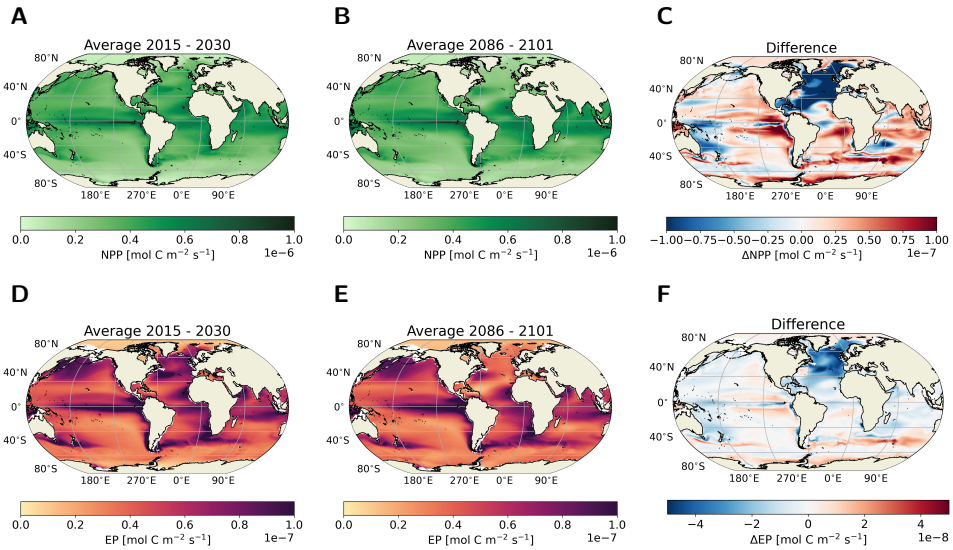


Figure 5.2: Changes in carbon-cycle relevant quantities in the CESM2 SSP5-8.5 emission driven simulation. Top row: Net Primary Production integrated over top 100 m in mol C m⁻² s⁻¹. Bottom row: Export Production at 100 m depth in mol C m⁻² s⁻¹. Note the different scaling per row; within a row, each subplot is scaled in a similar way. Left column: averages over period 2015-2030; middle column: averaged over period 2086-2101; right column: differences between the two (middle - left).

of both PFTs: the growth rate of diatoms peaks around 2035 and then gradually decreases, and the growth rate of small phytoplankton keeps on increasing. The reduced growth rate of diatoms does not completely explain the decrease in NPP and biomass, since the biomass of diatoms decreases throughout the entire period (Fig. D.10), while the growth rate of diatoms first increases (Fig. 5.4e). Another reason for the decrease in biomass is advective transport of diatoms out of the North Atlantic (Fig. D.10). Looking at the advective fluxes of diatom biomass over the region (45°N-70°N × 270°E-0°E), we can see that in the beginning of the 21st century relatively much biomass is lost due to advection over the southern and eastern boundaries of this region which explains the decreasing NPP over this time period. Total advection decreases mostly due reduced biomass concentrations near the southern boundary (Fig. D.10d, e). Small phytoplankton biomass is not affected by this advection, because biomass concentrations are low in the beginning of the boundary of this region century and only increase at the southern boundary of the region when diatom biomass decreases (Fig. D.9). Eventually, due to the reduced growth rate, the biomass of diatoms does not recover. This causes the decrease in diatom NPP and explains why small phytoplankton are able to outcompete diatoms in this region utilizing the nutrients not used by diatoms anymore. The changes in NPP and EP affect the concentrations of DIC and Alk. These two tracers affect the pCO₂ of the surface ocean, and thus the gas exchange with the

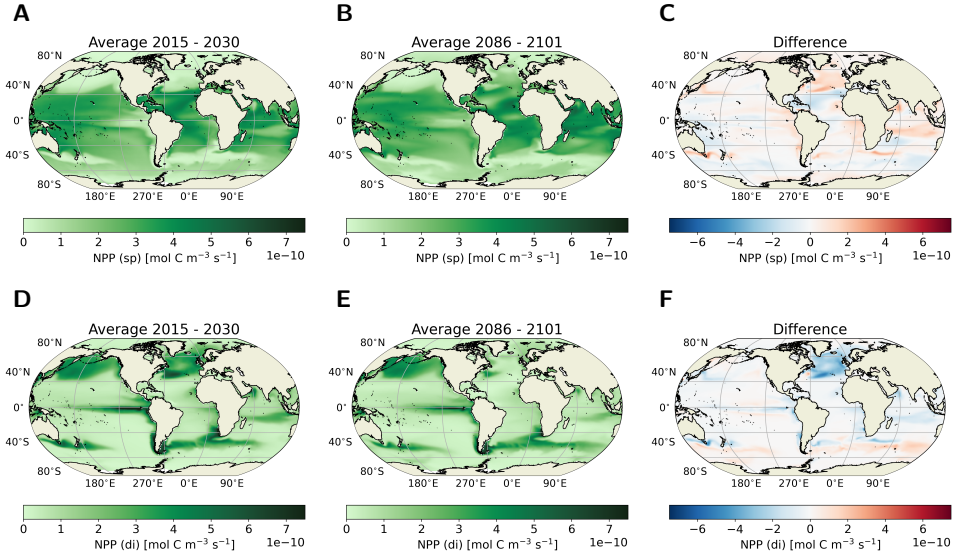


Figure 5.3: NPP averaged over top 100 m in $\text{mol C m}^{-3} \text{s}^{-1}$ for small phytoplankton (top row) and diatoms (bottom row) for the period 2015-2030 (left), the period 2086-2101 (middle) and the difference between the two (right).

atmosphere. Within CESM, it is difficult (without further simulations) to determine the effect of the reduced NPP and EP on the air-sea gas exchange and atmospheric $p\text{CO}_2$ as the latter quantity is determined by many other processes which cannot be separated. This effect, however, is crucial for establishing the sign of the plankton composition atmospheric CO_2 feedback associated with changes in EP. To assess the feedback strength, we use the SCP-M model in combination with the CESM2 data. To do this, we have included the option for variable biological fluxes in the North Atlantic as a function of atmospheric $p\text{CO}_2$. This function is determined from fitting CESM2 biological fluxes to CESM2 atmospheric $p\text{CO}_2$ (Fig. 5.5) and scaled to the original, constant fluxes in the SCP-M:

$$C_{bio,2} = \frac{p\text{CO}_2 * 0.0165 - 0.133}{p\text{CO}_{2,0} * 0.0165 - 0.133} \times -2.87 \times 10^{-10} \quad (5.2)$$

$$A_{bio,2} = \frac{-p\text{CO}_2 * 0.00616 + 0.0402}{|-p\text{CO}_{2,0} * 0.00616 + 0.0402|} \times \frac{16}{106} \times 2.87 \times 10^{-10} \quad (5.3)$$

These fits (Fig. 5.5c, d) represents the rate of change of DIC and Alk due to biological activity and the CESM2 output variables are averaged over the region $40^\circ\text{N}-60^\circ\text{N} \times 270^\circ\text{E}-30^\circ\text{E}$ in the top 150 m of the water column (Fig. 5.5a,b).

To determine the feedback strength we choose initial conditions in the SCP-M for the year 2015 from CESM2 output for DIC and Alk averaged over the regions corresponding to the boxes. First, we determine the uncaptured dynamics in the SCP-M with respect to the CESM2 with regard to atmospheric $p\text{CO}_2$ for every time step. For this we use constant biological fluxes for all boxes in the SCP-M. Initial conditions for

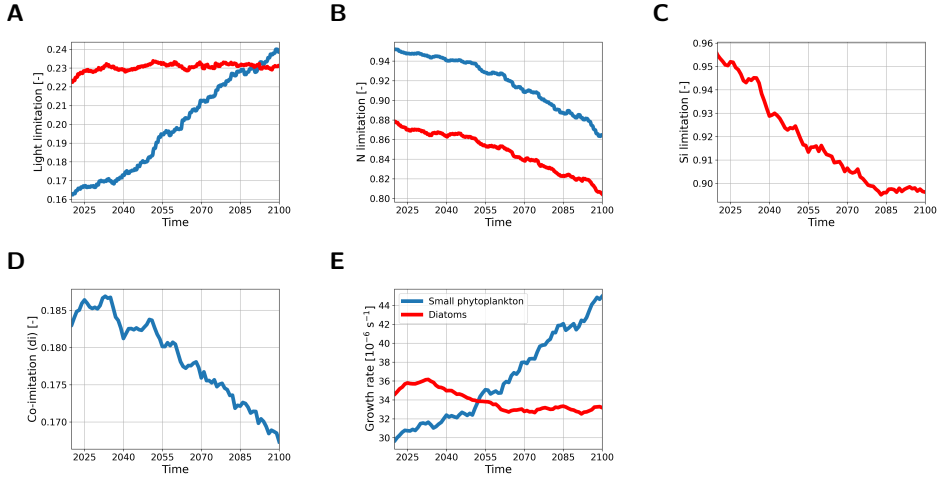


Figure 5.4: (a) Light limitation for small phytoplankton (blue) and diatoms (red) in the region $45^{\circ}\text{N}-70^{\circ}\text{N} \times 270^{\circ}\text{E}-30^{\circ}\text{E}$ in CESM2. Lower limitation values represent more limitation. (b) As in (a) but for nitrogen. (c) As in (a) but for silicate (diatom only). (d) Nutrient-light co-limitation in the same region. Different nutrient limitations are taken into account before averaging over mentioned region. Therefore the co-limitation is not simply the product of (a) and (b). (e) The growth rate in 10^{-6} s^{-1} averaged over the top 100 m averaged over the same region as in (a).

each timestep are adapted with a uncaptured dynamics parameter $Y(t)$, following

$$pCO_2^{SCPM*}(t) = pCO_2^{SCPM}(t) + Y(t) \quad (5.4)$$

Where we determine $Y(t)$ using a secant method, such that

$$pCO_2^{SCPM}(t+1) = pCO_2^{CESM}(t+1) \quad (5.5)$$

The relative uncaptured processes by the SCP-M amounts up to approximately 8% of the total atmospheric CO_2 concentration of the CESM2. After determining the uncaptured dynamics, we can determine the feedback strength (Fig. 5.5e, f). To do this, we use the variable biological fluxes in the North Atlantic box as a function of atmospheric pCO_2 (Eq. (5.2) and (5.3)). We then determine the feedback strength $X(t)$ for each time step following a similar method:

$$pCO_2^{SCPM*}(t) = pCO_2^{SCPM}(t) + Y(t) + X(t) \quad (5.6)$$

Where we search for $X(t)$, again using a secant method, such that

$$pCO_2^{SCPM}(t+1) = pCO_2^{CESM2}(t+1) \quad (5.7)$$

Note that if $X(t)$ is negative, the feedback strength is positive, i.e. we have to lower our ‘initial’ atmospheric CO_2 concentration, because the ocean takes up less carbon causing more atmospheric pCO_2 to reside in the atmosphere.

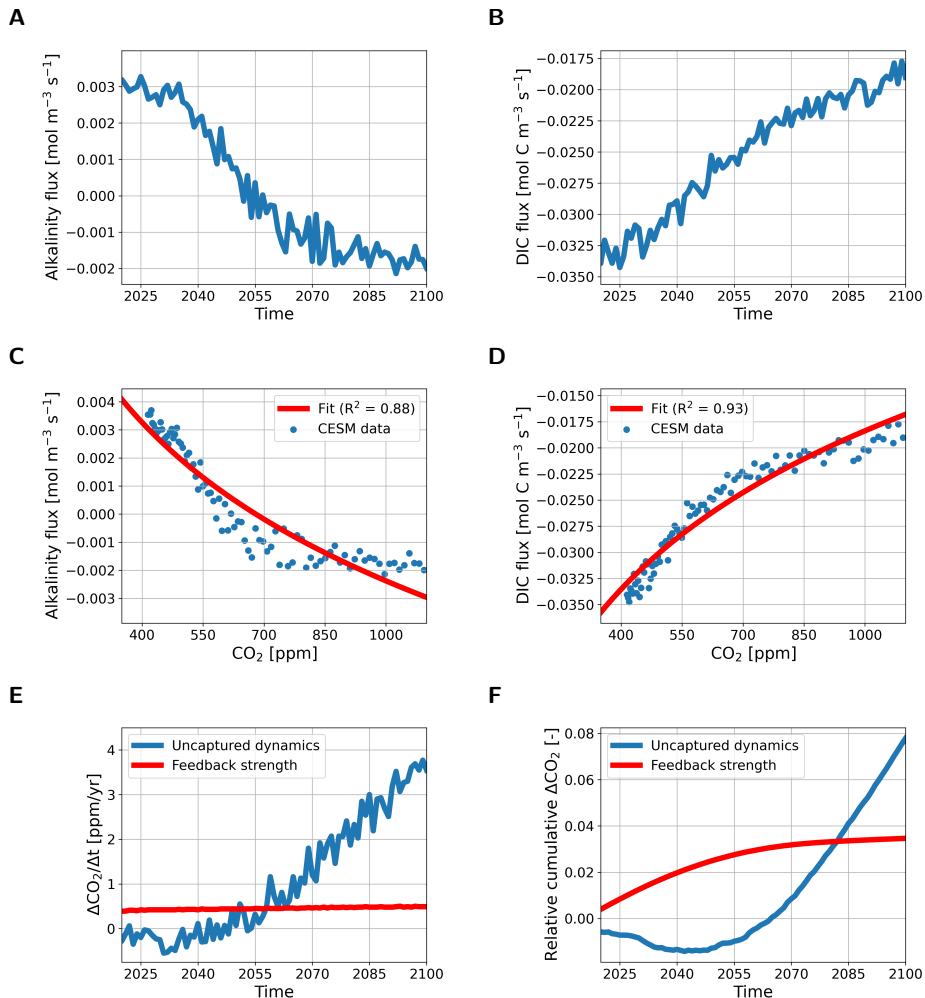


Figure 5.5: (a) Change of Alk flux in the region $40^{\circ}\text{N}-60^{\circ}\text{N} \times 270^{\circ}\text{E}-30^{\circ}\text{E}$ in the top 150 m of the water column due to biological activity in the CESM2 versus time. (b) As in (a) but for DIC. (c) Blue markers represent CESM2 data as in (a) but versus atmospheric CO₂ concentration, and the red line represents a logarithmic fit to this data. (d) As (c) but for DIC. (e) The uncaptured dynamics for atmospheric CO₂ concentrations in ppm/yr in the SCP-M with respect to CESM2 in blue, and the feedback strength in red. (f) As in (e) but cumulative and relative to the atmospheric CO₂ concentration.

Using our method we can give a first estimate of the order of magnitude of the feedback. We find that the effect of reduced NPP and EP causes variability in both DIC and Alk which results in a cumulative flux of approximately 294 GtCO₂ extra in the atmosphere in the year 2100, resulting in a 37.9 ppm higher CO₂ concentration in the atmosphere (Fig. 5.6). Over this time period global mean surface temperature

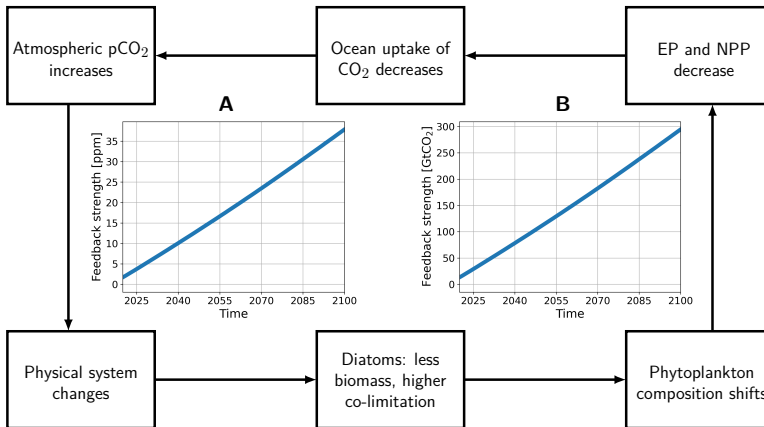


Figure 5.6: Positive feedback loop on how biological activity in the North Atlantic Ocean is coupled to atmospheric pCO₂. Left graph in the loop represents the increase of atmospheric pCO₂ due to the feedback loop in ppm. The right graph represents the equivalent cumulative change in air-sea gas exchange of CO₂ in GtCO₂.

rises 4.9 K (average 2096-2100 minus average 2015-2019). This process hence represents a positive feedback with a strength of $60 \left(\frac{294}{4.9}\right)$ GtCO₂/K warming where, due to increasing CO₂ concentrations, changes in the physical system such as an increase in stratification in the North Atlantic, result in an unfavorable environment for diatoms while small phytoplankton profit. This change in plankton composition decreases the flux of carbon from the surface to the deep ocean which increases DIC and decreases Alk concentrations in the surface ocean. The combined effect results in a decrease in the uptake of CO₂ in the ocean, further increasing atmospheric CO₂ concentrations.

5.4 Summary and discussion

In this study, we investigated the interaction of atmospheric pCO₂ and biological production in the Atlantic Ocean north of 45°N in an emission driven SSP5-8.5 scenario simulation in CESM2. We found that under these high emissions, net primary production (NPP) and export production (EP) decrease in this region. Similar results on NPP and EP have been obtained in CMIP5 simulations under the RCP8.5 scenario (Bopp et al., 2013). It was shown that in the CESM2 simulation, this could be attributed to reduced productivity of diatoms which could be explained by increasing co-limitation of light and nitrogen and decreasing biomass stocks. The increasing limitation was the result of stronger stratification in the North Atlantic, which could be partly explained by increasing atmospheric temperatures due to increasing atmospheric CO₂ levels. The shift in plankton composition from larger diatoms to small phytoplankton is in agreement with theory and model results suggesting that small

phytoplankton outcompete diatoms under increased nutrient stress (Marinov et al., 2013).

The results indicate the existence of a positive carbon cycle feedback where plankton composition plays a central role as shown in Fig. 5.6. Using an idealized carbon cycle model, we have made a first attempt to put an order of magnitude on the feedback strength. Obviously, this method has several caveats since the SCP-M captures less dynamics than the CESM2 and it is therefore difficult to assess the reliability of the results. In our method, the uncaptured dynamics is quite sensitive to initial conditions and parameter values. However, the actual feedback strength is only sensitive to the original strength of the biological flux. Using this simple method, it was shown that this feedback results in an increase in atmospheric CO₂ of 37.9 ppm in 2100, which is equivalent to approximately 294 GtCO₂. To put this into perspective, this is slightly smaller than the increased CO₂ storage of ~ 336 GtCO₂ in the North Atlantic in the Last Glacial Maximum due to a more efficient biological carbon pump (Yu et al., 2019), meaning that the order of magnitude of our feedback strength is in a realistic range. This positive feedback (Cabr e et al., 2015) seems to be relatively small, but it needs to be taken into account when estimating the safe carbon budget in future climate change. The safe carbon budget is estimated to be 308 GtCO₂ for a peak global warming of 1.5 K, and 994 GtCO₂ for a warming of 2 K (van der Ploeg, 2018). Assuming the assessed feedback strength is correct, this feedback accounts for approximately 29% and 12% of the 1.5 K and 2.0 K warming safe carbon budget respectively.

In summary, biological activity in the ocean is able to interact with the physical system and have an impact on variables such as global mean surface temperature via atmospheric CO₂ concentrations, with a substantial impact on our safe carbon budget. Furthermore, we want to stress that the numbers presented here should be viewed as an estimate on the order of magnitude of the feedback strength and not as an exact result because the used method to assess the feedback strength has multiple caveats.

Certainly this study has its limitations, as only a single Earth System Model with only a single member simulation for only one emission scenario is used. It might be very interesting to repeat such simulations and analysis with models having different plankton dynamics since responses of Earth System Models depend on the complexity of this dynamics (Dutkiewicz et al., 2013; Fu et al., 2016) and since there exists a large intermodel spread in NPP and EP among CMIP6 models (Kwiatkowski et al., 2020; Tagliabue et al., 2021). Furthermore, it would be useful to extend such simulations to, for example, 2300 to see whether the increased productivity of the small phytoplankton group is able to dampen the positive feedback, or whether they will also become more limited due to increasing stratification in the North Atlantic.

Response of atmospheric $p\text{CO}_2$ to a strong AMOC weakening under low and high emission scenarios

The Earth System is warming due to anthropogenic greenhouse gas emissions which increases the risk of passing a tipping point in the Earth System, such as a collapse of the Atlantic Meridional Overturning Circulation (AMOC). An AMOC weakening can have large climate impacts which influences the marine and terrestrial carbon cycle and hence atmospheric $p\text{CO}_2$. However, the sign and mechanism of this response are subject to uncertainty. Here, we use a state-of-the-art Earth System Model, the Community Earth System Model v2 (CESM2), to study the atmospheric $p\text{CO}_2$ response to an AMOC weakening under low (SSP1-2.6) and high (SSP5-8.5) emission scenarios. A freshwater flux anomaly in the North Atlantic strongly weakens the AMOC, and we simulate a weak positive $p\text{CO}_2$ response of 0.44 and 1.3 ppm increase per AMOC decrease in Sv for SSP1-2.6 and SSP5-8.5, respectively. For SSP1-2.6 this response is driven by both the oceanic and terrestrial carbon cycles, whereas in SSP5-8.5 it is solely the ocean that drives the response. However, the spatial patterns of both the climate and carbon cycle response are similar in both emission scenarios over the course of the simulation period (2015-2100), showing that the response pattern is not dependent on cumulative CO_2 emissions up to 2100. Though the global atmospheric $p\text{CO}_2$ response might be small, locally large changes in both the carbon cycle and the climate system occur due to the AMOC weakening.

This chapter is based on:

Boot, A.A., A.S. von der Heydt, and H.A. Dijkstra (2023), Response of atmospheric $p\text{CO}_2$ to a strong AMOC weakening under low and high emission scenarios, under review in *Climate Dynamics*

6.1 Introduction

Anthropogenic emissions of greenhouse gases cause the Earth System to change and warm up. As temperatures increase, we are at risk of crossing tipping points with possibly large detrimental effects on our climate, biodiversity and human communities (Armstrong-McKay et al., 2022; Lenton et al., 2008). One of these tipping points can occur in the Atlantic Meridional Overturning Circulation (AMOC) (Lenton et al., 2008). Currently, the AMOC is in a so-called on-state where it transports heat from the Southern Hemisphere to the Northern Hemisphere and thereby modulates global and especially European climate (Buckley & Marshall, 2016). In models, the AMOC can be strongly weakened and in this so-called collapsed state (or off-state), the northward heat transport is disrupted with large global climatic effects (Orihuela-Pinto et al., 2022).

Proxy-based evidence suggest that AMOC collapses have occurred frequently during the Pleistocene where they are a main source of millennial variability (e.g. the Dansgaard-Oeschger cycles; Lynch-Stieglitz, 2017; Rahmstorf, 2002). The disrupted heat transport causes warming of surface air temperature (SAT) and sea surface temperature (SST) in the Southern Hemisphere, while the Northern Hemisphere cools (also called the ‘bipolar seesaw’; Caesar et al., 2018; Vellinga & Wood, 2002), with local SAT changes up to 10°C (Cuffey & Clow, 1997; Rahmstorf, 2002). In models, the bipolar seesaw results in an increased northern hemispheric sea-ice extent and changes in atmospheric dynamics (Orihuela-Pinto et al., 2022; Vellinga & Wood, 2002). The changes in atmospheric dynamics are, for example, seen in wind fields with strengthened trade winds and strengthened Pacific Walker Circulation (Orihuela-Pinto et al., 2022), and a southward shift of the Intertropical Convergence Zone (ITCZ) (Jackson et al., 2015; Zhang & Delworth, 2005). The tipping threshold for the AMOC is estimated to be around 4 °C of warming relative to pre-industrial climate (Armstrong-McKay et al., 2022).

In addition to the climate system, also the carbon cycle is affected by an AMOC collapse. In the ocean, the change in ocean circulation affects the advection of important tracers such as Dissolved Inorganic Carbon (DIC) and nutrients (Zickfeld et al., 2008). An AMOC collapse can also change upwelling rates and surface stratification, processes that are important for driving Net Primary Production (NPP) and carbon sequestration in the deep ocean. Terrestrial primary productivity is affected by the changing temperature and precipitation patterns. Locally, this can lead to both a reduction or an increased uptake of CO₂ (e.g. Köhler et al., 2005). Several studies have looked into a potential feedback between AMOC dynamics and atmospheric pCO₂, which is controlled by the exchange of the atmosphere with the ocean and land carbon stocks. These studies (e.g. Köhler et al., 2005; Marchal et al., 1998; Schmittner & Galbraith, 2008), mostly focused on Pleistocene and pre-industrial conditions, show a wide range of possible responses. There is no clear consensus on the responses of the terrestrial and ocean carbon stock to an AMOC weakening, or to the net effect on atmospheric pCO₂, which can be attributed to different climatic boundary conditions, timescales assessed, and model detail used (Gottschalk et al.,

2019). In CMIP6 models, the AMOC gradually weakens up to 2100 and, independent of the used emission scenario (Weijer et al., 2020), no AMOC tipping is found. However, these models are thought to be biased towards a too stable AMOC (e.g. Cheng et al., 2018; Weijer et al., 2019), and a recent observation based study has indicated that the AMOC may tip between 2025 and 2095 (Ditlevsen & Ditlevsen, 2023).

The carbon cycle is also affected by climate change. In the ocean, the effect on the solubility pump is relatively straight forward: increased warming, and increased CO₂ concentrations, reduce ocean pH and the solubility of CO₂, which reduces the uptake capacity of the ocean (Sarmiento et al., 1998). The biological pump in Coupled Model Intercomparison Project 6 (CMIP6; Eyring et al., 2016) models is much more uncertain though (Henson et al., 2022; Wilson et al., 2022), especially given that the spread in NPP and Export Production (EP) has increased from CMIP5 to CMIP6 (Kwiatkowski et al., 2020; Tagliabue et al., 2021). The terrestrial biosphere is affected for example through increased primary production related to CO₂ fertilization (Zhu et al., 2022), but also increased respiration due to permafrost melt (Burke et al., 2020).

Studies looking at the combined effect of strong AMOC weakening and anthropogenic climate change on the future carbon cycle are limited. A projected AMOC weakening affects both the solubility and the biological carbon pumps (Liu et al., 2023), and generally leads to reduced uptake of (anthropogenic) carbon in the ocean (Liu et al., 2023; Obata, 2007; Zickfeld et al., 2008), which can be partially compensated for by the terrestrial biosphere (Zickfeld et al., 2008). However, the net effect has been found to be small due to competing effects (Swingedouw et al., 2007; Zickfeld et al., 2008). Though global effects might be weak, local effects can be quite strong. For example, a weakening of the AMOC can also result in a local reduction in primary productivity (Whitt & Jansen, 2020), changes in the plankton stock (Schmittner, 2005) and plankton composition (Boot et al., 2023a), which all can lead to reduced CO₂ uptake of the ocean (e.g. Boot et al., 2023a; Yamamoto et al., 2018). These local changes related to an AMOC weakening are strongest in the Atlantic Ocean (Katavouta & Williams, 2021).

The novel aspect of this paper is that we consider the effect of AMOC weakening on the carbon cycle under climate change in a state-of-the-art global climate model, the Community Earth System Model v2 (CESM2; Danabasoglu et al., 2020), as explained in Sections 2.4.5 and 6.2. We use a strong freshwater forcing in the North Atlantic to artificially weaken the AMOC and consider two different emission scenarios, Shared Socioeconomic Pathways (SSPs), with low (SSP1-2.6) and high (SSP5-8.5) emissions (O'Neill et al., 2020). In the results of Section 6.3 and the subsequent analysis, we focus on the mechanisms how a forced AMOC weakening affects atmospheric pCO₂ under climate change.

6.2 Method

In this chapter we analyze the output from the IMAU CESM2 simulations (Section 2.4.5). The ocean output is given on a displaced Greenland pole grid at a nominal horizontal resolution of 1°, with 60 non-equidistant vertical levels. In total four dif-

ferent, emission forced, simulations are used using two different emission scenarios: the low emission scenario SSP1-2.6 (126) and the high emission scenario SSP5-8.5 (585). For each emission scenario, a control (CTL) and a hosing (HOS) simulation were carried out. The CTL simulations were only forced with the greenhouse gas emissions, while the HOS simulations were forced with greenhouse gas emissions and an additional, artificial freshwater flux in the North Atlantic. This freshwater forcing is located in the North Atlantic Ocean over the latitudes 50°N - 70°N (Fig. 2.9). We will refer to the simulations by their simulation type (CTL or HOS) and the respective emission scenario (126 or 585), e.g. as CTL-126 and HOS-585. All simulations are run from year 2015 to year 2100 and are initialized by values of the NCAR CMIP6 emission driven historical simulation (Danabasoglu, 2019c). The used model output is based on monthly means, and line plots are smoothed with a 5-year running mean. When looking at the difference between the HOS and CTL simulations, we subtract the CTL simulations from the HOS simulations.

6.3 Results

6.3.1 Climate response

In CTL-126, an increase in atmospheric CO₂ concentration from 400 ppm to 467 ppm in the 2050s is found, after which the concentration decreases to 432 ppm in 2100 (Fig. 6.1c). This is accompanied by an increase in global mean surface temperature (GMST) of 1 °C (Fig. 6.1b), and an AMOC decrease from 17 Sv in 2015 to 9 Sv in 2100 (Fig. 6.1a). The weakening of the AMOC results in a cooling of the North Atlantic Ocean, while the rest of the Earth warms with the largest temperature increases found near the poles (Fig. 6.2a, b) as a response to the increase in greenhouse gas concentrations. In the water cycle we see a southward shift of the Pacific Intertropical Convergence Zone (ITCZ) of a few degrees (Fig. E.1a, b). Furthermore, wind fields in the Northern Hemisphere show a small weakening, whereas in the Southern Hemisphere the winds intensify (Fig. E.2a, b).

In CTL-585, the emissions increase the atmospheric CO₂ concentration from 400 ppm to 1094 ppm in 2100 (Fig. 6.1c) which results in a GMST warming of 5 °C (Fig. 6.1b). The AMOC weakens from 17 Sv to 7 Sv (Fig. 6.1a), which leads to a region without warming in the North Atlantic, whereas we see strong warming everywhere else (Fig. 6.2d, e). There is a strong southward shift of the ITCZ in the Pacific and a moderate shift in the Atlantic Ocean (Fig. E.1d, e). The changes in the wind field show similar patterns as CTL-126 but with a larger amplitude (Fig. E.2d, e).

The net effect of the AMOC weakening (i.e. HOS minus CTL) is shown in Fig. 6.1d-f. In the year 2100, atmospheric CO₂ concentrations are 2.6 ppm and 4.2 ppm higher in HOS-126 and HOS-585 compared to their respective CTL simulations. In both HOS simulations the AMOC quickly weakens from 17 Sv in 2015 to 6 Sv in 2045 after which the AMOC weakening starts to level off until the AMOC is weaker than 4 Sv in 2100 (Fig. 6.1d). Due to the AMOC weakening we observe a relative cooling of (locally) more than 3 °C in the Northern Hemisphere and warming in the Southern Hemisphere (Fig. 6.2c, f) (i.e. the bipolar seesaw). The cooling in the Northern Hemisphere results in an increase in sea-ice cover of the Arctic Ocean

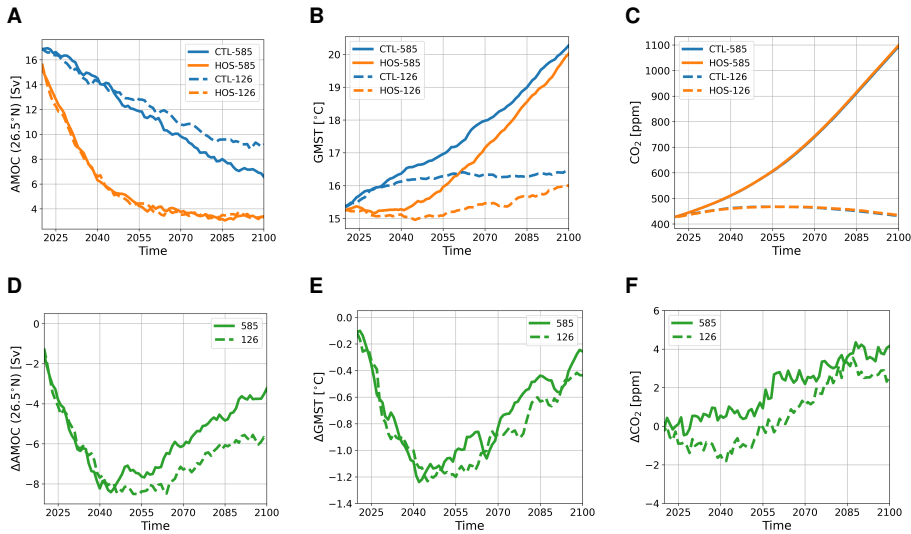


Figure 6.1: (a) AMOC strength at 26.5°N in Sv. (b) GMST in °C. (c) Atmospheric CO₂ concentration in ppm. In (a-c) blue lines represent the control (CTL) simulations, and orange lines the HOS simulations. (d-f) as in (a-c) but for the difference between the HOS simulations and the control simulations. In all subplots dashed lines represent SSP1-2.6 (126) and solid lines SSP5-8.5 (585).

(Fig. E.3), which for HOS-126 persists throughout the entire simulation period. The AMOC weakening also results in a stronger southward shift of the ITCZ in both the Pacific and Atlantic Ocean (Fig. E.1c, f), and winds are relatively intensified in the Northern Hemisphere and weakened in the Southern Hemisphere (Fig. E.2c, f), with a stronger response in SSP5-8.5.

6.3.2 Marine carbon cycle response

In CTL-126 we see that, integrated over the entire simulation period, there are regions in the ocean with net carbon uptake, and net carbon outgassing (Fig. 6.3a). The Southern Ocean between 45°S and 60°S, and the equatorial Pacific Ocean, are regions of carbon release from the ocean to the atmosphere. The region of strongest outgassing in the Pacific is located in the upwelling regions on the eastern side of the basin. Carbon uptake generally occurs in the rest of the ocean with the strongest uptake located in the Sea of Japan and the high latitude North Atlantic Ocean. Looking at the development over time (Fig. 6.4a, b) we see a negative trend over almost the entire ocean, meaning regions which take up carbon in the beginning of the simulation have lower uptake at the end, and regions which emit carbon in 2015 emit more carbon at the end of the simulation. Some regions, e.g. in the Southern Ocean, shift from a carbon uptake region to a region of outgassing.

In CTL-585, also integrated over the simulation period, only the eastern equatorial Pacific shows strong outgassing (Fig. 6.3d). In the other equatorial basins, there are also some small patches that show net outgassing, but the rest of the ocean shows

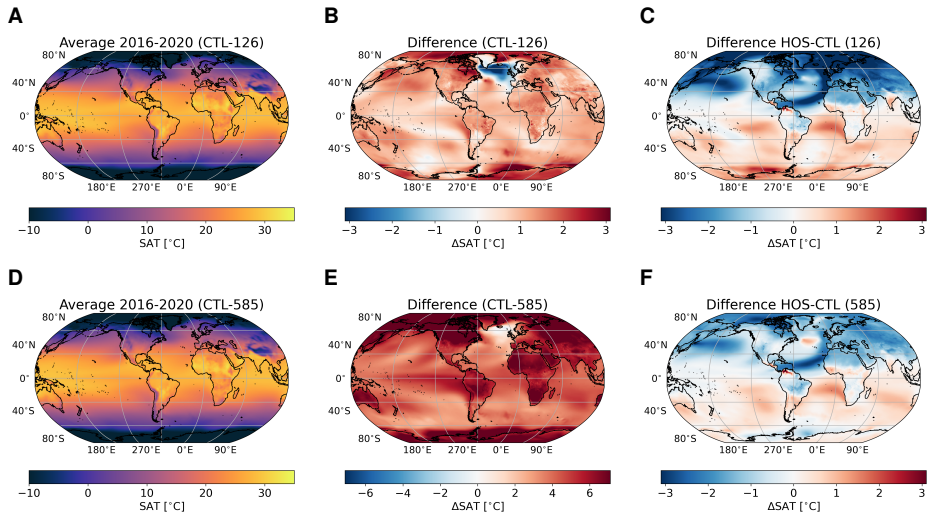


Figure 6.2: Results for Surface Air Temperature (SAT) in °C. The top row (a-c) is for SSP1-2.6, and the bottom row (d-f) for SSP5-8.5. The left column (a, d) represents the average over 2016-2020 in the control simulations. The middle row (b, e) represents the difference between the average of 2096-2100 and 2016-2020 for the control simulations. The right row (c, f) represents the difference between the HOS and CTL simulations averaged over 2096-2100. Note the different scaling between b and e.

net carbon uptake. Except for the high latitude North Atlantic Ocean and some small other regions, we see a positive trend (Fig. 6.4d, e), meaning that regions that take up carbon in the beginning, take up more carbon at the end of the simulation, and regions which show outgassing in the beginning show either reduced outgassing or go from being a region of outgassing to a region of CO₂ uptake. A remarkable region is the high latitude North Atlantic Ocean where the flux from the atmosphere into the ocean strongly decreases while atmospheric pCO₂ almost triples. Integrated over time, the spatial pattern of regions that see increased or decreased exchange with the atmosphere is very similar for SSP1-2.6 as for SSP5-8.5 (Fig. 6.3c, f). In total, the ocean takes up 7.4 PgC less due to the AMOC weakening in SSP1-2.6 and 15.6 PgC less in SSP5-8.5 (Fig. 6.5a, d).

Even though the climate system changes a lot due to the AMOC weakening, the CO₂ uptake of the ocean does not change a lot because of compensating effects. To obtain a better understanding of the mechanisms behind the reduced uptake, we have divided the ocean in 5 basins: the Arctic (north of 66°N), the Southern (south of 35°S), the Atlantic, Pacific and Indian Ocean (Fig. 6.5b, e). In the response (i.e. HOS-CTL), for both emission scenarios, all basins show the same sign, i.e. more uptake or less uptake due to the AMOC weakening.

In both emission scenarios the Arctic Ocean shows a decreased uptake (-6.0 PgC in SSP1-2.6 and -4.4 PgC in SSP5-8.5), which can be explained by looking at the sea-ice cover (Fig. E.3). The cooling in the Northern Hemisphere following the AMOC weakening in the HOS simulations, increases the sea-ice cover. The increase

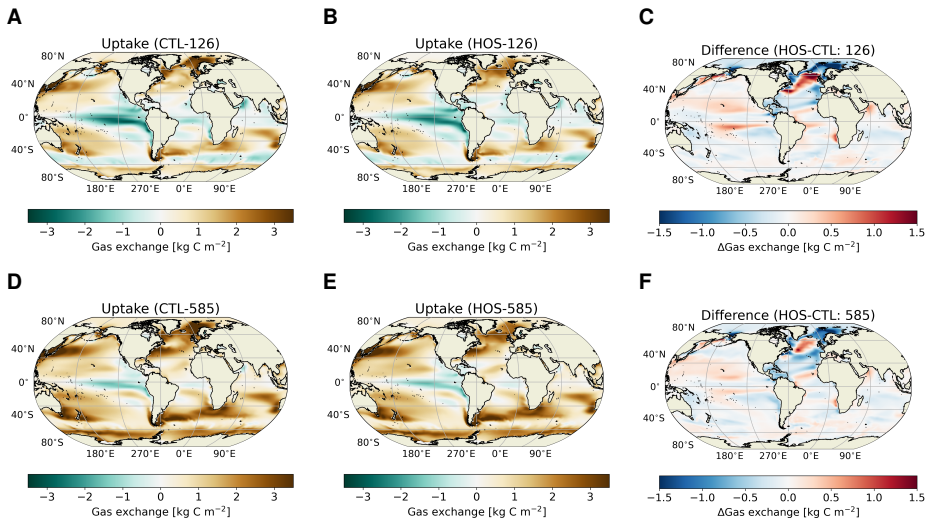


Figure 6.3: Results for the oceanic CO₂ uptake integrated over the entire simulation period in kg C m⁻². The top row (a-c) represents SSP1-2.6 and the bottom row (d-f) represents SSP5-8.5. The left column (a, d) represents the uptake in the control simulations, the middle column (b, e) the uptake in the HOS simulations, and the right column (c, f) the difference between the HOS and CTL simulations. In a, b, d, and e positive values (brown colors) represent net uptake, and negative values (blue colors) represent net outgassing.

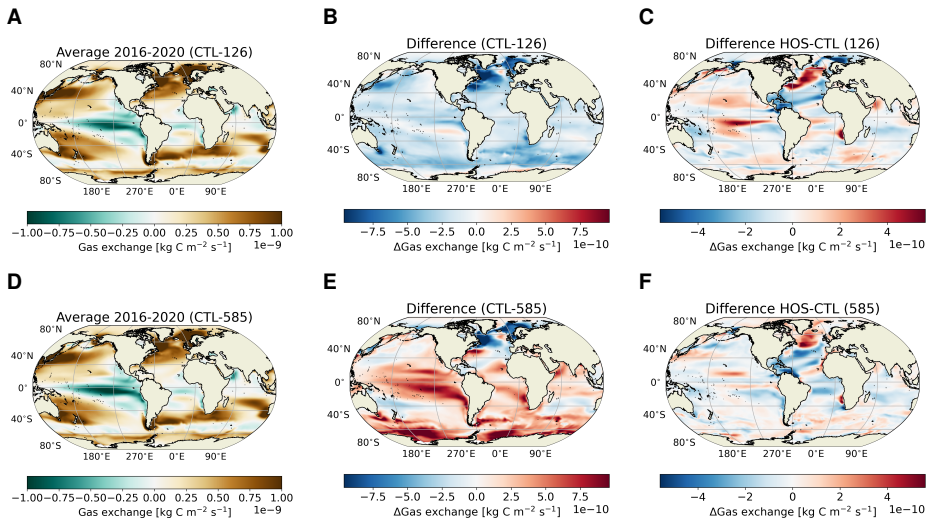


Figure 6.4: Results for oceanic CO₂ uptake in kg C m⁻² s⁻¹. Panels represent the same as in Fig. 6.2. Positive values (brown colors) in a and d represent uptake by the ocean and negative values (blue colors) represent outgassing.

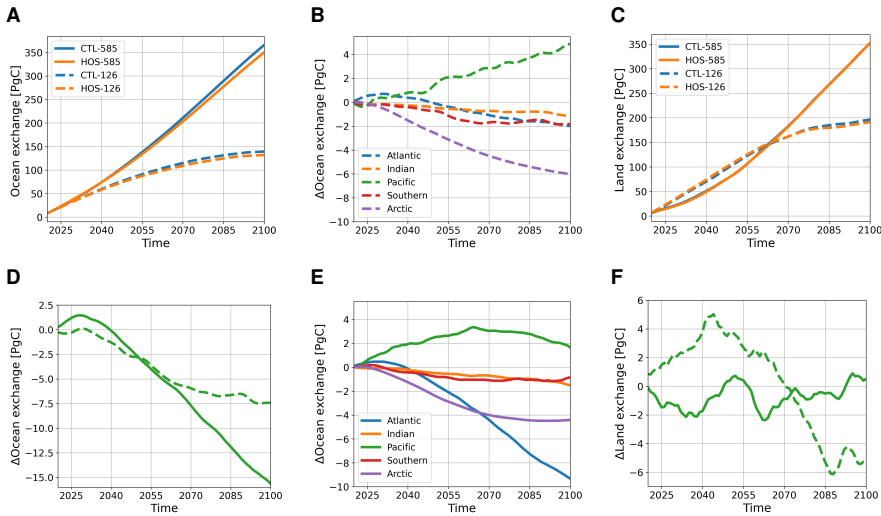


Figure 6.5: (a) Cumulative uptake of CO₂ in the ocean from 2016 onward in PgC. (b) Difference in the cumulative oceanic CO₂ uptake between the HOS and CTL simulations in SSP1-2.6 for different ocean basins. (c) As (a) but for the land. (d) The difference in the cumulative oceanic CO₂ uptake between the HOS and CTL simulations. (e) As in (b) but for SSP5-8.5. (f) As in (d) but for the land. In a and c blue lines represent the control simulations, and the orange lines the HOS simulations. In all subplots dashed lines represent SSP1-2.6 and solid lines SSP5-8.5. Negative values in b, d-f represent reduced uptake in the HOS simulations compared to the CTL simulations.

in sea-ice cover has two effects on the uptake of CO₂: (1) it reduces the ocean area available for exchange with the atmosphere; and (2) it increases light limitation and thereby reduces net primary production (NPP; Fig. E.5) and the carbon export to the subsurface ocean. In SSP5-8.5 most of the sea ice still disappears due to the strong warming, but in SSP1-2.6 most of the sea ice persists throughout the simulation period, which explains why the Arctic Ocean in SSP1-2.6 responds stronger compared to SSP5-8.5. We also find this effect in the sea-ice covered regions in the North Atlantic (e.g. the Labrador Sea).

The Pacific Ocean takes up more carbon in the HOS than in the CTL simulations (+4.9 PgC in SSP1-2.6 and +1.7 PgC in SSP5-8.5). To analyze what is happening in the Pacific, we considered three different regions: (1) the North Pacific (20°N-66°N), the Equatorial Pacific (20°N-10°S), and the South Pacific (10°S-35°S). In the North Pacific, the relative cooling of the surface ocean (Fig. E.6) results in an increase of solubility of CO₂ driving increased uptake (Fig. 6.3e, f). A similar, but opposite, response is seen in the South Pacific. Here the surface ocean becomes relatively warmer inhibiting the uptake of CO₂. The equatorial Pacific is characterized by a band with reduced uptake and one with increased uptake. This can be related to the stronger southward shift of the ITCZ in the Pacific in HOS compared to the CTL (Fig. E.1). Due to this shift, the dilutive fluxes related to net precipitation shift southward, causing relative increases of salinity in the northern section

due to reduced precipitation, and relative decreases due to increased precipitation in the southern section (Fig. E.7). This, in turn, also affects the stratification in these regions with a weakening in the north and a strengthening in the south (Fig. E.8). These changes affect the solubility of CO_2 in the equatorial regions causing decreased uptake in the northern section and increased uptake in the southern section.

We find the largest difference in carbon uptake (-2.0 PgC in SSP1-2.6 and -9.3 PgC in SSP5-8.5) in the Atlantic. The regions with sea ice show similar behavior as the Arctic Ocean with decreased uptake related to a larger sea-ice cover in the HOS simulations. In the ice-free subpolar region, an increase in uptake is observed which is associated to decreases in sea surface salinity (SSS; Fig. E.7) due to the applied freshwater forcing in this region which promotes the uptake of CO_2 . In the subtropical region we generally see a decrease in uptake. To explain this we consider several variables, i.e. SST (Fig. E.6), SSS (Fig. E.7), DIC (Fig. E.11), Alk (Fig. E.12) and NPP (Fig. E.5), which all show a relative decrease in this region. The net effect of the changes in these variables is a reduction in pH (Fig. E.15) and reduced uptake capacity of the ocean.

In the Canary Upwelling System and along the North Equatorial Current we do see an increase in NPP (Fig. E.5), due to increased nutrient concentrations (Fig. E.10) related to increased upwelling of nutrients (Fig. E.9 and E.14). In the region of the North Equatorial Current this leads to increased uptake of the ocean, and only in SSP5-8.5 also in the Canary Upwelling System. Outside the North Atlantic, large responses are seen in the equatorial region and the Benguela Upwelling System which are characterized by reduced upwelling (Fig. E.1), promoting additional uptake of CO_2 in the ocean. In the Atlantic Ocean, we find that DIC (Fig. 6.6) and nutrient (Fig. 6.7) concentrations decrease in the surface ocean due to the weakening of the AMOC and increase in the deep ocean. The reduction in DIC clearly shows the reduced uptake capacity of the ocean, and the reduction in PO_4^{3-} also explains the decrease in NPP (Fig. E.5) observed in the Atlantic basin.

The Indian Ocean has a relatively weak response and is very similar for both emission scenarios with a small decrease in uptake (-1.2 PgC in SSP1-2.6 and -1.5 PgC in SSP5-8.5). This is related to the relatively warmer SSTs in the HOS simulations (Fig. E.6). The Southern Ocean also has a small decrease in uptake, with a larger decrease in SSP1-2.6 (-1.8 PgC compared to -0.9 PgC in SSP5-8.5). This larger decrease can be explained by the fact that the sea-ice cover is larger in SSP1-2.6 compared to SSP5-8.5 (Fig. E.4).

6.3.3 Terrestrial carbon cycle response

In CTL-126, the terrestrial biosphere, integrated over the entire simulation period, shows a net uptake of CO_2 in most regions (Fig. 6.8a). The Net Biosphere Production (NBP) maxima are located on the equator for the tropical rainforests, the boreal forests in the high latitude Northern Hemisphere, and the eastern United States and China. The few locations that show net emission of CO_2 are very local and present in the high latitude Northern Hemisphere, the Tibetan Plateau, South East Asia and South America. If we look at the development over time (Fig. 6.9a, b) we see that the tropical rainforests have a lower NBP at the end of the simulation. There are

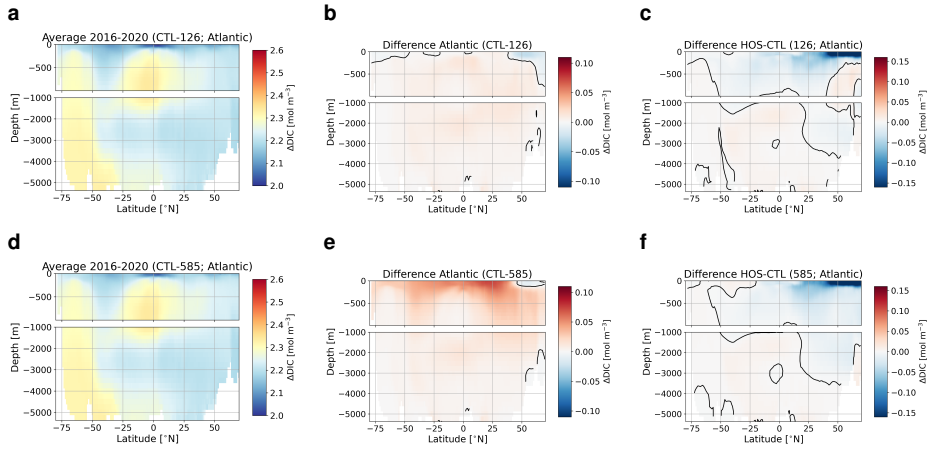


Figure 6.6: Results for zonally averaged DIC concentrations in the Atlantic basin in mol m^{-3} . Panels represent the same as in Fig. 6.2. Black contour lines in b, c, e and f represent the 0 mol m^{-3} contour. Note the different scaling of the surface ocean (top 1000 m) compared to the deep ocean.

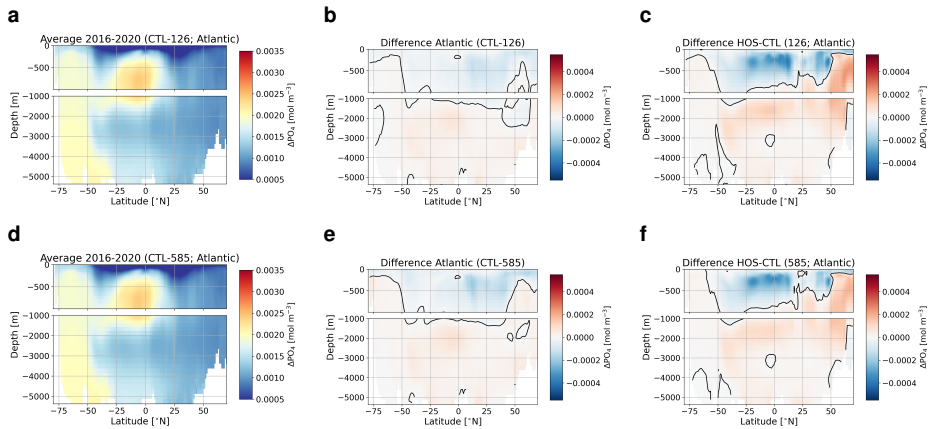


Figure 6.7: Results for zonally averaged PO_4^{3-} concentrations in the Atlantic basin in mol m^{-3} . Panels represent the same as in Fig. 6.2. Black contour lines in b, c, e and f represent the 0 mol m^{-3} contour. Note the different scaling of the surface ocean (top 1000 m) compared to the deep ocean.

some regions that have a higher NBP in 2100, e.g. the boreal forests in Scandinavia. The response in CTL-585 is very similar to CTL-126 with respect to the spatial pattern, except in central Africa (Fig. 6.8d). However, the amplitude of the response is much larger due to the CO₂ fertilization effect. Especially the tropical rainforests, but also the boreal forests, show more carbon uptake compared to CTL-126. The same is also true for regions that emit carbon, i.e., the region in the high latitude Northern Hemisphere that emits carbon is larger, and the amount of carbon emitted is also higher. The main difference with respect to CTL-126 is a region in the Congo basin which emits CO₂ in CTL-585 whereas in CTL-126 it is a region of relatively strong uptake, which is possibly related to increased wildfire activity in this region in SSP5-8.5 (Fig. E.16). When we look at the development over time (Fig. 6.9d, e) we find a completely different pattern in CTL-585 compared with CTL-126. The tropical rainforests show an increase in NBP related to the CO₂ fertilization effect whereas northern Siberia shows a decrease related to increased respiration due to permafrost melt (Fig. E.18 and E.19).

Integrated globally the terrestrial biosphere takes up 5.3 PgC less in SSP1-2.6 and 0.5 PgC more in SSP5-8.5 (Fig. 6.5) in the HOS simulations compared to the CTL simulations. However, looking at spatial patterns of the cumulative uptake, we see a very similar response to the AMOC weakening (HOS-CTL) for both emission scenarios (Fig. 6.8c, f). In both emission scenarios we find that the increased southward shift in the ITCZ in the HOS simulations lead to decreased NBP in central America, and increased NBP in Southern America. A similar shift can be seen in Africa, but with a smaller latitudinal shift and amplitude. The shift and amplitude are slightly stronger in SSP1-2.6. The boreal forests become relatively lower in NBP in the HOS simulations with a larger amplitude in SSP1-2.6. This is because in SSP1-2.6, the forests have lower Gross Primary Production (GPP; Fig. E.17) over the course of the century which can be related to the relative cooling in the Northern Hemisphere seen in the HOS simulations (Fig. E.7). This relative cooling is stronger in SSP1-2.6, related to the increased sea-ice cover and therefore higher albedo in the Arctic. Another effect of the Northern Hemispheric cooling is an increase in NBP in the permafrost regions in Siberia and North America in the HOS simulations. The cooling reduces permafrost melt (Fig. E.18) and therefore reduces soil respiration (Fig. E.19), with a larger amplitude in Siberia for SSP5-8.5.

6.3.4 Total response

In total, we see an increase of atmospheric CO₂ concentration of 2.6 and 4.2 ppm in 2100 in SSP1-2.6 and SSP5-8.5 due to the AMOC weakening (HOS-CTL). In SSP1-2.6 this response is caused partly due to reduced uptake of the ocean and partly due to reduced uptake of the land. In SSP5-8.5 it is completely driven by the ocean as the globally integrated uptake over the land is approximately the same in CTL-585 as in HOS-585. Eventually the AMOC strength in 2100 has decreased by 5.8 and 3.2 Sv in the HOS simulations compared to the CTL simulations. Under the assumption of linearity, this results in a positive feedback strength of 0.44 ppm Sv⁻¹ and 1.3 ppm Sv⁻¹ for SSP1-2.6 and SSP5-8.5, respectively. This can be considered a positive feedback since increased CO₂ concentrations in future climates are generally associated with a weakening of the AMOC (e.g. Weijer et al., 2020). This AMOC-

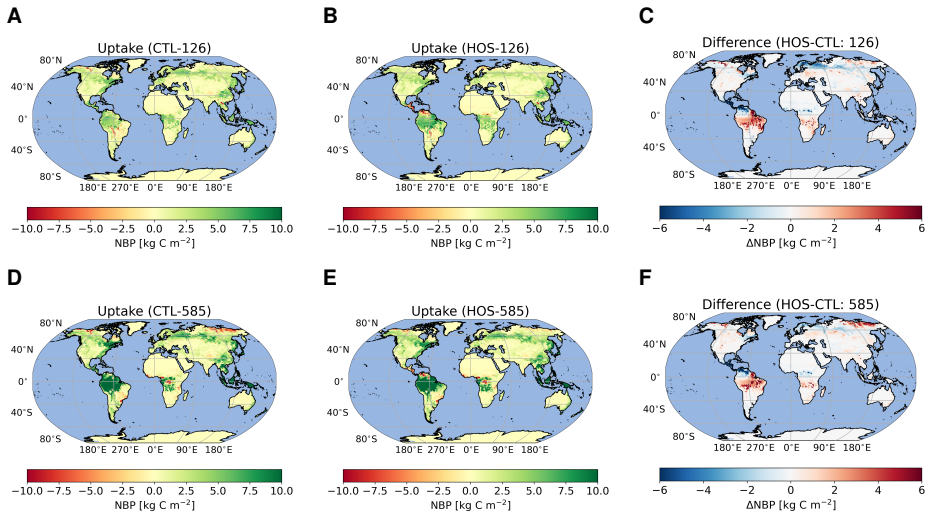


Figure 6.8: Results for the CO₂ exchange with the land integrated over the entire simulation period in kg C m⁻². The top row (a-c) represents SSP1-2.6 and the bottom row (d-f) represents SSP5-8.5. The left column (a, d) represents the uptake in the control simulations, the middle column (b, e) the uptake in the HOS simulations, and the right column (c, f) the difference between the HOS and CTL simulations. In a, b, d, and e green colors represent net CO₂ uptake by the land, and red colors represent net emissions into the atmosphere.

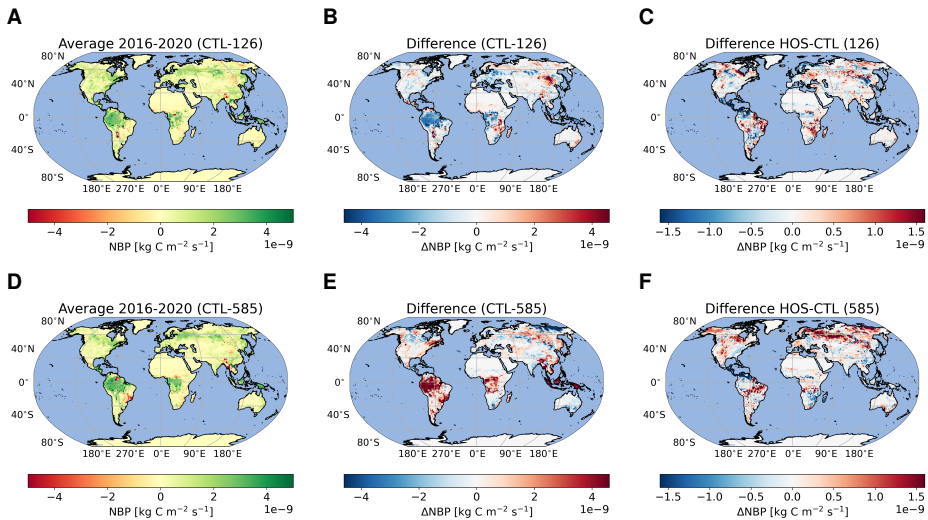


Figure 6.9: Results for Net Biosphere Production (NBP) in kg C m⁻² s⁻¹. Panels represent the same as in Fig. 6.2. Green colors represent uptake of CO₂ into the land and red colors represent emission of CO₂ to the atmosphere.

pCO₂ feedback is small on the global scale, due to competing effects but locally large changes in carbon uptake can occur.

Fig. 6.3.4 gives an overview of the most important climate changes and how the marine and terrestrial respond to these changes. In Fig. 6.3.4c, d the difference between SSP1-2.6 and 5-8.5 is highlighted. In the terrestrial biosphere the prime effect of the AMOC weakening is the southward shift of the GPP maxima in the tropical rainforests (Fig. E.17). Though this could potentially have beneficial effects for the southern regions, it could have detrimental effects for the northern regions (e.g. the Sahel region) and could for example increase the latitudinal extent of the Sahara desert. This shift, caused by a shift in precipitation (Fig. E.1), also has effects for the probability of wildfires (Fig. E.16), which can increase in regions with reduced precipitation. We cannot conclude whether the AMOC weakening would result in a collapse of the Amazonian rainforests or an increase in the Sahara desert since the model is used without a dynamic vegetation model. In the ocean a decrease in NPP (Fig. E.5) and surface nutrient concentrations (Fig. E.10) occurs. The changes in NPP can have effects on the entire food web and thereby have a negative impact on ecosystems and ecosystem functions. If the trend of the surface ocean becoming more depleted of nutrients (Fig. 6.7) continues, this might drive a large decline in NPP for the coming centuries. Another important effect of the AMOC weakening is increased ocean acidification (i.e. a decrease in pH; Fig. E.15). Lower pH values increase the stress on calcifying organisms and reduces the uptake capacity of the ocean, which might increase the AMOC-pCO₂ feedback strength on longer timescales.

In many climate and carbon cycle variables we see a similar response in spatial pattern, but sometimes with a slightly different amplitude (Fig. 6.3.4c, d). In the terrestrial biosphere, the main differences are seen in the boreal forests in Scandinavia and Russia (box 1 in Fig. 6.3.4), and in the Siberian permafrost regions (box 2). The difference in the boreal forests can be explained by looking at the temperature differences between the HOS and CTL simulations. In SSP1-2.6, the northern hemisphere cools more, which causes increased GPP reduction in the boreal forests. For the permafrost region we find a stronger response in SSP5-8.5, because in SSP1-2.6 there is not much permafrost melt in the CTL simulation; therefore the additional cooling in the HOS simulation does not have a large effect on the permafrost melt. In the ocean we find the largest changes in the subpolar North Atlantic and the Arctic sea-ice regions (boxes 7 and 8 in Fig. 6.3.4). In the subpolar region there is a relatively stronger decrease in SST and SSS (Fig. E.6 and E.7) in SSP1-2.6 compared to 5-8.5 leading to a larger increase in solubility of CO₂ and therefore more uptake. Because of the increased cooling, and lower background temperatures in SSP1-2.6, sea-ice cover does not diminish over the simulation whereas in SSP5-8.5 we see in both simulations a strong reduction in sea-ice cover (Fig. E.3). This is the reason why we see a stronger reduction in the Arctic in SSP1-2.6.

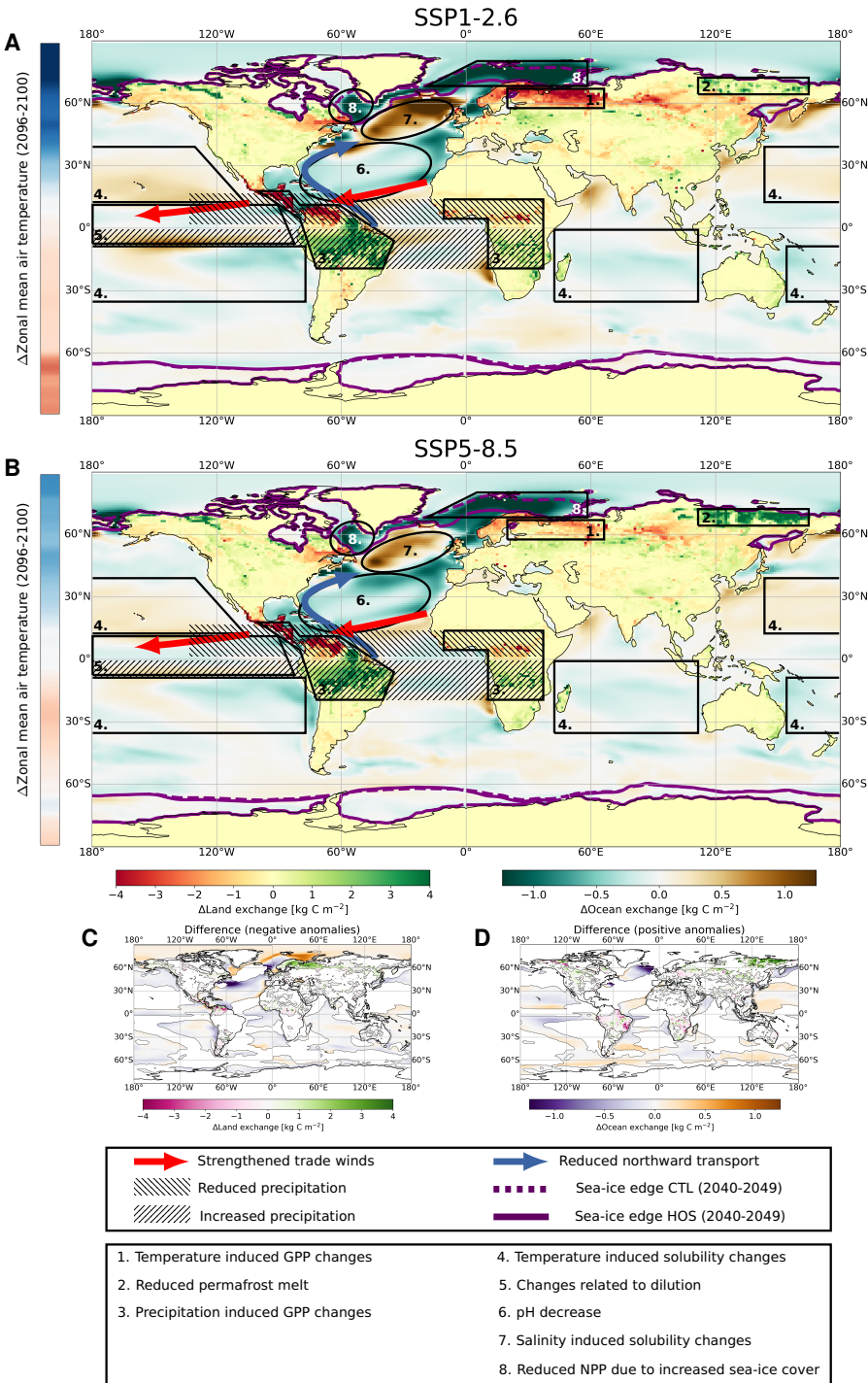


Figure 6.10: Summarizing figure with dominant mechanisms included for SSP1-2.6 (a) and SSP5-8.5 (b). (a) and (b) represent results from HOS minus the CTL simulations. The sea-ice edge is taken as where the ice fraction is 0.25 and denoted by the purple lines, where dashed lines represent the CTL simulations and solid lines the HOS simulations. The bar at the left shows the difference in zonal mean surface air temperature averaged over 2096-2100 between HOS and CTL. The scaling of this bar is between -2.5°C (dark blue) and 2.5°C (dark red). (c) The difference between SSP5-8.5 (b) and SSP1-2.6 (a) for the regions where (b) is negative. Negative values represent a higher negative anomaly in SSP5-8.5 compared to SSP1-2.6. (d) as in (c) but for positive anomalies. Positive values represent a higher positive anomaly in SSP5-8.5 compared to SSP1-2.6. The color bars in (c) and (d) apply to both subfigures.

6.4 Summary and discussion

In this study, we have investigated the carbon cycle response to a weakening of the Atlantic Meridional Overturning Circulation (AMOC) under climate change scenarios. We did this by forcing a state-of-the-art Earth System Model, the Community Earth System Model v2 (CESM2), on a nominal 1° resolution with emissions from two different SSP scenarios (SSP1-2.6 and SSP5-8.5) and an additional freshwater flux in the North Atlantic to artificially decrease the AMOC. To our knowledge, this is the first study that utilizes a model of this high complexity with a horizontal resolution of 1° to study the effects of an AMOC weakening on the carbon cycle. We find a positive feedback in both emission scenarios of 0.44 ppm Sv^{-1} and 1.3 ppm Sv^{-1} for SSP1-2.6 and SSP5-8.5, respectively. The response in SSP1-2.6 is driven by both the land and ocean carbon reservoirs, whereas in SSP5-8.5 it is driven solely by the ocean. The response is small, being the effect of many compensating effects over both the land and the ocean. Looking at regional response patterns, both emission scenarios show similar behavior in many climate and carbon cycle variables. In absolute numbers, the response is stronger in SSP5-8.5, but when the high CO_2 concentrations are taken into account, the relative response is actually weaker in SSP5-8.5 compared to SSP1-2.6.

Our simulations show the climate response to an AMOC weakening, such as a southward shift of the ITCZ and the bipolar seesaw, similar to many previous studies (Obata, 2007; Orihuela-Pinto et al., 2022; Zickfeld et al., 2008). The AMOC weakening in our simulations follows a very similar trajectory as in Orihuela-Pinto et al. (2022), which used an older version of CESM (i.e. v1.2) under pre-industrial boundary conditions. In our study, the AMOC weakening results in a small increase in atmospheric CO_2 concentrations. This small effect, especially on the multi-decadal to centennial timescales assessed here, was also found in more idealized models (e.g. Gottschalk et al., 2019; Nielsen et al., 2019; Zickfeld et al., 2008), but as described in Gottschalk et al. (2019) the relative response of the ocean and land reservoirs are dependent on climatic boundary conditions and the used model. Here, we have used a member of the newest generation of Earth System Models with a relatively high spatial resolution (i.e. nominal $1^{\circ} \times 1^{\circ}$ ocean grid). When considering studies

with induced AMOC weakening we find, integrated over the entire ocean, a similar response as in Zickfeld et al. (2008), and spatially as in Obata (2007), though local differences remain which can be attributed to the use of a higher resolution, and a more complex model in our study. It is also possible to collapse the AMOC without an additional freshwater forcing. In Nielsen et al. (2019) they used such an alternative method under Pleistocene conditions, which resulted in a much slower response in the ocean compared to our simulations. The response of the terrestrial biosphere, especially the changes related to the southward shift of the ITCZ, is also similar to that of previous studies using static vegetation (e.g. Nielsen et al., 2019; Obata, 2007). In Köhler et al. (2005) a dynamic vegetation model is used, and they show that an AMOC collapse affects vegetation type. This leads to reduced carbon storage in the high latitudes and increased carbon storage in the Northern Hemisphere midlatitudes. This dynamic behavior is not captured in our simulations and unfortunately, it is not possible to assess what the effect of dynamic vegetation would be based on Köhler et al. (2005) since they consider Pleistocene conditions. The result that the pattern of the carbon cycle response to an AMOC weakening is independent of the cumulative CO₂ emissions on multi-decadal to centennial timescales has been shown before. In Zickfeld et al. (2008), for example, the marine carbon cycle remains independent on the used emission scenario for the first 200 years of their simulation, and for the terrestrial carbon cycle this is 150 years. After this period the different emissions start to diverge, though the qualitative behavior remains similar. In our simulations, globally integrated variables show little change as a response to the AMOC weakening. However, on regional scales the effects of an AMOC weakening can be large, e.g. SATs can decrease or increase by more than 3 °C locally (Fig. 6.2) and some regions become much drier and other see a large increase in precipitation (Fig. E.1). These changing climate conditions, on top of already greenhouse gas driven climate change, require climate adaptation which might be difficult to achieve in such a short time frame (i.e. decades). The climate changes associated to an AMOC weakening also cause changes in the carbon cycle. Such changes can increase, for example, desertification and reduce (but also increase) crop yields. This may lead locally to increased food stress, potentially leading to more frequent and more severe famines. The changes in the ocean can lead to more frequent marine heatwaves in the Southern Hemisphere due to the warming, and reduced (global) NPP due to changing nutrient distributions, which might impact food web dynamics and ecosystem function. However, due to the cooling effect of the bipolar seesaw we can also expect a (relative) reduction in marine heatwaves in the Northern Hemisphere. These effects show that an AMOC collapse can have local effects that have a beneficiary impact or a detrimental impact on the terrestrial and marine biospheres.

Interestingly, the relative effects on multi-decadal timescales are independent to the (cumulative) greenhouse gas emissions. This means that the uncertainty around the effects of a possible AMOC collapse or weakening is not related to past emissions. However, in a future climate without AMOC weakening, emissions do have an influence on when the AMOC might collapse. Furthermore, the small positive feedback found in this study might make the AMOC more likely to tip earlier. Even though on these timescales the relative effects are not dependent on the greenhouse gas

emissions, this might be different on intermediate (multi-centennial to millennial) timescales. Because the ocean circulation is associated with timescales on the intermediate timescales, we can expect the most important effects to occur in this time frame. We find, for example, that the surface ocean is becoming more depleted of nutrients (Fig. 6.7), which might depress NPP for centuries.

Other long term effects that might be relevant are tipping cascades (e.g. Dekker et al., 2018), meaning that a collapse of the AMOC could set off an other tipping element in the Earth System. In our simulations, we find decreasing temperatures in the Northern Hemisphere due to the AMOC weakening, which reduces the probability of tipping for example melting of the Greenland Ice Sheet, Arctic sea ice, and Northern Hemispheric permafrost. However, due to the bipolar seesaw, the Southern Hemisphere becomes warmer, which might increase the probability of tipping the Antarctic Ice Sheets. Another tipping point connected to the AMOC is the die off of the Amazonian rainforest. Because we do not use a dynamic vegetation model in this study, we cannot investigate whether the AMOC weakening in our simulations would lead to such a die off.

By using a low and a high emission scenario we have tried to cover uncertainties regarding future emissions. However, we have only used one Earth System Model, which means that the results presented here could be model dependent. Especially ocean productivity shows large spread in the CMIP6 ensemble, which can influence the uptake capacity of the ocean. Another bias in Earth System Models is a too stable AMOC, meaning we need a large freshwater flux in the North Atlantic Ocean to weaken the AMOC. This flux is generally too high to represent for example Greenland Ice Sheet melt, but necessary to achieve a weakened AMOC. This large freshwater flux also leads to freshening of the surface ocean in the subpolar gyre which influences the carbonate chemistry and carbon uptake capacity unrealistically. We have not taken this effect into account explicitly, but it could potentially result in reduced uptake capacity of the ocean, and therefore more CO₂ in the atmosphere, increasing the feedback strength.

Finally, we have shown in a relatively high resolution, state-of-the-art Earth System Model, that the spatial pattern of the carbon cycle response to an AMOC weakening is not dependent on cumulative CO₂ emissions. As a follow-up study it would be interesting to see what happens on multi-centennial and longer timescales, and what the pCO₂ response would be under an AMOC recovery. Though not analyzed thoroughly, NPP in the ocean shows large decreases due to the AMOC weakening. This could affect food web dynamics in the ocean with possible (detrimental) changes in fishery yields, food securities and income. These ecosystem and socioeconomic effects are worth investigating, to see how a change in the climate system cascades through ecosystems to socioeconomic systems.

Summary, Conclusion and Outlook

In this thesis we have studied the interactions between the (marine) carbon cycle and the AMOC in the climate system. In this chapter the questions posed in Chapter 1 are answered, and a more general conclusion of the research is given. Lastly, an outlook with possible further research directions is given.

7.1 Summary

In Chapter 1 we posed four specific scientific questions. In this section follows an answer to these questions.

What is the effect of the Atlantic Meridional Overturning Circulation on atmospheric $p\text{CO}_2$ on long timescales?

We have investigated this question by using a carbon cycle box model (SCP-M; Section 2.1) in combination with a bifurcation and continuation software (AUTO-07p; Section 2.3). By using the AMOC strength as control parameter, we were able to determine the steady state solutions versus the AMOC parameter in the SCP-M, and determine the effect of coupling 3, i.e. the effect of changing advection on the carbon cycle, in Fig. 1.8a. On long timescales, the AMOC seems to have a small effect on atmospheric $p\text{CO}_2$. The sign of the relation, i.e. whether an AMOC increase causes an increase or decrease in atmospheric $p\text{CO}_2$ is dependent on the AMOC strength and specific (non-linear) feedbacks in the model. Since the original SCP-M is a linear model, we have included several of these (non-linear) feedbacks in the carbon cycle. The non-linear feedbacks did not have large effects on the AMOC- $p\text{CO}_2$ relation when the AMOC was used as control parameter. From the feedbacks added to the model, a coupling between biological export production and ocean circulation proved to have the most influence on the atmospheric $p\text{CO}_2$ -AMOC relation.

In addition, we have studied how atmospheric $p\text{CO}_2$ responds to changes in different carbon cycle processes (i.e. the piston velocity, biological export production, and the rain ratio) under different AMOC- $p\text{CO}_2$ coupling strengths. The results show that the AMOC- $p\text{CO}_2$ coupling works as a negative feedback in the model making the marine carbon cycle more stable. Another important result was that the ocean circulation seems to be very effective in damping changes in carbon cycle processes.

A large benefit from the continuation software is that we are able to efficiently scan the parameter space for bifurcations. An important finding is that there seems to be no saddle node bifurcations in the marine carbon cycle as modeled here. However, when the coupling between biological export production and atmospheric $p\text{CO}_2$ is large enough, a supercritical Hopf bifurcation can be found when the AMOC strength is varied. The Hopf bifurcation gives rise to an internal oscillation in the carbon cycle with a period between 5000 and 6000 years. The important driver of this oscillation is that both the sink and sources of alkalinity to the ocean are coupled to atmospheric $p\text{CO}_2$ values. As atmospheric $p\text{CO}_2$ increases, the riverine influx of alkalinity increases in the ocean, while the outflux of alkalinity to the sediments decreases due to reduced biological production related to a decreased efficiency of the biological pump. The timescale and mechanism behind this oscillation is related to a process termed the calcium carbonate homeostat. Though the simulated amplitude of the oscillation is too high, the underlying processes can be important for studying

atmospheric $p\text{CO}_2$ variations in past climates, e.g. in the Pleistocene.

How does the marine carbon cycle influence the multiple equilibria window of the Atlantic Meridional Overturning Circulation?

To study this question we have constructed a coupled ocean circulation - carbon cycle box model and implemented it in the same continuation software as the SCP-M. The main difference between the model used to answer this question and the SCP-M is the introduction of a dynamical AMOC that is able to switch between an on-state and an off-state through two saddle node bifurcations. The distance between these two saddle node bifurcations is termed the multiple equilibria window (MEW). In this study we also implemented several (non-linear) feedbacks in the carbon cycle model and couplings between the ocean circulation and the carbon cycle models. The most prominent coupling in this study is a logarithmic relation between atmospheric $p\text{CO}_2$ and net evaporation from the Atlantic Ocean between 30°S and 50°N ($E_s - p\text{CO}_2$ coupling). In this study, we have used an asymmetrical freshwater flux, that redistributes freshwater from the Southern Ocean to the high latitude North Atlantic, as a control parameter. The larger this parameter, the fresher the North Atlantic becomes, which reduces the thermohaline forcing of the AMOC.

We have varied this parameter to determine bifurcation diagrams of the AMOC, and the response of atmospheric $p\text{CO}_2$ to changes in the AMOC strength. As expected, we find that the AMOC has an on- and an off-state in the model with two saddle node bifurcations. Due to the coupling between the AMOC and the carbon cycle, the two saddle nodes are also visible in atmospheric $p\text{CO}_2$ values. The difference between the on- and the off-state varies between 25 and 40 ppm depending on which carbon cycle feedbacks are used. The MEW, i.e. the region in parameter space where the AMOC has multiple equilibria, does not vary a lot for cases with the default total carbon content in the system, since atmospheric $p\text{CO}_2$ changes are not large enough to have a large impact on the hydrological cycle to influence the location of the saddle nodes. However, when we vary the total carbon content in the system, the range of simulated atmospheric $p\text{CO}_2$ values increases. When the atmospheric $p\text{CO}_2$ values at the saddle node change, and the $E_s - p\text{CO}_2$ coupling is used, the MEW also changes. In the model, an increase in total carbon content leads to high atmospheric $p\text{CO}_2$ values which lead to larger net evaporation over the Atlantic. This necessitates a larger asymmetric freshwater forcing to tip the AMOC from the on- to an off-state, and a smaller forcing to go from the off- to the on-state, meaning that both saddle nodes move to increase the MEW. Another effect of increasing the total carbon content is the increase in difference of atmospheric $p\text{CO}_2$ values between the on- and the off-state.

The results can be explained by three mechanisms. (1) We can explain the fact that the off-branch has a lower atmospheric $p\text{CO}_2$ value by looking at how the carbon content of the ocean-atmosphere system changes. Carbon enters the system through a river flux which is linearly proportionate to atmospheric $p\text{CO}_2$ values. Carbon leaves the system through a sediment burial flux which depends on CaCO_3 produc-

tion and dissolution. The CaCO_3 production is coupled to ocean circulation and is larger in the AMOC on-state compared to the off-state. In steady state, the sink and source of carbon need to be equal to each other to keep the total carbon content in the ocean-atmosphere system constant over time. When the AMOC switches from an on- to an off-state, CaCO_3 production decreases, causing a decrease in carbon burial. To balance the decrease in the sink, the source also needs to decrease. This is achieved by lowering atmospheric pCO_2 , explaining the lower pCO_2 values in the off-state. (2) When the $E_s - \text{pCO}_2$ coupling is used, net evaporation over the Atlantic Ocean increases when atmospheric pCO_2 increases, which leads to a shift in the location of the saddle nodes versus the asymmetric freshwater forcing parameter. In the on-state, a higher E_s leads to salinification of the Atlantic thermocline, which due to the salt advection feedback increases the meridional density gradient. This therefore increases the thermohaline forcing of the AMOC and the AMOC itself. To counter this stronger forcing, a larger asymmetrical freshwater flux is necessary to tip the AMOC to an off-state. In the off-state, a larger E_s leads to salinification of the South Atlantic, which decreases the meridional density gradient. To be able to reinvigorate the AMOC, a relatively weaker asymmetric freshwater forcing is necessary to make the North Atlantic more saline. This mechanism explains the movement of the saddle nodes when the $E_s - \text{pCO}_2$ coupling is used. (3) We can explain the increasing difference in atmospheric pCO_2 between the on- and off-state when the total carbon content is increased by the non-linearities present in the carbonate chemistry. For this reason, the higher the total carbon content in the ocean-atmosphere system is, the more sensitive atmospheric pCO_2 is to tipping of the AMOC.

How do climate change induced adjustments in the marine biosphere feed back to atmospheric pCO_2 ?

For studying this question, we have made use of a single member NCAR CESM2 emission driven SSP5-8.5 simulation spanning the period of 2015 to 2100. The SSP5-8.5 scenario is a pessimistic, high emission scenario where atmospheric CO_2 concentration increases to 1100 ppm and global mean surface temperature increases more than 5 K at the end of the 21st century. Besides the strong warming, large changes are found in many other variables. We see, for example, changing wind and precipitation patterns in the atmosphere, and strong changes in sea surface temperatures, mixed layer depth and stratification in the ocean. Furthermore, the AMOC shows a near linear decrease from 18 Sv in 2015 to 9 Sv in 2100; a decrease of 50 %.

The changes in these variables also impact the marine carbon cycle. Looking at the gas exchange of CO_2 between the atmosphere and ocean, we see that almost all regions take up more carbon at the end of the century compared to the beginning, and of the regions that show a CO_2 flux from the ocean to the atmosphere, only the East Equatorial Pacific remains, albeit much reduced in strength. The subpolar North Atlantic Ocean is the only region that does not follow this trend. While atmospheric pCO_2 almost triples over the simulation, this specific region takes up less carbon at the end of the century compared to 2015. The subpolar North Atlantic Ocean has deep convection regions in CESM2 which are much reduced over the simulation. This reduced mixing over the water column has two important carbon cycle conse-

quences: (1) less DIC is transported from the surface ocean to the subsurface ocean through the ocean circulation, and (2) less nutrients from the nutrient rich subsurface are mixed upwards. In answering this question, we have specifically looked at the effect of the reduced nutrient influx on the marine biology in the model.

The Net Primary Production (NPP) and Export Production at 100 m (EP) both decrease over the course of the simulation. By looking at the e-ratio (EP divided by NPP), we see that the EP decreases more than NPP showing that the biological pump becomes less effective in transporting carbon from the surface ocean to the subsurface ocean. The subpolar region in 2015 is dominated by diatoms, while there is little small phytoplankton biomass, and no diazotroph biomass due to temperature limitations. Over the course of the simulation, diatom biomass sharply decreases, and they are partly replaced by small phytoplankton. This explains why EP decreases more than NPP, because the diatoms are more efficient in transporting carbon to the subsurface ocean. Diatom biomass decreases due to increased advection of biomass out of the subpolar region in combination with an increase in nutrient limitation. As diatom biomass decreases, small phytoplankton light limitation is lifted. Even though the small phytoplankton also see increased nutrient limitation, they are still able to increase their biomass since the light-nutrient co-limitation is lifted due to the decreased light limitation.

Next we wanted to know what the effect of this phytoplankton composition shift was on atmospheric $p\text{CO}_2$. For this we used the SCP-M forced with CESM2 output. Using the SCP-M we found a positive feedback in the system where the subpolar North Atlantic Ocean takes up 60 GtCO_2 less per $^\circ\text{C}$ of warming. This atmospheric $p\text{CO}_2$ - phytoplankton feedback accounts for approximately 29% and 12% of the 1.5 K and 2 K safe carbon budgets, decreasing the amount of carbon that can still be emitted to remain below 1.5 and 2 K warming compared to the pre-industrial.

What is the carbon cycle response to a strong AMOC weakening under low and high emission scenarios?

This question is similar to the first question, but here we specifically look to the effect of the AMOC on atmospheric $p\text{CO}_2$ on shorter timescales under anthropogenic climate change. We have used the IMAU CESM2 simulations to study this (Section 2.4.5). We make use of the low emission scenario SSP1-2.6, and the high emission scenario SSP5-8.5, both spanning 2015 to 2100. For each emission scenario there is a control simulation and a hosing simulation. In the control simulation, the model is forced with just the emissions, and in the hosing simulations, the model is forced with the same emissions and also an artificial freshwater forcing in the North Atlantic Ocean between 50°N and 70°N with the intended purpose to strongly weaken the AMOC. In all simulations, a climate change signal is present, and we can extract the signal from the additional AMOC weakening by subtracting the control simulations from the hosing simulations.

In both emission scenarios we see changes in climatic variables. We see, for example, increases in CO_2 concentrations, global warming, changes in wind and precipitation

patterns, and changes in sea-ice cover. The extent and amplitude of these changes do depend on the emission scenario. The low emission scenario sees for example a small increase in CO₂ concentrations to 430 ppm in 2100, accompanied by a warming of 1 K. In the high emission scenario these are 1100 ppm and more than 5 K. This difference also influences other climatic variables. In both emission scenarios the AMOC also decreases from about 17 Sv in 2015 to 9 and 7 Sv in 2100 for the low and high emission scenario, respectively.

In the high emission scenario, the ocean takes up more carbon over the course of the simulation. On the land, generally the gross primary production (GPP) increases due to the CO₂ fertilization effect. Due to changes in precipitation patterns, the patterns in GPP can shift, and warming causes increased soil respiration related to permafrost melt in the Northern Hemispheric high latitudes. In the low emission scenario, the ocean takes up less carbon at the end of the century compared to 2015. However, the pattern on the land is quite similar but less strong.

In the hosing simulations we see similar changes as in the control simulations. An important difference, however, is that the AMOC weakening is much faster and stronger. At the end of the century the AMOC is approximately 4 Sv with most of the weakening happening in the first 30 years of the simulation. This weaker AMOC influences some of the changes seen in the control simulations. Compared to the control simulations, the hosing simulations see, for example, cooling in the Northern Hemisphere in the low emission scenario and reduced warming in the high emission scenario, while the Southern Hemisphere sees increased warming in both scenarios. The Northern Hemispheric trade winds increase, and the ITCZ sees a stronger southward shift. Due to the cooling or reduced warming in the northern hemisphere, Arctic sea-ice cover increases compared to the control simulations.

The climatic changes due to the weakening of the AMOC influence both the marine and terrestrial carbon cycle, which causes an increase in atmospheric pCO₂ in both emission scenarios. However, this increase is relatively small, i.e. 2.6 and 4.2 ppm on absolute concentrations of 432 and 1094 ppm for the low and high emission scenarios. In the low emission scenario, the additional carbon in the atmosphere comes from both the land and the ocean, whereas for the high emission scenario it is only coming from the ocean. Upon further investigation, it appears that this small net response is the result of larger compensating effects in both the marine and terrestrial biosphere. Locally, the changes can be quite large in the carbon exchange with the atmosphere. Around the equator, we see for example that on the land the uptake decreases north of the equator, but increases south of the equator following the southward shift of the ITCZ. In the Northern Hemispheric high latitudes, we see a reduction in soil respiration due to reduced permafrost melt, but at the same time boreal forests become less productive due to the cooler temperatures. Also in the ocean we see many compensating effects. Due to temperature related solubility changes the North Pacific takes up more carbon, whereas the South Pacific and Indian Ocean take up less. By far the largest changes are observed in the Arctic and Atlantic Ocean. Due to increased sea-ice cover, the Arctic Ocean takes up less

carbon. Due to salinity and temperature related solubility changes, the subpolar North Atlantic takes up more carbon. And due to reduced pH related to reduced northward advection of important carbon cycle tracers, the subtropical North Atlantic Ocean takes up less. This pattern is very similar for the low and high emission scenario and only the local amplitude is different.

The compensating effects result in a potential positive feedback in the system. Atmospheric $p\text{CO}_2$ increases by 0.45 and 1.3 ppm for an AMOC decrease of 1 Sv for the low and high emission scenario, respectively. This is termed a positive feedback, since for future climate change, increasing atmospheric $p\text{CO}_2$ values are associated with a weakening of the AMOC. Interestingly, the spatial pattern of the carbon cycle response seems to be relatively independent of cumulative greenhouse gas emissions. Although the global response is small, locally large changes can occur in both climatic and carbon cycle variables that are too large and too fast to be able to adapt to. This means that an AMOC collapse could be a threat for society and ecosystems.

7.2 Conclusion

For this thesis there were two main issues of interests: (1) the existence of tipping behavior in the carbon cycle, and (2) the interactions between the carbon cycle and the AMOC.

In the models we have used, we did not find tipping behavior in the carbon cycle. One of the reasons could be that the models are too linear to show such behavior. However, even after including non-linear feedbacks, we did not find tipping behavior suggesting that past climate transitions are not likely to be caused by fast transitions in the carbon cycle. We did find an internal oscillation in the marine carbon cycle related to the calcium carbonate homeostat with a period of 5,000 to 6,000 years.

On long timescales, we saw that the AMOC hardly affects atmospheric $p\text{CO}_2$, suggesting that the AMOC is not important in determining atmospheric $p\text{CO}_2$ values on these timescales. We did find that the marine carbon cycle can influence the multiple equilibria window of the AMOC due to a coupling between CO_2 and freshwater forcing. However, also these effects are quite small.

Under climate change, we saw that the marine carbon cycle has feedbacks that can have a large gross impact, and that an AMOC weakening can have large local effects on the climate system and the carbon cycle. However, the net effect, especially globally, is often very small. We can explain this by compensating feedbacks in the carbon cycle itself, and compensating effects between different regions. When we look specifically at the effects of an AMOC weakening, these seem to be relatively independent of cumulative emissions on multi-decadal timescales. This implies that the trajectory of the carbon cycle response to an AMOC collapse is set on this timescale.

In the models used here, we find that interactions between AMOC and carbon cycle

seem limited on a global scale. In the box models this might be because models are very simple and approximately linear, decreasing the AMOC-pCO₂ sensitivity, while in the Earth System Model it is caused by regionally compensating effects.

7.3 Outlook

The research conducted for this thesis has its limitations, and led to new questions, which opens doors for further research.

Over the last years, computational resources have increased making it possible to do more, more complex, and higher resolution model simulations. This increase in computational resources is especially relevant for models using active ocean biogeochemistry since this is an expensive module in current Earth System Models. Even though a lot of progress has been made over the past decades, computational resources are still a large limitation. When more resources become available, this opens possibilities for further research.

For example, the ESM used in this study has a nominal 1° by 1° ocean grid, and currently there are some models that run on an eddy permitting 0.25° grid (Séférian et al., 2020). Studies with eddy resolving models (i.e. 0.1° grid) without ocean biogeochemistry show that the resolution has large effect on ocean currents. It does not only change the local ocean state, but it also changes the mean ocean state and reduces biases (Chassignet & Xu, 2021; Huck et al., 2015). These type of models are currently too expensive to run on a global scale and on timescales necessary for CMIP simulations when ocean biogeochemistry is used, even though we know that eddies can also play an important role in ocean biogeochemistry (McGillicuddy, 2016). When computational resources are available to conduct studies as performed in this thesis but on an eddy resolving resolution, it can provide valuable additional insights.

Currently, the marine ecosystem module of ESMs is often quite simple with only a few phyto- and zooplankton groups. Several models are currently being developed with more complex, trait-based plankton models that include more groups (see e.g. Le Gland et al., 2021; Negrete-García et al., 2022). It is also possible to couple the ESM output to global marine ecosystem models (MEMs; see e.g. Tittensor et al., 2021). The development of these MEMs is now a very active field. These MEMs might provide a more realistic result on ecosystem function such as carbon export to the deep ocean, which can influence the climate system through the CO₂ uptake capacity of the ocean. Both the MEMs and the more complex plankton models can add value to the current generation of ESMs and might provide insight in key feedback mechanisms in the marine carbon cycle that we were unable to study for this thesis. However, just as with the higher resolution, computational resources might be a limiting factor in increasing the complexity of the ecosystem modules.

The model simulations used here are only from one ESM and per simulation we only

have one ensemble member. This is an important limitation of these studies since the mechanisms we have shown in this thesis can be model dependent. It would therefore add value to perform these simulations with more models, and to include more ensemble members per model simulation. However, again this is limited by computational resources and might require a community based approach.

One of the reasons not many suitable model simulations are available is that in CMIP6 most models have been used in a concentration driven mode. This means that important feedbacks in the carbon cycle between the ocean and the atmosphere, and the atmosphere and the land are not taken into account. For this reason we have used emission driven simulations which do take these feedbacks into account. Fortunately, at the time of writing, the next CMIP phase, CMIP7, will probably change the protocols to make emission driven simulations the standard making it possible to study carbon cycle feedbacks with more models in more detail.

An important narrative in this thesis is based on timescales. We have looked at multi-decadal to centennial timescales with ESMs and at long timescales with box models. This means we did not capture the centennial to millennial timescales with our ESM simulations. Since the ocean is the most dominant component on these timescales, a good addition to the work done in this thesis is to study the marine carbon cycle on these timescales, especially under climate change. The response of the marine carbon cycle to the AMOC weakening might increase on longer timescales due to for example nutrient trapping in the deep ocean or the Southern Ocean (Moore et al., 2018). Not only can this affect the CO₂ uptake capacity of the ocean, it might also deprive phytoplankton of nutrients potentially affecting whole marine ecosystems.

Lastly, the marine carbon cycle did not show any tipping behavior in the models used here. This implies that the marine carbon cycle is a stable system that is resilient to changes. It might be interesting to further investigate the resilience of the marine carbon cycle and the most important mechanisms present there. This might especially be important for studying past climates.

SCP-M parameter values

A.1 Parameter values

In this appendix values and descriptions of the parameters in the extended SCP-M as used in Chapter 3 are given. In Tables A.1 to A.3 the parameter values used in the model are presented. The values presented here are for the pre-industrial configuration. The parameter values that are different in the Last Glacial Maximum configuration are presented in Table 2.1. All parameter values, except the biological efficiency (ϵ) parameters, are taken from the SCP-M. In Table A.4 we also present the literature where the expressions for the equilibrium constants were taken from.

Table A.1: Symbol (column 1), description (column 2), value (column 3), and units (column 4) of the general parameters used in the model.

Symbol	Description	Value	Units
V_{at}	Volume of the atmosphere	1.76×10^{20}	m^3
ρ	Sea water density	1029	kg m^{-3}
$F_{Ca,base}$	Base rain ratio	0.07	-
n	Order of CaCO_3 dissolution kinetics	1	-
P_C	Mass percentage of C in CaCO_3	0.12	-
D_{Ca}	Constant dissolution rate of CaCO_3	2.75×10^{-13}	$\text{mol m}^{-3} \text{s}^{-1}$
W_{SC}	Constant silicate weathering	2.4×10^{-12}	$\text{mol m}^{-3} \text{s}^{-1}$
W_{SV}	Variable silicate weathering parameter	1.6×10^{-8}	$\text{mol m}^{-3} \text{atm}^{-1} \text{s}^{-1}$
W_{CV}	Variable carbonate weathering parameter	6.3×10^{-8}	$\text{mol m}^{-3} \text{atm}^{-1} \text{s}^{-1}$
k_{CaCO_3}	Constant CaCO_3 dissolution rate	4.4×10^{-6}	s^{-1}
R_{PO_4}	River influx of PO_4^{3-}	1.5×10^4	
b	Exponent in Martin's law	0.75	-
d_0	Reference depth for biological productivity	100	m
α	Fraction of the GOC that flows through Box 7	0.5	-
γ_1	Bidirectional mixing between Box 4 and 6	29	Sv
γ_2	Bidirectional mixing between Box 1 and 3	40	Sv
ψ_1	General overturning circulation	29	Sv
$\psi_{2,base}$	Base value of the Atlantic Meridional Overturning Circulation	19	Sv
$k_{w,base}$	Base piston velocity	3	m/day
$R_{C:P}$	Redfield C:P ratio	130	mol C/mol P
$R_{P:C}$	Redfield P:C ratio	1/130	mol P/mol C

Table A.2: Symbol (column 1), description (column 2), value (column 3), and units (column 4) of parameters concerning the dimensions of the boxes used in the model.

Symbol	Description	Value	Units
V_1	Volume of Box 1	2.71425×10^{16}	m^3
V_2	Volume of Box 2	9.0475×10^{15}	m^3
V_3	Volume of Box 3	2.442825×10^{17}	m^3
V_4	Volume of Box 4	5.699925×10^{17}	m^3
V_5	Volume of Box 5	4.523750×10^{16}	m^3
V_6	Volume of Box 6	5.4285×10^{17}	m^3
V_7	Volume of Box 7	9.0475×10^{15}	m^3
A_1	Surface area Box 1	2.71425×10^{14}	m^2
A_2	Surface area Box 2	3.619×10^{13}	m^2
A_3	Surface area Box 3	2.71425×10^{14}	m^2
A_4	Surface area Box 4	3.43805×10^{14}	m^2
A_5	Surface area Box 5	1.8095×10^{13}	m^2
A_6	Surface area Box 6	3.619×10^{14}	m^2
A_7	Surface area Box 7	3.619×10^{13}	m^2
d_{f1}	Floor depth Box 1	100	m
d_{f2}	Floor depth Box 2	250	m
d_{f3}	Floor depth Box 3	1000	m
d_{f4}	Floor depth Box 4	2500	m
d_{f5}	Floor depth Box 5	2500	m
d_{f6}	Floor depth Box 6	4000	m
d_{f7}	Floor depth Box 7	250	m
d_{c3}	Ceiling depth Box 3	100	m
$d_{c4,1}$	Ceiling depth Box 4 (below Boxes 2 and 7)	250	m
$d_{c4,2}$	Ceiling depth Box 4 (below Box 3)	1000	m
d_{c6}	Ceiling depth Box 6	2500	m

Table A.3: Symbol (column 1), description (column 2), value (column 3), and units (column 4) of the other parameters used in the model.

Symbol	Description	Value	Units
$Z_{1,base}$	Base biological production Box 1	1.1	$\text{mol C m}^{-2} \text{ yr}^{-1}$
$Z_{2,base}$	Base biological production Box 2	4.5	$\text{mol C m}^{-2} \text{ yr}^{-1}$
$Z_{5,base}$	Base biological production Box 5	1.75	$\text{mol C m}^{-2} \text{ yr}^{-1}$
$Z_{7,base}$	Base biological production Box 7	5.325	$\text{mol C m}^{-2} \text{ yr}^{-1}$
$\epsilon_{1,base}$	Base biological efficiency Box 1	0.9	-
$\epsilon_{2,base}$	Base biological efficiency Box 2	1.25	-
$\epsilon_{5,base}$	Base biological efficiency Box 5	0.35	-
$\epsilon_{7,base}$	Base biological efficiency Box 7	0.62	-
$T_{1,base}$	Base temperature Box 1	23.34	$^{\circ}\text{C}$
$T_{2,base}$	Base temperature Box 2	9.1	$^{\circ}\text{C}$
T_3	Temperature Box 3	11.28	$^{\circ}\text{C}$
T_4	Temperature Box 4	3.24	$^{\circ}\text{C}$
$T_{5,base}$	Base temperature Box 5	0.93	$^{\circ}\text{C}$
T_6	Temperature Box 6	1.8	$^{\circ}\text{C}$
$T_{7,base}$	Base temperature Box 7	5.83	$^{\circ}\text{C}$
S_1	Salinity Box 1	35.25	g kg^{-1}
S_2	Salinity Box 2	34.27	g kg^{-1}
S_3	Salinity Box 3	34.91	g kg^{-1}
S_4	Salinity Box 4	34.76	g kg^{-1}
S_5	Salinity Box 5	34.43	g kg^{-1}
S_6	Salinity Box 6	34.77	g kg^{-1}
S_7	Salinity Box 7	34.17	g kg^{-1}
$[Ca]_1$	Calcium concentration Box 1	10.96	mol m^{-3}
$[Ca]_2$	Calcium concentration Box 2	10.66	mol m^{-3}
$[Ca]_3$	Calcium concentration Box 3	10.55	mol m^{-3}
$[Ca]_4$	Calcium concentration Box 4	10.51	mol m^{-3}
$[Ca]_5$	Calcium concentration Box 5	10.71	mol m^{-3}
$[Ca]_6$	Calcium concentration Box 6	10.51	mol m^{-3}
$[Ca]_7$	Calcium concentration Box 7	10.63	mol m^{-3}

Table A.4: The symbols and description of the equilibrium constants are presented in the first two columns. The third column presents the source of the used expression.

Symbol	Description	Expression
K_0	Solubility constant	Weiss, 1974
K_1	First dissociation constant of carbonic acid	Lueker et al. (2000)
K_2	Second dissociation constant of carbonic acid	Lueker et al. (2000)
$K_{sp,base}$	Equilibrium constant for CaCO_3 dissolution	Mucci (1983)
$K_{sp,press}$	Pressure correction for $K_{sp,base}$	Millero (1983)

Parameter values and model equations for the coupled carbon cycle - ocean circulation box model

B.1 Additional couplings, feedbacks and simulations

Besides the couplings and feedbacks presented in the main text we have introduced one additional coupling and two additional feedbacks to the carbon cycle. A summary of these cases and the results can be seen in Table B.1 and Fig. B.1. The main effects of these additional coupling and feedbacks is a shift in atmospheric $p\text{CO}_2$ values on the on-branch for cases with the piston velocity feedback (Eq. (B.3) and (B.4)). This shift is larger when also the climate sensitivity feedback is used. A description of the additional coupling and feedbacks is given below.

The additional coupling we have introduced is the addition of dilution fluxes for both DIC and Alk related to the freshwater fluxes E_s and E_a (Eq. B.1). Increasing the concentrations of DIC and Alk due to evaporation and decreasing the concentrations due to a net influx of freshwater at the surface.

$$C_{dil,i} = \lambda_D \times (E_s + E_a) \times \frac{C_i}{V_i} \quad (\text{B.1})$$

Where C_i is the tracer concentration in box i and V_i the volume, and λ_D is a parameter that determines whether the coupling is used ($\lambda_D = 1$) or not ($\lambda_D = 0$). The

dilutive fluxes for Alk are modeled in a similar fashion.

A first additional feedback we introduce is a linear temperature dependency in the biological efficiency (Eq. B.2) which was introduced in the biological coupling. Under an SST increase, the efficiency will decrease following

$$\epsilon_i = (\lambda_\epsilon \times -0.1\Delta T) + \epsilon_{i,base} \quad (\text{B.2})$$

For this feedback it is necessary to also use the climate sensitivity feedback and the strength can be regulated with λ_ϵ .

The second additional feedback allows the piston velocity (k_w) to vary with the SSTs (Eq. B.3). When the climate sensitivity feedback is used, this also affects the piston velocity. The temperature dependency is introduced by making the piston velocity a function of the Schmidt number (Eq. B.4) following

$$k_{w,i} = (1 - \lambda_P) \times k_{w,ibase} + \lambda_P k_{w,ibase} \times \left(\frac{Sc_i}{660}\right)^{-0.5} \quad (\text{B.3})$$

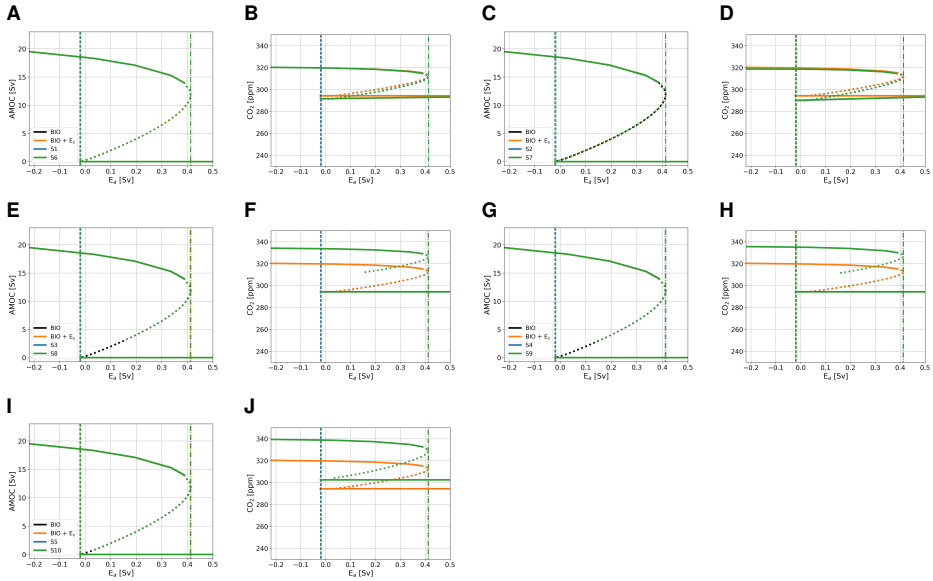
Where

$$Sc_i = 2116.8 - 136.25T_i + 4.7353T_i^2 - 0.092307T_i^3 + 0.0007555T_i^4 \quad (\text{B.4})$$

In this case the feedback can either be switched on ($\lambda_P = 1$) or off ($\lambda_P = 0$). Without this feedback the piston velocity is similar for all boxes, but with this feedback the piston velocity will differ per box.

Table B.1: Additional cases not included in the main text using additional feedbacks as described in this document. Results of these cases can be seen in Fig. B.1.

Notation	S-1	S-2	S-3	S-4	S-5	S-6	S-7	S-8	S-9	S-10
λ_{BI}	1	1	1	1	1	1	1	1	1	1
λ_T	1	0	0	1	1	1	0	0	1	1
λ_P	0	0	1	1	1	0	0	1	1	1
λ_D	0	1	0	0	0	0	1	0	0	0
λ_ϵ	0	0	0	0	1	0	0	0	0	1
λ_E	0	0	0	0	0	1	1	1	1	1



B

Figure B.1: Bifurcation diagrams showing the sensitivity of the model to E_a for additional cases as defined in Table B.1. Solid lines represent stable steady state solutions, dotted lines represent unstable states, dash-dotted lines represent the location of the saddle node on the on-branch, and dashed lines the location of the saddle node on the off-branch. The black lines represent a case with only the biological coupling (BIO), the orange lines with the logarithmic CMP6 based E_s and biological coupling ($E_s + \text{BIO}$), and the blue and green lines represent the cases defined in Table B.1. Results are for the AMOC strength in Sv (a, c, e, g, i) and atmospheric pCO_2 in ppm (b, d, f, h, j).

B.2 Model parameters

The model parameters are presented in Tables B.2 to B.4. For several carbon cycle parameters, the values shown in Appendix A are used.

Table B.2: Symbol (column 1), description (column 2), value (column 3), and units (column 4) of the general parameters used in the ocean circulation model based on (Cimatoribus et al., 2014).

Symbol	Description	Value	Units
$V_{0,A}$	Total volume of the Atlantic basin	3×10^{17}	m^3
V_n	Volume of box n	3×10^{15}	m^3
V_s	Volume of box s	9×10^{15}	m^3
A_t	Surface area box t	1×10^{14}	m^2
L_{xA}	Zonal extent of the South Atlantic Ocean	1×10^7	m
L_y	Meridional extent of the frontal region of the Southern Ocean	1×10^6	m
L_{xS}	Zonal extent of the Southern Ocean	3×10^7	m
τ	Average zonal wind stress amplitude	0.1	N m^{-2}
A_{GM}	Eddy diffusivity	1700	$\text{m}^2 \text{s}^{-1}$
f_S	Coriolis parameter	-1×10^{-4}	s^{-1}
ρ_0	Reference density	1027.5	kg m^{-3}
κ	Vertical diffusivity	1×10^{-5}	$\text{m}^2 \text{s}^{-1}$
S_0	Reference salinity	35	g/kg
T_0	Reference temperature	5	$^{\circ}\text{C}$
$T_{n,base}$	Base temperature box n	5	$^{\circ}\text{C}$
$T_{ts,base}$	Base temperature box ts	10	$^{\circ}\text{C}$
η	Hydraulic constant	3×10^4	m s^{-1}
α	Thermal expansion coefficient	2×10^{-4}	K^{-1}
β	Haline contraction coefficient	8×10^{-4}	$(\text{g/kg})^{-1}$
r_S	Transport by the southern subtropical gyre	10×10^6	$\text{m}^3 \text{s}^{-1}$
r_N	Transport by the northern subtropical gyre	5×10^6	$\text{m}^3 \text{s}^{-1}$

Table B.3: Symbol (column 1), description (column 2), value (column 3), and units (column 4) of the general parameters used in the ocean circulation model added or changed with respect to (Cimatoribus et al., 2014).

Symbol	Description	Value	Units
E_s	Symmetric freshwater flux	0.39×10^6	$\text{m}^3 \text{s}^{-1}$
E_p	Freshwater flux from box ps to box s	0.99×10^6	$\text{m}^3 \text{s}^{-1}$
V_0	Total volume of the ocean	1.5×10^{18}	m^3
V_{ps}	Volume Box ps	9×10^{16}	m^3
V_{pd}	Volume Box pd	1.11×10^{18}	m^3
d_{ps}	Depth Box ps	300	m
d_{fn}	Floor depth Box n	300	m
d_{ft}	Floor depth Box t	variable (D)	m
d_{fts}	Floor depth Box ts	variable (D)	m
d_{fs}	Floor depth Box s	300	m
d_{fd}	Floor depth Box d	4000	m
$T_{t,base}$	Base temperature Box t	23.44	$^{\circ}\text{C}$
$T_{s,base}$	Base temperature Box s	0.93	$^{\circ}\text{C}$
T_d	Temperature Box d	1.8	$^{\circ}\text{C}$
T_{ps}	Temperature Box ps	23.44	$^{\circ}\text{C}$
T_{pd}	Temperature Box pd	1.8	$^{\circ}\text{C}$
r_P	Transport by the subtropical gyre between box s and ps	90×10^6	$\text{m}^3 \text{s}^{-1}$

Table B.4: Symbol (column 1), description (column 2), value (column 3), and units (column 4) of the parameters used in the carbon cycle model that have been changed compared to Chapter 3.

Symbol	Description	Value	Units
$Z_{n,base}$	Base biological production Box n	1.9	$\text{mol C m}^{-2} \text{yr}^{-1}$
$Z_{t,base}$	Base biological production Box t	2.1	$\text{mol C m}^{-2} \text{yr}^{-1}$
$Z_{ts,base}$	Base biological production Box ts	2.1	$\text{mol C m}^{-2} \text{yr}^{-1}$
$Z_{s,base}$	Base biological production Box s	1.1	$\text{mol C m}^{-2} \text{yr}^{-1}$
$\epsilon_{n,base}$	Base biological efficiency Box n	0.1	-
$\epsilon_{t,base}$	Base biological efficiency Box t	0.5	-
$\epsilon_{ts,base}$	Base biological efficiency Box ts	0.3	-
$\epsilon_{s,base}$	Base biological efficiency Box s	0.1	-
$F_{Ca,base}$	Base rain ratio	0.15	-
$pCO_{2,0}$	Base atmospheric pCO_2 value	320	ppm

B.3 Model equations

There are in total 30 state variables: salinity, DIC, alkalinity, and PO_4^{3-} in the 7 boxes, the pycnocline depth D , and atmospheric pCO_2 . The state variables in the deep Atlantic box are determined using conservation laws. The salinity equations are given by Eq. (B.5)-(B.10), the conservation of salt in the model is given by Eq. (B.12), and the pycnocline depth is determined using Eq. (B.11). The volume fluxes are determined using Eq. (B.13) to (B.17), and the equation of state is given by Eq. (B.18). The equations for the carbon cycle model are given by Eq. (B.19) to Eq. (B.23).

$$\frac{d(V_t S_t)}{dt} = q_S(\theta(q_S)S_{ts} + \theta(-q_S)S_t + q_U S_d - \theta(q_N)q_N S_t + r_s(S_{ts} - S_t) + r_N(S_n - S_t) + 2E_s S_0 \quad (\text{B.5})$$

$$\frac{d(V_{ts} S_{ts})}{dt} = q_{Ek} S_s - q_e S_{ts} - q_S(\theta(q_S)S_{ts} + \theta(-q_S)S_t) + r_S(S_t - S_{ts}) \quad (\text{B.6})$$

$$V_n \frac{dS_n}{dt} = \theta(q_N)q_N(S_t - S_n) + r_N(S_t - S_n) - (E_s + E_a)S_0 \quad (\text{B.7})$$

$$V_s \frac{dS_s}{dt} = q_S(\theta(q_S)S_d + \theta(-q_S)S_s) + q_e S_{ts} - q_{Ek} S_s - (E_p + E_s - E_a)S_0 + (r_P + \psi_1)(S_{ps} - S_s) \quad (\text{B.8})$$

$$V_{ps} \frac{dS_{ps}}{dt} = (\gamma_1 + \psi_1) * (S_{pd} - S_{ps}) + (r_P * (S_s - S_{ps})) + E_p \quad (\text{B.9})$$

$$V_{pd} \frac{dS_{pd}}{dt} = \gamma_1 * (S_{ps} - S_{pd}) + \psi_1(S_d - S_{pd}) \quad (\text{B.10})$$

$$\left(A + \frac{L_{xA}L_y}{2}\right) \frac{dD}{dt} = q_U + q_{Ek} - q_e - \theta(q_N)q_N \quad (\text{B.11})$$

$$S_0 V_0 = V_n S_n + V_d S_d + V_t S_t + V_{ts} S_{ts} + V_s S_s + V_{ps} S_{ps} + V_{pd} S_{pd} \quad (\text{B.12})$$

Where θ is a step function which takes a value of 1 for a positive argument, and takes a value of 0 for a negative argument. The volume fluxes are given by:

$$q_{Ek} = \frac{\tau L_{xS}}{\rho_0 |f_S|} \quad (\text{B.13})$$

$$q_e = A_{GM} \frac{L_{xA}}{L_y} D \quad (\text{B.14})$$

$$q_U = \frac{\kappa A}{D} \quad (\text{B.15})$$

$$q_N = \eta \frac{\rho_n - \rho_{ts}}{\rho_0} D^2 \quad (\text{B.16})$$

$$q_S = q_{Ek} - q_e \quad (\text{B.17})$$

$$\rho_i = \rho_0(1 - \alpha(T_i - T_0) + \beta(S_i - S_0)) \quad (\text{B.18})$$

Where i represents any box.

The carbon cycle equations are given by Eq. (B.19) to Eq. (B.23). The different fluxes are determined using Eq. (B.24) to Eq. (B.31).

$$\frac{d[DIC]_i}{dt} = C_{phys,i} + C_{bio,i} + C_{carb,i} + C_{air,i} + C_{river,t} \quad (\text{B.19})$$

$$\frac{d[Alk]_i}{dt} = A_{phys,i} + A_{carb,i} + A_{river,t} \quad (\text{B.20})$$

$$\frac{d[PO_4^{3-}]_i}{dt} = P_{phys,i} + P_{bio,i} + P_{river,t} \quad (\text{B.21})$$

$$\frac{dC_{tot}}{dt} = C_{river,t} \times V_t + \sum_{i=1}^5 (C_{carb,i} V_i) + \sum_{i=1}^5 (C_{bio,i} V_i) \quad (\text{B.22})$$

$$\frac{dAlk_{tot}}{dt} = Alk_{river,t} \times V_t + Alk_{river,ps} \times V_{ps} + \sum_{i=1}^7 (Alk_{carb,i} V_i) \quad (\text{B.23})$$

In these equations the different terms represent advective fluxes (X_{phys}), biological fluxes (X_{bio}), carbonate fluxes (X_{carb}), air-sea gas exchange (C_{air}) and the river influx (X_{river}). From these fluxes, C_{air} only acts on the surface boxes, and X_{river} only on box t and box ps . X_{phys} is determined following:

$$X_{phys,i} = \frac{1}{V_i} \left(\sum_{i=1} (q_{j \rightarrow i} \times X_j) - \sum_{i=1} (q_{i \rightarrow j} \times X_i) \right) \quad (\text{B.24})$$

This equation represents that the concentration of tracer X changes through an advective flux flowing out of box i to box j ($q_{i \rightarrow j}$ times the concentration in box i (X_i), and a flux flowing into box i from box j ($q_{j \rightarrow i}$) times the concentration in box j (X_j). There can be fluxes from multiple boxes into one box.

$$C_{air,i} = \frac{K_{0,i} \times k_{w,i} \times \rho_0 \times (CO_2^{atm} - pCO_{2,i})}{V_i} \quad (\text{B.25})$$

For i is n , t , ts , s or ps . K_0 is the solubility constant, k_w the piston velocity, CO_2^{atm} the atmospheric CO_2 concentration, pCO_2 the partial pressure of CO_2 in the ocean and V the volume of the ocean box.

$$C_{carb,i} = -\frac{Z_i \times A_i \times F_{Ca,i}}{V_i} + ([CO_3^{2-}]_i [Ca^{2+}]_i) \rho_0 \times k_{Ca} \left(1 - \frac{([CO_3^{2-}]_i [Ca^{2+}]_i)}{K_{sp,i}}\right)^n \times PerC + DC \quad (B.26)$$

For i is n , t , ts , s or ps . Z represent biological production, A the surface area of the box, F_{Ca} the rain ratio and V the volume. Other variables are the carbonate ion concentration ($[CO_3^{2-}]$), calcium concentration ($[Ca^{2+}]$), and equilibrium constant for $CaCO_3$ dissolution (K_{sp}).

For box pd the carbonate flux is determined following

$$C_{carb,i} = ([CO_3^{2-}]_{pd} [Ca^{2+}]_{pd}) \rho_0 k_{Ca} \left(1 - \frac{([CO_3^{2-}]_{pd} [Ca^{2+}]_{pd})}{K_{sp,pd}}\right)^n PerC + ([CO_3^{2-}]_{pd} [Ca^{2+}]_{pd}) \rho_0 k_{Ca} \left(1 - \frac{([CO_3^{2-}]_{pd} [Ca^{2+}]_{pd})}{K_{sp,sed}}\right)^n \times PerC + DC \quad (B.27)$$

Where there is a distinction between water column dissolution of $CaCO_3$ and dissolution in the sediments.

The biological fluxes in the surface ocean are given by:

$$C_{bio,i} = \frac{Z_i \times A_i}{V_i} \times \left(\frac{d_{fi}}{d_0}\right)^{-b} \quad (B.28)$$

For i is n , t , ts , s or ps . Z represent biological production, A the surface area of the box, V the volume, and d_{fi} the floor depth of the box.

The biological flux for box pd is given by:

$$C_{bio,i} = \frac{Z_{ps} \times A_{ps}}{V_{ps}} \times \left(\left(\frac{d_{fps}}{d_0}\right)^{-b} - \left(\frac{d_{tot}}{d_0}\right)^{-b}\right) \quad (B.29)$$

Alkalinity and phosphate fluxes are proportionate to DIC fluxes following:

$$A_{carb,i} = 2 \times C_{carb,i} \quad (B.30)$$

$$P_{bio,i} = r_{P:C} \times C_{bio,i} \quad (B.31)$$

Where $r_{P:C}$ is a constant stoichiometric P to C parameter.

An explanation and the value of all parameters are given in the tables in Appendix B.2.

List of CMIP6 models used in Chapter 4

In Chapter 4 a CMIP6 ensemble is used. The models that were used to create this ensemble are displayed in Table C.1.

Table C.1: Models used in Chapter 4: model name (column 1), member used (column 2), corresponding variable (column 3; either water flux (wfo) or virtual salt flux (vsf)), reference (column 4).

Name	Member	Variable	Reference
ACCESS-CM2	r1i1p1f1	wfo	Dix et al. (2019)
ACCESS-ESM1-5	r1i1p1f1	wfo	Ziehn et al. (2019)
CESM2	r1i1p1f1	vsf	Danabasoglu (2019b)
CESM2-WACCM-FV2	r1i1p1f1	vsf	Danabasoglu (2020)
CMCC-CM2-HR4	r1i1p1f1	wfo	Scoccimarro et al. (2021)
CMCC-ESM2	r1i1p1f1	wfo	Lovato et al. (2021)
CNRM-CM6-1-HR	r1i1p1f2	wfo	Voltaire (2019)
CNRM-ESM2-1	r1i1p1f2	wfo	Seferian (2018)
CanESM5	r1i1p1f1	wfo	Swart et al. (2019a)
CanESM5-1	r1i1p1f1	wfo	Swart et al. (2019b)
E3SM-2-0	r1i1p1f1	wfo	E3SM (2022)
E3SM-2-0-NARRM	r1i1p1f1	wfo	E3SM (2023)
FGOALS-f3-L	r1i1p1f1	vsf	Yu (2019)
FGOALS-g3	r2i1p1f1	vsf	Li (2019)
FIO-ESM-2-0	r1i1p1f1	wfo	Song et al. (2020)
GFDL-CM4	r1i1p1f1	wfo	Guo et al. (2018)
GFDL-ESM4	r1i1p1f1	wfo	Krasting et al. (2018)
GISS-E2-1-G	r1i1p1f1	wfo	NASA (2018)
GISS-E2-2-G	r1i1p1f1	wfo	NASA (2019)
HadGEM3-GC31-LL	r1i1p1f3	wfo	Ridley et al. (2019)
HadGEM3-GC31-MM	r1i1p1f3	wfo	Ridley et al. (2020)
IPSL-CM5A2-INCA	r1i1p1f1	wfo	Boucher et al. (2020)
IPSL-CM6A-LR	r1i1p1f1	wfo	Boucher et al. (2018)
MCM-UA-1-0	r1i1p1f1	wfo	Stouffer (2019)
MIROC-ES2L	r1i1p1f2	wfo	Hajima et al. (2019)
MIROC6	r1i1p1f1	wfo	Tatebe & Watanabe (2018)
MPI-ESM-1-2-HAM	r1i1p1f1	wfo	Neubauer et al. (2019)
MPI-ESM1-2-LR	r1i1p1f1	wfo	Wieners et al. (2019)
MRI-ESM2-0	r1i1p1f1	wfo	Yukimoto et al. (2019)
NESM3	r1i1p1f1	wfo	Cao & Wang (2019)
NorCPM1	r1i1p1f1	vsf	Bethke et al. (2019)
NorESM2-MM	r1i1p1f1	vsf	Bentsen et al. (2019)
SAM0-UNICON	r1i1p1f1	wfo	Park & Shin (2019)

Additional results NCAR SSP5-8.5 simulation

The results presented here are from the NCAR SSP5-8.5 simulation that is used in Chapter 5.

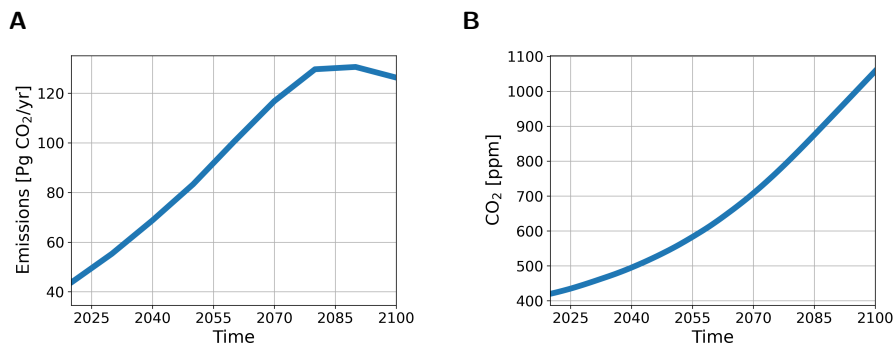


Figure D.1: (a) Emissions of CO₂ in Pg CO₂ per year in the SSP5-8.5 scenario. (b) CO₂ concentrations in ppm as simulated in CESM2.

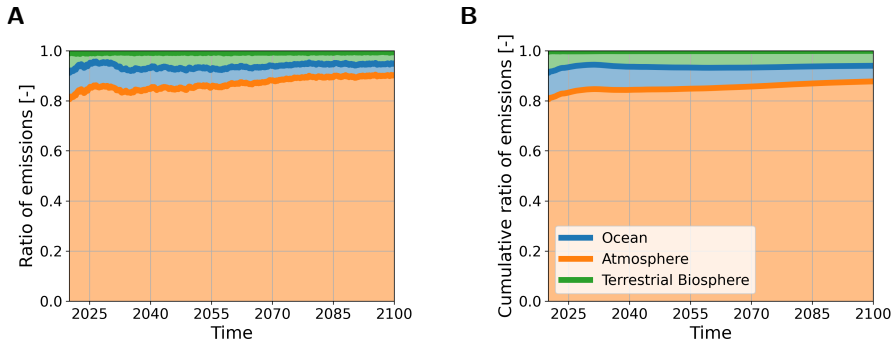


Figure D.2: (a) Ratio of how the emitted CO₂ is distributed over the three different reservoirs atmosphere (orange), ocean (blue) and terrestrial biosphere (green) per time step in CESM2. (b) As in (a) but cumulative.

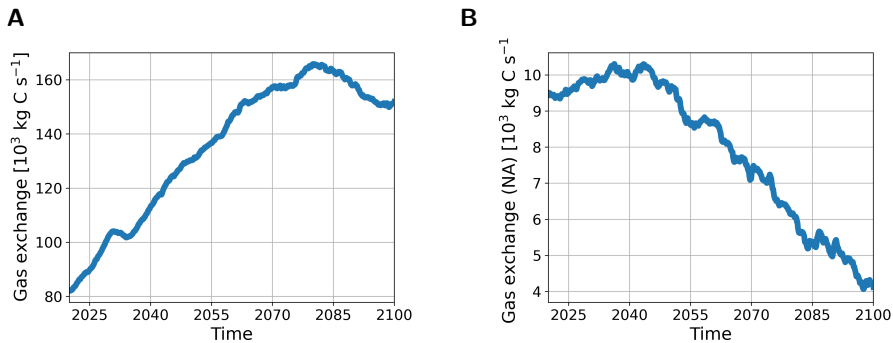


Figure D.3: (a) Globally integrated air-sea gas exchange in 10⁻³ kg C s⁻¹ in CESM2. (b) As in a, but integrated over the high latitude North Atlantic (45°-70°N × 270°-30°E).

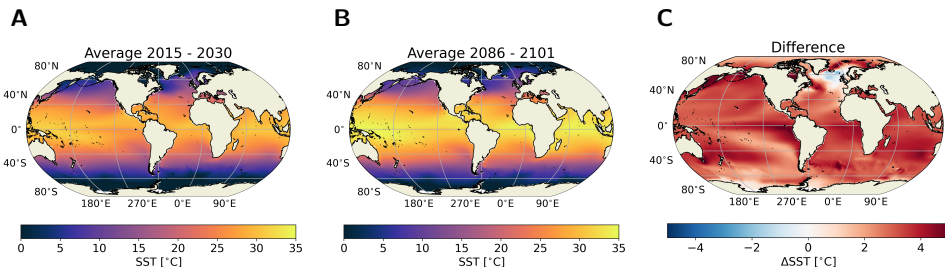


Figure D.4: (a) Sea surface temperatures averaged over 2015-2030 in °C in CESM2. (b) As in (a) but for the period 2086-2101. (c) The difference between the two. Red colors represent warming over the century, blue colors cooling.

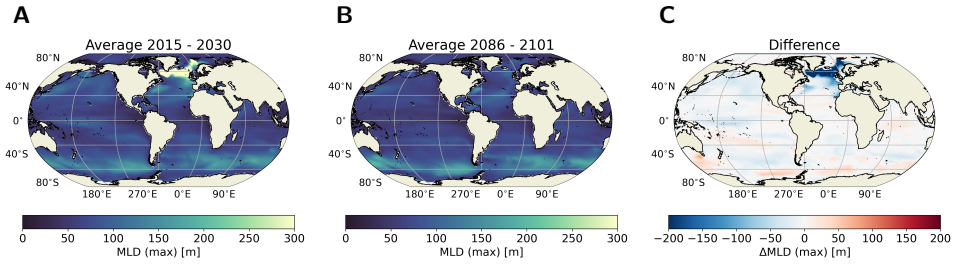


Figure D.5: (a) Annual maximum mixed layer depth in m averaged over 2015-2030 in CESM2. (b) As in (a) but for the period 2086-2101. (c) The difference between the two. Red colors represent increasing depth over the century, blue colors decreasing depth.

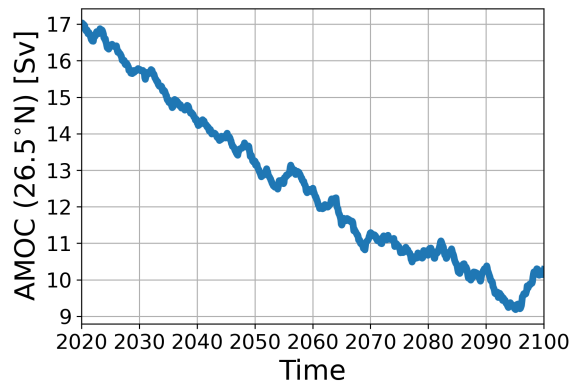


Figure D.6: AMOC strength at 26.5°N in Sv as simulated in CESM2.

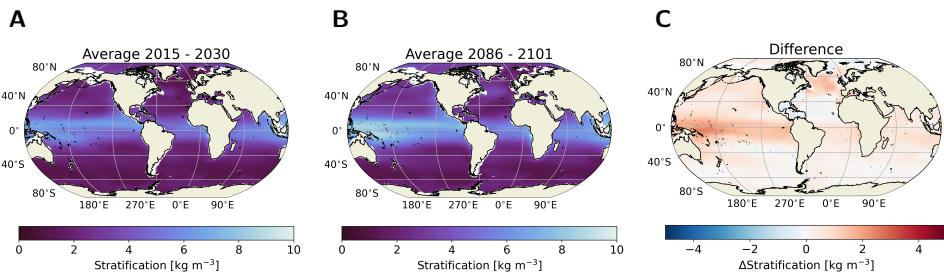


Figure D.7: (a) Stratification in kg m^{-3} averaged over 2015-2030 in CESM2. Stratification is measured as the density difference between the surface and $z=200$ m Behrenfeld et al., 2006. (b) As in (a) but for the period 2086-2101. (c) The difference between the two. Red colors represent increasing stratification over the century, blue colors decreasing stratification.

D

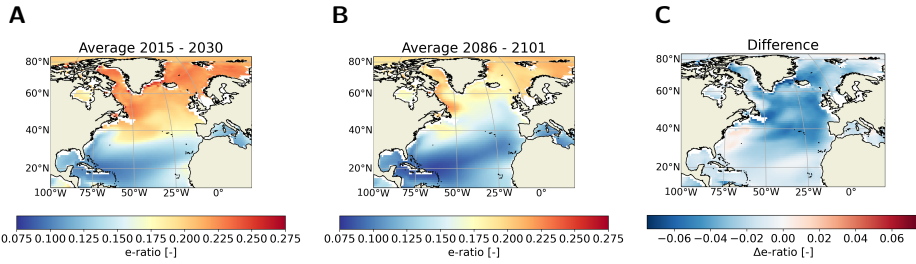


Figure D.8: (a) Export production divided by Net Primary Production in the North Atlantic averaged over 2015-2030 in CESM2. (b) As in a but for the time period 2086-2101. (c) The difference between the two.

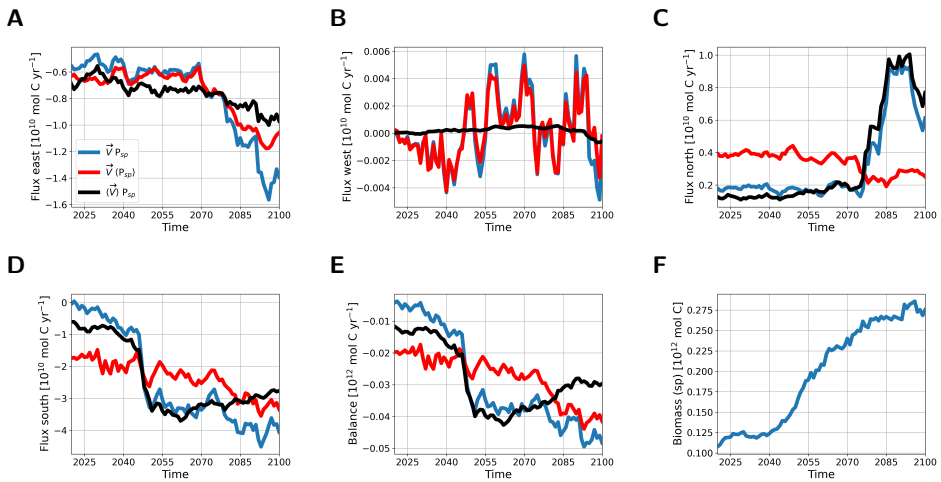


Figure D.9: Advective fluxes of small phytoplankton biomass in and out of the region 45°-70°N × 270°-0°E for the top 150 m of the water column for (a) the eastern boundary, (b) the western boundary, (c) the northern boundary, (d) the southern boundary, and (e) the sum of the four in CESM2. (a-d) In 10^{10} mol C yr⁻¹. (e) In 10^{10} mol C yr⁻¹. (f) The biomass content of this same region in 10^{10} mol C. Blue lines represent the actual calculated flux, red lines represent a flux where the biomass is time averaged over the entire period, and the black line a flux where the velocity field is time averaged over the entire period.

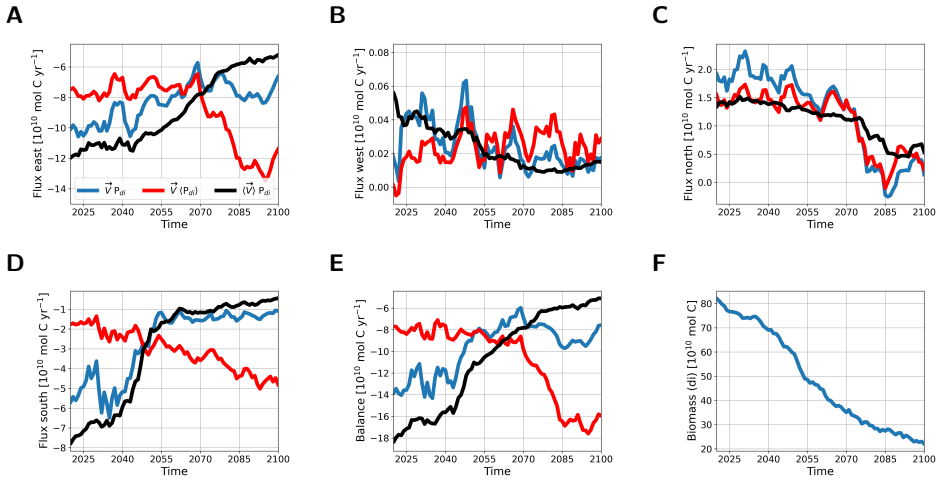


Figure D.10: As in Fig. D.9 but for diatoms instead of small phytoplankton.

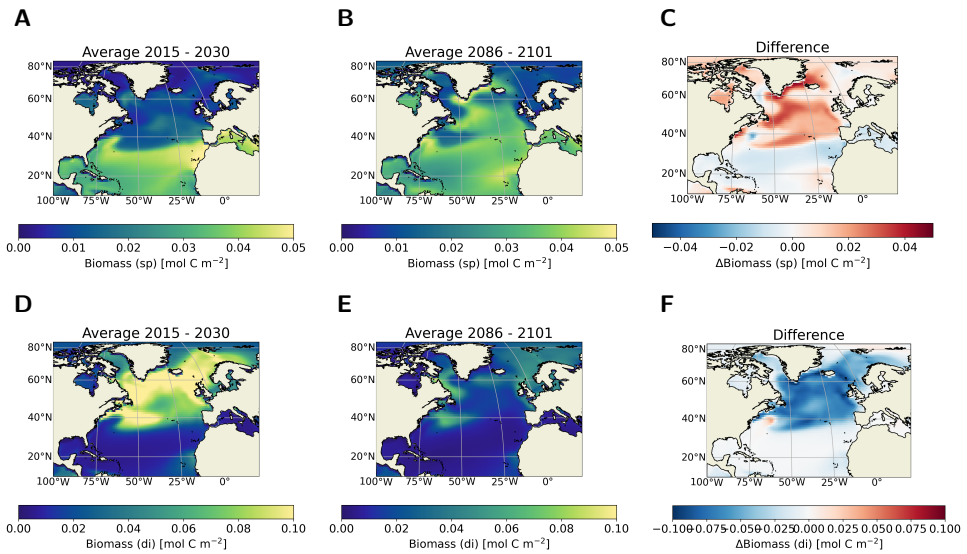


Figure D.11: Phytoplankton biomass in mol C m^{-2} over the top 150 m for small phytoplankton (top row) and diatoms (bottom row) in CESM2. Note the different scaling for the diatoms. The left panels represent the average over 2015-2030, the middle panel the average over 2086-2101, and the right panel the difference between the two.

Additional results IMAU CESM2 simulations

The results presented here are from the IMAU CESM2 simulations that is used in Chapter 6.

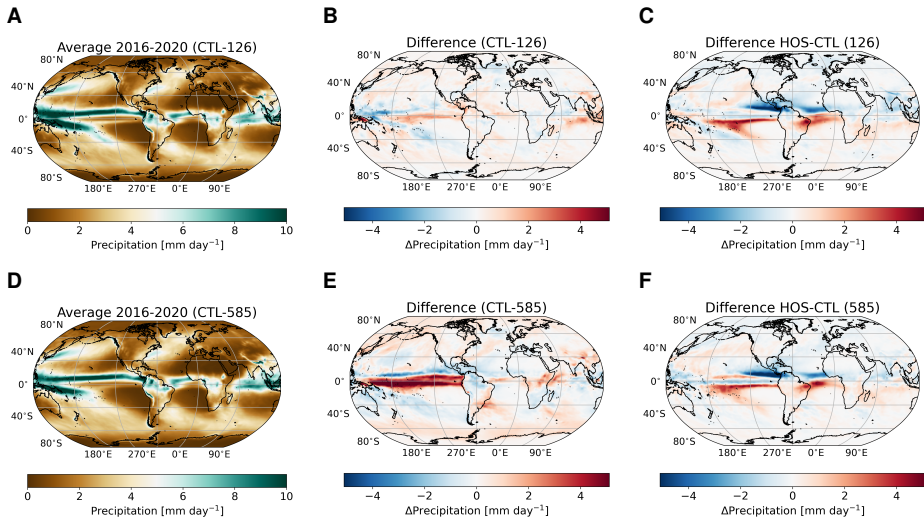


Figure E.1: Results for precipitation in mm day^{-1} . The top row (a-c) is for SSP1-2.6, and the bottom row (d-f) for SSP5-8.5. The left column (a, d) represents the average over 2016-2020 in the control simulations. The middle row (b, e) represents the difference between the average of 2096-2100 and 2016-2020 for the control simulations. The right row (c, f) represents the difference between the hosing and control simulations averaged over 2096-2100. Note the different scaling between b and e.

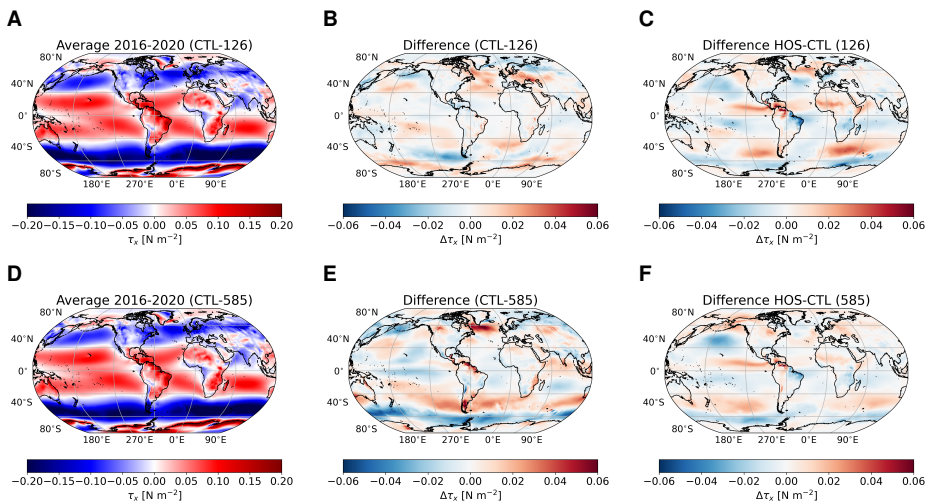


Figure E.2: Results for the zonal wind stress in N m^{-2} . Panels represent the same as in Fig. E.1.

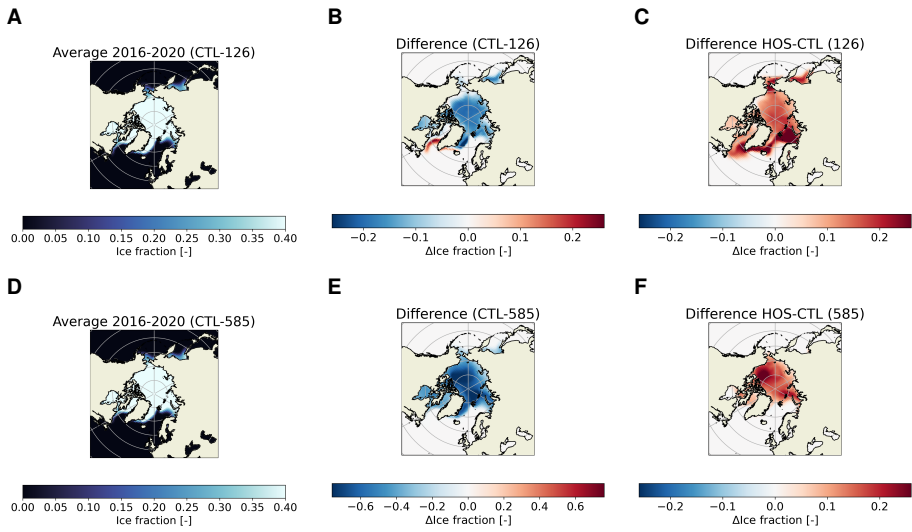


Figure E.3: Results for the ice fraction in the Arctic. Panels represent the same as in Fig. E.1. Note the different scaling for e.

E

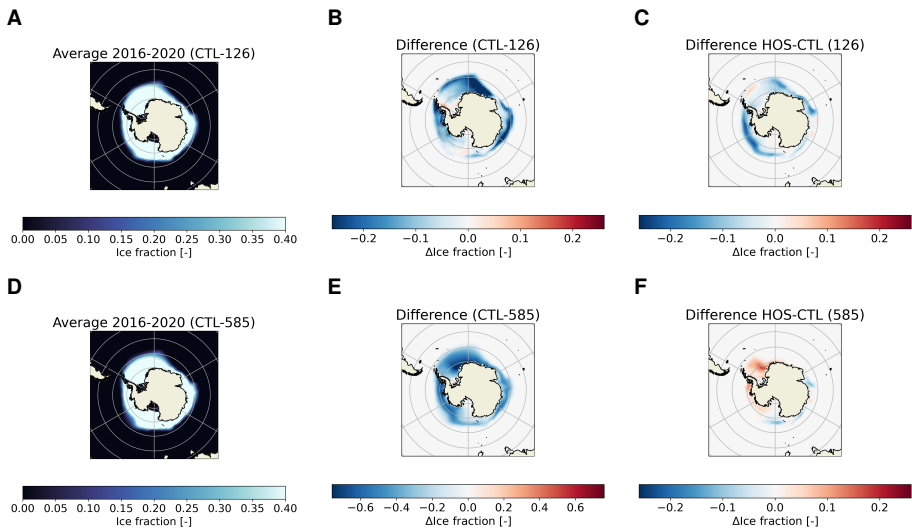


Figure E.4: Results for the ice fraction in the Antarctic. Panels represent the same as in Fig. E.1. Note the different scaling for e.

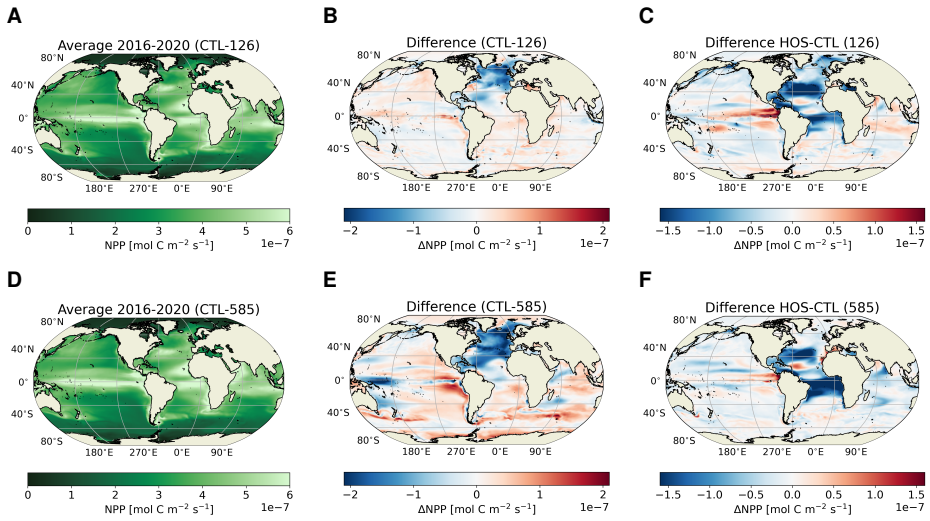


Figure E.5: Results for Net Primary Production (NPP) integrated over the surface layer (0-150 m) in $\text{mol m}^{-2} \text{s}^{-1}$. Panels represent the same as in Fig. E.1

E

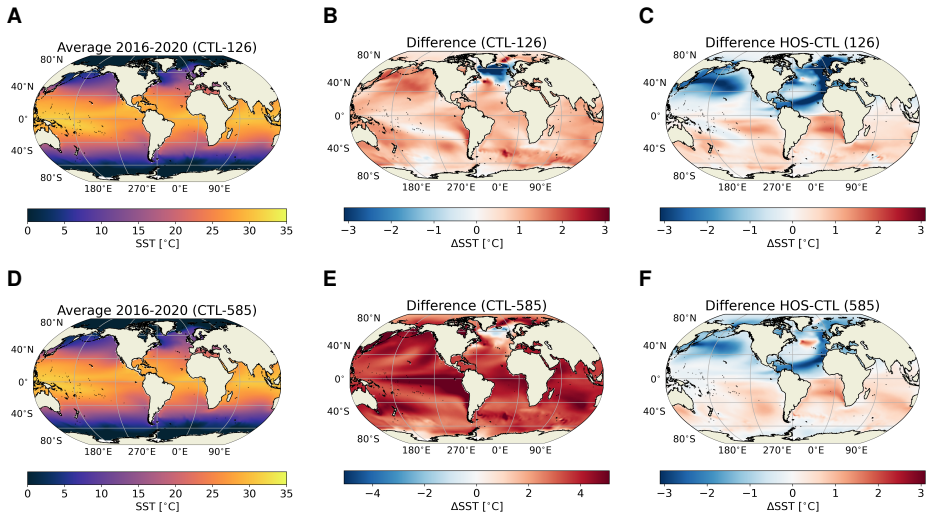


Figure E.6: Results for Sea Surface Temperature (SST) in $^{\circ}\text{C}$. Panels represent the same as in Fig. E.1. Note the different scaling in e.

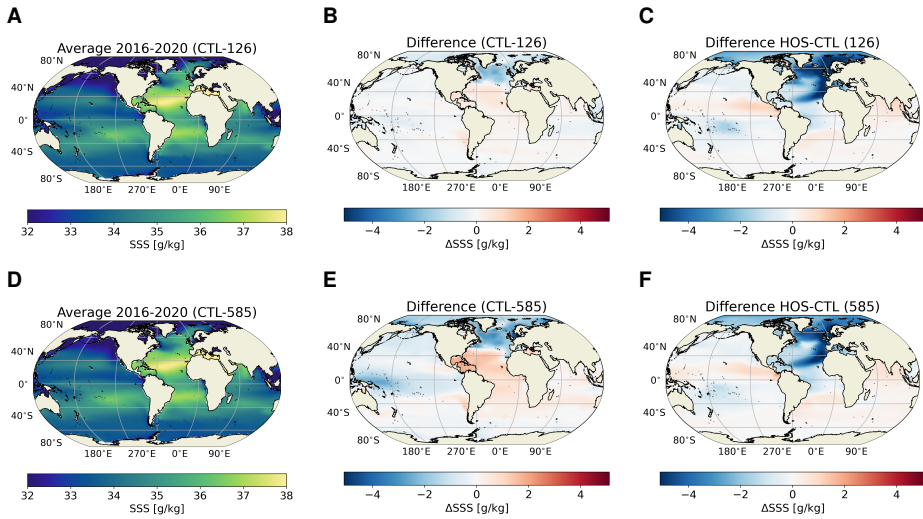


Figure E.7: Results for Sea Surface Salinity (SSS) in g/kg. Panels represent the same as in Fig. E.1.

E

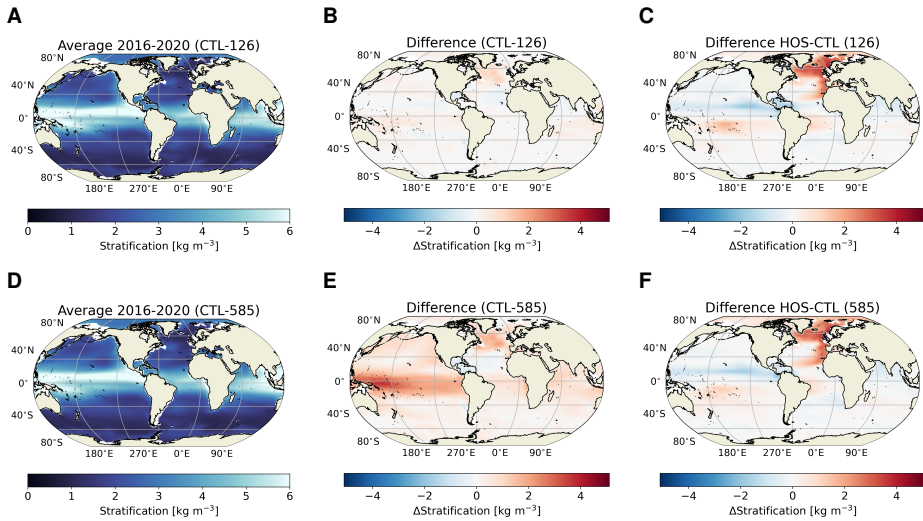


Figure E.8: Results for stratification in kg m⁻³, where stratification is defined as the density difference between 200 m depth and the surface (ref). Panels represent the same as in Fig. E.1.

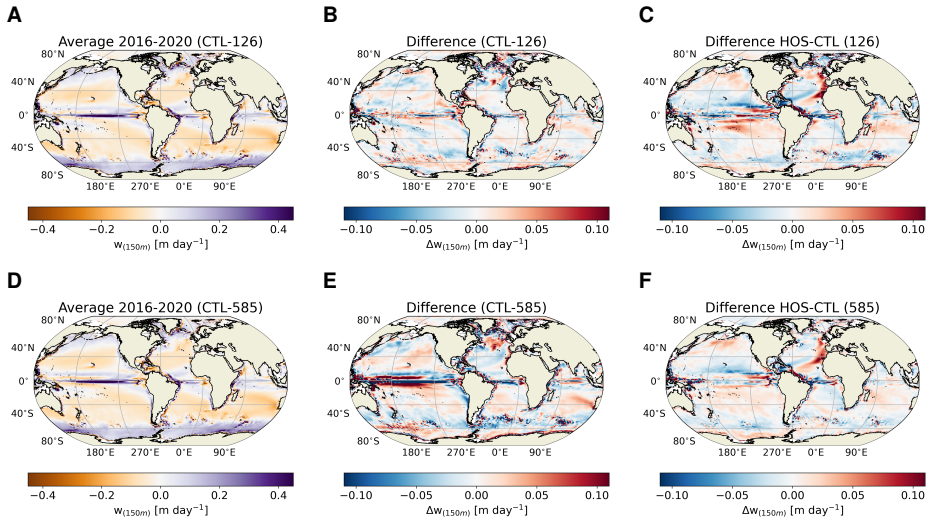


Figure E.9: Results for vertical velocities at 150 m depth in m day^{-1} . Panels represent the same as in Fig. E.1. Positive values (purple colors) in a and e represent upwelling and negative values (orange colors) downwelling.

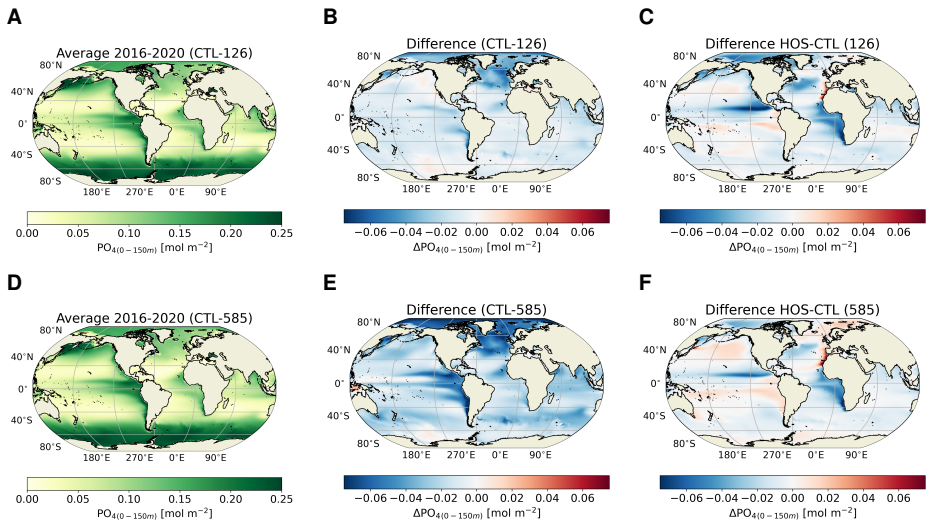


Figure E.10: Results for PO_4^{3-} concentrations integrated over the surface layer (0-150 m) in mol m^{-2} . Panels represent the same as in Fig. E.1.

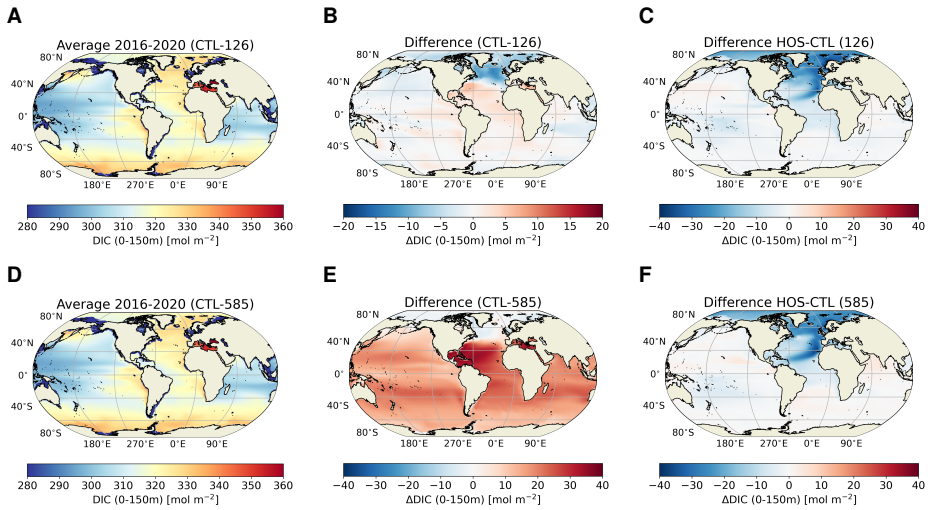


Figure E.11: Results for DIC concentrations integrated over the surface layer (0-150 m) in mol m⁻². Panels represent the same as in Fig. E.1. Note the different scaling in e.

E

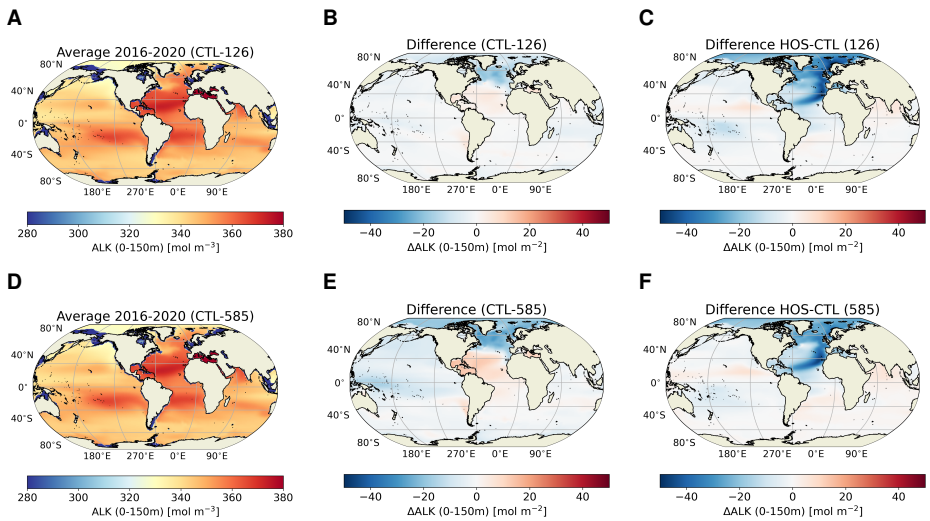


Figure E.12: Results for alkalinity concentrations integrated over the surface layer (0-150 m) in mol m⁻². Panels represent the same as in Fig. E.1. Note the different scaling in e.

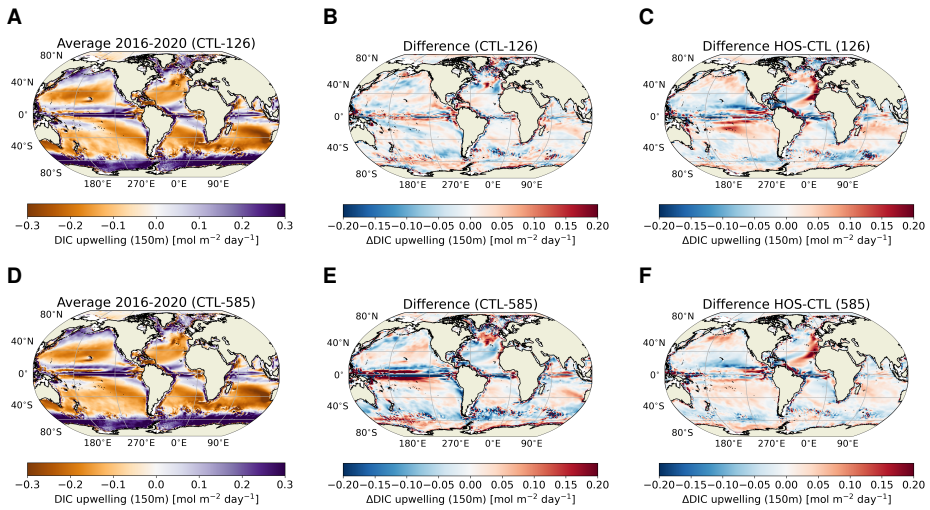


Figure E.13: Results for upwelling of DIC at 150 m depth in mol m⁻² day⁻¹. Panels represent the same as in Fig. E.1. Positive values (purple colors) in a and d represent a flux going into the surface layer (top 150 m).

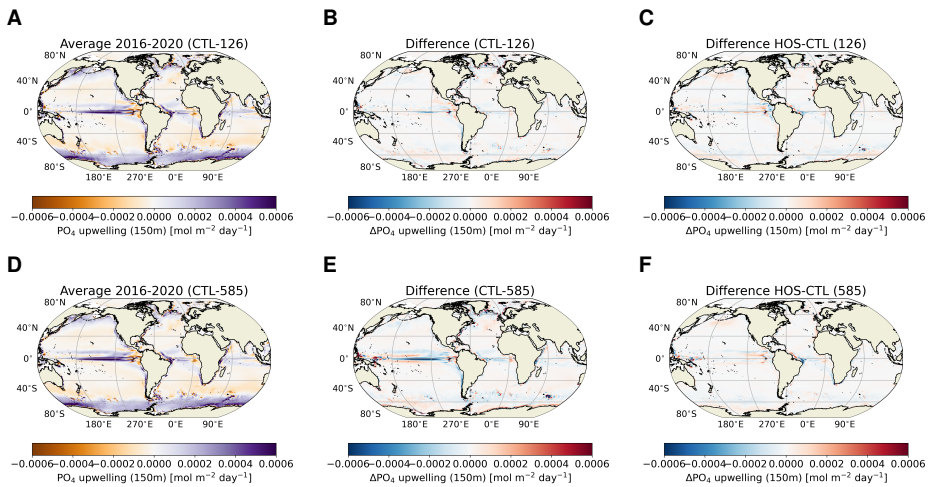


Figure E.14: Results for upwelling of PO₄³⁻ at 150 m depth in mol m⁻² day⁻¹. Panels represent the same as in Fig. E.1.

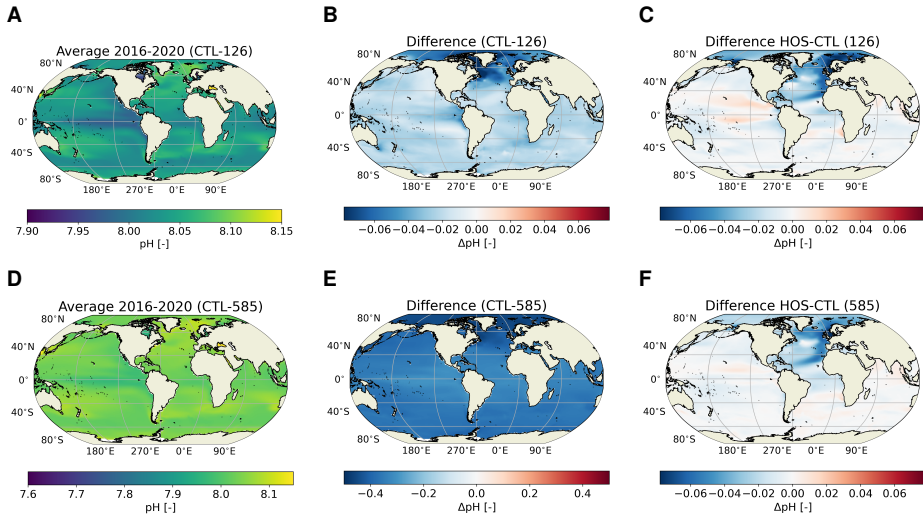


Figure E.15: Results for surface pH. Panels represent the same as in Fig. E.1. Note that the scaling of the colorbar is different for the subplots.

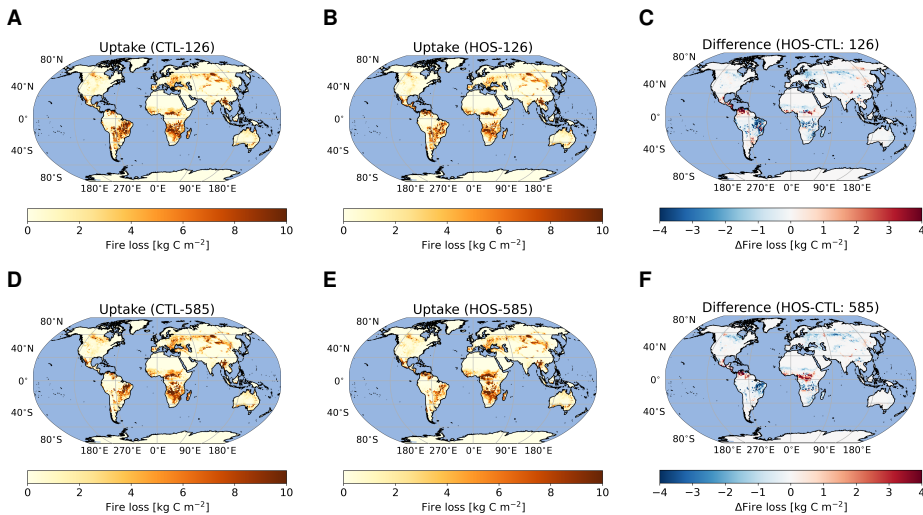


Figure E.16: Results for biomass loss due to fire integrated over the entire simulation period in kg C m⁻². The top row (a-c) represents SSP1-2.6 and the bottom row (d-f) represents SSP5-8.5. The left column (a, d) represents the uptake in the control simulations, the middle column (b, e) the uptake in the hosing simulations, and the right column (c, f) the difference between the hosing and control simulations.

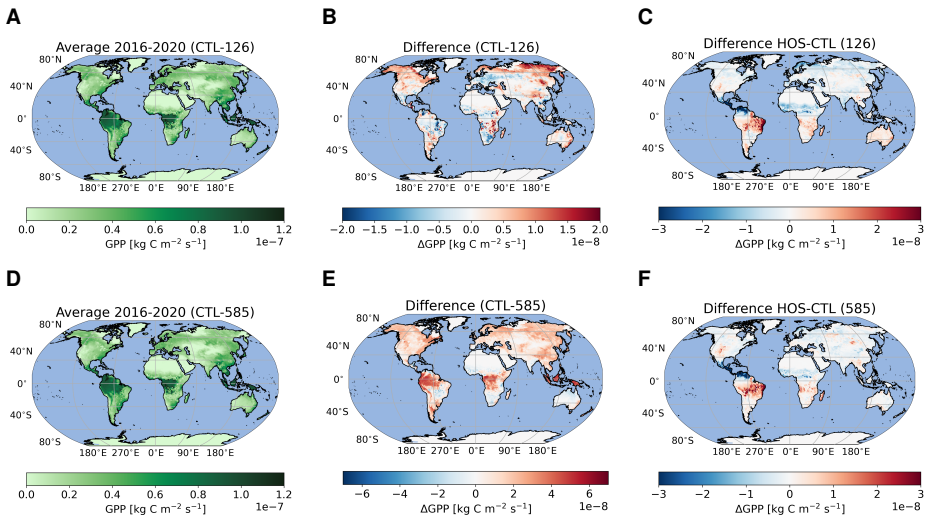


Figure E.17: Results for Gross Primary Production (GPP) in $\text{kg C m}^{-2} \text{s}^{-1}$. Panels represent the same as in Fig. E.1. Note the different scaling in e.

E

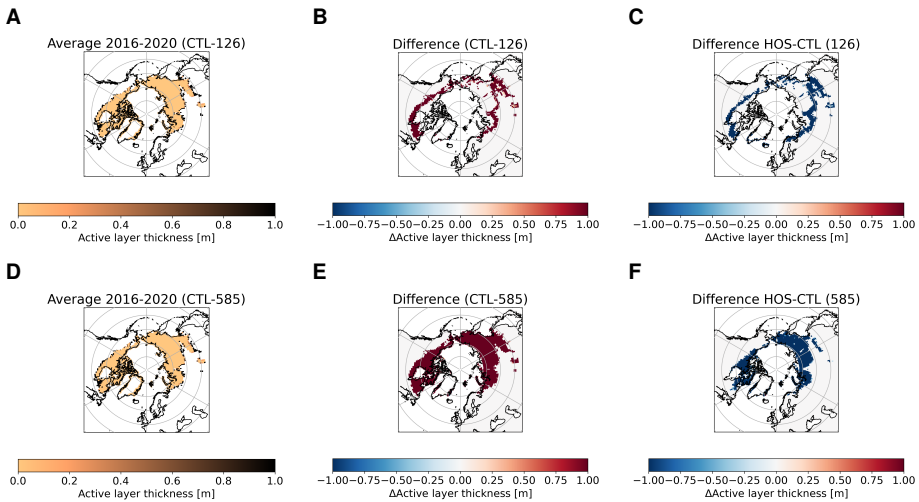


Figure E.18: Results for Active Layer Thickness (ALT) in m, which serves as a proxy for annually minima of (horizontal) permafrost extent. Panels represent the same as in Fig. E.1.

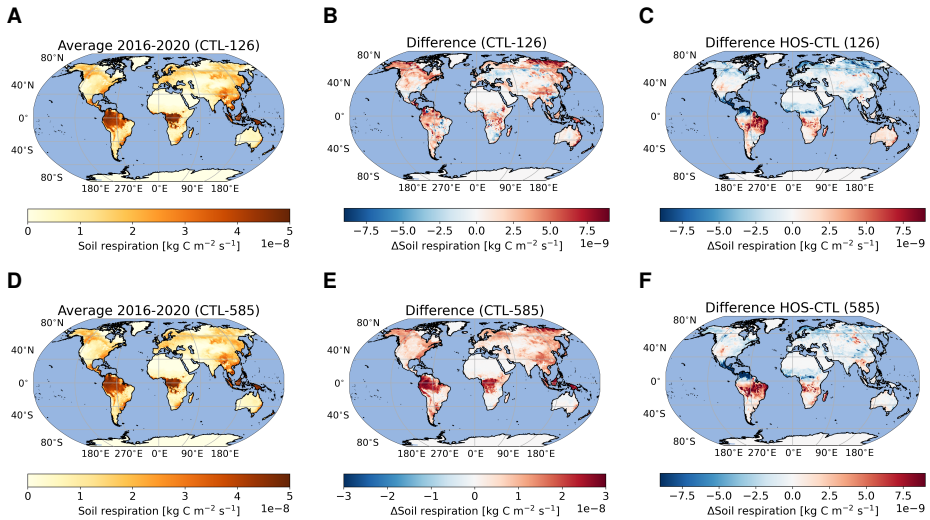


Figure E.19: Results for soil respiration in $\text{kg C m}^{-2} \text{s}^{-1}$. Panels represent the same as in Fig. E.1. Note the different scaling in e.

E

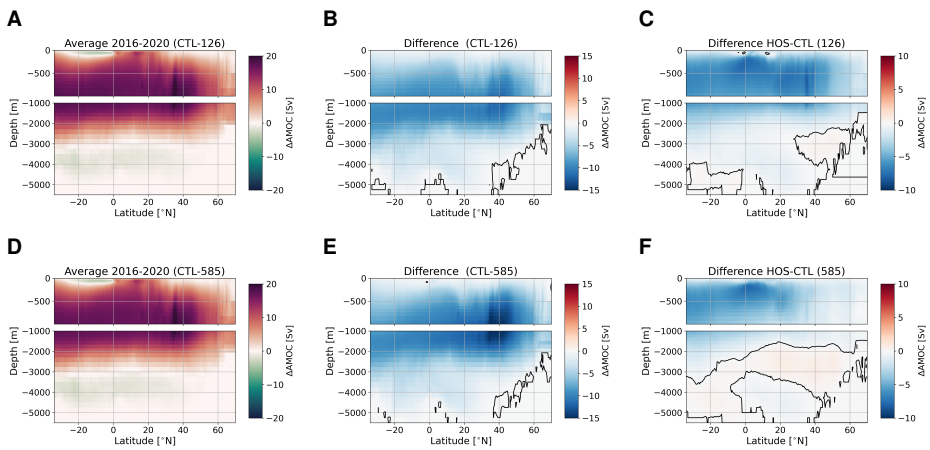


Figure E.20: Results for the Atlantic Meridional Overturning Circulation in Sv. Panels represent the same as in Fig. E.1. Black contour lines in b, c, e and f represent the 0 Sv contour. Note the different scaling of the surface ocean (top 1000 m) compared to the deep ocean.

Bibliography

- Allen, S, S Henson, A Hickman, C Beaulieu & D. PC (2020), "Interannual stability of phytoplankton community composition in the North-East Atlantic ", *Marine Ecology Progress Series*, vol. 655, pp. 43–57.
- Andersson, A. et al. (2017), *Hamburg Ocean Atmosphere Parameters and Fluxes from Satellite Data - HOAPS 4.0*.
- Archer, D & E Maier-Reimer (1994), "Effect of deep-sea sedimentary calcite preservation on atmospheric CO₂ concentration", *Nature*, vol. 367, no. 6460, pp. 260–263.
- Archer, D., H. Kheshgi & E. Maier-Reimer (1997), "Multiple timescales for neutralization of fossil fuel CO₂", *Geophysical Research Letters*, vol. 24, no. 4, pp. 405–408.
- Armstrong, R. A., C. Lee, J. I. Hedges, S. Honjo & S. G. Wakeham (2001), "A new, mechanistic model for organic carbon fluxes in the ocean based on the quantitative association of POC with ballast minerals", *Deep Sea Research Part II: Topical Studies in Oceanography*, vol. 49, no. 1, pp. 219–236.
- Armstrong-McKay, D. I. et al. (2022), "Exceeding 1.5°C global warming could trigger multiple climate tipping points", *Science*, vol. 377, no. 6611, eabn7950.
- Arnscheidt, C. W. & D. H. Rothman (2021), "Asymmetry of extreme Cenozoic climate–carbon cycle events", *Science Advances*, vol. 7, no. 33, eabg6864.
- Bakker, P et al. (2016), "Fate of the Atlantic Meridional Overturning Circulation: Strong decline under continued warming and Greenland melting", *Geophysical Research Letters*, vol. 43, no. 23, pp. 12,212–252,260.
- Barker, S., J. Chen, X. Gong, L. Jonkers, G. Knorr & D. Thornalley (2015), "Icebergs not the trigger for North Atlantic cold events", *Nature*, vol. 520, no. 7547, pp. 333–336.
- Barker, S. & H. Elderfield (2002), "Foraminiferal Calcification Response to Glacial-Interglacial Changes in Atmospheric CO₂", *Science*, vol. 297, no. 5582, 833 LP – 836.
- Barker, S. & G. Knorr (2021), "Millennial scale feedbacks determine the shape and rapidity of glacial termination", *Nature Communications*, vol. 12, no. 1, p. 2273.

- Barker, S., G. Knorr, M. J. Vautravers, P. Diz & L. C. Skinner (2010), “Extreme deepening of the Atlantic overturning circulation during deglaciation”, *Nature Geoscience*, vol. 3, no. 8, pp. 567–571.
- Bauska, T. K., S. A. Marcott & E. J. Brook (2021), “Abrupt changes in the global carbon cycle during the last glacial period”, *Nature Geoscience*, vol. 14, no. 2, pp. 91–96.
- Beaugrand, G. (2009), “Decadal changes in climate and ecosystems in the North Atlantic Ocean and adjacent seas”, *Deep Sea Research Part II: Topical Studies in Oceanography*, vol. 56, no. 8, pp. 656–673.
- Beaugrand, G., P. C. Reid, F. Ibañez, J. A. Lindley & M. Edwards (2002), “Reorganization of North Atlantic Marine Copepod Biodiversity and Climate”, *Science*, vol. 296, no. 5573, pp. 1692–1694.
- Behrenfeld, M. J. et al. (2006), “Climate-driven trends in contemporary ocean productivity”, *Nature*, vol. 444, no. 7120, pp. 752–755.
- Bennington, V., G. A. McKinley, S. Dutkiewicz & D. Ullman (2009), “What does chlorophyll variability tell us about export and air-sea CO₂ flux variability in the North Atlantic?”, *Global Biogeochemical Cycles*, vol. 23, no. 3.
- Bentsen, M. et al. (2019), *NCC NorESM2-MM model output prepared for CMIP6 CMIP 1pctCO2*.
- Bethke, I. et al. (2019), *NCC NorCPM1 model output prepared for CMIP6 CMIP 1pctCO2*.
- Blais, M. et al. (2017), “Contrasting interannual changes in phytoplankton productivity and community structure in the coastal Canadian Arctic Ocean”, *Limnology and Oceanography*, vol. 62, no. 6, pp. 2480–2497.
- Boot, A, A. S. von der Heydt & H. A. Dijkstra (2022), “Effect of the Atlantic Meridional Overturning Circulation on Atmospheric pCO₂ Variations”, *Earth Syst. Dynam.*, pp. 1–26.
- Boot, A, A. S. von der Heydt & H. A. Dijkstra (2023a), “Effect of Plankton Composition Shifts in the North Atlantic on Atmospheric pCO₂”, *Geophysical Research Letters*, vol. 50, no. 2, e2022GL100230.
- Boot, A, R. M. van Westen & H. A. Dijkstra (2021), “Multidecadal polynya formation in a conceptual (box) model”, *Ocean Science*, vol. 17, no. 1, pp. 335–350.
- Boot, A. A., A. S. von der Heydt & H. A. Dijkstra (2023b), “Potential effect of the marine carbon cycle on the multiple equilibria window of the Atlantic Meridional Overturning Circulation”, *Earth System Dynamics Discussions*, vol. 2023, pp. 1–27.
- Boot, A. A., A. S. von der Heydt & H. A. Dijkstra (2023c), “Response of atmospheric pCO₂ to a strong AMOC weakening under low and high emission scenarios”, *Under review at Climate Dynamics*.
- Bopp, L, O Aumont, P Cadule, S Alvain & M Gehlen (2005), “Response of diatoms distribution to global warming and potential implications: A global model study”, *Geophysical Research Letters*, vol. 32, no. 19.
- Bopp, L et al. (2013), “Multiple stressors of ocean ecosystems in the 21st century: projections with CMIP5 models”, *Biogeosciences*, vol. 10, no. 10, pp. 6225–6245.
- Bopp, L. et al. (2001), “Potential impact of climate change on marine export production”, *Global Biogeochemical Cycles*, vol. 15, no. 1, pp. 81–99.

- Boucher, O. et al. (2018), *IPSL IPSL-CM6A-LR model output prepared for CMIP6 CMIP 1pctCO2*.
- Boucher, O. et al. (2020), *IPSL IPSL-CM5A2-INCA model output prepared for CMIP6 CMIP 1pctCO2*.
- Broecker, W. S., D. M. Peteet & D. Rind (1985), “Does the ocean–atmosphere system have more than one stable mode of operation?”, *Nature*, vol. 315, no. 6014, pp. 21–26.
- Bryan, F. (1986), “High-latitude salinity effects and interhemispheric thermohaline circulations”, *Nature*, vol. 323, no. 6086, pp. 301–304.
- Buckley, M. W. & J. Marshall (2016), “Observations, inferences, and mechanisms of the Atlantic Meridional Overturning Circulation: A review”, *Reviews of Geophysics*, vol. 54, no. 1, pp. 5–63.
- Burke, E. J., Y Zhang & G Krinner (2020), “Evaluating permafrost physics in the Coupled Model Intercomparison Project 6 (CMIP6) models and their sensitivity to climate change”, *The Cryosphere*, vol. 14, no. 9, pp. 3155–3174.
- Cabr e, A., I. Marinov & S. Leung (2015), “Consistent global responses of marine ecosystems to future climate change across the IPCC AR5 earth system models”, *Climate Dynamics*, vol. 45, no. 5, pp. 1253–1280.
- Cael, B. B., K. Bisson & M. J. Follows (2017), “How have recent temperature changes affected the efficiency of ocean biological carbon export?”, *Limnology and Oceanography Letters*, vol. 2, no. 4, pp. 113–118.
- Caesar, L, S Rahmstorf, A Robinson, G Feulner & V Saba (2018), “Observed fingerprint of a weakening Atlantic Ocean overturning circulation”, *Nature*, vol. 556, no. 7700, pp. 191–196.
- Cao, J. & B. Wang (2019), *NUIST NESMv3 model output prepared for CMIP6 CMIP 1pctCO2*.
- Castellana, D., S. Baars, F. W. Wubs & H. A. Dijkstra (2019), “Transition Probabilities of Noise-induced Transitions of the Atlantic Ocean Circulation”, *Scientific Reports*, vol. 9, no. 1, p. 20284.
- Caves, J. K., A. B. Jost, K. V. Lau & K. Maher (2016), “Cenozoic carbon cycle imbalances and a variable weathering feedback”, *Earth and Planetary Science Letters*, vol. 450, pp. 152–163.
- Chassignet, E. P. & X. Xu (2021), “On the Importance of High-Resolution in Large-Scale Ocean Models”, *Advances in Atmospheric Sciences*, vol. 38, no. 10, pp. 1621–1634.
- Cheng, W. et al. (2018), “Can the Salt-Advection Feedback Be Detected in Internal Variability of the Atlantic Meridional Overturning Circulation?”, *Journal of Climate*, vol. 31, no. 16, pp. 6649–6667.
- Cimatoribus, A. A., S. S. Drijfhout & H. A. Dijkstra (2014), “Meridional overturning circulation: stability and ocean feedbacks in a box model”, *Climate Dynamics*, vol. 42, no. 1, pp. 311–328.
- Cole, C, A. A. Finch, C Hintz, K Hintz & N Allison (2018), “Effects of seawater pCO₂ and temperature on calcification and productivity in the coral genus *Porites* spp.: an exploration of potential interaction mechanisms”, *Coral Reefs*, vol. 37, no. 2, pp. 471–481.

- Cuffey, K. M. & G. D. Clow (1997), “Temperature, accumulation, and ice sheet elevation in central Greenland through the last deglacial transition”, *Journal of Geophysical Research: Oceans*, vol. 102, no. C12, pp. 26383–26396.
- Danabasoglu, G et al. (2020), “The Community Earth System Model Version 2 (CESM2)”, *Journal of Advances in Modeling Earth Systems*, vol. 12, no. 2, e2019MS001916.
- Danabasoglu, G. (2019a), *NCAR CESM2 model output prepared for CMIP6 CMIP esm-ssp585*.
- Danabasoglu, G. (2019b), *NCAR CESM2 model output prepared for CMIP6 CMIP 1pctCO2*.
- Danabasoglu, G. (2019c), *NCAR CESM2 model output prepared for CMIP6 CMIP esm-hist*.
- Danabasoglu, G. (2020), *NCAR CESM2-WACCM-FV2 model output prepared for CMIP6 CMIP 1pctCO2*.
- Danabasoglu, G. et al. (2012), “The CCSM4 ocean component”, *Journal of Climate*, vol. 25, no. 5, pp. 1361–1389.
- Dekker, M. M., A. S. von der Heydt & H. A. Dijkstra (2018), “Cascading transitions in the climate system”, *Earth System Dynamics*, vol. 9, no. 4, pp. 1243–1260.
- DeVries, T., M. Holzer & F. Primeau (2017), “Recent increase in oceanic carbon uptake driven by weaker upper-ocean overturning”, *Nature*, vol. 542, no. 7640, pp. 215–218.
- Dey, D. & K. Döös (2020), “Atmospheric Freshwater Transport From the Atlantic to the Pacific Ocean: A Lagrangian Analysis”, *Geophysical Research Letters*, vol. 47, no. 6, e2019GL086176.
- Dijkstra, H. A. (2007), “Characterization of the multiple equilibria regime in a global ocean model”, *Tellus A*, vol. 59, no. 5, pp. 695–705.
- Dijkstra, H. A. & W. Weijer (2005), “Stability of the Global Ocean Circulation: Basic Bifurcation Diagrams”, *Journal of Physical Oceanography*, vol. 35, no. 6, pp. 933–948.
- Ditlevsen, P. & S. Ditlevsen (2023), “Warning of a forthcoming collapse of the Atlantic meridional overturning circulation”, *Nature Communications*, vol. 14, no. 1, p. 4254.
- Dix, M. et al. (2019), *CSIRO-ARCCSS ACCESS-CM2 model output prepared for CMIP6 CMIP 1pctCO2*.
- Doedel, E. J. et al. (2007), *AUTO-07p: Continuation and Bifurcation Software for Ordinary Differential Equations*.
- Doedel, E. J. et al. (2021), *auto-07p*.
- Doney, S. C. et al. (2009), “Mechanisms governing interannual variability in upper-ocean inorganic carbon system and air–sea CO₂ fluxes: Physical climate and atmospheric dust”, *Deep Sea Research Part II: Topical Studies in Oceanography*, vol. 56, no. 8, pp. 640–655.
- Doney, S. C. et al. (2011), “Climate Change Impacts on Marine Ecosystems”, *Annual Review of Marine Science*, vol. 4, no. 1, pp. 11–37.
- Drijfhout, S. (2015), “Competition between global warming and an abrupt collapse of the AMOC in Earth’s energy imbalance”, *Scientific Reports*, vol. 5, no. 1, p. 14877.

- Duplessy, J. C., N. J. Shackleton, R. G. Fairbanks, L. Labeyrie, D. Oppo & N. Kallel (1988), “Deepwater source variations during the last climatic cycle and their impact on the global deepwater circulation”, *Paleoceanography*, vol. 3, no. 3, pp. 343–360.
- Dutkiewicz, S, J. R. Scott & M. J. Follows (2013), “Winners and losers: Ecological and biogeochemical changes in a warming ocean”, *Global Biogeochemical Cycles*, vol. 27, no. 2, pp. 463–477.
- E3SM (2022), *E3SM-Project E3SM2.0 model output prepared for CMIP6 CMIP 1pctCO2*.
- E3SM (2023), *E3SM-Project E3SM2.0NARRM model output prepared for CMIP6 CMIP 1pctCO2*.
- Edwards, M., G. Beaugrand, L. Kléparski, P. Hélaouët & P. C. Reid (2022), “Climate variability and multi-decadal diatom abundance in the Northeast Atlantic”, *Communications Earth & Environment*, vol. 3, no. 1, p. 162.
- EEA (2019).
- Eyring, V et al. (2016), “Overview of the Coupled Model Intercomparison Project Phase 6 (CMIP6) experimental design and organization”, *Geosci. Model Dev.*, vol. 9, no. 5, pp. 1937–1958.
- Follows, M. J., T. Ito & S. Dutkiewicz (2006), “On the solution of the carbonate chemistry system in ocean biogeochemistry models”, *Ocean Modelling*, vol. 12, no. 3, pp. 290–301.
- Francis, T. B. et al. (2012), “Climate shifts the interaction web of a marine plankton community”, *Global Change Biology*, vol. 18, no. 8, pp. 2498–2508.
- Friedlingstein, P et al. (2020), “Global Carbon Budget 2020”, *Earth System Science Data*, vol. 12, no. 4, pp. 3269–3340.
- Friedlingstein, P et al. (2022), “Global Carbon Budget 2022”, *Earth System Science Data*, vol. 14, no. 11, pp. 4811–4900.
- Fu, W, J. T. Randerson & J. K. Moore (2016), “Climate change impacts on net primary production (NPP) and export production (EP) regulated by increasing stratification and phytoplankton community structure in the CMIP5 models”, *Biogeosciences*, vol. 13, no. 18, pp. 5151–5170.
- Galbraith, E. & C. de Lavergne (2019), “Response of a comprehensive climate model to a broad range of external forcings: relevance for deep ocean ventilation and the development of late Cenozoic ice ages”, *Climate Dynamics*, vol. 52, no. 1, pp. 653–679.
- Ganachaud, A. & C. Wunsch (2000), “Improved estimates of global ocean circulation, heat transport and mixing from hydrographic data”, *Nature*, vol. 408, no. 6811, pp. 453–457.
- Gent, P. R. & J. C. McWilliams (1990), *Isopycnal Mixing in Ocean Circulation Models*.
- Goosse, H et al. (2010), “Description of the Earth system model of intermediate complexity LOVECLIM version 1.2”, *Geoscientific Model Development*, vol. 3, no. 2, pp. 603–633.
- Gottschalk, J. et al. (2019), “Mechanisms of millennial-scale atmospheric CO₂ change in numerical model simulations”, *Quaternary Science Reviews*, vol. 220, pp. 30–74.

- Green, C, D Carlisle, B. C. O'Neill, B. J. van Ruijven, C Boyer & K Ebi (2021), *Shared Socioeconomic Pathways (SSPs) Literature Database, v1, 2014-2019*, Palisades, New York.
- Gregg, W. W., C. S. Rousseaux & B. A. Franz (2017), "Global trends in ocean phytoplankton: a new assessment using revised ocean colour data", *Remote Sensing Letters*, vol. 8, no. 12, pp. 1102–1111.
- Grégoire, M. et al. (2023), *Ocean oxygen: The role of the Ocean in the oxygen we breathe and the threat of deoxygenation*, ISBN: 9789464206180.
- Gregory, J. M. et al. (2005), "A model intercomparison of changes in the Atlantic thermohaline circulation in response to increasing atmospheric CO₂ concentration", *Geophysical Research Letters*, vol. 32, no. 12.
- Gruber, N., P. Landschützer & N. S. Lovenduski (2019), "The Variable Southern Ocean Carbon Sink", *Annual Review of Marine Science*, vol. 11, no. 1, pp. 159–186.
- Guo, H. et al. (2018), *NOAA-GFDL GFDL-CM4 model output 1pctCO2*.
- Hajima, T. et al. (2019), *MIROC MIROC-ES2L model output prepared for CMIP6 CMIP 1pctCO2*.
- Hays, J. D., J. Imbrie & N. J. Shackleton (1976), "Variations in the Earth's Orbit: Pacemaker of the Ice Ages", *Science*, vol. 194, no. 4270, pp. 1121–1132.
- Henson, S. A., C. Laufkötter, S. Leung, S. L. C. Giering, H. I. Palevsky & E. L. Cavan (2022), "Uncertain response of ocean biological carbon export in a changing world", *Nature Geoscience*, vol. 15, no. 4, pp. 248–254.
- Heuzé, C (2021), "Antarctic Bottom Water and North Atlantic Deep Water in CMIP6 models", *Ocean Science*, vol. 17, no. 1, pp. 59–90.
- von der Heydt, A. S. et al. (2021), "Quantification and interpretation of the climate variability record", *Global and Planetary Change*, vol. 197, p. 103399.
- Hilligsøe, K. M., K. Richardson, J. Bendtsen, L.-L. Sørensen, T. G. Nielsen & M. M. Lyngsgaard (2011), "Linking phytoplankton community size composition with temperature, plankton food web structure and sea–air CO₂ flux", *Deep Sea Research Part I: Oceanographic Research Papers*, vol. 58, no. 8, pp. 826–838.
- Hinder, S. L., G. C. Hays, M. Edwards, E. C. Roberts, A. W. Walne & M. B. Gravenor (2012), "Changes in marine dinoflagellate and diatom abundance under climate change", *Nature Climate Change*, vol. 2, no. 4, pp. 271–275.
- Huck, T., O. Arzel & F. Sévellec (2015), "Multidecadal Variability of the Overturning Circulation in Presence of Eddy Turbulence", *Journal of Physical Oceanography*, vol. 45, no. 1, pp. 157–173.
- Huiskamp, W. N. & K. J. Meissner (2012), "Oceanic carbon and water masses during the Mystery Interval: A model-data comparison study", *Paleoceanography*, vol. 27, no. 4.
- Hunke, E. C., W. H. Lipscomb, A. K. Turner, N. Jeffrey & S. Elliott (2015), *CICE: The Los Alamos Sea Ice Model documentation and software user's manual, version 5.1. Doc*, tech. rep., LA-CC-06-012, 116 pp., <http://www.ccpo.odu.edu>.
- IPCC (2021), *Climate Change 2021: The Physical Science Basis. Contribution of Working Group I to the Sixth Assessment Report of the Intergovernmental Panel on Climate*

- Change*, vol. In Press, Cambridge, United Kingdom and New York, NY, USA: Cambridge University Press.
- IPCC (2022), *Climate Change 2022: Impacts, Adaptation and Vulnerability*, Summary for Policymakers, Cambridge, UK and New York, USA: Cambridge University Press, pp. 3–33, ISBN: 9781009325844.
- Ito, T. & M. J. Follows (2005), “Preformed phosphate, soft tissue pump and atmospheric CO₂”, *Journal of Marine Research*, vol. 63, no. 4, pp. 813–839.
- Jackson, L. C. et al. (2015), “Global and European climate impacts of a slowdown of the AMOC in a high resolution GCM”, *Climate Dynamics*, vol. 45, no. 11, pp. 3299–3316.
- Jacques-Dumas, V, R. M. van Westen, F Bouchet & H. A. Dijkstra (2023), “Data-driven methods to estimate the committor function in conceptual ocean models”, *Nonlinear Processes in Geophysics*, vol. 30, no. 2, pp. 195–216.
- Jiang, X. & Y. L. Yung (2019), “Global Patterns of Carbon Dioxide Variability from Satellite Observations”, *Annual Review of Earth and Planetary Sciences*, vol. 47, no. 1, pp. 225–245.
- Jouzel, J et al. (2007), “Orbital and Millennial Antarctic Climate Variability over the Past 800,000 Years”, *Science*, vol. 317, no. 5839, pp. 793–796.
- Kang, S. M., D. M. W. Frierson & I. M. Held (2009), “The Tropical Response to Extratropical Thermal Forcing in an Idealized GCM: The Importance of Radiative Feedbacks and Convective Parameterization”, *Journal of the Atmospheric Sciences*, vol. 66, no. 9, pp. 2812–2827.
- Kang, S. M., I. M. Held, D. M. W. Frierson & M. Zhao (2008), “The Response of the ITCZ to Extratropical Thermal Forcing: Idealized Slab-Ocean Experiments with a GCM”, *Journal of Climate*, vol. 21, no. 14, pp. 3521–3532.
- Kaszás, B., U. Feudel & T. Tél (2019), “Tipping phenomena in typical dynamical systems subjected to parameter drift”, *Scientific Reports*, vol. 9, no. 1, p. 8654.
- Katavouta, A & R. G. Williams (2021), “Ocean carbon cycle feedbacks in CMIP6 models: contributions from different basins”, *Biogeosciences*, vol. 18, no. 10, pp. 3189–3218.
- Kohfeld, K. E., Q. C. Le, H. S. P. & A. R. F. (2005), “Role of Marine Biology in Glacial-Interglacial CO₂ Cycles”, *Science*, vol. 308, no. 5718, pp. 74–78.
- Köhler, P., F. Joos, S. Gerber & R. Knutti (2005), “Simulated changes in vegetation distribution, land carbon storage, and atmospheric CO₂ in response to a collapse of the North Atlantic thermohaline circulation”, *Climate Dynamics*, vol. 25, no. 7, p. 689.
- Krasting, J. P. et al. (2018), *NOAA-GFDL GFDL-ESM4 model output prepared for CMIP6 CMIP 1pctCO2*.
- Kuhlbrodt, T, A Griesel, M Montoya, A Levermann, M Hofmann & S Rahmstorf (2007), “On the driving processes of the Atlantic meridional overturning circulation”, *Reviews of Geophysics*, vol. 45, no. 2.
- Kwiatkowski, L et al. (2020), “Twenty-first century ocean warming, acidification, deoxygenation, and upper-ocean nutrient and primary production decline from CMIP6 model projections”, *Biogeosciences*, vol. 17, no. 13, pp. 3439–3470.

- Kwon, E. Y. & F. Primeau (2008), "Optimization and sensitivity of a global biogeochemistry ocean model using combined in situ DIC, alkalinity, and phosphate data", *Journal of Geophysical Research: Oceans*, vol. 113, no. C8.
- Lawrence, D. M. et al. (2019), "The Community Land Model Version 5: Description of New Features, Benchmarking, and Impact of Forcing Uncertainty", *Journal of Advances in Modeling Earth Systems*, vol. 11, no. 12, pp. 4245–4287.
- Le Gland, G, S. M. Vallina, S. L. Smith & P Cermeño (2021), "SPEAD 1.0 – Simulating Plankton Evolution with Adaptive Dynamics in a two-trait continuous fitness landscape applied to the Sargasso Sea", *Geoscientific Model Development*, vol. 14, no. 4, pp. 1949–1985.
- Lenton, T. M. et al. (2019), "Climate tipping points - too risky to bet against", *Nature*, vol. 575, pp. 592–595.
- Lenton, T. M. et al. (2008), "Tipping elements in the Earth's climate system", *Proceedings of the National Academy of Sciences*, vol. 105, no. 6, pp. 1786–1793.
- Li, H. et al. (2013), "A Physically Based Runoff Routing Model for Land Surface and Earth System Models", *Journal of Hydrometeorology*, vol. 14, no. 3, pp. 808–828.
- Li, L. (2019), *CAS FGOALS-g3 model output prepared for CMIP6 CMIP 1pctCO2*.
- Li, W. K. W., F. A. McLaughlin, C Lovejoy & E. C. Carmack (2009), "Smallest Algae Thrive As the Arctic Ocean Freshens", *Science*, vol. 326, no. 5952, p. 539.
- Liu, Y, J. K. Moore, F Primeau & W. L. Wang (2023), "Reduced CO2 uptake and growing nutrient sequestration from slowing overturning circulation", *Nature Climate Change*, vol. 13, no. 1, pp. 83–90.
- Long, M. C. et al. (2021), "Simulations With the Marine Biogeochemistry Library (MARBL)", *Journal of Advances in Modeling Earth Systems*, vol. 13, no. 12, e2021MS002647.
- Lovato, T., D. Peano & M. Butenschön (2021), *CMCC CMCC-ESM2 model output prepared for CMIP6 CMIP 1pctCO2*.
- Lueker, T. J., A. G. Dickson & C. D. Keeling (2000), "Ocean pCO₂ calculated from dissolved inorganic carbon, alkalinity, and equations for K₁ and K₂: validation based on laboratory measurements of CO₂ in gas and seawater at equilibrium", *Marine Chemistry*, vol. 70, no. 1, pp. 105–119.
- Lynch-Stieglitz, J. (2017), "The Atlantic Meridional Overturning Circulation and Abrupt Climate Change", *Annual Review of Marine Science*, vol. 9, no. 1, pp. 83–104.
- Manabe, S & R. J. Stouffer (1988), "Two Stable Equilibria of a Coupled Ocean-Atmosphere Model", *Journal of Climate*, vol. 1, no. 9, pp. 841–866.
- Marchal, O., T. F. Stocker & F. Joos (1998), "Impact of oceanic reorganizations on the ocean carbon cycle and atmospheric carbon dioxide content", *Paleoceanography*, vol. 13, no. 3, pp. 225–244.
- Marinov, I., S. C. Doney, I. D. Lima, K Lindsay, J. K. Moore & N Mahowald (2013), "North-South asymmetry in the modeled phytoplankton community response to climate change over the 21st century", *Global Biogeochemical Cycles*, vol. 27, no. 4, pp. 1274–1290.

- Mariotti, V, L Bopp, A Tagliabue, M Kageyama & D Swingedouw (2012), “Marine productivity response to Heinrich events: a model-data comparison”, *Climate of the Past*, vol. 8, no. 5, pp. 1581–1598.
- Martin, J. H., G. A. Knauer, D. M. Karl & W. W. Broenkow (1987), “VERTEX: carbon cycling in the northeast Pacific”, *Deep Sea Research Part A. Oceanographic Research Papers*, vol. 34, no. 2, pp. 267–285.
- Martinez, E., D. Antoine, F. D’Ortenzio & C de Boyer Montégut (2011), “Phytoplankton spring and fall blooms in the North Atlantic in the 1980s and 2000s”, *Journal of Geophysical Research: Oceans*, vol. 116, no. C11.
- Matsumoto, K. & Y. Yokoyama (2013), “Atmospheric $\Delta^{14}\text{C}$ reduction in simulations of Atlantic overturning circulation shutdown”, *Global Biogeochemical Cycles*, vol. 27, no. 2, pp. 296–304.
- Matthews, D. H. et al. (2021), “An integrated approach to quantifying uncertainties in the remaining carbon budget”, *Communications Earth & Environment*, vol. 2, no. 1, p. 7.
- McGillicuddy, D. J. (2016), “Mechanisms of Physical-Biological-Biogeochemical Interaction at the Oceanic Mesoscale”, *Annual Review of Marine Science*, vol. 8, no. 1, pp. 125–159.
- Meinshausen, M et al. (2020), “The shared socio-economic pathway (SSP) greenhouse gas concentrations and their extensions to 2500”, *Geosci. Model Dev.*, vol. 13, no. 8, pp. 3571–3605.
- Mengis, N et al. (2020), “Evaluation of the University of Victoria Earth System Climate Model version 2.10 (UVic ESCM 2.10)”, *Geoscientific Model Development*, vol. 13, no. 9, pp. 4183–4204.
- Menviel, L, M. H. England, K. J. Meissner, A Mouchet & J Yu (2014), “Atlantic-Pacific seesaw and its role in outgassing CO₂ during Heinrich events”, *Paleoceanography*, vol. 29, no. 1, pp. 58–70.
- Menviel, L, A Timmermann, A Mouchet & O Timm (2008), “Meridional reorganizations of marine and terrestrial productivity during Heinrich events”, *Paleoceanography*, vol. 23, no. 1.
- Middelburg, J. J., K. Soetaert & M. Hagens (2020), “Ocean Alkalinity, Buffering and Biogeochemical Processes”, *Reviews of Geophysics*, vol. 58, no. 3, e2019RG000681.
- Millero, F. J. (1983), “CHAPTER 43 - Influence of Pressure on Chemical Processes in the Sea”, in: ed. by RILEY, J. P. & CHESTER, R. B. T. C. O., Academic Press, pp. 1–88, ISBN: 978-0-12-588608-6.
- Moore, C. M. et al. (2013a), “Processes and patterns of oceanic nutrient limitation”, *Nature Geoscience*, vol. 6, no. 9, pp. 701–710.
- Moore, J. K., S. C. Doney & K. Lindsay (2004), “Upper ocean ecosystem dynamics and iron cycling in a global three-dimensional model”, *Global Biogeochemical Cycles*, vol. 18, no. 4.
- Moore, J. K., K. Lindsay, S. C. Doney, M. C. Long & K. Misumi (2013b), “Marine Ecosystem Dynamics and Biogeochemical Cycling in the Community Earth System Model [CESM1(BGC)]: Comparison of the 1990s with the 2090s under the RCP4.5 and RCP8.5 Scenarios”, *Journal of Climate*, vol. 26, no. 23, pp. 9291–9312.

- Moore, J. K. et al. (2018), “Sustained climate warming drives declining marine biological productivity”, *Science*, vol. 359, no. 6380, 1139 LP–1143.
- Moore, J., S. C. Doney, J. A. Kleypas, D. M. Glover & I. Y. Fung (2001), “An intermediate complexity marine ecosystem model for the global domain”, *Deep Sea Research Part II: Topical Studies in Oceanography*, vol. 49, no. 1, pp. 403–462.
- Morán, X. A. G., Á. López-Urrutia, A. Calvo-Díaz & W. K. W. Li (2010), “Increasing importance of small phytoplankton in a warmer ocean”, *Global Change Biology*, vol. 16, no. 3, pp. 1137–1144.
- Morice, C. P. et al. (2021), “An Updated Assessment of Near-Surface Temperature Change From 1850: The HadCRUT5 Data Set”, *Journal of Geophysical Research: Atmospheres*, vol. 126, no. 3, e2019JD032361.
- Mucci, A (1983), “The solubility of calcite and aragonite in seawater at various salinities, temperatures, and one atmosphere total pressure”, *American Journal of Science*, vol. 283, pp. 780–799.
- Muller, R. A. & G. J. MacDonald (2000), *Ice Ages and Astronomical Causes*, Springer-Verlag, ISBN: 1-85233-634-X.
- Munday, D. R., H. L. Johnson & M. D. P (2014), “Impacts and effects of mesoscale ocean eddies on ocean carbon storage and atmospheric pCO₂”, *Global Biogeochemical Cycles*, vol. 28, no. 8, pp. 877–896.
- Munhoven, G (2013), “Mathematics of the total alkalinity–pH equation - pathway to robust and universal solution algorithms: the SolveSAPHE package v1.0.1”, *Geoscientific Model Development*, vol. 6, no. 4, pp. 1367–1388.
- NASA (2018), *NASA-GISS GISS-E2.1G model output prepared for CMIP6 CMIP 1pctCO2*.
- NASA (2019), *NASA-GISS GISS-E2-2-G model output prepared for CMIP6 CMIP 1pctCO2*.
- Negrete-García, G., J. Y. Luo, M. C. Long, K. Lindsay, M. Levy & A. D. Barton (2022), “Plankton energy flows using a global size-structured and trait-based model”, *Progress in Oceanography*, p. 102898.
- Neubauer, D. et al. (2019), *HAMMOZ-Consortium MPI-ESM1.2-HAM model output prepared for CMIP6 CMIP 1pctCO2*.
- Nielsen, S. B., M. Jochum, J. B. Pedro, C. Eden & R. Nuterman (2019), “Two-Timescale Carbon Cycle Response to an AMOC Collapse”, *Paleoceanography and Paleoclimatology*, vol. 34, no. 4, pp. 511–523.
- Obata, A. (2007), “Climate Carbon Cycle Model Response to Freshwater Discharge into the North Atlantic”, *Journal of Climate - J CLIMATE*, vol. 20, pp. 5962–5976.
- O’Neill, B. C. et al. (2020), “Achievements and Needs for the Climate Change Scenario Framework”, *Nature Climate Change*, vol. 10.
- O’Neill, C. M., A. M. Hogg, M. J. Ellwood, S. M. Eggins & B. N. Opdyke (2019), “The [simple carbon project] model v1.0”, *Geoscientific Model Development*, vol. 12, no. 4, pp. 1541–1572.
- Orihuela-Pinto, B., M. H. England & A. S. Taschetto (2022), “Interbasin and interhemispheric impacts of a collapsed Atlantic Overturning Circulation”, *Nature Climate Change*, vol. 12, no. 6, pp. 558–565.
- Osman, M. B. et al. (2019), “Industrial-era decline in subarctic Atlantic productivity”, *Nature*, vol. 569, no. 7757, pp. 551–555.

- Palter, J. B. (2015), “The Role of the Gulf Stream in European Climate”, *Annual Review of Marine Science*, vol. 7, no. 1, pp. 113–137.
- Park, S. & J. Shin (2019), *SNU SAMO-UNICON model output prepared for CMIP6 CMIP 1pctCO2*.
- Petit, J. R. et al. (1999), “Climate and atmospheric history of the past 420,000 years from the Vostok ice core, Antarctica”, *Nature*, vol. 399, no. 6735, pp. 429–436.
- van der Ploeg, F. (2018), “The safe carbon budget”, *Climatic Change*, vol. 147, no. 1, pp. 47–59.
- Possenti, L et al. (2023), “Predicting the contribution of climate change on North Atlantic underwater sound propagation”, *PeerJ*, vol. 11, no. e16208.
- Rae, J. W. B., Y. G. Zhang, X. Liu, G. L. Foster, H. M. Stoll & R. D. M. Whiteford (2021), “Atmospheric CO₂ over the Past 66 Million Years from Marine Archives”, *Annual Review of Earth and Planetary Sciences*, vol. 49, no. 1, pp. 609–641.
- Rahmstorf, S (1996), “On the freshwater forcing and transport of the Atlantic thermohaline circulation”, *Climate Dynamics*, vol. 12, no. 12, pp. 799–811.
- Rahmstorf, S. (2002), “Ocean circulation and climate during the past 120,000 years”, *Nature*, vol. 419, no. 6903, pp. 207–214.
- Riahi, K. et al. (2017), “The Shared Socioeconomic Pathways and their energy, land use, and greenhouse gas emissions implications: An overview”, *Global Environmental Change*, vol. 42, pp. 153–168.
- Richardson, A. J. & D. S. Schoeman (2004), “Climate impact on plankton ecosystems in the Northeast Atlantic.”, *Science (New York, N.Y.)*, vol. 305, no. 5690, pp. 1609–1612.
- Ridgwell, A et al. (2007), “Marine geochemical data assimilation in an efficient Earth System Model of global biogeochemical cycling”, *Biogeosciences*, vol. 4, no. 1, pp. 87–104.
- Ridley, J., M. Menary, T. Kuhlbrodt, M. Andrews & T. Andrews (2019), *MOHC HadGEM3-GC31-LL model output prepared for CMIP6 CMIP 1pctCO2*.
- Ridley, J., M. Menary, T. Kuhlbrodt, M. Andrews & T. Andrews (2020), *MOHC HadGEM3-GC31-MM model output prepared for CMIP6 CMIP 1pctCO2*.
- Rivero-Calle, S., A. Gnanadesikan, E. C. Del Castillo, B. W. M. & G. S. D. (2015), “Multidecadal increase in North Atlantic coccolithophores and the potential role of rising CO₂”, *Science*, vol. 350, no. 6267, pp. 1533–1537.
- Rooth, C. (1982), “Hydrology and ocean circulation”, *Progress in Oceanography*, vol. 11, no. 2, pp. 131–149.
- Rothman, D. H. (2015), “Earth’s carbon cycle: A mathematical perspective”, *Bulletin of the American Mathematical Society*, vol. 52, pp. 47–64.
- Rothman, D. H. (2019), “Characteristic disruptions of an excitable carbon cycle”, *Proceedings of the National Academy of Sciences*, vol. 116, no. 30, 14813 LP–14822.
- Rousseaux, C. S. & W. W. Gregg (2015), “Recent decadal trends in global phytoplankton composition”, *Global Biogeochemical Cycles*, vol. 29, no. 10, pp. 1674–1688.
- Sabine, C. L. et al. (2004), “The oceanic sink for anthropogenic CO₂.”, *Science (New York, N.Y.)*, vol. 305, no. 5682, pp. 367–371.

- Saenko, O. A., D. Yang & P. G. Myers (2017), “Response of the North Atlantic dynamic sea level and circulation to Greenland meltwater and climate change in an eddy-permitting ocean model”, *Climate Dynamics*, vol. 49, no. 7, pp. 2895–2910.
- Sanders, R. et al. (2014), “The Biological Carbon Pump in the North Atlantic”, *Progress in Oceanography*, vol. 129, pp. 200–218.
- Sarmiento, J. L., T. M. C. Hughes, R. J. Stouffer & S. Manabe (1998), “Simulated response of the ocean carbon cycle to anthropogenic climate warming”, *Nature*, vol. 393, no. 6682, pp. 245–249.
- Sarmiento, J. L. & N. Gruber (2006), *Ocean biogeochemical dynamics*, English, Princeton SE - xii, 503 pages, 8 pages of plates : illustrations (some color), maps (some color) ; 29 cm: Princeton University Press, ISBN: 9780691017075 0691017077.
- Schmittner, A. (2005), “Decline of the marine ecosystem caused by a reduction in the Atlantic overturning circulation”, *Nature*, vol. 434, no. 7033, pp. 628–633.
- Schmittner, A., E. J. Brook & J. Ahn (2007), *Impact of the ocean’s Overturning circulation on atmospheric CO₂*.
- Schmittner, A. & E. D. Galbraith (2008), “Glacial greenhouse-gas fluctuations controlled by ocean circulation changes”, *Nature*, vol. 456, no. 7220, pp. 373–376.
- Scoccimarro, E., A. Bellucci & D. Peano (2021), *CMCC CMCC-CM2-HR4 model output prepared for CMIP6 CMIP 1pctCO₂*.
- Seferian, R. (2018), *CNRM-CERFACS CNRM-ESM2-1 model output prepared for CMIP6 CMIP for experiment 1pctCO₂*.
- Séférian, R. et al. (2020), “Tracking Improvement in Simulated Marine Biogeochemistry Between CMIP5 and CMIP6”, *Current Climate Change Reports*, vol. 6, no. 3, pp. 95–119.
- Setty, S. et al. (2023), “Loss of Earth system resilience during early Eocene transient global warming events”, *Science Advances*, vol. 9, no. 14, eade5466.
- Sinet, S, A. S. von der Heydt & H. A. Dijkstra (2023), “AMOC Stabilization Under the Interaction With Tipping Polar Ice Sheets”, *Geophysical Research Letters*, vol. 50, no. 2, e2022GL100305.
- Smeed, D. et al. (2015), *Atlantic meridional overturning circulation observed by the RAPID-MOCHA-WBTS (RAPID-Meridional Overturning Circulation and Heatflux Array-Western Boundary Time Series) array at 26N from 2004 to 2014*. en.
- Smith, R. et al. (2010), “The Parallel Ocean Program (POP) reference manual: Ocean component of the Community Climate System Model (CCSM)”, in.
- Song, Z., F. Qiao, Y. Bao, Q. Shu, Y. Song & X. Yang (2020), *FIO-QLNM FIO-ESM2.0 model output prepared for CMIP6 CMIP 1pctCO₂*.
- Steinacher, M et al. (2010), “Projected 21st century decrease in marine productivity: a multi-model analysis”, *Biogeosciences*, vol. 7, no. 3, pp. 979–1005.
- Stocker, T. F. & S. J. Johnsen (2003), “A minimum thermodynamic model for the bipolar seesaw”, *Paleoceanography*, vol. 18, no. 4.
- Stommel, H. (1961), “Thermohaline Convection with Two Stable Regimes of Flow”, *Tellus*, vol. 13, no. 2, pp. 224–230.
- Stouffer, R. (2019), *UA MCM-UA-1-0 model output prepared for CMIP6 CMIP 1pctCO₂*.
- Sun, Y. et al. (2022), “Ice sheet decline and rising atmospheric CO₂ control AMOC sensitivity to deglacial meltwater discharge”, *Global and Planetary Change*, vol. 210, p. 103755.

- Swart, N. C. et al. (2019a), *CCCma CanESM5 model output prepared for CMIP6 CMIP 1pctCO2*.
- Swart, N. C. et al. (2019b), *CCCma CanESM5.1 model output prepared for CMIP6 CMIP 1pctCO2*.
- Swingedouw, D, L Bopp, A Matras & P Braconnot (2007), “Effect of land-ice melting and associated changes in the AMOC result in little overall impact on oceanic CO2 uptake”, *Geophysical Research Letters*, vol. 34, no. 23.
- Tagliabue, A. et al. (2021), “Persistent Uncertainties in Ocean Net Primary Production Climate Change Projections at Regional Scales Raise Challenges for Assessing Impacts on Ecosystem Services”, *Frontiers in Climate*, vol. 3.
- Talley, L. D. (2013), “Closure of the Global Overturning Circulation Through the Indian, Pacific, and Southern Oceans: Schematics and Transports”, *Oceanography*, vol. 26, no. 1, pp. 80–97.
- Tatebe, H. & M. Watanabe (2018), *MIROC MIROC6 model output prepared for CMIP6 CMIP 1pctCO2*.
- Taylor, K. E., R. J. Stouffer & G. A. Meehl (2012), “An Overview of CMIP5 and the Experiment Design”, *Bulletin of the American Meteorological Society*, vol. 93, no. 4, pp. 485–498.
- Tittensor, D. P. et al. (2021), “Next-generation ensemble projections reveal higher climate risks for marine ecosystems”, *Nature Climate Change*, vol. 11, no. 11, pp. 973–981.
- Toggweiler, J. R. & J. Russell (2008), “Ocean circulation in a warming climate”, *Nature*, vol. 451, no. 7176, pp. 286–288.
- Vellinga, M. & R. A. Wood (2002), “Global Climatic Impacts of a Collapse of the Atlantic Thermohaline Circulation”, *Climatic Change*, vol. 54, no. 3, pp. 251–267.
- Vellinga, M. & R. A. Wood (2008), “Impacts of thermohaline circulation shutdown in the twenty-first century”, *Climatic Change*, vol. 91, no. 1, pp. 43–63.
- Voldoire, A. (2019), *CNRM-CERFACS CNRM-CM6-1-HR model output prepared for CMIP6 CMIP 1pctCO2*.
- Volk, T. & M. I. Hoffert (1985), “Ocean Carbon Pumps: Analysis of Relative Strengths and Efficiencies in Ocean-Driven Atmospheric CO2 Changes”, in: *The Carbon Cycle and Atmospheric CO2: Natural Variations Archean to Present*, American Geophysical Union (AGU), pp. 99–110, ISBN: 9781118664322.
- Wanninkhof, R. (1992), “Relationship between wind speed and gas exchange over the ocean”, *Journal of Geophysical Research: Oceans*, vol. 97, no. C5, pp. 7373–7382.
- Weijer, W, W Cheng, O. A. Garuba, A Hu & B. T. Nadiga (2020), “CMIP6 Models Predict Significant 21st Century Decline of the Atlantic Meridional Overturning Circulation”, *Geophysical Research Letters*, vol. 47, no. 12, e2019GL086075.
- Weijer, W et al. (2019), “Stability of the Atlantic Meridional Overturning Circulation: A Review and Synthesis”, *Journal of Geophysical Research: Oceans*, vol. 124, no. 8, pp. 5336–5375.

- Weiss, R. F. (1974), “Carbon dioxide in water and seawater: the solubility of a non-ideal gas”, *Marine Chemistry*, vol. 2, no. 3, pp. 203–215.
- van Westen, R. M. & H. A. Dijkstra (2023a), “Persistent Climate Model Biases in the Atlantic Ocean’s Freshwater Transport”, *EGUsphere*, vol. 2023, pp. 1–29.
- van Westen, R. M. & H. A. Dijkstra (2023b), “Asymmetry of AMOC Hysteresis in a State-Of-The-Art Global Climate Model”, *Geophysical Research Letters*, vol. 50, no. 22, e2023GL106088.
- Westerhold, T. et al. (2020), “An astronomically dated record of Earth’s climate and its predictability over the last 66 million years”, *Science*, vol. 369, no. 6509, pp. 1383–1387.
- Whitt, D. B. & M. F. Jansen (2020), “Slower nutrient stream suppresses Subarctic Atlantic Ocean biological productivity in global warming”, *Proceedings of the National Academy of Sciences*, vol. 117, no. 27, pp. 15504–15510.
- Wieners, K.-H. et al. (2019), *MPI-M MPI-ESM1.2-LR model output prepared for CMIP6 CMIP 1pctCO2*.
- Williams, R. G. & M. J. Follows (2011), *Ocean Dynamics and the Carbon Cycle: Principles and Mechanisms*, Cambridge: Cambridge University Press, ISBN: 9780521843690.
- Wilson, J. D. et al. (2022), “The biological carbon pump in CMIP6 models: 21st century trends and uncertainties”, *Proceedings of the National Academy of Sciences*, vol. 119, no. 29, e2204369119.
- Wood, R. A., J. M. Rodríguez, R. S. Smith, L. C. Jackson & E. Hawkins (2019), “Observable, low-order dynamical controls on thresholds of the Atlantic meridional overturning circulation”, *Climate Dynamics*, vol. 53, no. 11, pp. 6815–6834.
- Wunderling, N, J. F. Donges, J Kurths & R Winkelmann (2021), “Interacting tipping elements increase risk of climate domino effects under global warming”, *Earth System Dynamics*, vol. 12, no. 2, pp. 601–619.
- Yamamoto, A, A Abe-Ouchi & Y Yamanaka (2018), “Long-term response of oceanic carbon uptake to global warming via physical and biological pumps”, *Biogeosciences*, vol. 15, no. 13, pp. 4163–4180.
- Yu, J et al. (2019), “More efficient North Atlantic carbon pump during the Last Glacial Maximum”, *Nature Communications*, vol. 10, no. 1.
- Yu, Y. (2019), *CAS FGOALS-f3-L model output prepared for CMIP6 CMIP 1pctCO2*.
- Yukimoto, S. et al. (2019), *MRI MRI-ESM2.0 model output prepared for CMIP6 CMIP 1pctCO2*.
- Zeebe, R. E. (2012), “LOSCAR: Long-term Ocean-atmosphere-Sediment Carbon cycle Reservoir Model v2.0.4”, *Geoscientific Model Development*, vol. 5, no. 1, pp. 149–166.
- Zeebe, R. E. & P. Westbroek (2003), “A simple model for the CaCO₃ saturation state of the ocean: The “Strangelove,” the “Neritan,” and the “Cretan” Ocean”, *Geochemistry, Geophysics, Geosystems*, vol. 4.
- Zeebe, R. E., J. C. Zachos & G. R. Dickens (2009), “Carbon dioxide forcing alone insufficient to explain Palaeocene–Eocene Thermal Maximum warming”, *Nature Geoscience*, vol. 2, no. 8, pp. 576–580.

- Zelinka, M. D. et al. (2020), “Causes of Higher Climate Sensitivity in CMIP6 Models”, *Geophysical Research Letters*, vol. 47, no. 1, e2019GL085782.
- Zhang, R. & T. L. Delworth (2005), “Simulated Tropical Response to a Substantial Weakening of the Atlantic Thermohaline Circulation”, *Journal of Climate*, vol. 18, no. 12, pp. 1853–1860.
- Zhang, X., G. Knorr, G. Lohmann & S. Barker (2017), “Abrupt North Atlantic circulation changes in response to gradual CO₂ forcing in a glacial climate state”, *Nature Geoscience*, vol. 10, no. 7, pp. 518–523.
- Zhu, J, X Zeng, X Gao & H Zhang (2022), “Response of Terrestrial Net Primary Production to Quadrupled CO₂ Forcing: A Comparison between the CAS-ESM2 and CMIP6 Models”, *Biology*, vol. 11, no. 12.
- Zhu, J., Z. Liu, J. Zhang & W. Liu (2015), “AMOC response to global warming: dependence on the background climate and response timescale”, *Climate Dynamics*, vol. 44, no. 11, pp. 3449–3468.
- Zickfeld, K., M. Eby & A. J. Weaver (2008), “Carbon-cycle feedbacks of changes in the Atlantic meridional overturning circulation under future atmospheric CO₂”, *Global Biogeochemical Cycles*, vol. 22, no. 3.
- Ziehn, T. et al. (2019), *CSIRO ACCESS-ESM1.5 model output prepared for CMIP6 CMIP 1pctCO2*.

Acknowledgements

The past four years have been quite an intense journey, professionally and especially personally. Looking back, it sometimes feels like my personal life has been a huge mess more often than not. However, I finally had the courage to take the first steps in finding and becoming 'me'. Though the road is and will be bumpy, the destination is a better place than where I was and am. I am thankful to have Kayla, my cute, little fur baby, by my side. You are the best daughter I could wish for.

Professionally, I want to start with thanking Henk and Anna for their supervision these past years. The freedom and trust I received really motivated me these past four years and I look forward to continuing to work with you. You also gave me time to figure myself out when I really needed it. It really helped to release some of the pressure I was under. Thank you!

Next I want to thank all the wonderful people at the IMAU. The IMAU has been a great place to study and work for these past years and that is of course in large part due to the people of IMAU. During my PhD I was part of the ocean, and paleo group and I want to thank all past and current members of these groups for listening and providing feedback on my work, as well as sharing yours. My special thanks go out to Rene, for your very enthusiastic supervision during my master's thesis. I am not sure I would have pursued a PhD if it was not for working with you on my master's thesis. I also want to thank Arthur and Siren, it was (and is) great to share an office with you. Though I find it difficult to share some of my struggles, you both were able to make me feel safe and accepted which makes it so much easier to share them. Thank you! Lastly, I want to thank Floor, Clara, Judith and Mariken for the organizational support at IMAU and Michael for your efforts on the CESM2 simulations.

During my PhD I had the privilege to meet many new people. First, I want to thank all the people at NESSC for interesting workshops, conferences and discussions, and I want to especially thank Shruti. Our projects were closest to each other, and I am happy we were able to get a collaboration out of it, which will (hopefully) make a very nice publication. Next, I want to thank the people I met at the Urbino Summer School for Paleoclimatology. Though I learnt a lot about paleoclimates these weeks, my highlight from this summer school was all the new people I met. My special thanks go out to Anna, Blanka, Elena, Irene, and Mery. You really pulled me

through this summer school and without you the experience would not have been half as good. Anna, I want to thank you for keeping in touch and hosting me in Graz a couple of times and of course for agreeing to be my paranymph. Lastly, I want to thank all organizers and attendees of the ClimEco8 Summer School. Also this summer school was a great, inspiring experience and definitely one of the highlights of my PhD.

And last, but not least, I need to thank a lot of people who have contributed to making this world a safer place to live in for LGBTQIA+ people. Often in the face of hate, violence and (death) threats there are people who have put themselves out there to fight for LGBTQIA+ rights. Without a lot of these people I would not be able to be who I am today. I cannot do justice to all the people who have made a meaningful contribution over the past decades, but thank you!



List of Publications

Lead Author

Published

(1) Boot, A, R. M. van Westen & H. A. Dijkstra (2021), “Multidecadal polynya formation in a conceptual (box) model”, *Ocean Science*, vol. 17, no. 1, pp. 335–350.

(2) Boot, A, A. S. von der Heydt & H. A. Dijkstra (2022), “Effect of the Atlantic Meridional Overturning Circulation on Atmospheric pCO₂ Variations”, *Earth Syst. Dynam.*, pp. 1–26.

(3) Boot, A, A. S. von der Heydt & H. A. Dijkstra (2023a), “Effect of Plankton Composition Shifts in the North Atlantic on Atmospheric pCO₂”, *Geophysical Research Letters*, vol. 50, no. 2, e2022GL100230.

Under review

(4) Boot, A. A., A. S. von der Heydt & H. A. Dijkstra (2023b), “Potential effect of the marine carbon cycle on the multiple equilibria window of the Atlantic Meridional Overturning Circulation”, *Earth System Dynamics Discussions*, vol. 2023, pp. 1–27.

(5) Boot, A. A., A. S. von der Heydt & H. A. Dijkstra (2023c), “Response of atmospheric pCO₂ to a strong AMOC weakening under low and high emission scenarios”, *Under review at Climate Dynamics*.

Co-Author

(1) Possenti, L, G Reichart, L de Nooijer, F Lam, C de Jong, M Colin, et al. (2023), “Predicting the contribution of climate change on North Atlantic underwater sound propagation”, *PeerJ*, vol. 11, no. e16208.

About the Author

Amber Boot was born on 13 September 1994 in Ede. During her youth she was already keen on learning about the natural world around her. After finishing high school she moved to Enschede to study the Bachelor Civil Engineering at the University of Twente. In 2015, she switched universities and moved to the Delft University of Technology to study Hydraulic Engineering. Quite soon she realized that true engineering was not her thing, but fluid dynamics was. After courses on physical oceanography and stratified flows, she looked towards opportunities to extend this knowledge. She found this in the Climate Physics master at Utrecht University, which immediately was the right fit. For her master's thesis she looked at multi-decadal polynya formation in the Weddell Sea.

In her PhD she started working on the feedbacks between the marine carbon cycle and the Atlantic Meridional Overturning Circulation. She has worked with box models and Earth System Models to better understand the feedbacks between the two components. The interdisciplinary topic of her PhD was an important motivator during her PhD. Amber will continue her journey as a postdoc within the same group working on tipping of the Atlantic overturning circulation.



“Freedom of speech?
Freedom means nothing
when you could shoot me down
with the push of a button

Freedom of speech?
Freedom means nothing
when I don't own my body”

Pink Barbie Bandaid by Scene Queen (2022)

